

Electrical Transport in Metal Wire Networks : Experimental Strategies and Theoretical Insights

A Thesis

Submitted for the Degree of
DOCTOR OF PHILOSOPHY

by

ANKUSH KUMAR



CHEMISTRY AND PHYSICS OF MATERIALS UNIT
JAWAHARLAL NEHRU CENTRE FOR ADVANCED SCIENTIFIC
RESEARCH

(A Deemed University)

Bangalore – 560 064

November 2017

Dedicated to nature....

DECLARATION

I hereby declare that the matter embodied in the thesis entitled “**Electrical Transport in Metal Wire Networks : Experimental Strategies and Theoretical Insights**” is the result of investigations carried out by me at the Chemistry and Physics of Materials Unit, Jawaharlal Nehru Centre for Advanced Scientific Research, Bangalore, India under the supervision of **Professor Giridhar U. Kulkarni**, and that it has not been submitted elsewhere for the award of any degree or diploma.

In keeping with the general practice in reporting scientific observations, due acknowledgment has been made whenever the work described is based on the findings of other investigators. Any omission which might have occurred by oversight or error in judgement is regretted.

Ankush Kumar

CERTIFICATE

I hereby certify that the matter embodied in this thesis entitled “**Electrical Transport in Metal Wire Networks : Experimental Strategies and Theoretical Insights**” has been carried out by **Mr. Ankush Kumar** at the Chemistry and Physics of Materials Unit, Jawaharlal Nehru Centre for Advanced Scientific Research, Bangalore, India under my supervision and that it has not been submitted elsewhere for the award of any degree or diploma.

Professor Giridhar U. Kulkarni
(Research Supervisor)

Acknowledgements

It is my pleasure to acknowledge my research supervisor Professor Giridhar U. Kulkarni for his complete guidance in this research journey. I am thankful to him to give me ample freedom and suggesting the projects. His broad thinking, enthusiasm, approach to looking at problem and passion for science will remain an inspiration to me. I acknowledge Prof. C. N. R. Rao who is constant energy and inspiration source for all of us and creating this research centre.

I acknowledge my all collaborators Prof Timothy Fisher (Purdue University), Prof. Amy Marconnet (Purdue University), Prof. N. S. Vidhyadhiraja (JNCASR, Bangalore), Prof. Sujata Tarafdar (Jadavpur University) , Prof. Tapati Dutta (St. Xavier's College, Kolkata), Prof. Sapati Sadhukhan (Jogesh Chandra Chaudhuri College, Kolkata) and lab members Dr. Ritu Gupta (currently IIT Jodhpur), Dr. K. D. M Rao (currently IACS, Kolkata), Dr. S. Kiruthika, Rajashekhara Pujar, Sunil Walia , Indrajit Mondol and Nikita Gupta. It was learning and enjoyable to work with all of them.

I acknowledge my other all past and present lab members Dr. Boya Radha, Dr. Narendra Kurra, Dr. Umesha Mogera, Dr. Gangaiah Mettela, Dr. Murali Gedda, Dr. Shobhin L.R., Dr. Ashutosh K. Singh, Suman, Chaitali, Amala, Aman Anand and Suchitra for useful discussions and many learning lab talks. I acknowledge all my Int-PhD batchmates for their help and nice time during course-work.

I thank faculty members, Prof. Chandrabhas Narayana, Prof. Balasubramanian Sundaram, Prof. M. Eswaramoorthy, Prof. G. U. Kulkarni, Prof. K. S. Narayan, Prof. S. M. Shivaprasad, Prof. A. Sundaresan, Prof. Tapas Kumar Maji, Prof. Subi Jacob George, Prof. T. Govindaraju, Prof. H. Ila, Dr. Sebastian C Peter, Prof. Swapan K.

Pati, Dr. Ranjani Viswanatha, Dr. Sridhar Rajaram and Prof. K. R. Sreenivas for their useful course-works.

I acknowledge past and present CPMU chairman, administrative officer, Int-PhD coordinators and JNC president. I acknowledge timely and ready assistance of Dr. S. Basavaraj, Mrs. Selvi, Mr. Vasu for various instruments. I thank library staff where I spent maximum duration in Ph.D., Complab facilities, hostel facilities, administrative and academic staff. I especially thank Vanitha and Sunil V. for various lab activities.

I utmost thank editors and reviewers for reviewing my manuscripts and giving useful advice. I acknowledge open source community for providing the operating system and various languages and software. I thank authors and publishers for providing the copyrighted materials for analysis. I thank Prof C. Liu (Nanjing University) for providing CIAS software and Dr. Mehar Prakash for bringing our attention.

I acknowledge JNCASR for fellowship and Department of Science and Technology, India for funding and IUSSTF for the travel grant to Purdue University. Prof. Balasubramanian Sundaram for the CCMS computational facility. I acknowledge Centre for Nano and Soft Matter for facilities and hospitality. I acknowledge direct/indirect taxpayer's money for supporting the research.

I am thankful for the legacy of great scientists and teachers, their lives and words inspire me to enjoy science. I am happy to thank all my great and cheerful friends of JNC for their cooperation, happiness, and love. I utmost thank them for their thesis corrections as well. Indumati madam, Poorna, and Teju, thanks for the get-togethers. I acknowledge my family for inexpressible support. At last, I am especially grateful to this beautiful nature which is an inspiration for my science.

Abstract

The thesis work pertains to experimental investigations and theoretical efforts towards understanding electrical and thermal conduction properties of metal wire networks and their effective usage as optically transparent conductors. As background to the subject matter, **Chapter 1** introduces various patterning tools and lithography in device fabrication while citing examples of interconnected patterns in nature. The discussion then extends to crack networks used as templates to obtain fine metal meshes, their importance in transparent conducting electrode (TCE) devices as well as literature efforts in modelling network based TCEs including an introduction to Graph theory approach and electrical percolation.

Chapter 2 deals with different kinds of metal network based TCEs. Here, a model of TCE based on graph theory is introduced and effective medium theory to calculate sheet resistance based on network properties is also presented. The optimum conditions for efficient TCE have been identified, which are minimum curvilinearity, high compactness, low wire width distribution and a high degree of connectivity. An algorithm developed for quantifying the current carrying backbone as against dangling and isolated wires is presented. The backbone is also calculated based on analytical treatments. The current distribution in the network obtained from a crack template is compared with those found in networks formed by depositing metal nanowires. Theoretical models dealing with metal mesh electrodes used in different contexts, solar cells and strain sensors have been developed and presented in this chapter.

The crack formation by desiccation although spontaneous can be guided or manipulated using external agents. **Chapter 3** discusses few strategies for modulating crack

templates for efficient TCEs. An attempt has been made to improve the understanding of desiccation induced crack network formation using a spring fusion model. The optimum mechanical parameters required for efficient TCEs are explored with this approach. Repeated wet-drying cycles of already formed crack templates lead to higher crack density and enhanced connectivity important for efficient charge collection in solar cells. Instead of using a single solvent for crack dispersion, the azeotropic mixture of water and isopropanol has proved useful to bring down the crack width, < 500 nm with a very high degree of connectivity. Further, a simple technique involving gravity flow of the dispersion has been developed to obtain parallel grating type crack patterns. The same is shown to be due to the gradient in the dried layer thickness naturally created by the gravity flow.

Chapter 4 deals with thermal transport properties of metal networks when used as Joule heaters. IR microscopy has been employed to measure the temperature distribution in the network in the thermal background of the substrate. A theoretical model is proposed to link the network structure with the steady state temperature. The breakdown mechanism of the network-based heater has also been explored. Using Green's function approach, the transient heat transfer process has been examined to study how the heat generated in the wire regions spreads down to and across the substrate area to make the temperature uniform with time.

In crack networks, the crack width variation is inevitable. **Chapter 5** explores the hierarchy of crack networks- wide cracks to the narrowest ones, and how hierarchy plays important role in efficient TCE fabrication. The chapter also presents a strategy and the associated image analysis method which when applied on fully formed crack pattern provides an insight into the time sequence of crack formation. The approach has been generalized to include hierarchy among road networks, vein networks in leaves etc. Finally, a Figure of Merit has been defined to compare various hierarchical structures.

Chapter 6 discusses the scope of thesis and future possibilities.

Table of contents

List of figures	xvii
List of tables	xxxiii
1 Introduction	1
1.1 Patterns in nature and technology	2
1.2 Crack patterns	4
1.2.1 Crack networks as templates for metal meshes	5
1.3 Metal network as transparent electrodes	5
1.4 Modelling a transparent electrode	7
1.4.1 Graph theory	8
1.4.2 Percolation theory	10
1.5 Experimental and computational tools	12
1.6 Scope of the present thesis	13
2 Comparing different metal network based transparent conductors	15
2.1 Evaluating conducting network-based transparent electrodes from geometrical considerations	16
2.1.1 Summary	16
2.1.2 Introduction	17
2.1.3 Scope of the present investigations	20
2.1.4 Results and Discussion	21
2.1.5 Conclusion	35

2.2	Current distribution in conducting nanowire networks	36
2.2.1	Summary	36
2.2.2	Introduction	36
2.2.3	Scope of the present investigations	39
2.2.4	Results and Discussion	39
2.2.5	Conclusion	53
2.3	Aspects related to charge collection by a metal network	55
2.3.1	Summary	55
2.3.2	Introduction	56
2.3.3	Scope of the present investigations	57
2.3.4	Results and Discussion	58
2.3.5	Conclusion	70
2.4	Embedded metal mesh as a strain sensor	71
2.4.1	Summary	71
2.4.2	Introduction	71
2.4.3	Scope of the present investigations	72
2.4.4	Results and discussion	72
2.4.5	Conclusion	80
3	Modulating crack network patterns for efficient transparent electrodes	81
3.1	Designing optimum crack pattern template for fabricating transparent conducting electrodes: A spring network simulation in 3 dimensions . .	82
3.1.1	Introduction	82
3.1.2	Scope of the present investigations	83
3.1.3	Experiment	83
3.1.4	The Simulation Procedure	84
3.1.5	Conductivity calculation	86
3.1.6	Simulation Results	89
3.1.7	Discussion	95

3.1.8	Conclusion	96
3.2	Modulation via wet-drying cycles of crack template	97
3.2.1	Introduction	97
3.2.2	Scope of the present investigations	98
3.2.3	Results and Discussion	99
3.2.4	Conclusion	106
3.3	Modulation by using mixture of solvents	107
3.3.1	Introduction	107
3.3.2	Scope of the present investigations	108
3.3.3	Results and Discussions	108
3.3.4	Conclusion	113
3.4	Designing of parallel cracks using a simple gravity flow method	114
3.4.1	Introduction	114
3.4.2	Scope of the present investigations	115
3.4.3	Results and Discussions	115
3.4.4	Conclusion	124
4	Thermal transport properties of metal networks	125
4.1	Microscopic evaluation of electrical and thermal conduction in metal wire networks	126
4.1.1	Introduction	126
4.1.2	Scope of the present investigations	128
4.1.3	Results and Discussion	128
4.1.4	Conclusion	143
4.2	Transient studies of thermal transport using Green's function	144
4.2.1	Summary	144
4.2.2	Introduction	144
4.2.3	Scope of the present investigations	145
4.2.4	Results and Discussion	146
4.2.5	Conclusion	153

5	Attempts to explore Hierarchical networks	155
5.1	Prediction of time evolution and hierarchy of cracks	156
5.1.1	Introduction	156
5.1.2	Scope of present investigations	157
5.1.3	Experimental	157
5.1.4	Results and Discussion	158
5.1.5	Conclusion	167
5.2	Optimum hierarchical network for efficient transport	168
5.2.1	Summary	168
5.2.2	Introduction	168
5.2.3	Scope of the present investigations	170
5.2.4	Results and Discussion	170
5.2.5	Conclusion	177
6	Summary and Outlook	179
6.1	Summary	179
6.2	Outlook	180
	References	183

List of figures

1.1	Patterns in nature (a) periodic patterns in butterfly, (b) hierarchical pattern in leaves, (c) tree pattern in lightning, (d) ripple pattern in sand, (e) tree pattern in trees and (f) radial and connected pattern in spiral webs.	2
1.2	(a) Patterns on integrated chips (b)compact disk (c) photonic crystals (d) steps of photolithography (e) photograph showing the difficulty of the process.	3
1.3	Examples of a few desiccating cracks.	4
1.4	(a) Crack patterns at different film thicknesses and (b) crack spacing and width varying with film thickness.	4
1.5	(a) Steps of obtaining metal mesh from crack template (b) crack template and corresponding (c) metal mesh (d) large area image of metal mesh.	6
1.6	Metal networks obtained by different techniques. Metal networks from (a) Ag NWs (b) electrospinning (c) bubble template (d) leaves and spider web templates.	7
1.7	Schematic of a network based transparent conducting electrode.	8
1.8	Schematic showing the typical transmittance and sheet resistance values of different types of transparent conductors. Reproduced with permission from ref [90]. Copyright 2015 Elsevier.	9

1.9	Example of bond percolation model with bonds being occupied with probabilities (a) 0.25 and (b) 0.52. (c) probability of percolating cluster with site density.	11
1.10	(a) Photograph of graphite sheet with holes of density 0.268. (b) the fraction of percolating path (c) conductivity variation (d) computational conductivity calculations of binary mixtures.	12
1.11	Scope of the thesis	13
2.1	Emerging transparent conducting electrodes obtained by different methods with corresponding features.	20
2.2	(a) A schematic showing random conducting network placed in bus bar geometry. Electric field is applied from top to bottom (b) Zoom in image of the network showing a wire segment placed at angle θ_i with the electric field (c) Actual curvilinear wire segment length and shortest wire segment length	22
2.3	An example showing calculation of edge density of a randomly conducting network from two similar images.	24
2.4	Algorithm for classifying different regions of networks	28
2.5	(a) An example of a metal network obtained from crack template [86] and (b) obtained from deposited wire networks. [154] (c) and (d) show pie chart of contribution for different regions in both network networks. See Figure 2.4 for detailed algorithm.	30
2.6	(a) An optical microscope image and (b) corresponding skeletonized image of crack template [55] with active backbone edges (shown in yellow), dangling edges (shown in blue) and isolated edges (shown in red) (c) Pie-chart showing fractional contribution of different regions. .	30
2.7	(a-b) Conducting wire-based networks of different densities with (c-d) corresponding backbone	40

2.8	(a) -(c) Conducting wire based networks of different densities. n_c represents critical percolation density. (d-f) represent corresponding backbone. (g) Plot of variation of connected, backbone, and void fraction with density of conducting wires. Numerical results go well with analytical for higher densities. (h) the binary image of a typical templated metal mesh obtained from a crack template and (i) its corresponding backbone.	41
2.9	(a) Schematic of nanowire network. (b) Two outermost wire segments (shown in red) are not participating in backbone.	42
2.10	(a) Effective Wire network resistance (neglecting junction resistance) and (b) Effective junction resistance in a network (neglecting wire resistance) w.r.t wire density.	44
2.11	Current map of (a) conducting wires based network (created by Monte Carlo for density = 1.5 times critical percolation density). It is clear in conducting wires based network there is a significant area with (b) negligible current and (c) hot spots. Current map of (d) templated metal mesh. Here, (e) wires carrying negligible current, is negligible and (f) there is no wire segment with a very high current. (Empty! represents there is no region with hot spots).	47
2.12	(a) Conducting wires based network with $2n_c$ density and (b) corresponding backbone. (c) Current map of the central region of obtained backbone and regions of (c) negligible current and (d) hot spots. . . .	48
2.13	Current distribution for two other networks having $2n_c$ density.	48
2.14	current density map of template based network (a) current map and (b) frequency distribution (in %).	50
2.15	Current distribution in conducting wires at two different densities and templated metal mesh.	51

-
- 2.16 (a-c) Current maps varying from periodic to the random network. $R = c$ represents point is randomly distributed anywhere between 0 and c where 1 is the unit cell spacing. (d) the current distribution of these networks. 51
- 2.17 (a) Collection efficiency of conducting ring (shown in yellow) collecting charge carriers generated within it. Schematic showing charge carrier generated in an arbitrary ring of radius r and thickness dr moving towards conducting ring of radius R . (b) An example of binary image of a metal network obtained from crack template with inset showing nearest wire distance of two random points, P and M to be PQ and MN (c) Nearest wire distance map (minimum distance travelled by charge carrier at the point to reach the wire) (d) charge collection probability map for $\lambda = 10\mu\text{m}$ and (e) for $20\mu\text{m}$ with inset showing the zoom in image of a polygon with scale bar of $50\mu\text{m}$ (f) Efficiency based on charge collection shown by solid squares and fitting for equivalent radius. Best fitted radius represents random network behaves equivalent to a conducting ring of radius $R = 30\mu\text{m}$ 59
- 2.18 (a) A 9-pixel image demonstrating the concept of nearest wire distance. Here, black represents metal and white represents void. (b) Nearest wire distance map calculated by determining distance between the pixel from nearest black pixel (c) The nearest map data is converted into color map. 60
- 2.19 Comparison of different transparent electrodes in terms of calculated equivalent ring radius (R), void fraction (V) and efficiency (η) at $1\mu\text{m}$. The calculation procedure is based on Figure 2.17 61

2.20	Comparison of efficiencies of solar cells for different network structures with respect to diffusion length. The rate of increase depends on the equivalent radius (R) and the void fraction (V). Labels (a-g) represent various networks mentioned in Figure 2.19. (a) Grain boundary lithography, (b) spider web layers, (c) electron beam lithography, (d) electrospinning (e) Ag NW by dip coating (f) coffee ring effect (g) leaf ventilations.	62
2.21	(a) A randomly conducting wire network with density = 1.5 times critical percolation density (b) nearest wire distance map (c) charge carriers collection map for $\gamma = 0.1L$ and (d) $0.2L$ (e) Efficiency variation with ratio of diffusion length and rod length for rods of different aspect ratio (f) efficiency variation with aspect ratio of rods for different ratio of diffusion length and wire width.	64
2.22	Schematic showing light absorption by thickness dz	65
2.23	Schematic showing the solar cell with TCE as top electrode and continuous film as bottom electrode. (b) Efficiency comparison for the random network and complete film (like ITO) based TCE at $\mu = 50\mu\text{m}$ (c) Efficiency comparison for different rod density and diffusion length (γ) at given optical length ($\mu = 0.5L$ for $\nu_a = \nu_b$).	66
2.24	(a) Schematic of a metal network. Inset showing the zoom in the image. θ is the angle of a wire and strain direction. (b) the metal network is elongated to $\lambda \times a$ and based on the angle, different wires are elongated. (c) elongation map of network.	73
2.25	(a-b) Elongation profile for $\lambda = 1.01\lambda_c$ and $1.10\lambda_c$. On stretching the network to $\lambda = \lambda_c$, the wires which experience this elongation breaks down (shown in white).	74

2.26	(a) Resistance variation when wires having angle less than critical angle breaks during elongation, (b) variation of resistance with elongation, (c-d) theoretical resistance and gauge factor variation with strain for Au network.	77
2.27	(a) An optical microscope image of metal wire network obtained from crack template and (b-c) are numerically calculated backbone of networks after breakdown of wires at different strain values. (d-e) Resistance of network varying with critical angle and strain.	79
3.1	(a) Schematic of spring fusion model. It is the 2D view of 3D geometry. (b) Dark grey denote particles and light grey denote the liquid bridging the two.	84
3.2	Simulated crack patterns of different film thicknesses	89
3.3	Simulated images at different Y	90
3.4	Crack patterns with distribution in constant Y value.	91
3.5	Crack geometry on the film obtained from TiO_2 nano-particles of (a) uniform size of 25 nm diameter and (b) non uniform size with mean diameter of 16nm.	92
3.6	Change in crack geometry of clay on addition of polymer.	93
3.7	Deviation in crack geometry of TiO_2 colloidal film on addition of Al_2O_3	93
3.8	Variation in breaking threshold S of the springs.	93
3.9	Crack properties versus breaking threshold S	94
3.10	Variation of crack parameters with variable b and r used in the drying rule.	94
3.11	Effect of drying temperature on crack patterns of TiO_2 film.	95

- 3.12 (a) Schematic showing the steps to obtain crack network with repeated wet-drying cycles. Crack network obtained after (b) first desiccation and (c-d) 5 and 20 repeated wet-drying cycles. The insets show the complete film of size 2.5x 2.5 cm² showing there is not a much visual difference in the film (e-f) Comparison of features before drying cycles and after 20 drying cycles. (g-h) variation of crack width and crack fill factor with wet-drying cycles. Inset of (g) shows cracks are U-shaped before drying cycles and are more V-shaped after drying cycles. Scale bar = 2 μm 99
- 3.13 Newly formed cracks are acting as a backbone and initiated new cracks formation as indicated by arrows inside (a-f) to show the progress in crack formation. 101
- 3.14 (a-c) Comparison of sheet resistance and transmittance of the metal network obtained from the templates before and after drying cycles and shows real images of derived TCE on institution logo showing high transmittance in both the cases. Microscopic images of a crack network (d) before and (g) after 20 drying cycles, (e and h) represents corresponding binary skeletonized images and (f and i) are corresponding current carrying backbone wires. Note that dangling and isolated wires are ineffective for current transport. The circle represents an area, which is not having any backbone wire initially (f) has considerable backbone wires after drying cycles (i). 102
- 3.15 Crack patterns on PET substrate before and after 10 drying cycles. . . 103
- 3.16 Steps for transparent electrode fabrication for top and cross-section view. Briefly, a crackle precursor is spin-coated resulting in the crack template formation. Metal is evaporated on the crack template using physical vapor deposition technique and the template was then removed by dissolving in the solvent (chloroform). 103

3.17	Comparison of theoretical solar cell efficiency of TCE obtained from the crack template (a) before drying cycles (b) after 10 drying cycles showing the equivalent radius is reduced to half. Here, R is the equivalent radius and V is area fraction occupied by voids. (c) Comparison of current collection for n-doped Si for networks using networks without and with drying cycles. The inset shows photographs of n-Si coated with Au network before (black) and after (red) drying cycles. The increase in wire density in Si sample with wetting drying cycles is apparent from the golden tinge on the substrate.	104
3.18	(a-b) Au network on Si before drying cycles and (c-d) after drying cycles.	105
3.19	Crack patterns formed with pure IPA and water.	108
3.20	(a) Preparation of colloidal solution of acrylic resin with solvents consisting of water and IPA of variable compositions. (b) Crack networks formed after ambient drying of 5 ml colloidal solutions in the petri dish.	109
3.21	Comparison of evaporation rate and boiling points of different compositions.	110
3.22	(a) Optical images of films formed by drop coating 20 μ l solutions of different compositions. The box size is 2 cm x 2 cm. (b) Variation of size of drop for different compositions	111
3.23	Effect of substrate adhesion on cracking.	111
3.24	Crack patterns obtained by spin coating for different compositions. . .	112
3.25	Effect of substrate adhesion on cracking.	113

3.26	(a) Photograph demonstrating film formation process using gravity flow. Here, θ represents the inclination angle. The inset shows a typical film formed on a glass substrate by the process. Optical microscopy images of the film showing cracks at (b) the drop coating region and (c) central region. (d) and (e) are images of parallel crack covering most of the area of the film at low and high magnification respectively (f) Schematic illustrating crack formation at different regions of the substrate. (g) Variation of film thickness with respect to θ (h) Variation of crack width and periodicity with the film thickness.	116
3.27	Schematic for mechanism of the parallel crack formation process.	118
3.28	(a)-(d) Optical images showing the effect of defects on crack propagation. The black circle represents a defect. The periodicity of the crack pattern is not much affected by the defects in the film, as cracks slow down on the defects and move with faster speed after it to match the speed of neighbouring cracks. Note: a shift in the microscope field of view in (d). (Scale bar 200 μm)	119
3.29	Optical images of parallel cracks at different drying temperatures. (a) Drying at room temperature. The short perpendicular interconnects lead to brick-wall like appearance. Drying at (b) 65 $^{\circ}\text{C}$ and (c) 100 $^{\circ}\text{C}$. (d) Variation of the number of perpendicular interconnects with respect to drying temperature. (Scale bar 100 μm)	119
3.30	Experimental setup of preparing cracks at higher temperatures. The hot plate was inclined at certain angle and temperature of hot plate was maintained at desired temperature.	120
3.31	Optical image of cracks with no downward inclination at the center (backbone) as CP flow was confined on a narrow strip of PET (scale bar 200 μm).	121

- 3.32 (a) Schematic showing the film with a random crack at the scotch tape boundary side and parallel cracks at the open boundary side. (b) and (c) is the optical images of crack at the open boundary and scotch tape boundary side respectively. The absence of film thickness gradient at the scotch tape side results in the formation of random cracks rather than parallel cracks. (scale bar $200 \mu\text{m}$). Arrow represents the direction of gravity flow. 122
- 3.33 Optical image of cracks formed by using water-IPA mixtures as a solvent instead of only water. Since such mixtures tend to have higher evaporation rates and good wettability, a thickness gradient was not observed in the obtained film. As expected, random cracks rather than parallel cracks were observed to be formed (scale bar $100 \mu\text{m}$) 122
- 3.34 Optical images of radial cracks at the (a) edge and (b) center respectively (scale bar $200 \mu\text{m}$). (c) schematic of radial cracks propagating towards center 123
- 4.1 (a) Schematic demonstrating the steps involved in the fabrication of metal networks using crack templating method. (b) Optical microscope image of the network at 20X (inset shows 5X image) and the corresponding (c) three-dimensional optical profilometric image of the Au network showing metal wire widths in the range of $2\text{-}10 \mu\text{m}$ and wire spacings of $50\text{-}100 \mu\text{m}$ for the film thickness of 80 nm . (d) Schematic showing the set up for Joule heating of the wire-network of dimensions $a \times b$. (e) Variation in the measured resistance with respect to the inverse of effective thickness ($1/t_{eff}$). (f) Steady state temperature of different networks as a function t_{eff} 131

-
- 4.2 (a) Experimental set-up for infrared thermal imaging consisting of the Au metal wire network ($1.5 \text{ mm} \times 1 \text{ mm}$ area) connected to a power supply and placed under the IR microscope for imaging. (b) Optical image of a typical Au metal wire network on glass used for thermal analysis. (c) Typical emissivity map as obtained by the calibration step. (d) Thermal map of the Au wire network at an applied voltage of 1.5 V at $1 \times$ resolution. 134
- 4.3 (a) Infrared radiance image, (b) emissivity map, and the corresponding infrared thermal maps of Au/PET at (c) 0.7, (d) 0.9, (e) 1.0 and (f) 1.2 V, respectively. (g) The average rise in the temperature of Au/PET heater with time from the data shown in c-f. The bias voltage is applied from $\approx 5 \text{ s}$ to 33 s, after which the voltage is turned off and the films cool. (h) Temperature profiles from another Au/PET sample with a resistance of 7Ω at applied voltages of 2, 4, 6 and 8 V fitted using the approximate lumped capacitance model (dashed lines) 135
- 4.4 (a) Temperature distribution across a wire on PET substrate at different power densities. Here, the yellow shaded area represents the region with the wire, while the unshaded region represents the bare PET substrate. (b) Variations of the temperature of wire and the PET substrate with power density with error bars corresponding to measurements from 10 different wires. 137

- 4.5 (a-e) Sequential thermal images at different times showing the breakdown of Au wire network on PET at 1.3 V. The temperature of Au wire network increases with time, leading to hotspots, and finally to the breakage of the wire network. Note that in panel c, grey regions near the center of the heater indicate image saturation and are indicative of the hottest spots in the heater network. (f) Infrared radiance image of the unpowered network after breakdown clearly showing the broken wires in the light region near the center of the network. (g) SEM images of the network from the breakdown regions (highlighted by the red circles). (h-i) High magnification optical images showing the breakdown locations. 140
- 4.6 (a) High-resolution thermal map of the wider Ag wire network on PET. (b) Bar-graph representing statistical analysis of the temperature distribution in regions 1, 2, 3, and 4 marked in a. (c) Spatial temperature distribution between the two electrodes measured from twelve consecutive thermal maps at high resolution for the network for 1.3 V applied voltage. (d) Temperature profile across the two electrodes extracted from the combined images in (c). Note that the spikes in the profile correspond to the temperature of the wires in the network while the background at ≈ 56.1 °C represents the substrate temperature. 142
- 4.7 Schematic of (a) wire network based heater on transparent substrate. (b) The polygons are approximated with circles. (c) Finding temperature at P due to heat flux at P' based on Green's function. 146
- 4.8 Steady state temperature as a function of radial distance. The calculations are performed based on series summation (Eq. (4.27)) and log expression (Eq. (4.30)). (a) in range 0.9 - 1.1 and (b) 0 - 2. It shows the series summation is slow converging and thus > 100 terms are required to model it accurately near the ring. 149

4.9	Temperature as a function of radial distance at differnt time. In begining, only the ring is at higher temperature. With increase in time, the temperature increases and heat distibutes within and outside the ring.	150
4.10	Tempearure profile by using 3 rings at differnt time	151
4.11	Tempearure profile of multiple ring with time.	152
4.12	Tempearure profile in different regions for large number of rings at two differnt times.	153
5.1	Optical microscope images and corresponding binary images of the film undergoing crack formation with time (t=0 represents initiation of cracks)	158
5.2	Binary images at different threshold	159
5.3	Dynamic images of crack formation after image processing (t=0 represents initiation of cracks). With passage of time new cracks nucleates with crack propagation and broadening of existing cracks. It shows nucleation (Red) propagation of primary (green), secondary (blue) and tertiary (pink) cracks.	159
5.4	Variation of area fraction of cracks in (a) linear and (b) log-log scale. (c) Broadening of crack at four locations with time (d) Images of the film at transition points.	161
5.5	Variation of crack length in (a) linear and (b) log sale (c) Cracks formation shown in different time regimes, A to B (green) , B to C (blue) , C to D (pink)	161
5.6	Theoretically predicted time evolution on the basis of crack width filters. The filtered image shows cracks regions only above certain crack width mentioned below here 1 pixel represent 0.64 μm	163
5.7	(a) Commutative distribution of Crack length w.r.t crack width of final image (b) Labeling of Primary (green), secondary (blue) and tertiary cracks (pink) based on crack width filters (c) Pie chart showing area fraction of different generation cracks.	163

-
- 5.8 Predicted images of transition points B and C based on crack width filters. 164
- 5.9 The experimental time evolution reported by Vogel et al. and below corresponding theoretically predicted time evolution based on crack width filters on final pattern. Slight deviation may be due to low resolution of images. Reproduced with permission from ref [165]. Copyright 2005 Elsevier. 164
- 5.10 Algorithm for identifying generation of crack segments. The algorithm can be used for N generations, here only 3 generations are classified for clarity. 165
- 5.11 The hierarchical nature of cracks is obtained from width or angle. Classified cracks segment based on (a) angle and (b) width. (c) Frequency distribution of primary secondary and tertiary cracks. Please note that the distribution obtained by angle analysis matches well with the distribution obtained using width analysis. 166
- 5.12 (a) A typical example of a hierarchical network with division matrix [3,4,2] bisecting spacing into 3,4,2 divisions respectively and (b) Network of equal width but having same fill factor as shown by (a). For very small distances, the path length is lower for the non-hierarchical network, while for rest of the region path length is lower for the hierarchical network. S and T show an example of a source and a target having the path length of 6.833 and 11.76 in the hierarchical and non-hierarchical network. (c) Comparison of Variation of effective width with distance between points. 171

-
- 5.13 A network with 3 generations and zoom in of 2nd generation. For transportation an object from lower to higher hierarchical order with the shortest path. An object at P takes PQ way to reach red line, while an object at R takes RS way to reach red line. Consider an object is at position x from the center of the red circle, it needs to travel $\frac{D}{2} - x$ distance to reach the red line. 173
- 5.14 (a) Parameters of ideal network with least Path length (b) A schematic of ideal network. For least path length, the divisions per generation should be ≈ 5 176

List of tables

2.1	Sheet Resistance, Transmittance and Figure of merits of TCE defined by Coleman et al. (F_C)and Haacke (F_H).	19
2.2	Comparison of various conducting wire networks. Here $\sqrt{N_E}$ was calculated by drawing the equipotential line on the literature image similar to Figure 2.2 and counting the number of intersecting edges on the line (as shown in Figure 2.3). This step was repeated for 5-10 equipotential lines. *(corresponding data not available)	25
3.1	Sheet Resistance (R_s), Transmittance (T) and Figure of merits of TCE defined by Coleman et al. (F_C)and Haacke (F_H).	101
3.2	Comparison of the crack spacing of different networks from the literature of similar transmittance. The resistance values are not mentioned as it depends on film thickness, which is different in different studies	105
4.1	Approximate geometrical parameters of various Au networks prepared over an area of $2 \times 2mm^2$. Network (A-D) are made of quartz and networks (E-F) are made on glass.	132

Chapter 1

Introduction

1.1 Patterns in nature and technology

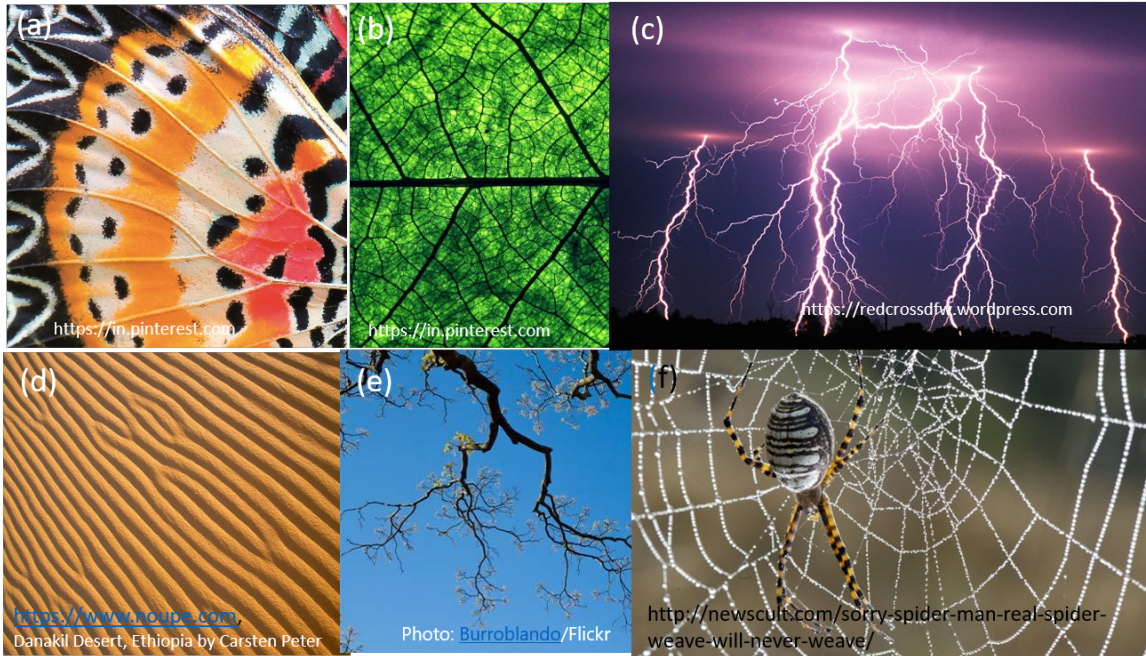
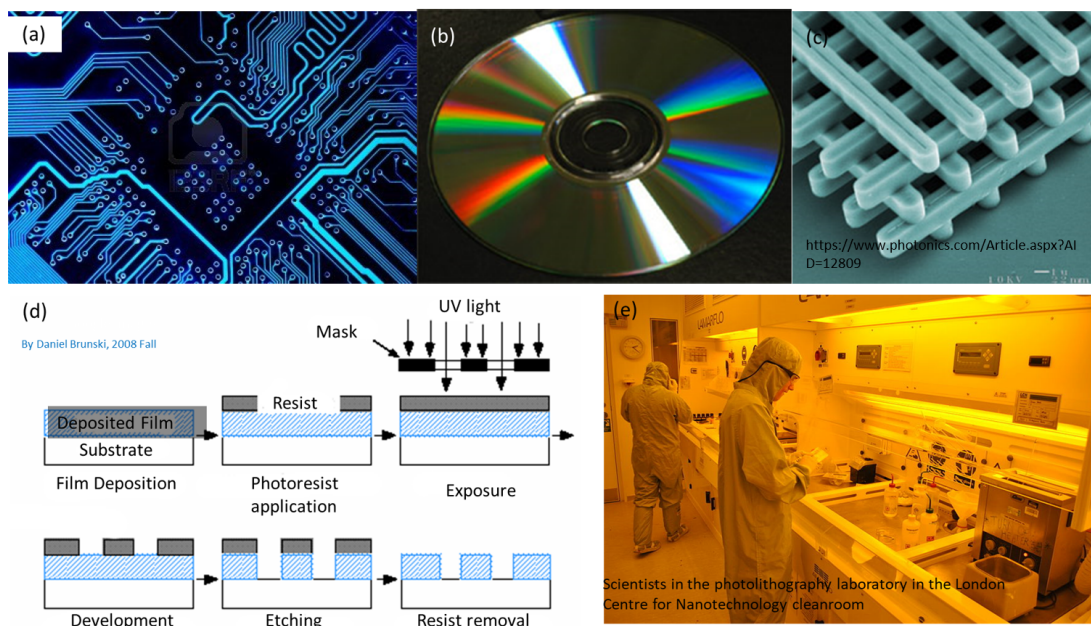


Fig. 1.1 Patterns in nature (a) periodic patterns in butterfly, (b) hierarchical pattern in leaves, (c) tree pattern in lightning, (d) ripple pattern in sand, (e) tree pattern in trees and (f) radial and connected pattern in spiral webs.

Patterns in Nature: Nature is filled with versatile beautiful patterns of different shapes such as periodic, hierarchical, tree shape, spiral, waves, and myriad etc. as shown in Figure 1.1. [159, 36, 118] The shape depends on compositions and combined effect of forces acting on it and nature chooses a particular structure for its effective functionality. As an example, the periodic line patterns are responsible for beautiful colours in butterflies, branch structure in plants are important to gather light and air and to supply the nutrients at minimum effort, honey bees choose close-packed hexagonal structure to have a maximum number of cells for laying eggs at minimum material etc. Similarly, the lotus possesses micro-nano structural architecture to maintain its surface superhydrophobic, required for its self-cleaning and the golden spiral arrangement of sunflowers provides a maximum number of seeds that can be packed into the seed head. Nature creates this pattern to a very large scale spontaneously using a few biochemical reactions.

Patterns in technology: Patterns are important for various technological applications as well (Figure 1.2 a-c). The electronic circuits, compact disks, casting rods, optical gratings etc. have certain specific patterns for their functionality. The patterning is important for devices such as touch screens, where patterns help in determining the coordinate of finger touch. However, patterning at a micro and nanoscale is not so easy and one needs to rely on various lithography techniques such as electron beam lithography, photolithography, ion-beam lithography, soft lithography etc. which are instrument and chemical expensive, involve multiple processing steps and are not scalable. Figure 1.2d and Figure 1.2e shows the difficulty and the sophistication required for the process. Thus, it is need of the hour to replace the conventional lithography techniques with certain alternatives.



Patterning in technology relies on sophisticated lithography techniques.

Fig. 1.2 (a) Patterns on integrated chips (b) compact disk (c) photonic crystals (d) steps of photolithography (e) photograph showing the difficulty of the process. Source: Google images.

1.2 Crack patterns



Fig. 1.3 Examples of a few desiccating cracks. Source: Google images.

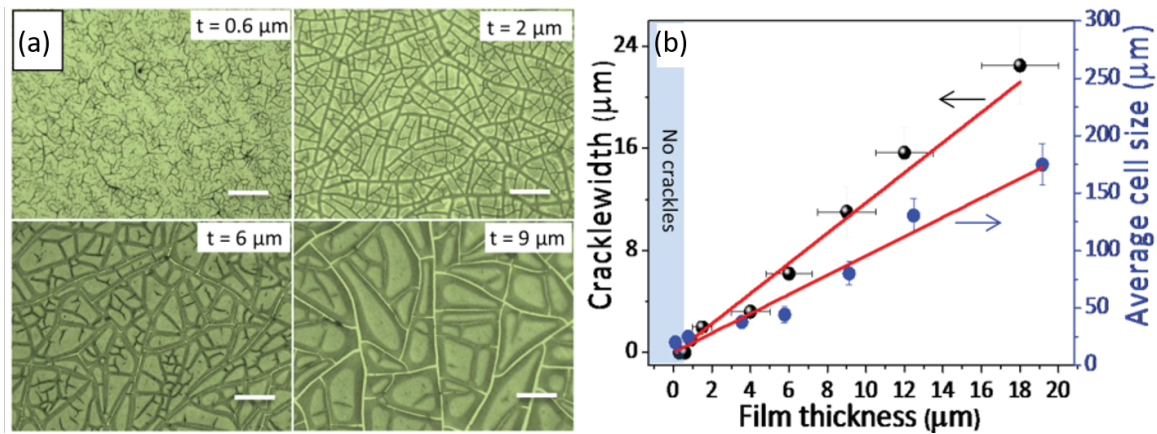


Fig. 1.4 (a) Crack patterns at different film thicknesses and (b) crack spacing and width varying with film thickness. Reproduced with permission from ref [142]. Copyright 2014 John and Wiley Sons.

Desiccating cracks are another beautiful natural patterns forming self-similar structure and can be widely seen in mud, wall and other films consisting of colloidal particles (Figure 1.3). The crack pattern forms a well-connected structure to a very large scale. These structures and scale of these patterns can be controlled by varying the mechanical properties of the film and solvent evaporation conditions. As an example, a decrease in the colloidal film thickness decreases the crack spacing and crack width, however, below a certain film thickness a film does not form the cracks (Figure 1.4). Substrate friction is an essential condition for cracking and thus crack density increases with friction [44]. The stress formation during the desiccation has been modulated using the electric field to obtain radial cracks, [76] and vibrational field

to attain parallel cracks [89] etc. Typically cracks are undesirable as it deteriorates film performance. However, recently these crack patterns are used as templates for the lithography.

1.2.1 Crack networks as templates for metal meshes

Desiccation cracks with high interconnectivity and narrow width can also be used as templates to obtain metal mesh structure [142] [55]. The process involves depositing a colloidal film on a transparent substrate, allowing desiccation to obtain crack patterns. Metals such as Au is deposited on the crack template with thickness lesser than the colloidal film thickness. The crack template is further washed to obtain metal mesh structure on a transparent substrate (Figure 1.5). The metal mesh on a transparent substrate can be an important device in optoelectronics as a transparent conducting electrode.

1.3 Metal network as transparent electrodes

Transparent conductors are the materials which are optically transparent and electrically conducting. Transparent conducting electrodes (TCE) are an essential component of optoelectronic devices such as solar cells, light emitting diodes and also necessary for transparent heaters, smart windows etc. However, materials are either optically transparent such as glasses or electrically conducting such as metals but does not show both properties simultaneously. As for high optical transmittance, band gap should be higher, while for high electrical conductance band gap should be zero. Both these conditions are difficult to meet and only a few materials such as tin-doped indium oxide (ITO) show these properties with proper band engineering. However, ITO is brittle, expensive, require high-temperature processing. Graphene is another alternative, however, high-quality graphene preparation is expensive and is not scalable.

Thus obtained metal network can act as transparent conducting electrodes. Here, voids are optically transparent while conducting network is electrically conducting as

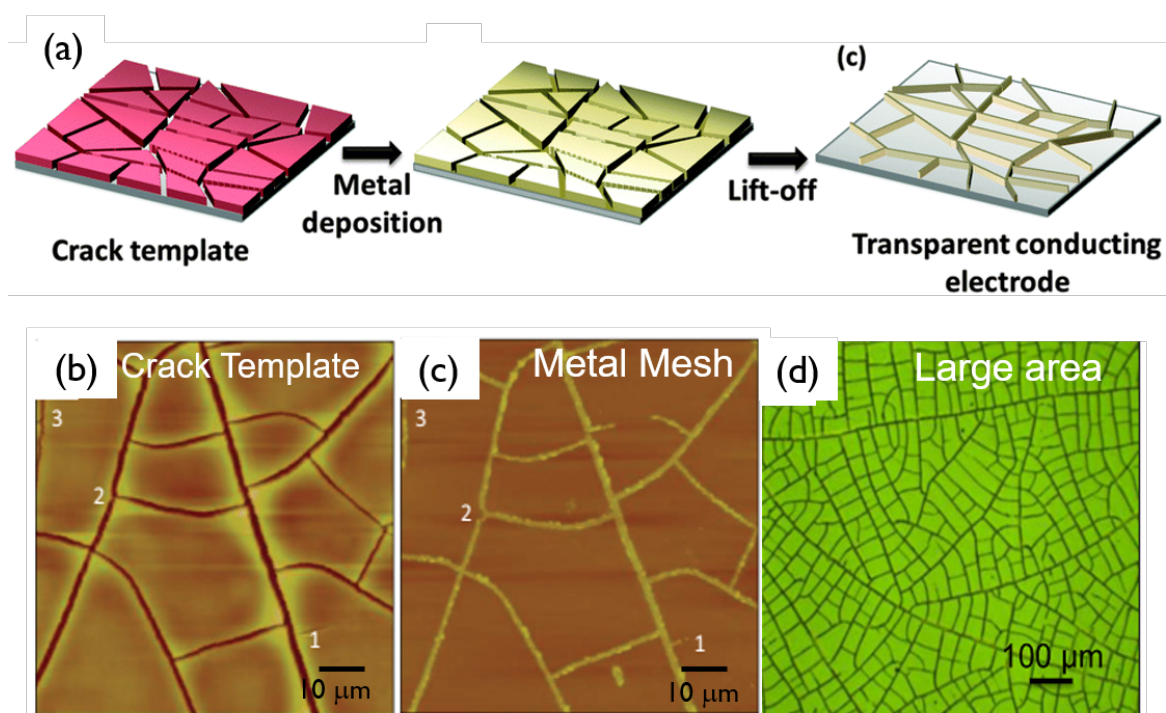


Fig. 1.5 (a) Steps of obtaining metal mesh from crack template (b) crack template and corresponding (c) metal mesh (d) large area image of metal mesh. (a) Reproduced with permission from ref [139] Copyright 2014 PCCP Owner Societies. (b-c) Reproduced with permission from ref [142]. Copyright 2014 John and Wiley Sons. (d) Reproduced with permission from ref [52]. Copyright 2014 American Chemical Society.

the wire width is just a few μm and thus network is invisible to the naked eyes (Figure 1.8). Other emerging candidates include networks of silver nanowires [98, 154, 45] and carbon nanotubes [9, 64]. However, a nanowire-based network has shortcomings such as high junction resistance and incomplete connectivity. To overcome it, metal meshes are obtained from template-based techniques providing seamless junctions and high connectivity such as templates of grain boundaries [46], organized polystyrene beads [106], electrospun fibre meshes [174, 6], patterns formed in inorganic crystal layers [104] and bio-inspired templates like leaf venation and spider webs [54] etc. Other techniques include the formation of a network by self-assembly, examples being printing holes by de-wetting solution [100], bubble template [162], self-assembly of alkyl coated Au NPs [124] and inkjet printing of CNT using coffee ring effect [155] etc (henceforth named as template based networks). Different experimental techniques

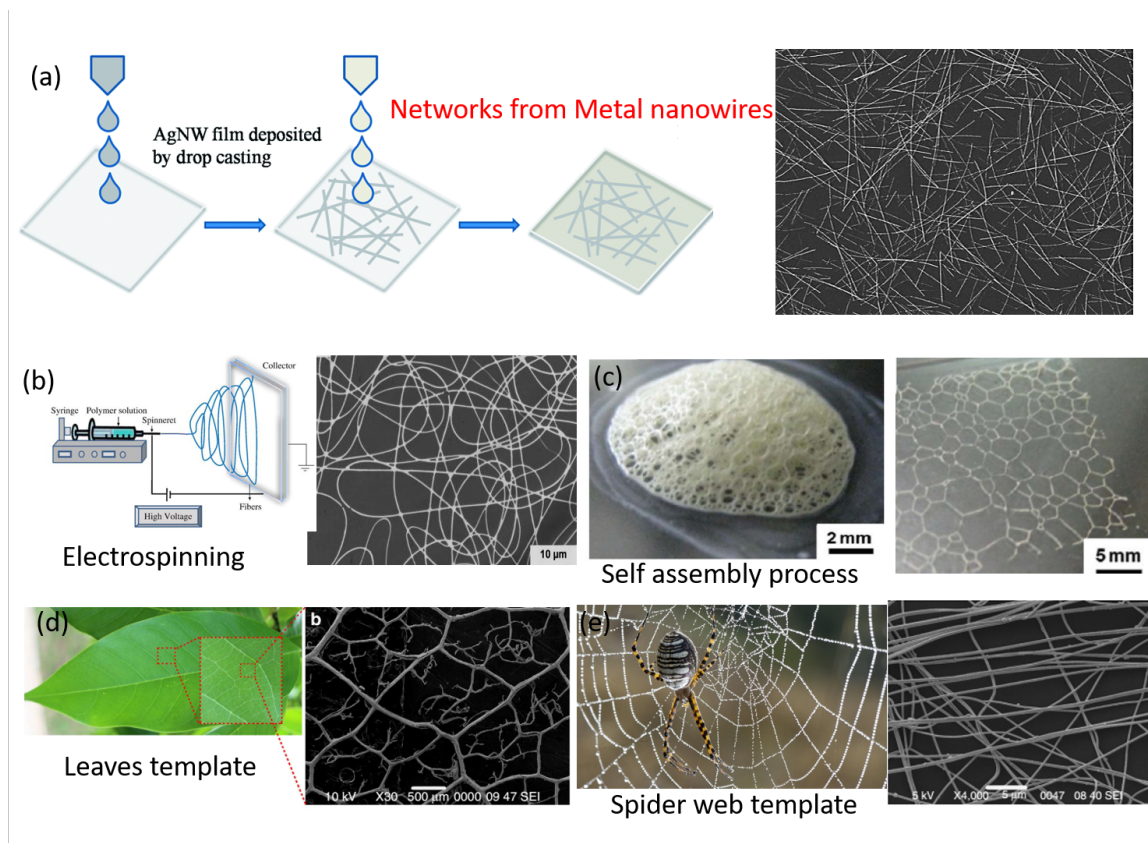
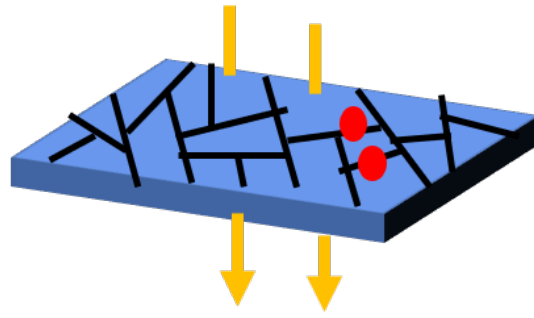


Fig. 1.6 Metal networks obtained by different techniques. Metal networks from (a) Ag NWs (b) electrospinning (c) bubble template (d) leaves and spider web templates. (a) Reproduced with permission from ref [48] Copyright 2015 RSC Publications. (b) Reproduced with permission from ref [6] Copyright 2014 Elsevier. (c) Reproduced with permission from ref [162] Copyright 2015 American Chemical Society. (d-e) Reproduced with permission from ref [54] Copyright 2014 Nature Publishing Group.

provide different kinds of network structures. It is important to know, which network structure is suitable for high transmittance and low sheet resistance.

1.4 Modelling a transparent electrode

Transparent electrodes have an inherent trade-off between low sheet resistance and high transmittance which depends on the network structure. For achieving high transmittance, the wire density should be lower, while for low sheet resistance, the wire density should be higher. Thus an optimum network is desired for the maximum



Voids : Optically transparent
Network: Electrically conducting

Fig. 1.7 Schematic of a network based transparent conducting electrode.

transmittance and low sheet resistance. The conducting wires may be represented by a graph with vertex being the points where wires meet and edges being the connection between the junctions. Concepts of graph theory can be employed to understand the metal networks.

1.4.1 Graph theory

Graph theory started with Euler who was asked to find a nice path across the seven Königsberg bridges. The path should cross over each of the seven bridges exactly once. [16] Currently, it is used in wide applications such as understanding social networks, transport networks, and biological networks. A graph $G = (V, E)$ is a pair of vertices (or nodes) V and a set of edges E , assumed finite i.e. $|V| = n$ and $|E| = m$. [16, 26] Graphs are represented visually by drawing a dot or circle for every vertex, and drawing an arc between two vertices if they are connected by an edge, with entries being nodes and interactions between entities as edges. If the graph is directed, the direction is indicated by drawing an arrow. Graphs can be represented as list structures or matrix structures. The list structure contains three columns edge 1, edge 2 and weight of the connection. The list structure is more suitable for sparse graphs, to save computational memory, however, it compromises accessibility. On the

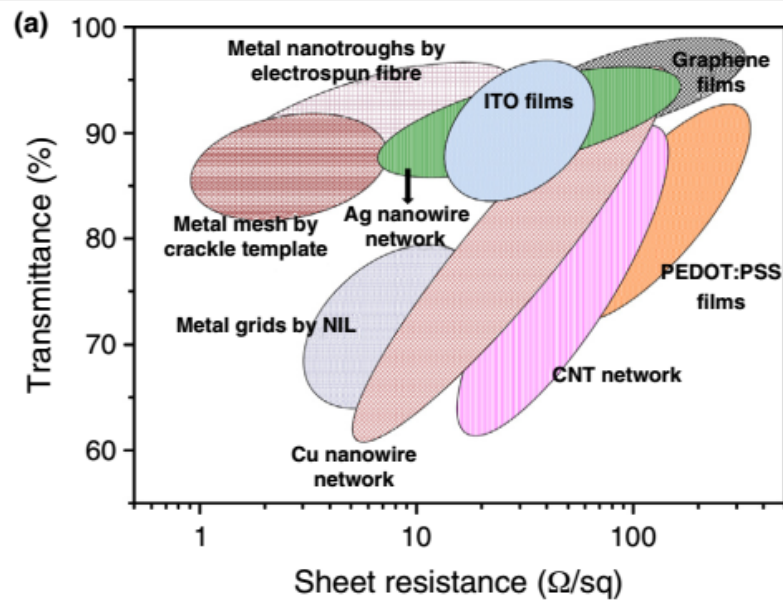


Fig. 1.8 Schematic showing the typical transmittance and sheet resistance values of different types of transparent conductors. Reproduced with permission from ref [90]. Copyright 2015 Elsevier.

other hand, the matrix structure is fast for computational accessibility and easy to perform computation but consume more memory. Based on the requirement either list structure or matrix structure is used. Matrix structure includes weighted and unweighted incidence matrix and Laplacian matrix .

The adjacency matrix of a weighted graph G will be denoted A , and is given by

$$A(i, j) = \begin{cases} w(i, j) & \text{if } (i, j) \in E \\ 0 & \text{otherwise} \end{cases} \quad (1.1)$$

The degree matrix of a weighted graph G will be denoted D and is the diagonal matrix such that

$$D(i, i) = \sum_j A(i, j) \quad (1.2)$$

The Laplacian of the matrix of a weighted graph G can be denoted as L and can be written as

$$L = D - A \quad (1.3)$$

Measure of graphs

The clustering coefficient of a node is the ratio of existing links connecting a node's neighbours to each other to the maximum possible number of such links.

The weighted path length, $L(i, j)$ between i and j , is defined as the smallest sum of the weights of the links throughout all possible paths from node i to node j . The characteristic path length of a network is defined as the average of the path length between two points.

Clustering coefficient of i^{th} junction is

$$C_i = \frac{2e_i}{K_i(K_i - 1)} \quad (1.4)$$

where, K_i is the number of neighbours of the i^{th} node, and e_i is the number of connections between these neighbours. Efficiency of a network is defined as the arithmetic mean of the inverses of the path length between the node and all other nodes in the network.

$$E = \frac{1}{N(N-1)} \sum_{i < j \in G} \frac{1}{d_{ij}} \quad (1.5)$$

A metal network is also a graph with junctions being the point of intersection of wires.

1.4.2 Percolation theory

Percolation theory describes the nature and properties of connected clusters in a random graph. Percolation theory tries to address what is the required void fraction for a material to have transferred from one end to another. The model can be either site or bond percolation. The percolation model is made on a regular lattice such

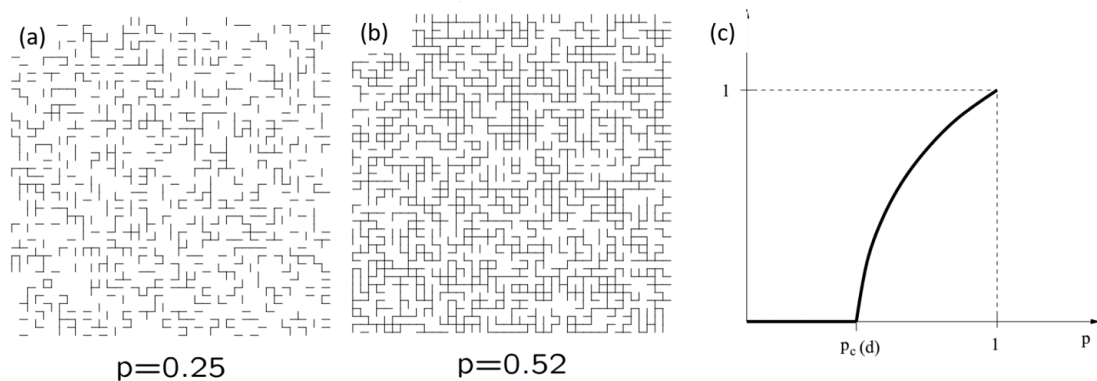


Fig. 1.9 Example of bond percolation model with bonds being occupied with probabilities (a) 0.25 and (b) 0.52. (c) probability of percolating cluster with site density. Source: Google Images.

as square lattice with certain "occupying" sites (vertices) or bonds (edges) with a statistically independent probability p to obtain a random structure as shown in Figure 1.9. If the probability of the site/bond is less than critical percolation density, clusters are finite and there is no global connectivity. If the probability of site/bond is greater than critical percolation density, an infinite cluster appears. While if the probability equals the critical percolation density, clusters of all sizes are present, and there is a fractal structure. Different lattices have different critical percolation densities. As an example, in a square lattice for bond and site percolation, the values are 0.50 and 0.59 respectively.

Percolation and conduction

The percolation theory has also been explored in the direction of electrical conduction (Figure 1.10). Last et al. [99] have taken a conducting graphite paper and punctured holes in it at random positions to study its electrical properties. The conductivity was expected to be proportional to the area fraction of graphene paper, however, it was found to be lower. The reason could be due to non-participation of complete graphite area in the network. Similar computational experiment with a binary mixture of two materials was performed by Kirkpatrick. [83]

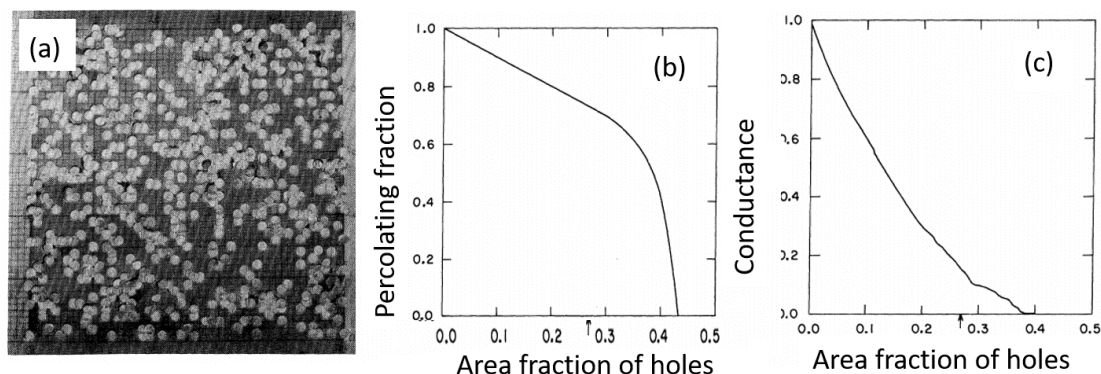


Fig. 1.10 (a) Photograph of punctured graphite sheet of 0.268 density (b) fraction of percolating path (c) conductivity variation. Reproduced with permission from ref [99]. Copyright 1979 APS Publications.

1.5 Experimental and computational tools

Transparent conducting electrodes are characterized using several microscopic techniques. Scanning Electron Microscope (SEM) measurements are performed using a NanoSEM 600 equipment (FEI Co, Netherlands). The film thickness is measured using Wyko NT9100 (Veeco, USA) optical profiler and Dektak 6M (Veeco, USA) stylus profiler. The reflective metal wire surface and the exposed substrate surface produce interfering beams from which the wire thickness is extracted. With the sophisticated optics provided with the system, Veeco NT 9100 sub-nanometer resolution is possible for the thickness measurement. As the wire width is sufficiently larger than the wavelength of the light used for the measurement, it may be approximated to thin film scenario. UV-Visible spectra are recorded using a Perkin-Elmer Lambda 900 UV/Vis/NIR spectrometer. The optical images were obtained from the microscope of Laben, India. The images were captured using pixel link software.

For computation, the work primarily uses self-written codes in Fortran and Python languages. The shell scripts are developed for bulk processing. Matlab, Image J and CIAS software by C. Liu (Nanjing University) are used for image processing.

Depending on the task, computation time for a single calculation takes 10 minutes to 10 hours on a regular desktop with 16 GB RAM and I5 processor.

1.6 Scope of the present thesis

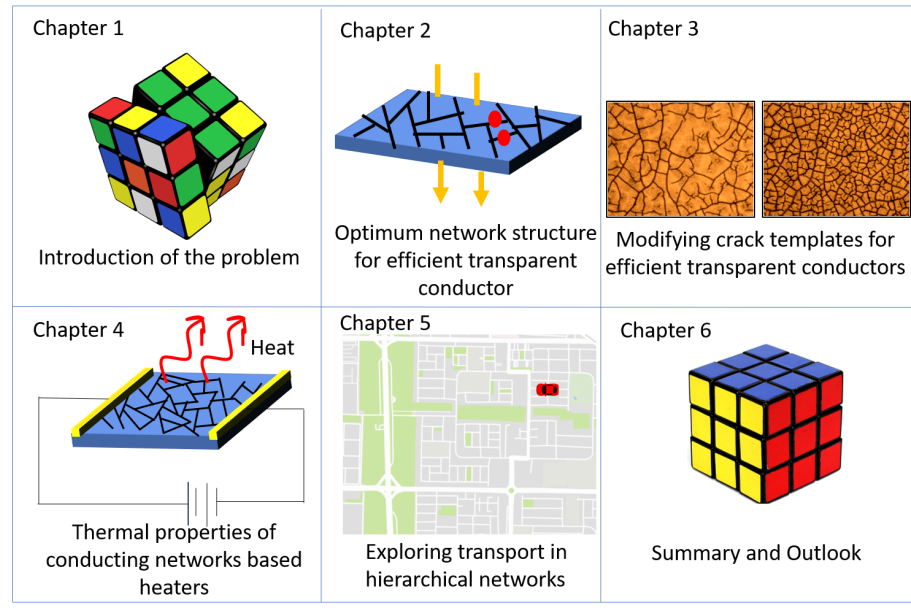


Fig. 1.11 Scope of the thesis

Chapter 1 discusses the importance of studying electrical transport in a metal network. Chapter 2 deals with the optimum network structure for efficient transparent electrodes. Chapter 3 describes the strategies to modify the crack patterns to achieve efficient transparent electrodes. Chapter 4 discusses the thermal properties of the metal network. Chapter 5 is an exploratory chapter discussing the hierarchical nature of cracks and transport in hierarchical networks. Chapter 6 concludes the thesis and discusses the summary and outlook. (Figure 1.11)

Chapter 2

Comparing different metal network based transparent conductors

2.1 Evaluating conducting network-based transparent electrodes from geometrical considerations

2.1.1 Summary

Conducting nanowire networks have been developed as a viable alternative to existing indium tin oxide-based transparent conducting electrode (TCE). The nature of electrical conduction and process optimization for electrodes have gained much from the theoretical models based on percolation transport using Monte Carlo approach and applying Kirchhoff's law on individual junctions and loops. While most of the literature work pertaining to theoretical analysis is focussed on networks obtained from conducting rods (mostly considering only junction resistance), hardly any attention has been paid to those made using template-based methods, wherein the structure of network is neither similar to network obtained from conducting rods nor similar to well periodic geometry. Here, an analytical treatment based on geometrical arguments and image analysis on practical networks is proposed to gain deeper insight into conducting networked structure particularly in relation to sheet resistance and transmittance. Many literature examples reporting networks with straight or curvilinear wires with distributions in wire width and length have been analysed by treating the networks as two-dimensional graphs and evaluating the sheet resistance based on wire density and wire width. The sheet resistance values from our analysis compare well with the experimental values. Our analysis of various examples has revealed that low sheet resistance is achieved with high wire density and compactness with straight rather than curvilinear wires and with narrower wire width distribution. Similarly, the higher transmittance for given sheet resistance is possible with narrower wire width but of higher thickness, minimal curvilinearity, and maximum connectivity. For the purpose of evaluating the active fraction of the network, the algorithm was made to distinguish and quantify current carrying backbone regions as against regions containing only dangling or isolated wires. The treatment can be helpful in predicting the properties

of a network simply from image analysis and will be helpful in improvisation and comparison of various TCEs and a better understanding of electrical percolation.

2.1.2 Introduction

A transparent conducting electrode, widely known as TCE, is an essential component of any optoelectronic device- liquid crystal displays (LCDs), touchscreens, organic light-emitting diodes (OLEDs) and solar cells, all make use of at least one transparent electrode. Optoelectrical applications such as transparent heaters also rely on transparent electrodes. As an active material of TCEs, tin-doped indium oxide also known as indium tin oxide (ITO) is most widely used because of its high optical transmittance and high electrical conductivity, a combination which is rather rare as there is always a trade-off between the two properties. But the scarcity of indium, non-flexibility of the oxide film and poor transmission in UV and IR regions limit ITO applicability as a flexible TCE [94, 32]. Thus, there is intense activity globally in industrial and academic circles to replace ITO with suitable alternatives such as networks of AgNWs [98, 154, 45] and CNTs [9, 64], formed by depositing pre-prepared wires or tubes at the desired concentration on a transparent substrate (henceforth named as deposited wire networks). Here, optical and electrical properties are essentially decoupled such that light finds its way out through void regions in between the percolative conducting paths. However, such networks show high sheet resistance due to the resistance associated with cross-bar junctions and incomplete connectivity. In order to avoid increased resistance due to junctions, there is some effort in the literature to develop template-based methods, which serve as sacrificial layers during metal deposition and produce metal patterns with seamless junctions. Spontaneously formed crack networks [140, 55], grain boundaries [46], organized polystyrene beads [106], electrospun fibre meshes [174, 6], patterns formed in inorganic crystal layers [104] and bio-inspired templates like leaf venation and spider webs [54] are some examples of template-based methods. Other techniques include the formation of a network by self-assembly, examples being printing holes by de-wetting solution [100], bubble

template [162], self-assembly of alkyl coated Au NPs [124] and inkjet printing of CNT using coffee ring effect [155] etc (henceforth named as template based networks). While templating methods have shown advancement in TCE fabrication, the sheet resistance and optical properties do depend on the geometry of the network. There is an only limited effort in the literature providing insight into how the geometry of the template and the resulting metal structure influence the TCE properties. Here, an influence of the geometry of the conducting wires in template-based methods on electrical properties is explored.

Theoretical treatment in this area is mainly devoted to percolation of random conducting rods representing Ag NWs or CNTs etc by Monte Carlo approach. The studies have been successful in estimating the critical filler concentration for percolation, the number of contacts per individual CNT [61] and parameters affecting percolation thresholds such as anisotropy [28], waviness [112] and aspect ratio [125]. The variation of conductivity with wire density is found to obey the power law with the exponent (known as conductivity exponent) of 1.3 in case of 2D randomly conducting network [9, 125]. Motiso et al. [125] generated sheet resistance versus transmittance plot as a function of the aspect ratio of rods, areal density and mixture of short and long conducting rods. In all such cases, the treatment is restricted to percolating conducting rods often with negligible rod resistance, following simply the Kirchhoff's law on individual junctions and loops. Percolation treatment has been developed alternatively using effective medium theory on a perfect lattice with a certain fraction of edges randomly removed [84]. Electrical transport properties of macroscopically homogeneous metal and insulator composition are successfully studied by finite element method and is computationally expensive [144]. Alternatively, the sheet resistance is considered equal to area fraction of the film [183] which may not always be true due to the incomplete and random connectivity of the network. Coleman and coworkers [24] have paid attention to the Figure of Merit (FoM) in the context of percolation and defined a percolative figure of merit by introducing certain corrections on the original definition as

Table 2.1 Sheet Resistance, Transmittance and Figure of merits of TCE defined by Coleman et al. (F_C) and Haacke (F_H).

Method	R_{sn} (Ω/sq)	T (%)	F_C	F_H	comment
Using crack template [55]	4.2	82	430	3.2×10^{-2}	t = 60 nm
Using crack template [52]	0.9	84	2445	1.9×10^{-1}	
Using Nanotrough [174]	2	90	1742	1.7×10^{-1}	
Using Bubble template [162]	6.4	82	282	2.1×10^{-2}	t = 4-30 μm
Ag Nanowires [23]	100	92	500	4.2×10^{-3}	
Ag Nanowires [23]	3.4	75	360	1.6×10^{-2}	
Ag Nanowires [154]	10.2	89.9	339	3.4×10^{-2}	
Cu Nanowires [47]	51	93	100	9.5×10^{-3}	
Cu Nanowires [47]	7.7	68.4	117	2.9×10^{-3}	
Cu Nanowires [47]	1.4	14	80	2.0×10^{-9}	

$$F_C = \frac{\sigma_{DC}}{\sigma_{OP}} = \frac{Z_o}{2R_s(T^{-1/2} - 1)} \quad (2.1)$$

Another commonly used Figure of merit is defined by Haacke [53] and can be written as

$$F_H = \frac{T^{10}}{R_s} \quad (2.2)$$

The typical values of sheet resistance, transmittance and FoM of various TCE are shown in Table 2.1.

Emerging TCEs (See Figure 2.1) contain mesh-like conducting networks from template methods that have to be treated rather differently, not simply as films with finite fill fraction. Neither do they belong to regular periodic wire lattices [180] nor do they resemble the percolating networks. They are close to fully connected regular lattices, but they do contain some isolated wires. The wire width may also have ample distribution. In addition, the wires may be zig-zag or curvilinear in nature enclosing irregular cells. This warrants a study focused on mesh-like TCE, taking into consideration of the above facts.

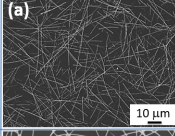
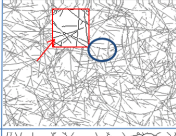
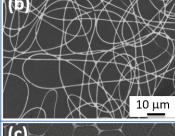
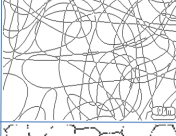
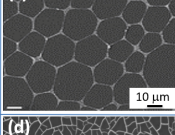
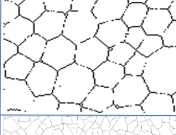
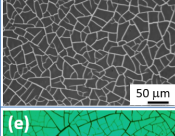
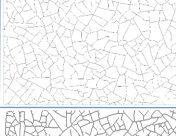
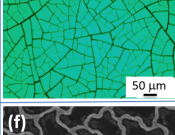
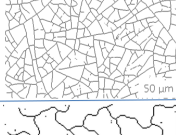
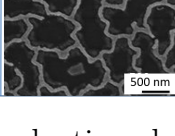

Category	Methodology	Literature image	Skeletonized image	Remarks related to network
Deposited wire networks	Ag NW network by dip coating in ethanol solution			Isolated nanowires (Red box) and dangling part (blue circle) ends passive for current transport are present.
Template based networks	Al nanowire networks by wet chemical etching with electrospun nanofiber mask template			Curvilinear network
	Self assembly of alkyl coated Au NPs within surfactant monolayer template			Non uniform size of polygons
	Crack template (TiO ₂ gel)			Uniform wire width but distribution in polygon sizes.
	Crack template (Acrylic resin)			Non uniform wire width and distribution in polygon sizes.
	Grain boundary lithography			Waviness in the network

Fig. 2.1 Emerging transparent conducting electrodes obtained by different methods with corresponding features. (b) Reproduced with permission from ref [6] Copyright 2014 Elsevier. (c) Reproduced with permission from ref [124]. Copyright 2011 John Wiley and Sons.(d) Reproduced with permission from ref. [55]. Copyright 2014 John and Wiley Sons. (e) Reproduced with permission from ref. [140]. Copyright 2014 RSC Publications. (f) Reproduced with permission from ref [45]. Copyright 2014 Nature Publishing Group.

2.1.3 Scope of the present investigations

The aim of these investigations is to compute sheet resistances of TCEs from template based methods reported in the literature. Here, analytical expressions of sheet resistance of randomly conducting wire network as a function of geometrical parameters of the network have been developed. To show the applicability, microscopy images of wire network were converted into binary image followed by calculation of its geometrical parameters such as the number of edges, curvilinearity, connectivity and compactness. The theoretical model is compared with the experimental works and found to be in

agreement. An algorithm based on image analysis for classifying current carrying backbones, dangling wires and dead wires are evaluated in this work. The analysis has shown that an ideal TCE must possess high edge density, minimum and mono-disperse wire width, least curvilinearity and maximum compactness for better performance.

2.1.4 Results and Discussion

Theoretical model

A conducting random wire network obtained from a template is shown schematically in Figure 2.2 which from an abstract point of view may be considered as a two-dimensional graph. Here, a junction is a point where two or more wires meet in the same plane and the junction is seamless so that the edges form the enclosed polygon. Consider a random network with a sheet resistance of R_{sn} with size $a \times b$ with wire thickness (height) t consisting of isotropically distributed wire segments (henceforth termed as edges) with density (no. of edges per unit area) N_E , mean edge length L_{am} and assumed mono-disperse width w for the present case. The electric field E (along a), is applied using the bus bar positioned on either side of the random network. This bus bar geometry is taken as a simple example; the results obtained are however general in nature as will be shown at the end. We are starting with simple case of non-curvilinear edges, curvilinear edges will be dealt later on. For a good transparent conductor, the fill factor is always uniform irrespective of the electrode area (in other words, it is assumed that edge density is considerably high with edge length \ll sample size) and therefore, one may assume that the electric potential drops uniformly from top to bottom (Figure 2.2a) and there are equipotential lines perpendicular to E .

Consider an edge of length L_i placed in E at an angle θ_i (see Figure 2.2b). The potential difference across the edge, V_i , therefore depends on the orientation of edge- maximum if placed in the direction of electric field, and zero, if placed on an equipotential line.

$$V_i = EL_i \cos \theta_i \quad (2.3)$$

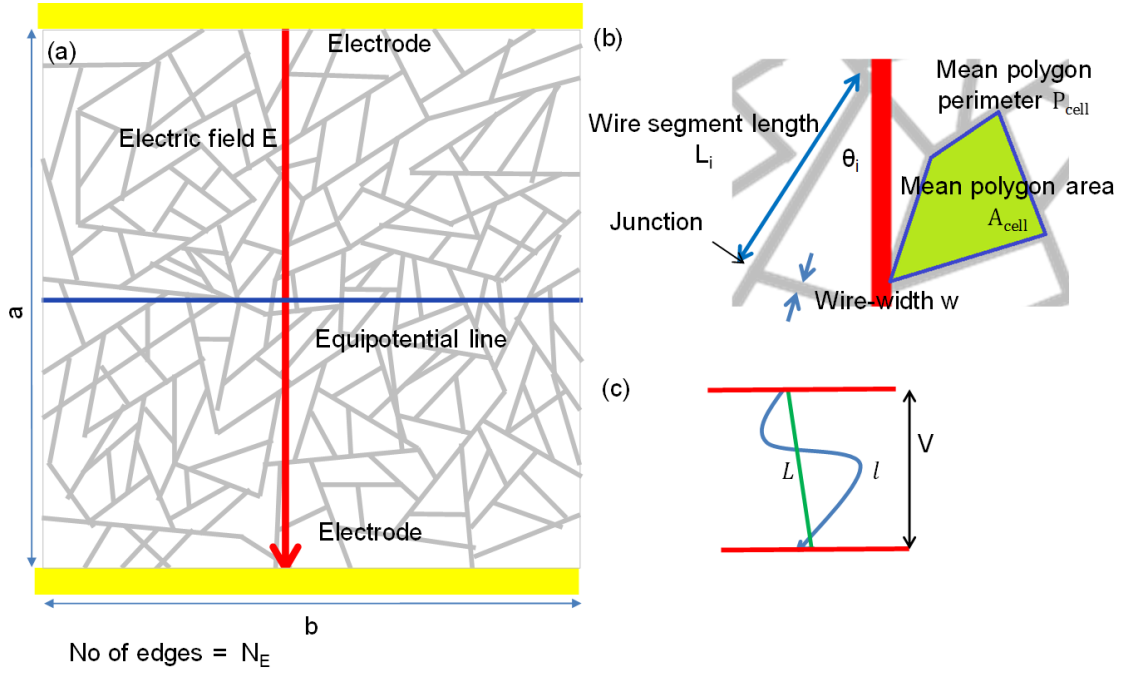


Fig. 2.2 (a) A schematic showing random conducting network placed in bus bar geometry. Electric field is applied from top to bottom (b) Zoom in image of the network showing a wire segment placed at angle θ_i with the electric field (c) Actual curvilinear wire segment length and shortest wire segment length

Since θ_i and L_i are independent, the mean potential difference, V_{am} across N edges of random wires showing variable orientations ($-\frac{\pi}{2}$ to $\frac{\pi}{2}$) can be calculated as

$$V_{am} = \frac{2}{\pi} E L_{am} \quad (2.4)$$

The mean current, I_{am} passing through an individual edge of conductivity σ , can be written as $\frac{\sigma A_{cs} V_{am}}{L_{am}}$, Here, A_{cs} is the cross-sectional area of an individual wire which equals wt in case of rectangular wires obtained from a template with rectangular grooves.

Using the value of V_{am} from Eq. (2.4) one can write as

$$I_{am} = \frac{\sigma wt}{L_{am}} \frac{2}{\pi} E L_{am} = \frac{2}{\pi} \sigma E wt \quad (2.5)$$

The current passing across an equipotential line, I_{eq} , depends on the current carried by a single edge and the total number of edges on the equipotential line which equals $\sqrt{N_E} b$ by symmetry arguments.

$$I_{eq} = \sqrt{N_E} I_{am} b = \frac{2}{\pi} \sigma E w t \sqrt{N_E} b \quad (2.6)$$

Using $E = \frac{V}{a}$ and applying Ohm's law, resistance, R can be written as

$$R = \frac{\pi}{2} \frac{\rho}{w t \sqrt{N_E}} \frac{a}{b} \quad (2.7)$$

Here ρ is resistivity of the material. Thus, sheet resistance of the network, R_{sn} ($= R \frac{b}{a}$) can be written as

$$R_{sn} = \frac{\pi}{2} \frac{\rho}{w t \sqrt{N_E}} \quad (2.8)$$

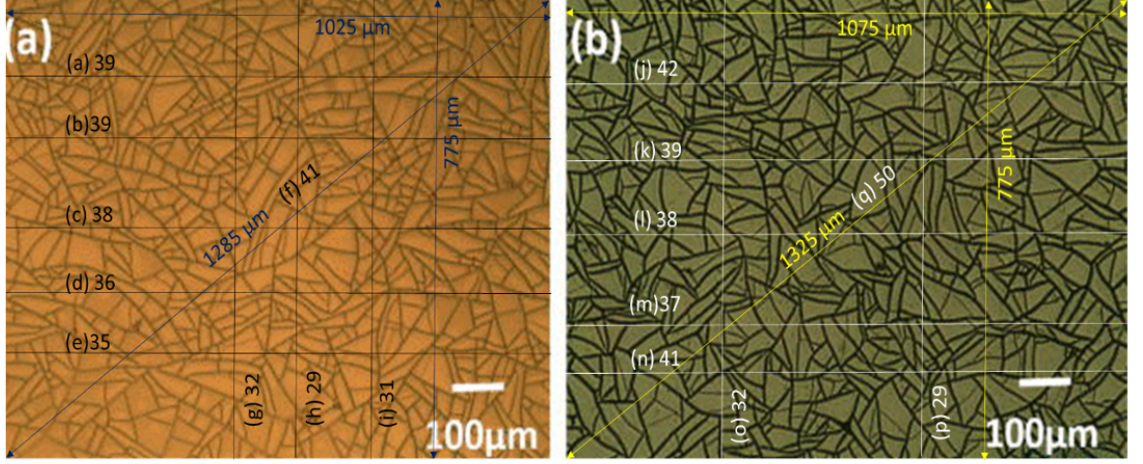
Here the first term depends on the symmetry of network which equals $\pi/2$ for random orientation and varies for different lattice geometry.

It can be written in terms of the sheet resistance of the bulk film, R_s as

$$R_{sn} = \frac{\pi}{2} \frac{1}{w \sqrt{N_E}} R_s \quad (2.9)$$

Hence, the sheet resistance of a network can be reduced by increasing edge density or by increasing wire width.

Table 2.2 compares wire networks from various literature examples obtained using different templating methods. In the calculations, average values by drawing 5 -10 equipotential lines over the whole image leading to small standard deviations are taken. In order to apply our method to varied examples, efforts to access 'good' quality images of the wire networks from the literature were done. Currently, there are not many experimental images easily available; wherever good images could be made available, were used for the analysis. The sheet resistance values computed on the basis of linear edge density and approximate mean wire width are compared with



$$\sqrt{N_E} = \frac{1000}{17} \times \left(\frac{39}{1025} + \frac{39}{1025} + \frac{38}{1025} + \frac{36}{1025} + \frac{35}{1025} + \frac{41}{1285} + \frac{32}{775} + \frac{29}{775} + \frac{31}{775} + \frac{42}{1025} + \frac{39}{1025} + \frac{38}{1025} + \frac{37}{1025} + \frac{41}{1025} + \frac{32}{1025} + \frac{29}{1025} + \frac{50}{1025} \right) = 37.2 \pm 2.4$$

Fig. 2.3 An example showing calculation of edge density of a randomly conducting network from two similar images. Reproduced with permission from ref [133]. Copyright 2015, AIP Publishing LLC.

the corresponding experimental values. Transmittance, T and 2- D metal fill factor (fraction of area occupied by metal), F is also provided. As seen in Table 2.2 that linear edge density, $\sqrt{N_E}$ shows large variation among the examples chosen, from 1.7 to 2000 edges per mm. Similarly, the edge width, w ranges from 90 nm to 75 μm . Nonetheless, the theoretical sheet resistance values agree well with the experimental values. The latter is slightly higher due to aspects which are not taken into consideration in computation such as polycrystalline nature and impurities in the wires, which depend on the metal deposition conditions while resistivity values used in theoretical treatment are the bulk pure metal values. Rao et al. [140] showed that up to 40% reduction in the sheet resistance can be achieved by joule annealing of the network. Thus, the model can be useful in obtaining the lower limit of sheet resistance of a network geometry beyond which one can't reduce sheet resistance for a particular geometry. As an example network obtained from bubble template show sheet resistance of just 0.06 Ω/sq (with $w = 50\mu\text{m}$, $t = 25\mu\text{m}$ and obtained $\sqrt{N_E} = 0.5$) while experimental value is 6.2 Ω/sq . The values are differing by 100, due to the dispersion of prepared wires

Table 2.2 Comparison of various conducting wire networks. Here $\sqrt{N_E}$ was calculated by drawing the equipotential line on the literature image similar to Figure 2.2 and counting the number of intersecting edges on the line (as shown in Figure 2.3). This step was repeated for 5-10 equipotential lines. *(corresponding data not available)

Method	App. $\sqrt{N_E}$ per mm	w μm	t μm	R_{sn} (Exp.) Ω/sq	R_{sn} (Theo.) Ω/sq	Remarks
Grain boundary lithography [46]	2000	0.09	0.05	4.25	7	$R_{sn}^c = 5.31 \Omega/sq$
TiO ₂ gel crack template [55]	115	2	0.06	2.3	1.8	T =66%, F =17.4%
Acrylic resin crack template [140]	60	2	0.22	3.1	1.5	T =87%
Polymer crack template [133]	37	2	0.05	6.8	6.74	T =86%, F = 14%
Self assembly [68]	7	5	3	15	2.4	
Crackle paint template [86]	3	85	0.3	1	0.33	T = 77 %, F =20.4%
Leaf venation template [54]	1.7	75	*	3	—	

forming cross-bar junctions having high resistance. Incidentally, the transmittance of a network is related to 2D metal fill factor ($F = N_E w L_{am}$), thus it can be increased by decreasing edge width, as expected. In the above treatment, edges are considered to be straight and of uniform widths. In reality, networks often contain wires which vary in width being curvilinear in nature and some staying out of the conducting paths. In what follows, the treatment is modified to take these three factors into account.

Curvilinearity and waviness of the wire

The conducting wires of the network in many cases are curved and zig-zag in nature (see images of grain boundaries and electrospinning in Figure 2.1). In such cases wire length between junctions, l_i is not equal to the shortest Euclidean distance, L_i .

As discussed in Eq. (2.4), the potential difference across an edge depends on shortest distance, L given by $V_{Mean} = \frac{2}{\pi} E L_i$ while, conductance of an edge is inversely proportional to actual curvilinear distance, l given by $C_d = \frac{\sigma w t}{l}$. Similar to Eq. (2.58) current passing through a single wire segment, I_{edge} can be written as

$$I_{edge} = \left(\frac{\sigma w t}{l_i} \right) \left(\frac{2}{\pi} E L_i \right) \quad (2.10)$$

Thus obtained sheet resistance, R_{sn}^c for the network with curvilinear wire segments can be written as

$$R_{sn}^c = \frac{\pi}{2} \frac{\rho}{wt\sqrt{N_E}} \left(\frac{l}{L}\right)_{am} = \frac{l}{L} R_{sn} \quad (2.11)$$

Since, $l/L > 1$, the curvilinearity in the network increases the sheet resistance. Hence, curvilinear networks obtained from grain boundary lithography [46] and similar techniques are expected to show higher sheet resistance. For example, for the network image shown in Figure 2.1 from grain boundary method, a l/L ratio of 1.25 was obtained leading to calculated sheet resistance of $5.31 \Omega/sq$ which is more closer to experimental value of $7 \Omega/sq$; the uncorrelated value assuming linear edges was $4.25 \Omega/sq$. While the sheet resistance is bound to increase with curvilinearity, the transmittance of the network would decrease as transmittance is given by $T = 1 - aF$ and F depends on actual curvilinear distance given by $F = N_E w l$. Thus, curvilinearity should be avoided as much to reduce the sheet resistance and increase transmittance.

Wire width distribution

A conducting network may not necessarily have mono disperse wire width [140, 105]. To account for this distribution, Lee et al. [105] used mean value as an effective value of Ag-NW width in Monte-Carlo calculations. However, a random network is a combination of parallel and series resistances and in this study it treats differently. The equivalent width for wires in parallel arrangement is taken as their arithmetic mean (AM) ($w_{eff} = \sum w_i/n$), while for series arrangement, it will be the harmonic mean ($\frac{1}{w_{eff}} = \frac{1}{n} \sum \frac{1}{w_i}$). Thus, equivalent width w_{eff} in a random network is therefore due to both contributions and is expected to be closer to the arithmetic-harmonic mean which in other words, is nearly equal to the geometrical mean (GM) by Bolzano–Weierstrass theorem. The sheet resistance depends on w_{eff} , hence, w can be considered as $w_{eff} \approx w_{gm}$.

$$R_{sn}^{wd} = \frac{\pi}{2} \frac{\rho}{w_{eff} t \sqrt{N_E}} = \frac{w_{am}}{w_{eff}} R_{sn} \quad (2.12)$$

Thus, the correction factor due to width distribution is, $C_{WD} = \frac{w_{am}}{w_{eff}}$, Here, $C_{WD} > 1$ as $GM < AM$ hence, any increase in width distribution of wires leads to increase in sheet resistance. Thus, one should use a network with mono-disperse wire width to reduce the sheet resistance.

Compactness and geometry

The 2-D metal fill factor can also be written in other geometrical forms. We define P_{cell} as the mean perimeter, L_{am} the mean edge length, n_s the mean sidedness and A_{cell} , the mean area of individual cells. Thus, the 2D metal fill factor can be written as $F = \frac{P_{cell}w}{2A_{cell}}$ and in terms of edge density as, $F = L_{am}wN_E$. Using these and applying Eq. (2.9)

$$R_{sn} = \frac{\pi}{2} \frac{\rho}{t} \frac{1}{\beta F} \sqrt{\frac{P_{cell}^2}{2A_{cell}}} \frac{1}{\sqrt{n_s}} \quad (2.13)$$

With Eq. (2.13) emerge some silent features of a random wire network in the context of transparent conducting electrode. Here, the first term depends on symmetry of the lattice which equals $\pi/2$ for a random lattice and its value for non-random lattices can be calculated. The second term is the sheet resistance of film (ρ/t) which is a material property, $1/F$ represents contribution due to 2D metal fill factor which is the deviation from thin film due to open voids and P_{cell}^2/A_{cell} is decided by the geometry. P^2/A is defined as inverse of compactness of a geometrical structure [123] thus P_{cell}^2/A_{cell} can be considered as inverse of effective compactness of a network.

For minimum sheet resistance, at constant fill factor P_{cell}^2/A_{cell} should be as low as possible or in other words, compactness should be high. It can be achieved with the maximum circularity of polygon or to put differently, with maximum sidedness and regularity of polygons. P_{cell}^2/A_{cell} value for regular hexagon, quadrilateral and triangle are 6.92, 8.00 and 10.39 respectively. Thus, a random network generally consisting of irregular sided quadrilaterals, hexagons and triangles, must have more fraction of hexagons and minimum fraction of triangles and the irregularity in polygon sides should be minimum. Thus, networks with the mean angle of 120° are better than a network

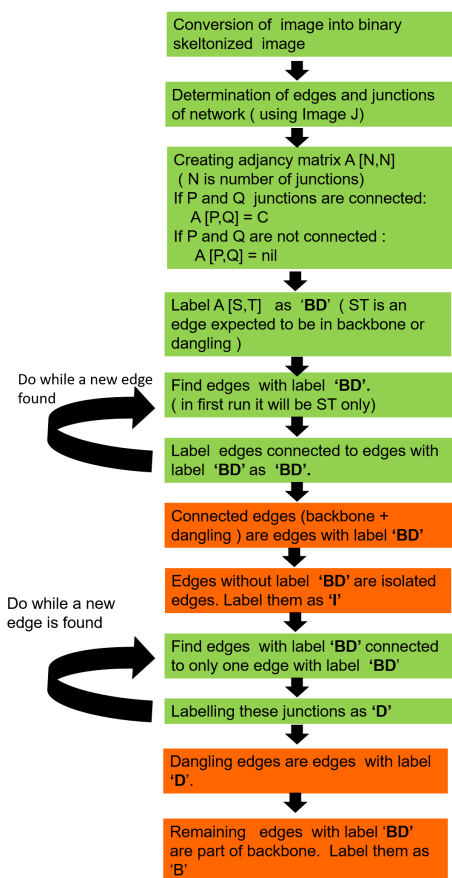


Fig. 2.4 Algorithm for classifying different regions of networks

with junctions with the mean angle of 90° . Eq. (2.13) can be applied to compare different periodic lattices by replacing $\pi/2$ with suitable structural factor (mean of $\cos \theta_i$) which is currently done experimentally [113] in absence of a straight-forward treatment.

Unconnected wires

A network in many cases may not be fully inter-connected and active for current conduction. A network consists of three regions (a) region connected to percolation path as backbone for current transport, (b) region connected to a percolation path as a dangling edge while not being part of the network backbone (ineffective for carrying any current) and (c) the region not connected to any percolation path, isolated edges. Figure 2.4a shows one such example of a network obtained from a crack template.

Please note that out of these regions only conducting backbone (region (a)) effectively participates in current flow [34, 144] and remaining regions merely block the light and cuts down transmittance. Let β is the perimeter of the backbone of the network which is only active for current transport (region a). Thus for a network with mono-disperse width, the effective fill factor, $F_B = \beta F$. To evaluate the emerging TCEs to classify various regions of TCE images provided in this literature, self-written python [163] programs were developed, (see Figure 2.4 for the algorithm).

In an example shown in Figure 2.5a, the crack template obtained from crackle paint show 75% of region(a), 20% of region(b) and 5% of region(c) with $\beta \approx 75\%$. Thus, 25% of area merely blocks the light. Similarly classification of various regions of crack template of TiO_2 gel [55] show 86% of region (a) and $> 99\%$ of combined region (a) and (b) (see Figure 2.6). The templates should be designed so as to have $\beta \rightarrow 100\%$. For accuracy, the edge density and wire width should be calculated from current carrying backbone (region (a)) of an image instead of image consisting of all regions which are taken care in calculations of $\sqrt{N_E}$ for crackle paint crack template (Table 1). Please note that regions (a) and (b) are important for solar cells and OLEDs while only region (a) is relevant for transparent heaters and touch screen devices. This treatment provides an approach of evaluating active regions important in a given context.

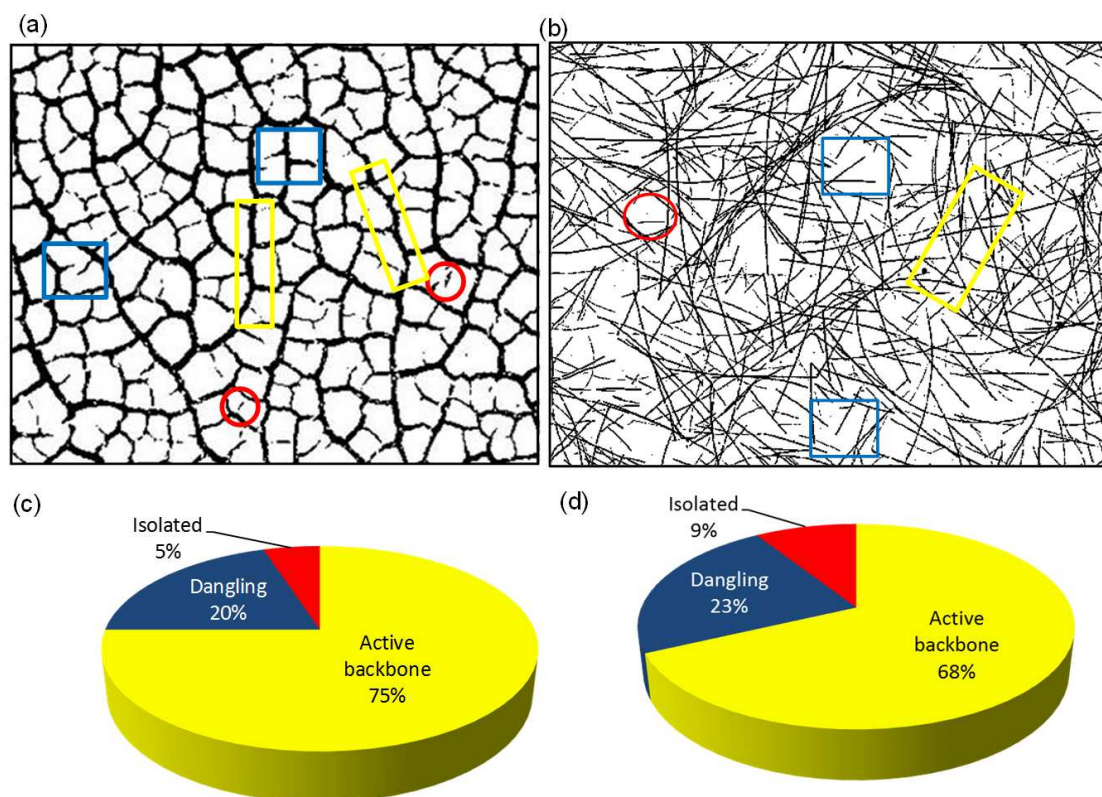


Fig. 2.5 (a) An example of a metal network obtained from crack template [86] and (b) obtained from deposited wire networks. [154] (c) and (d) show pie chart for contribution of different regions in both network networks. See Figure 2.4 for detailed algorithm. (a) Reproduced with permission from ref [86]. Copyright 2014 RSC Publishing.

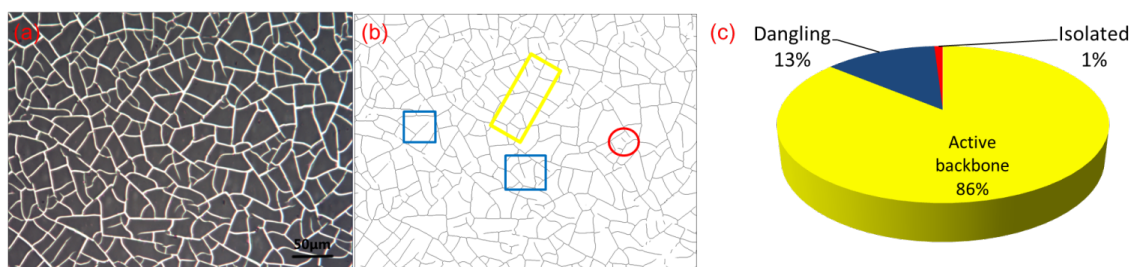


Fig. 2.6 (a) An optical microscope image and (b) corresponding skeletonized image of crack template [55] with active backbone edges (shown in yellow), dangling edges (shown in blue) and isolated edges (shown in red) (c) Pie-chart showing fractional contribution of different regions.

Cross bar junction

The treatment discussed for template-based networks can further be extended to deposited nanowire networks (dense networks). These networks differ from template-based network in two aspects, firstly nanowire networks possess junction resistance (say, R_j), secondly, the area of cross-section of individual wire, A_{cs} is given by $\pi D^2/4$ rather than wt .

Substituting these values, mean conductance of a individual edge can be written as

$$C = \frac{1}{\frac{4L_{am}}{\sigma\pi D^2} + R_j} \quad (2.14)$$

Carrying out similar calculations, sheet resistance can be obtained as.

$$R_{sn} = \frac{\pi}{2\sqrt{N_E}} \left(\frac{4\rho}{\pi D^2} + \frac{R_j}{L_{am}} \right) \quad (2.15)$$

Above expression is very important if junction resistance is comparable to skelton resistance by treatments on junctions[145]. Here, the first term is resistance due to rod R_{rod} , while the second term is resistance due to junction R_j . Taking limiting cases, if $R_j \ll R_{rod}$ then,

$$R_{sn} = \frac{2\rho}{\sqrt{N_E} D^2} \quad (2.16)$$

While if $R_j \gg R_{rod}$ which is a realistic case in case of metal NWs with untreated junctions and CNT networks then

$$R_{sn} = \frac{\pi}{2\sqrt{N_E}} \frac{R_j}{L_{am}} \quad (2.17)$$

Thus, the sheet resistance increases linearly with junction resistance, which is in good agreement with experimental studies performed for CNT networks by C-AFM studies [129] and numerical studies for Ag NW network. [125]. A network should have minimum junction resistance, maximum edge density and higher edge length to reduce

the sheet resistance. Using the above expression, one can determine R_j of a network prepared by any method, which may be helpful in optimization steps.

Connectivity quantification is performed in the case of deposited wire networks as well. As an example image of AgNW networks of Sepulveda et al. [154] as shown in Figure 2.5b show 68% of region (a) and 91% of combined region (a) and (b) (see Figure 2.5d). The conductance of deposited wire networks is percolation limited ($\beta < 1$) and depends on the aspect ratio of rods.

Figure of merit of a network

Transparent conducting electrodes is quantitatively compared with the value of Figure of Merit values as the ratio of electrical and optical conductivity as given in Eq. 2.1 which should be maximum and >35 for industrial standards [24]. In the expression sheet resistance of a network can be written as

$$R_{sn} = C \frac{\pi}{2} \frac{\rho}{A_{cs} \sqrt{N_E}} \quad (2.18)$$

Here, $\sqrt{N_E}$ should be calculated from current carrying backbone (region (a)) for better accuracy and C is the combined correction factor due to width distribution and curvilinearity correction. The fill factor can be related to transmittance [125] using

$$T = 1 - aF \quad (2.19)$$

Here, parameter a can be obtained experimentally by plotting fill factor v/s transmittance or by using FDTD simulations [12] which depends on film thickness, wavelength of light and the geometry of network. The transmittance of a network with mono-disperse width can be related to backbone fill factor, F_B as

$$T = 1 - \frac{aF_B}{\beta} \quad (2.20)$$

Here, backbone fraction in case of templates can be written as

$$F_B = N_E l_{am} w \quad (2.21)$$

And in case of nanowires as

$$F_B = N_E l_{am} D \quad (2.22)$$

From Eq. (2.15) and Eq. (2.20), the trade off between optical transmittance and electrical conductance is apparent. Moreover in case of NW networks, junction resistance and percolation limited low value of β pose limitations to achieve high FoM.

On the other hand in case of template-based networks, though wire width and edge density show the similar trade off between optical transmittance and electrical conductance, the wire thickness (practically the film thickness) is an additional parameter which can reduce sheet resistance without compromising optical transmittance, in principle. Additionally, they do not possess junction resistance and can show $\beta \rightarrow 1$. Hence, template-based conducting networks may be more promising randomly conducting TCEs. Collective expression connecting transmittance and sheet resistance involving various corrections can be written as

$$T = 1 - \frac{\pi^2}{4} a \frac{1}{\beta} \frac{l}{w} \frac{l}{L} \frac{\rho^2}{t^2 R_{sn}^2} \quad (2.23)$$

Thus, the high transmittance for constant sheet resistance can be attained by lower value of curvilinearity l/L , lower value of a (extra-ordinary transmission), the high film thickness (t) and maximum connectivity (β). Above formula should be modified for low w and t as ρ is no longer constant with w and t comparable to mean free path of electrons (which is 20-30 nm for Ag) or grain boundaries [14]. Similarly, T depends on film thickness (as a is a function of t), but in the networks obtained from templates with high t , it will have no virtual effect as shown in experimental work as compared to variation in electrical properties [142]. However, in this context, FoM as defined in Eq. (2.1) is not a competent indicator as it depends only on average sheet

resistance and transmittance properties of complete film and hence is incapable to tell about associated spacial uniformity and functional resolution of TCE which is equally important. In other words, apart from high value of FoM, a network must have high Local Figure of Merit [50] which is important for good optoelectronic performance (like resolution of touch screens, uniformity in heating in case of transparent heaters and effective charge collection of solar cells which have exciton mean free path $< 100\text{nm}$). Edge density (considering connectivity quantification) defined and computed in this section can help in giving information about resolution in addition to sheet resistance and transmittance. Increase in edge density increases the ensemble size leading to uniform properties from pixel to pixel. Higher is the edge density, smaller can be the pixel size of a device. Thus, the networks showing low edge density (< 5) from bubble template [162], leaf venation template [54] or from wide crack template [86] are less suitable for high resolution TCE, while finer crack templates [140, 55] and grain boundary templates [46] produce networks with high edge densities, which may be more suitable. Moreover, it can be seen that the value of edge density is sensitive to template preparation conditions [55]. Proper care should be taken in comparing templates by FoM as it is not just dependent on network efficiency but depends on metal film thickness, thus must be normalized with t and ρ for template comparison. A TCE should have uniform values of mean wire width and edge density in different samples and different regions to have consistent optoelectronic properties. Apart from optoelectronic properties, a TCE should be robust for accidental damage of few edges. More is the edge density, more will be robustness. Thus information of edge density and wire width can give superior information than FoM. For a better optoelectronic properties, high resolution and better robustness a network should have high edge density and less wire width.

On comparing deposited wire network (like CNT or Ag NW) and network obtained from crack template, in case of random deposited wire network complete backbone fraction is never possible as a newly introduced nanowire (CNT or AgNW etc) in percolating cluster can either act as isolated, dangling or backbone depending on

its location which is not under control [34]; but, on the other hand a new and secondary crack always interconnect primary cracks for maximum stress release and hierarchical nature of crack formation [15] and can essentially lead to complete backbone connectivity under controlled conditions. Thus, in terms of connectivity networks obtained from crack template [55, 140] are superior than deposited wire networks such as Ag NW and CNT networks.

2.1.5 Conclusion

A generalised method for evaluating randomly conducting wire networks has been developed. It is solely based on the geometry of the network characterized by random wire orientation, curvilinearity, wire width distribution, polygonal area and perimeter. It is found that for low sheet resistance and high transmittance, the edge (wire) density should be maximum with minimum wire width. It has been shown that curvilinearity and wire width distribution increase the sheet resistance. The sheet resistance not only depends on the 2D metal fill factor but is also affected by the compactness of the network. A network polygon should have a higher value for sidedness, least irregularity and the maximum number of tri-junctions (hexagonal structures are more compact than square structures). The sheet resistance values from our analysis compare well with the experimental values, the later value is somewhat higher due to defects of smaller length-scales. A treatment is provided to evaluate the fraction of an active region of a network, a parameter important for device fabrication. It is found that if lower wire widths can be managed (as with chemically prepared metal network), the template based networks can score over non-template based nanowire networks as the former possess higher compactness, higher interconnectivity and seamless junctions with negligible junction resistance. In a typical template method, the well connected active region can be as high as 86% (compared to 68% in deposited wire networks) with dangling wires accounting to 13% and completely isolated, 1%.

2.2 Current distribution in conducting nanowire networks

2.2.1 Summary

Conducting nanowire networks find diverse applications in solar cells, touch-screens, transparent heaters, sensors, and various related transparent conducting electrode (TCE) devices. The performances of these devices depend on effective resistance, transmittance, and local current distribution in these networks. Although there have been rigorous studies addressing resistance and transmittance in TCE, not much attention is paid to studying the distribution of current. Present work addresses this compelling issue of understanding current distribution in TCE networks using analytical as well as Monte-Carlo approaches. We quantified the current carrying backbone region against isolated and dangling regions as a function of wire density (ranging from percolation threshold to many multiples of threshold) and compared the wired connectivity with those obtained from template-based methods. Further, the current distribution in the obtained backbone is studied using Kirchhoff's law, which reveals that a significant fraction of the backbone (which is believed to be an active current component) may not be active for end-to-end current transport due to the formation of intervening circular loops. The study shows that conducting wire-based networks possess hot spots (extremely high current carrying regions) which can be potential sources of failure. The fraction of these hot spots is found to decrease with increase in wire density, while they are completely absent in template-based networks. Thus, the present work discusses unexplored issues related to current distribution in conducting networks, which are necessary to choose the optimum network for best TCE applications.

2.2.2 Introduction

Transparent conducting electrodes are essential components of various optoelectronic devices such as solar cells and organic light emitting diodes. [90, 151] TCE also

find applications in other modern devices such as touchscreens, sensors, transparent heaters, thermo-chromic and electrochromic devices etc. [23, 94] As conventional oxide-based transparent conductor films suffer from several disadvantages such as brittleness, non-flexibility and high cost [122], there have been tremendous efforts in the literature in the recent past to replace it. [90] The promising candidates include networks of 1D conducting objects such as carbon nanotubes and Ag or Cu nanowires as against transparent thin layers of graphene and metal thin films. Networks of highly conducting 1D structures are preferred for assured electrical conductivity. Template based techniques such as crack templates [52], electrospinning of nanofibers [174] have also been employed to produce such networks. Here, light transmission takes place through the void regions while electrical conduction comes from the interconnected tubes or wires. Thus, the visible transmittance and the sheet resistance essentially decide the figure of merit of the electrode [50] which depends on current distribution in the network. The downside of network-based TCE is obviously the reluctant wires staying out of percolative current paths. Although the effective electrical resistance and transmittance of these networks have been explored in detail using analytical, numerical as well as experimental approaches, not much attention has been paid to understand current carrying fraction of the wires in the percolative network and the current distribution in these networks. In this work, both these aspects are carefully investigated. Wire networks may be broadly classified into two categories, namely networks based on randomly placed wires such as AgNW and CNTs, and templated patterns based on interconnected cracks or grain boundaries of the template as well as electrospun networks. In both categories, a wire in the network may be part of a current carrying percolative backbone, be it dangling being a part of the percolative network but not carrying current, or be it entirely isolated from any current carrying region. [92] The dangling regions are important for charge collection in the applications like solar cells [91] but does not contribute to reducing the sheet resistance of any derived device. Below, the literature efforts giving insight into different modes of wire participation are examined. Using conducting Atomic Force Microscope (C-AFM),

Coleman et al. [23] and Boland et al. [33] have obtained current maps of AgNW networks while biasing one edge of the electrode. With this biasing geometry, the percolating region could be identified effectively; however, the dangling was also shown as part of the current carrying network. In another study, [152] nano-manipulators have been used to obtain resistance between two points on the network; however, this method would not allow one identify the different categories mentioned above. Similarly, IR microscopy would not be helpful as regions not carrying current also attain similar temperatures owing high thermal conductivity of the metal. Recently, sophisticated thermorefectance measurements have been performed which relates emissivity, temperature and resistance. [19] However, no information regarding dangling and isolated regions were made available. It is rather challenging to identify active current carrying regions using experimental techniques, especially when the electrode area is large. There have been theoretical studies related to electrical transport in wire networks focusing mainly on the variation of parameters such as the effective resistance and the percolation threshold of the network with respect to aspect ratio [12], waviness [112] of the wires as well as variation in the length. [125] The studies show that conductivity follows a power law with wire density as $\sigma = \sigma_o(N - N_c)^t$ with N is the rod density, N_c the critical density of percolation and t , the conductivity exponent of value 1.3. Using Monte Carlo approach, current maps have been examined to identify active junctions participating in the electrical transport, generally considering only junction resistances while neglecting wire resistances. [33] Žežel et al. [186] have shown the variation of the conducting exponent (t) for different ratios of junction and wire resistances. Das et al [22] defined effective thickness to express equivalent thickness of percolating networks. Recently, Chan et al. [19] using finite element method obtained current maps of template-based networks and derived the hot spots in the network. Very recently, Callaghan et al. [130] developed an effective medium theory for AgNW networks and obtained effective resistances of the networks. In this direction, earlier work attempted [92] as discussed in Section 2.1 to classify the different regions in random networks assuming uniform current flow; however, the work was limited to

experimental image analysis, not discussing the variation of the size of the current carrying backbone with wire density and was silent on distribution of current and presence of hot spots in the network.

2.2.3 Scope of the present investigations

This work addresses the important issues of electrical properties in network by systematically studying backbone fraction of NWs of different densities using analytical as well as Monte-Carlo approach. The current distribution of these networks using Kirchhoff's law are studied. Strikingly the whole backbone is not effective for current transport and there are hot spots in the network. Current distribution in the template-based network and conducting rod based networks of different densities are also compared.

2.2.4 Results and Discussion

Conducting wires based network

Nanowires were distributed at random positions and angles computationally using uniform random number generators (see Figure 2.8a). The intersection points of these wires were identified and the junction numbers were assigned to the points of intersection and similarly, wire segment (edge) numbers were assigned to wire segments joining neighbouring junctions. The three regions namely (a) current carrying backbone (b) dangling wire connected to a percolating region but ineffective for current transport and (c) isolated wire not connected to any region, have been classified for different densities and shown in Figure 2.7 and Figure 2.8a-f.

$$\text{Connected Fraction} = \frac{\text{Backbone} + \text{Dangling}}{\text{Backbone} + \text{Dangling} + \text{Isolated}} \quad (2.24)$$

and

$$\text{Backbone Fraction} = \frac{\text{Backbone}}{\text{Backbone} + \text{Dangling} + \text{Isolated}} \quad (2.25)$$

Corresponding fractions are plotted in figure 2.8g with red and blue squares respectively. Consider L to be the wire-length, n , number of wires in the area L^2 and n_c , the critical

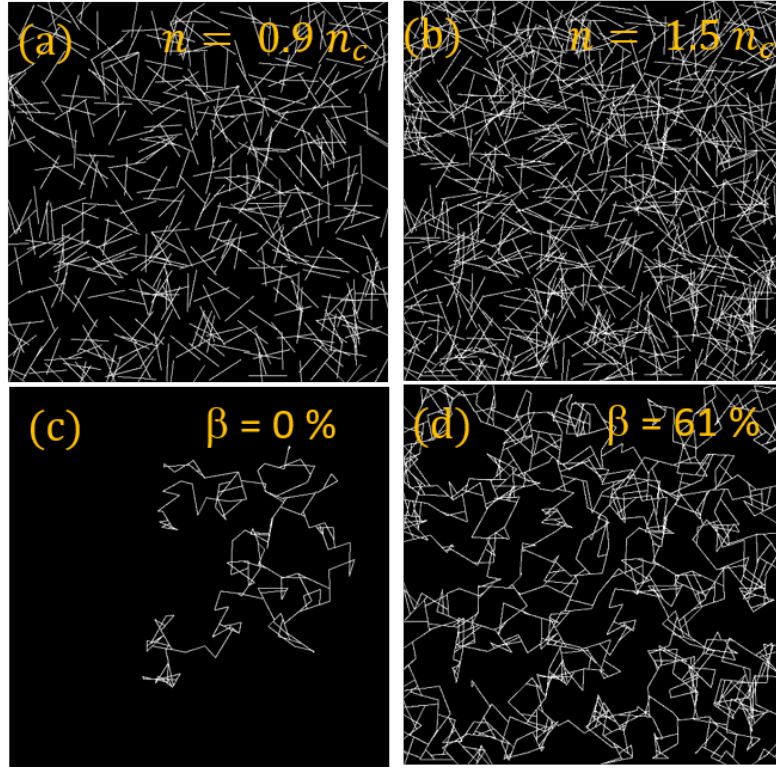


Fig. 2.7 (a-b) Conducting wire-based networks of different densities with (c-d) corresponding backbone

wire density, which is 5.6372. The approximate backbone of a dense network can also be analytically calculated based on the intersections. A wire with k contacts (junctions) forms $k + 1$ segments, but the outermost segments (two) do not take part in the backbone (see Figure 2.9). Thus in a network, only the $\frac{k-1}{k+1}$ fraction participates in the backbone, while $\frac{2}{k+1}$ fraction is lost as dangling. Please note that the argument is valid if there are negligible isolated wires (in other words, almost all wires participate in the percolation network, which is the case for higher densities), else the analytical treatment tends to overestimate the backbone fraction. In a network, the number of contacts a wire makes is highly varied, anywhere between zero (dangling) to small numbers (up to say 10) in sparse networks but the number can be quite high in dense networks. The number of contacts made by a rod in a random network has been evaluated using geometrical and statistical approaches. [61] The distribution of the number of intersecting contacts (k) per rod is given in terms of Poisson's distribution

as

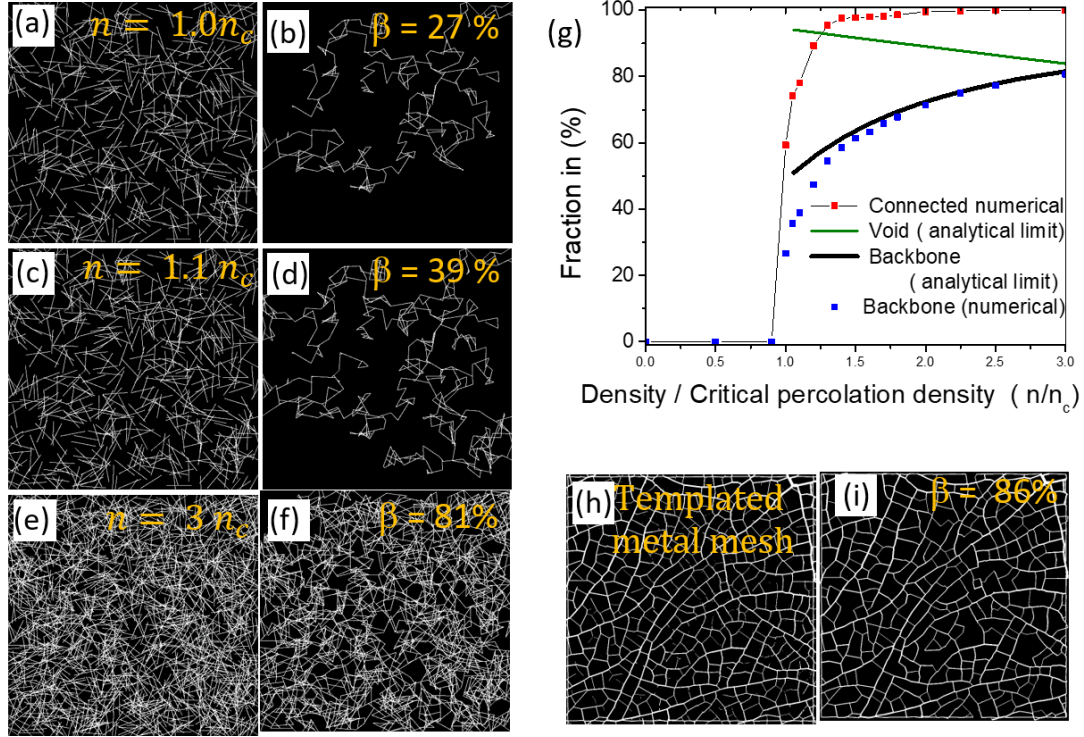


Fig. 2.8 (a) -(c) Conducting wire based networks of different densities. n_c represents critical percolation density. (d-f) represent corresponding backbone. (g) Plot of variation of connected, backbone, and void fraction with density of conducting wires. Numerical results go well with analytical for higher densities. (h) the binary image of a typical templated metal mesh obtained from a crack template and (i) its corresponding backbone.

$$P_c(k) = \frac{(cn)^k e^{-cn}}{k!} \quad (2.26)$$

Here, c is a constant with a value of 0.2017π obtained with analytical as well as Monte Carlo treatments. As an example, for $n = 1.5n_c = 1.5 \times 5.6732$, the probability of 3 contacts is 12.32%. We have applied this distribution to evaluate the backbone fraction of the network. For the sake of generality, the backbone fraction (β) can be written as (after removing two outer wire segments from all):

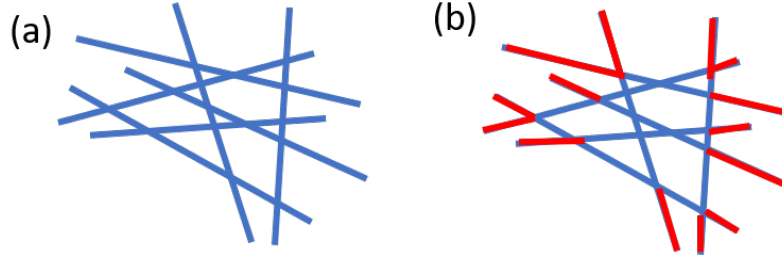


Fig. 2.9 (a) Schematic of nanowire network. (b) Two outermost wire segments (shown in red) are not participating in backbone.

$$\beta = \sum_{k=1}^{\infty} P_c(k) \frac{k-1}{k+1} \quad (2.27)$$

From Eq. (2.26) which can be written as:

$$\beta = \sum_{k=1}^{\infty} \frac{(cn)^k e^{-cn}}{k!} \frac{k-1}{k+1} \quad (2.28)$$

On series expansion, which can be expressed as:

$$\beta = 1 + e^{-cn} + \frac{2}{cn}(e^{-cn} - 1) \quad (2.29)$$

Eq. (2.29) may be used to obtain the backbone fraction at any given network density. An example is given in Figure 2.8g comparing with numerical results. There is good agreement between the two except at lower wire densities, where analytical treatment (Eq. (2.29)) overestimates the numerical backbone fraction, as it considers all wires to be part of the backbone. Calculated backbone fraction can be further applied in obtaining resistance value using our geometrical model (section 2.1.4) or the effective medium approach. [130] As shown in section 2.1.4, we calculated variation of resistance in terms of the total number of wire segments (N_E), wire diameter (D), junction resistance (R_j) and mean wire segment length (d).

$$R_{sn} = \frac{\pi}{2\sqrt{N_E}} \left(\frac{4\rho}{\pi D^2} + \frac{R_j}{d} \right) \quad (2.30)$$

Here, the first term represents resistance contribution due to junction resistance while the second term represents contribution due to wire segments. However, N_E and d were not evaluated in the previous treatment. The wire density of backbone depends on wires as well wire segments of individual wires, which can be obtained using contact probability and hence, the wire density can be written as

$$N_E = n \sum_{k=1}^{\infty} P_c(k)(k-1) = n(cn + e^{-cn} - 1) \quad (2.31)$$

Similarly, the average length of wire segment in backbone (d) can be written as

$$d = \sum_{k=1}^{\infty} \frac{P_c(k)}{k+1} = \sum_{k=1}^{\infty} \frac{(cn)^k e^{-cn}}{(k+1)!} \quad (2.32)$$

On series expansion it becomes

$$d = \frac{1 - e^{-cn} - e^{-cn}cn}{cn} \quad (2.33)$$

Thus, sheet resistance of a network with only wire resistance (neglecting junction resistance) can be obtained by substituting Eq. (2.31) in Eq. (2.30).

$$R_{sn} = \frac{2\rho}{\sqrt{n(cn + e^{-cn} - 1)}D^2} \quad (2.34)$$

While sheet resistance of a network with only considering junction resistance can be written as $R_{sn} = \frac{\pi R_j}{2\sqrt{N_E}d}$ from Eq. (2.30) which can be rewritten after substituting $\sqrt{N_E}$ from Eq. (2.31) and d from Eq. (2.32) as

$$R_{sn} = \frac{\pi R_j}{2\sqrt{n(cn + e^{-cn} - 1)}} \frac{cn}{1 - e^{-cn} - e^{-cn}cn} \quad (2.35)$$

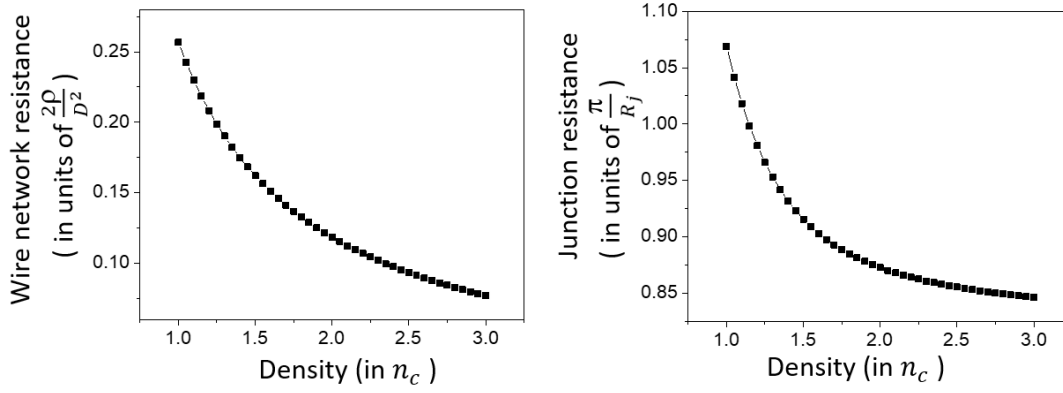


Fig. 2.10 (a) Effective Wire network resistance (neglecting junction resistance) and (b) Effective junction resistance in a network (neglecting wire resistance) w.r.t wire density.

Both these expressions Eq. (2.34) and Eq. (2.35) representing the contribution of wire segments and junctions respectively are plotted in Figure 2.10 which shows sheet resistance decreases with density in both the cases. The variation in wire segment resistance with density is more significant than junction resistance variation with densities. In other words, effective network junction resistance varies only a little with wire density as compared to variation in effective wire segment resistance with density. However, a point should be noted that the treatment is valid only if equipotential lines are parallel to each other which is true only at high densities (typically $n > 2$). The obtained values of sheet resistance can be very useful in estimating the temperature rise ΔT of a transparent heater obtained from these wire networks by substituting R_{sn} value in the following equation from Sorel et al. [158]

$$\Delta T = \frac{V_o^2}{R h_{eff} a b} = \frac{V_o^2}{R_{sn} h_{eff} a^2} \quad (2.36)$$

Here, V_o is the applied voltage, R and R_{sn} are the resistance and sheet resistance of network of size $a \times b$ (with a in the direction of the field and b along perpendicular direction of the field), and h_{eff} is the effective heat transfer coefficient considering convection and radiation losses to the surroundings. The thermal properties of metal

networks on a transparent substrate are studied in detail in future section 4.1.3. The optical transmittance of the network also depends sensitively on the wire density [12]. The transmittance has been studied experimentally as well as using finite difference time domain (FDTD) and is found to be proportional to void fraction (1-fill factor, the latter being the area fraction occupied by metal wires) of the network with the proportionality constant depending on wavelength of light and also on the material property etc. The area fraction occupied by a single wire is $\frac{wL}{L^2}$, thus the area fraction occupied by n wires would be $\frac{nwL}{L^2}$. However, it is noted that the contact area (where two wires meet) was added twice in the earlier treatment. [12, 137] While this does not make much of a difference at low wire densities, but may become significant for wire densities higher than $2n_c$ or in other words, higher fill factors. A network with n wire density with $P_c(k)$ probability of k contacts per wire, makes a total of $n \sum_{k=1}^{\infty} P_c(k)k$ contacts in a network which accounts for the total area fraction of the contacts, $\frac{nw^2}{L^2} \sum_{k=1}^{\infty} P_c(k)k$. Hence, considering the fill factor and the total area fraction of contacts, the percentage void fraction, V can be written as:

$$V = 1 - \frac{nw}{L} + \frac{nw^2}{2L^2} \sum_{k=1}^{\infty} \frac{(cn)^k e^{-cn}}{k!} k \quad (2.37)$$

On series expansion it can be obtained as

$$V = 1 - \frac{nw}{L} + c \frac{n^2 w^2}{2 L^2} \quad (2.38)$$

The second term in the above equation becomes significant only at higher wire densities; for example for $n = 3n_c$, V values are 83.0% and 84.8% without and with the contact area correction, respectively. An increase in the wire density increases the backbone fraction (Eq. 2.29) while it decreases the void fraction (Eq. 2.38) which is shown in Figure 2.8g. However, as seen from Figure 2.8g, the percolating backbone fraction is small (<50%) for low wire densities (n between 1 and 1.2). For example, for $1.2n_c$ assuming an aspect ratio L/w of wires as 100, the void fraction turns out to be 94%. However, the backbone fraction is just 38% implying that most of the wires

in the network area are out of the percolative path for electrical transport, merely blocking the light. Notably, even very high density of wires ($>2n_c$) does not lead to complete backbone fraction ($\beta=1$). Doubling the density ($2n_c$) takes the backbone fraction to 71.4% only; the void fraction, however, stood close to 89%. Interestingly, despite wires being nearly random in the network, the wires in the obtained backbones are not quite evenly spread out, dense in some places and sparse somewhere else (compare networks in Figure 2.8 a, c, and e with the corresponding backbone portions in Figure 2.8 b, d and f, respectively). The unevenness of the wire distribution in the backbone is found to be an inherent property of the network and is seen significantly irrespective of random configurations. Moreover, current being unidirectional possess another limitation for the overall current flow. Thus, the uniformity of dispersed nanowires does not guarantee the uniformity of the backbone and in turn, the electrical properties.

To understand these aspects in more detail, electrical properties of the obtained backbones are studied. The analysis is performed by biasing the two opposite boundaries and applying Kirchhoff's law on individual local current loops formed by polygonal arrangements of wires in the network. Each loop was solved numerically. Figure 2.11a shows the current map of backbone for $1.5n_c$ with the current scale normalized in such a way that the mean current in a wire from the backbone is set to a value of 1.0. The wires not forming the backbone (carrying zero current) have been removed for clarity. The map in Figure 2.11a clearly shows that the current distribution in the backbone is highly non-uniform with large fraction of wires (8%) carrying negligible current (< 0.1 of the mean current) as shown in Figure 2.11b and significant (2.7%) rather high current ($\sim 5-10$ of mean current) as shown from Figure (2.11c); this leads to two scenarios namely loops which feed current into other loops thus enabling further distribution of current and loops which feed nearly within themselves. See locations 1-2 showing regions of negligible current (zoomed in for clarity). In location 1, current carrying path A-B-C-D is quite greater than minimum path A-D, hence its resistance is higher leading to low current. It is in agreement with our previous results which shows

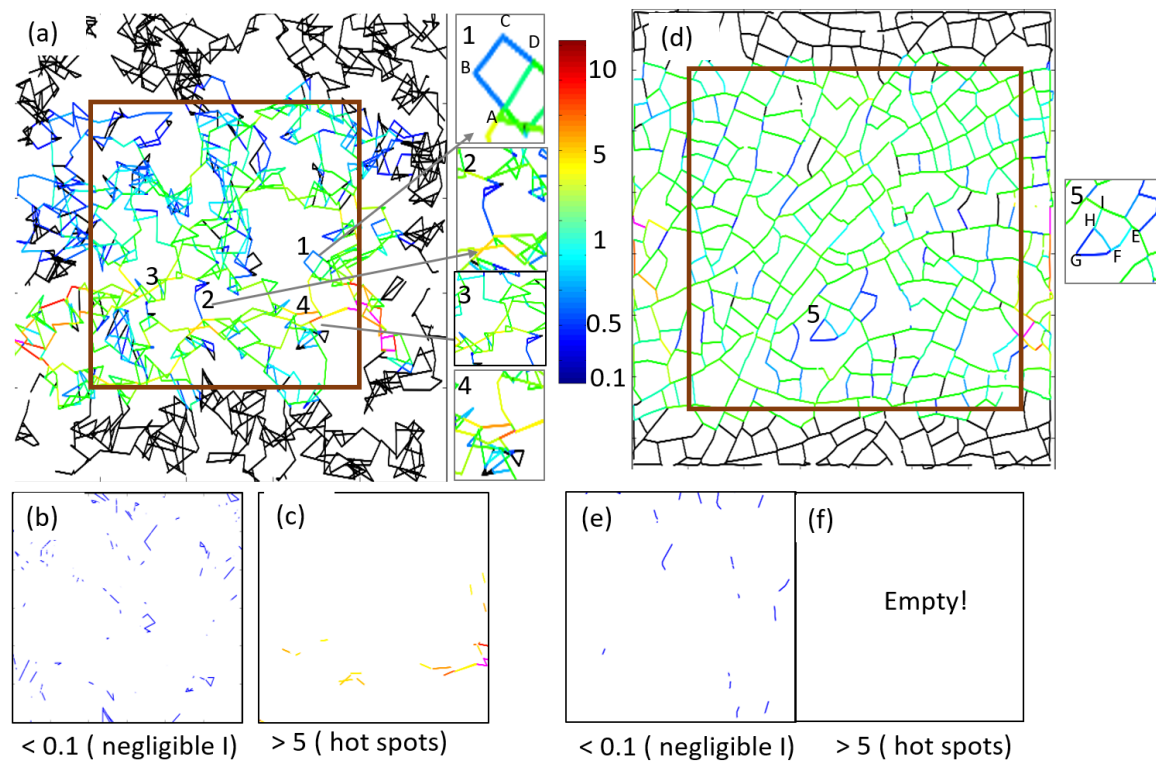


Fig. 2.11 Current map of (a) conducting wires based network (created by Monte Carlo for density = 1.5 times critical percolation density). It is clear in conducting wires based network there is a significant area with (b) negligible current and (c) hot spots. Current map of (d) templated metal mesh. Here, (e) wires carrying negligible current, is negligible and (f) there is no wire segment with the very high current. (Empty! represents there is no region with hot spots). Inset showing Locations 1 and 5, carrying negligible current due to loop not enabling current distribution, location 2 represents wires with negligible current due to wire ends lying on equipotential lines, location 3 enables further current distribution and is good for the network while location 4 shows hot spots. Current distribution is studied only for networks within the brown coloured square to avoid errors due to boundaries.

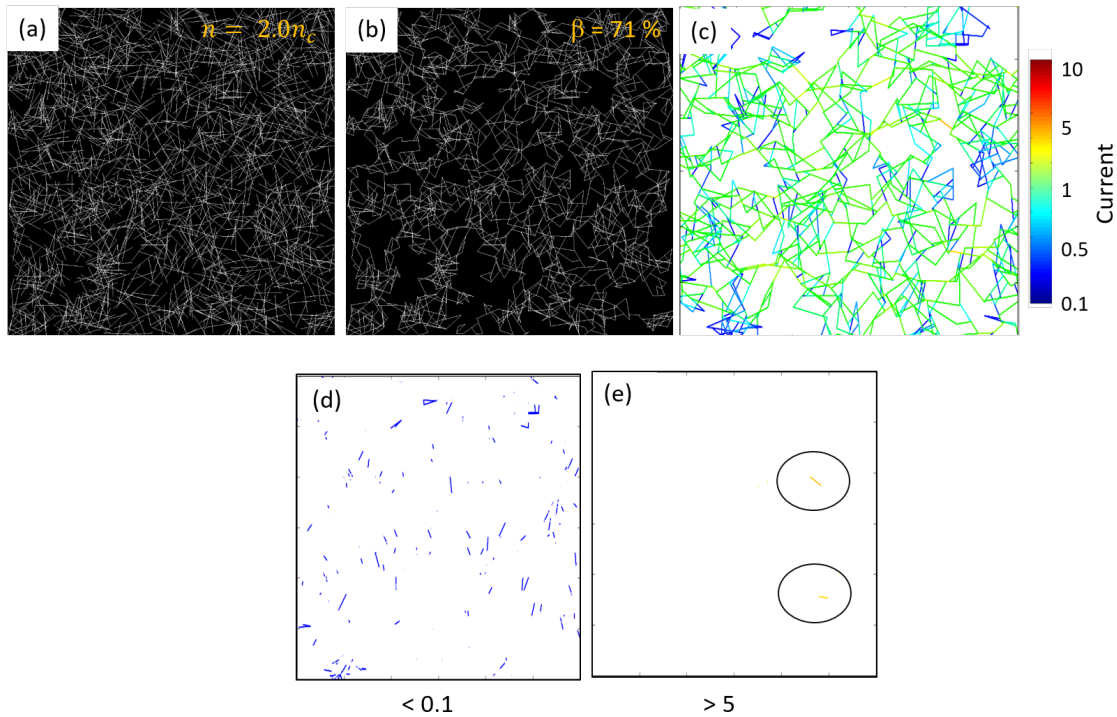


Fig. 2.12 (a) Conducting wires based network with $2n_c$ density and (b) corresponding backbone. (c) Current map of the central region of obtained backbone and regions of (c) negligible current and (d) hot spots.

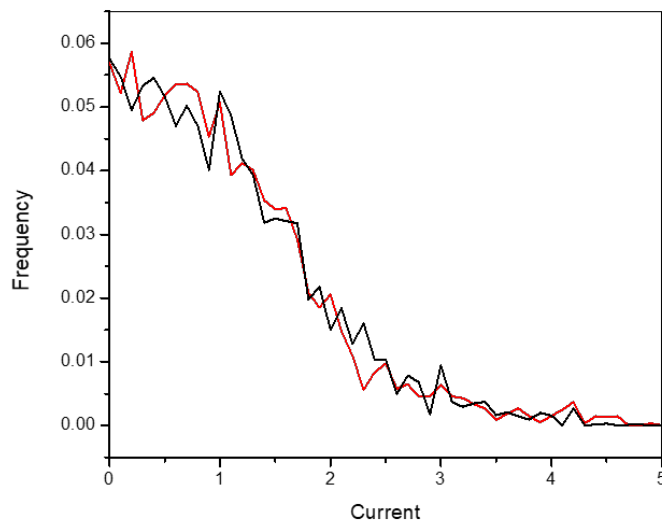


Fig. 2.13 Current distribution for two other networks having $2n_c$ density.

curvilinear wires have higher resistance. (section 2.1.4 and our paper [92]) Location 2 may be carrying low current due to its end points lying on equipotential lines. The locations 3 are loops which are enabling further current distribution and good for electrical transport. Furthermore, a significant area carries too high currents (> 5 times mean current) which are indicated in Figure 2.11c. The regions are the hotspots of the network forming a bottleneck as indicated in the zoom-in image of location 4 where two wires carry the current load to connect two clusters. As shown by Behnam et al. [11] in case of CNT networks, the bottlenecks may be potential points of failure at high current densities and decides the failure of the network. Breakage of these areas can lead to cascade effect leading to complete breakdown of the network. [11] Thus, it is clear these networks limit the maximum working current density, which reduces the maximum achievable temperature of the derived heaters significantly proportional to $(\frac{I_{max}}{I_{avg}})^2$. A similar analysis was performed for a network with higher density, $2n_c$ as shown in Figure 2.12 and 2.13. The features are similar, however, the fraction of lower and higher current carrying region is reduced which is quantified later. Thus, networks with increased density of wires can sustain a relatively higher current density before failing.

Templated metal mesh

Templated metal mesh is another important TCE candidates which are obtained from cracks [52, 56] grain boundaries and electrospinning [174] etc. Figure 2.8h shows a typical template metal mesh obtained from a crack template. To understand the backbone of these microscopic images, CIAS software [115] is used to extract wire segments and corresponding wire widths. The obtained wire segments information is filtered for image artefacts and corresponding backbone is obtained from our algorithm. As shown in Figure 2.8i the network shows high void and backbone fractions of 86% and 87% respectively. As a benchmark, it may be noted that to achieve such a high backbone fraction in an equivalent conducting wires based network, the required density of conducting wires is $4.3n_c$ which would have a void fraction of just 77% (in

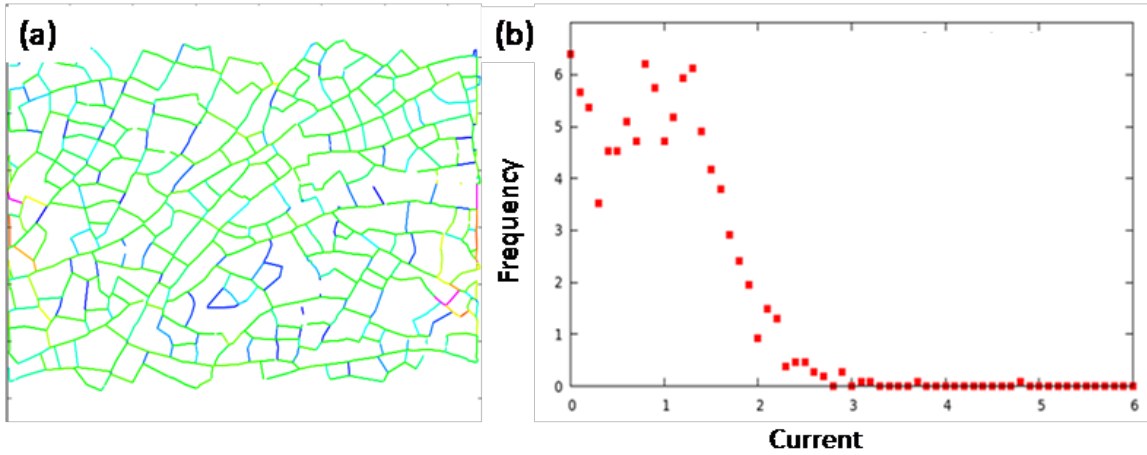


Fig. 2.14 current density map of template based network (a) current map and (b) frequency distribution (in %).

contrast to 86% in case of crack template). Furthermore, backbone wires of template metal mesh are evenly distributed unlike conducting wire network. The uniformity in backbone leads to uniform current flow in the network as shown in Figure 2.11d. Only a very little region in these networks carry negligible current (Figure 2.11e) which are mainly in the regions having multiple paths between two junctions. As an example in location 5 there are three paths between EI that are EI, EFHI and EFGHI; however, the current is negligible in the longer path EFGHI. More importantly, here no hotspots or regions (Figure 2.11f) having very high current is observed. The absence of bottlenecks in the network can allow high current density to be used in these networks without the danger of failure. The current density also shows similar characteristics as shown in Figure 2.14.

The uniformity of current in the backbone is quantified in the form of frequency distribution as shown in Figure 2.15. In case of conducting wires network (see green plot) maximum area does not carry current, significant fraction carries high current and a very few fractions carries current that is close to mean current. With the increase in density (see blue plot) of wires, the fraction of low and high current carrying region reduces. Thus, increase in density increases the uniformity of current distribution. On the other hand, in case of template metal mesh (see red plot) most of the area carries

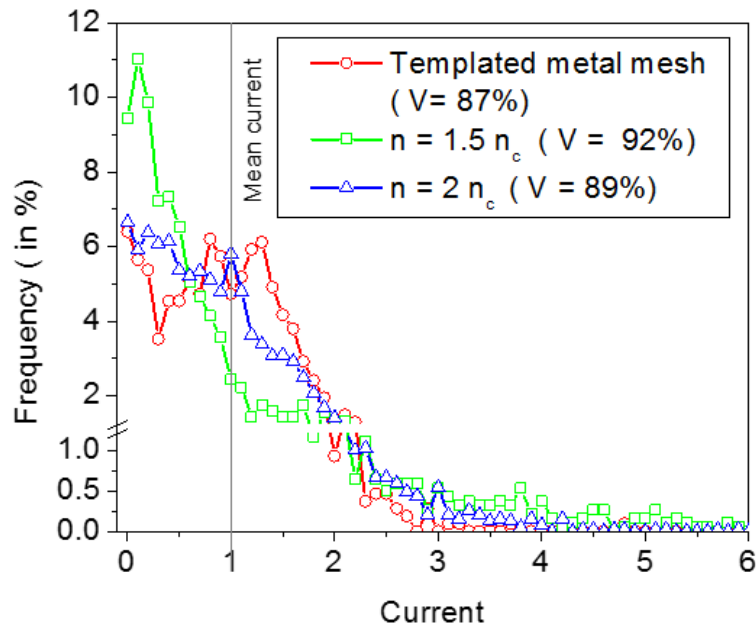


Fig. 2.15 Current distribution in conducting wires at two different densities and templated metal mesh.

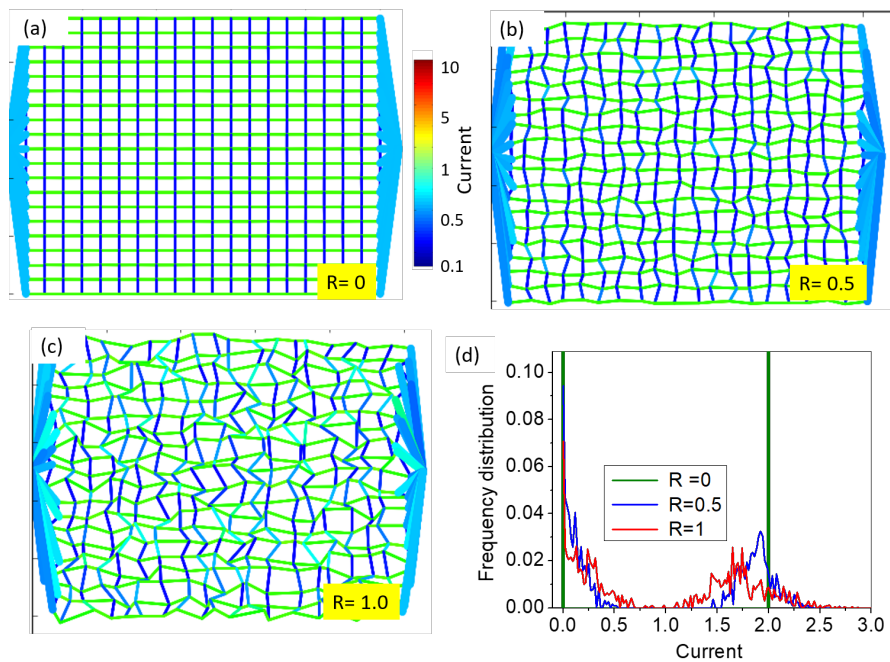


Fig. 2.16 (a-c) Current maps varying from periodic to the random network. $R = c$ represents point is randomly distributed anywhere between 0 and c where 1 is the unit cell spacing. (d) the current distribution of these networks.

around average current and fraction of low and very high current carrying region is very low. To understand the effect of polygon size distribution in electrical transport, a square lattice is deformed incrementally to a random network by introducing random deformations but with a given limit (see Figure 2.16). It may be noted that for square lattice, the distribution is two delta functions as wires in the direction of field carry equal maximum current while wires perpendicular to the electric field do not participate the electrical transport. As shown, increase in the deformation from square lattice leads to broadening of distribution and the formation of hot spots. Thus, a network should have uniform polygon size for even current distribution. As shown, template metal mesh outcores conducting wire network based networks in terms of current uniformity, which is due to more uniform polygon size in the backbone.

It is evident that the template-based network exhibits high backbone fraction, uniform current and absence of hot spots despite having unequal wire width, wire spacing and irregular polygonal geometry while networks obtained from nanowires possess a low fraction of uneven backbone with a lot of hot spots despite containing evenly distributed equal sized nanowires. The numerical analysis can be utilized to obtain the sheet resistance of a network. We used two points resistance method [172] to determine sheet resistance of crack network by adding electrodes in the left and right side. The calculation involves determination of eigenvalues and eigenvectors of network and using following equation from Wu et al. [172] .

$$R_{\alpha\beta} = \sum_{i=2}^N \frac{1}{l_i} \|\Psi_{i\alpha} - \Psi_{i\beta}\|^2 \quad (2.39)$$

Here, l_i are non-zero eigenvalues with corresponding eigenvectors Ψ_i and α and β are nodes, in between resistance is measured. We calculated eigenvectors and eigenvalues of our metal mesh networks. The obtained sheet resistance value is found to be $19.1 \frac{\rho}{t}$ with ρ being resistivity of the film while t being thickness of the film. For a typical film of Ag of 100 nm which translates to $2.8 \Omega/\square$. The conventional method [39] based on

fill factor $R_{sn} = \frac{1}{F} \frac{\rho}{t}$ calculates it as $1.13 \Omega/\square$. From the section 2.1.4, our analytically obtained sheet resistance of these networks can be written as

$$R_{sn} = \frac{\pi}{2} \frac{1}{\sqrt{F_B}} \sqrt{\frac{l}{w}} \frac{\rho}{t} \quad (2.40)$$

Here, F_B is backbone fill factor, l is mean wire segment (edge) length and w is mean wire width. The analytically obtained value is found to be $1.7 \Omega/\square$ using average $\frac{l}{w}$ as 5.67. Thus, Eq. (2.40) is closer to numerical value as compared to conventional approach considering only fill factor. However, Eq. (2.40) still, underestimates the sheet resistance value; it could be due to circular loops and multiple paths between two junctions as indicated in inset of Figure 2.11b. These kind of multiple paths should be minimum in a network for enabling effective current distribution.

Thus, the study shows that an understanding of the current distribution in the wire network is an important aspect, in choosing a network for TCE application. The conducting wire-based networks possess incomplete connectivity and a significant fraction of wires not participating in electrical transport, which is an inherent property of the distribution and may not be possible to improve. On the other hand, template metal mesh has high connectivity (86% in the typical example), which can be further improved by optimizing the conditions of template preparation. Furthermore, the backbone obtained by conducting wires is uneven and show irregular polygonal shapes, while templated metal mesh show regular and even polygon shape hosting uniform current distribution and absence of vulnerable hot stops. Thus, the work shows that the templated metal mesh is closer to being ideal than deposited nanowires based network.

2.2.5 Conclusion

The work studies and compares the current carrying fraction of randomly placed conducting wires based network and templated metal mesh. It is shown that, near the percolation density (n between 1 and 1.2), a very small fraction (<50%) of the network

participates in the electrical transport, while rest of the network merely blocks the light. The current distribution in the current carrying backbone contains numerous current loops suggesting that most of the backbone is also ineffective in electrical transport. Such networks possess hot spots where the wires carry high currents, which may lead to the breakdown at high current densities. The template-based networks, on the other hand, show high backbone fraction (86% in the typical example) and a homogeneous current flowing in different wires. Thus, template-based networks can be more suitable TCE candidates if wire density and wire width can be further reduced.

2.3 Aspects related to charge collection by a metal network

2.3.1 Summary

Efficiency of a solar cell is directly correlated with the performance of its transparent conducting electrodes (TCEs) which dictates its two core processes, viz., absorption and collection efficiencies. Emerging designs of a TCE involve active networks of carbon nanotubes, silver nanowires and various template-based techniques providing diverse structures; here, voids are transparent for optical transmittance while the conducting network acts as a charge collector. However, it is still not well understood as to which kind of network structure leads to an optimum solar cell performance; therefore, mostly an arbitrary network is chosen as a solar cell electrode. Herein, it is proposed a new generic approach for understanding the role of TCEs in determining the solar cell efficiency based on analysis of shadowing and recombination losses. A random network of wires encloses void regions of different sizes and shapes which permit light transmission; two terms, void fraction and equivalent radius, are defined to represent the TCE transmittance and wire spacings, respectively. The approach has been applied to various literature examples and their solar cell performance has been compared. To obtain high-efficiency solar cells, optimum density of the wires and their aspect ratio as well as active layer thickness are calculated. Our findings show that a TCE well suitable for one solar cell may not be suitable for another. For high diffusion length based solar cells, the void fraction of the network should be high while for low diffusion length based solar cells, the equivalent radius should be lower. The network with less wire spacing compared to the diffusion length behaves similar to continuous film based TCEs (such as indium tin oxide). The present work will be useful for architectural as well as material engineering of transparent electrodes for improvisation of solar cell performance.

2.3.2 Introduction

Transparent conducting electrode (TCE) is an essential component of solar cells regardless of its type, geometry and material. Illuminated side of a solar cell must have high optical transmittance for charge carrier generation in active material and high electrical conductance for efficient charge collection. However, the criteria of high conductance and transmittance are generally not met simultaneously in the same material and only a few oxides, such as indium tin oxide (ITO) fulfil this criteria. However, ITO is brittle, expensive and non-flexible and hence there have been tremendous efforts in the direction of its suitable alternatives. The promising candidates include carbon nanotubes [146, 1] (CNTs), silver nanowires [175, 185, 97, 154] (AgNWs), conducting periodic [181] or random meshes [142] and hybrids [82]. In such network architectures, voids act as transparent windows for light harvesting while wire network acts as a charge collector. These are fabricated by various printing techniques, roll to roll process [5], spray coating [146], self-assembly of nanoparticles [100] and template-based techniques, such as crack [142, 55, 143] grain boundary [46], electro-spinning [6] and bio-inspired strategies [54]. Electrodes obtained from these techniques are extensively demonstrated in silicon [185, 82], polymer [146], perovskite and dye /quantum dot sensitized solar cells [107]. There have been efforts in optimising work function and bettering interface contact between TCE and active material [59]. However, the conducting networks are arbitrarily used for such purposes with no specific attention being paid on how these influence the solar cell performance.

The efficiency of a solar cell, η broadly depends on absorption efficiency (fraction of photons absorbed η_a), dissociation efficiency (fraction of electrons and holes that are dissociated, η_d), and fraction of dissociated charges that reach the electrodes, η_c .

$$\eta = \eta_a \times \eta_d \times \eta_c \quad (2.41)$$

Choosing a suitable network structure for TCE is highly essential in enhancing solar cell efficiency as it decides absorption as well as collection efficiencies. The

high density of wires increases the shadowing losses (decreasing absorption efficiency) while the low density of wires increases recombination losses (decreasing collection efficiency) due to long distance travelled by charge carriers to reach the electrode network. Thus, an optimised TCE network is desired to serve high absorption and collection simultaneously. The bulk recombination losses depend on diffusion length of active material. The probability of charge carrier, N_c to be collected at a distance x in a medium of diffusion length, γ can be written as:

$$N_c = e^{-\frac{x}{\gamma}} \quad (2.42)$$

Diffusion length is a material property which is a function of diffusion coefficient, D and time constant, τ which can be given as $\gamma = \sqrt{D\tau}$. It can be measured using time of flight, double injection transients, charge extraction by linearly increasing voltage etc [136]. Thus, different solar cells made from a different type and quality of active material have different diffusion lengths (their typical values are provided later). Theoretical treatment in understanding optimised structure of solar cells is always essential for improvisation of solar cell efficiency [35, 74]. Despite increasing interest in network-based TCE, it remains elusive how the network structure decides absorption and collection efficiency and which network structure is suitable for best solar cell performance. Variable parameters like wire width, wire spacing, polygon size, hierarchical structure of networks make it difficult in terms of evaluating solar cell performance.

2.3.3 Scope of the present investigations

The present work proposes an approach for estimation of solar cell efficiency based on calculating the distance travelled by charge carriers to reach the nearest electrode followed by calculating their probability to be collected. The result reveals the optimum network structure for best performance solar cells. The work compares the solar cell

performance of continuous film based TCE with network based TCE and also calculate optimum active layer thickness for maximum absorption and minimum recombination.

2.3.4 Results and Discussion

2-dimensional case

In solar cells, charge carriers are collected by top (TCE) and bottom electrodes based on their polarity. To begin with, let us consider a simple case of 2-dimensional geometry with negligible solar cell thickness (realistic 3D case of the solar cell of finite thickness will be dealt later on). Consider a conducting ring of radius R acting as a charge collector for charges generated within the ring (see Figure 2.17a). Further, assume uniform charge carrier flux within the circle (the number of charge carriers within the circle per unit time), N_0 . Thus, the number of charge carriers generated in an arbitrary ring of radius, r and thickness dr , can be written as $N_G(r) = N_0 \frac{2\pi r dr}{\pi R^2}$. Therefore, the distance travelled by a charge carrier generated at r to reach the nearest point on the ring is $(R - r)$. Considering recombination losses on the way with diffusion length, γ , according to Eq. (2.42), the number of charge carriers, $N_c(r)$ collected from the ring of radius r , is given by

$$N_c(r) = N_G(r) e^{-\frac{(R-r)}{\gamma}} \quad (2.43)$$

Thus, total number of charge carriers, N_c^{total} collected from complete circle can be written as

$$N_c^{total}(r) = N_0 \int_0^R \frac{2\pi r}{\pi R^2} e^{-\frac{(R-r)}{\gamma}} dr \quad (2.44)$$

$$N_c^{total} = 2N_0 \frac{\gamma}{R} \left(\frac{\gamma}{R} \left(e^{-\frac{R}{\gamma}} - 1 \right) + 1 \right) \quad (2.45)$$

Hence, collection efficiency can be written as $\eta_c = 2 \frac{\gamma}{R} \left(\frac{\gamma}{R} \left(e^{-\frac{R}{\gamma}} - 1 \right) + 1 \right)$, which is plotted in Figure 1a exhibiting collection efficiency increases with diffusion length. Furthermore, the increase is sharp in beginning and saturates afterwards. As an

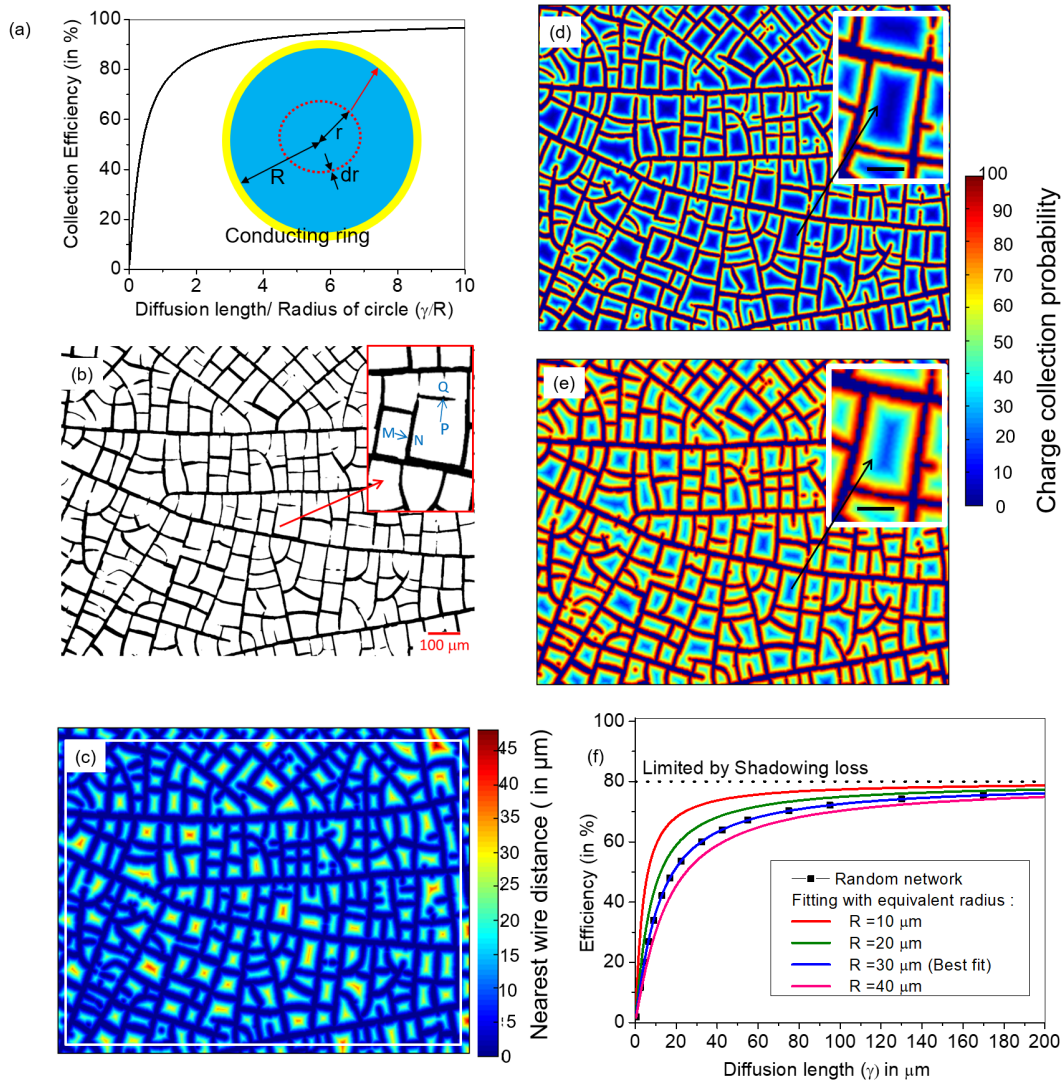


Fig. 2.17 (a) Collection efficiency of conducting ring (shown in yellow) collecting charge carriers generated within it. Schematic showing charge carrier generated in an arbitrary ring of radius r and thickness dr moving towards conducting ring of radius R . (b) An example of binary image of a metal network obtained from crack template with inset showing nearest wire distance of two random points, P and M to be PQ and MN (c) Nearest wire distance map (minimum distance travelled by charge carrier at the point to reach the wire) (d) charge collection probability map for $\lambda = 10 \mu\text{m}$ and (e) for $20 \mu\text{m}$ with inset showing the zoom in image of a polygon with scale bar of $50 \mu\text{m}$ (f) Efficiency based on charge collection shown by solid squares and fitting for equivalent radius. Best fitted radius represents random network behaves equivalent to a conducting ring of radius $R = 30 \mu\text{m}$.

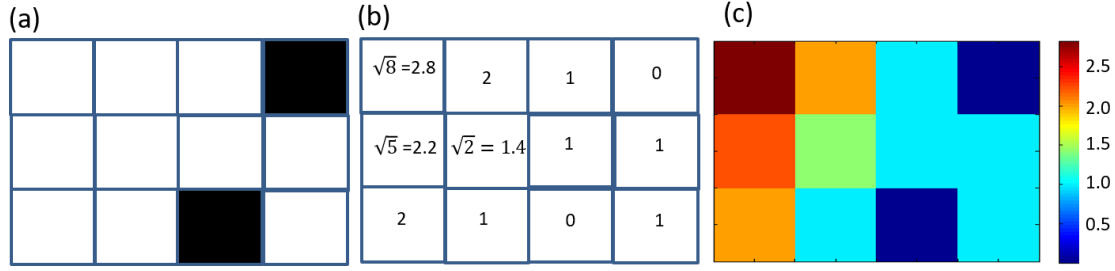


Fig. 2.18 (a) A 9-pixel image demonstrating the concept of nearest wire distance. Here, black represents metal and white represents void. (b) Nearest wire distance map calculated by determining distance between the pixel from nearest black pixel (c) The nearest map data is converted into color map.

example, charge collection efficiency at $\gamma = R$ is $\frac{2}{e} = 73.58\%$ and $\gamma = 3R$ is 90% respectively.

Now, consider a random conducting network as a charge carrier collector. Figure 2.17b shows an example of typical metal network obtained using crack template. [142, 143]. Here, the charge carriers are generated in the voids (shown in white) and are being collected by conducting wires (shown in black). The charge carriers generated at a certain point prefers to move towards the nearest point on the wire network due to the high potential of the network (potential decreases with distance hence, the nearest point of wire network attracts the charge carrier with maximum force). For instance, charge carriers generated at P and M are collected by Q and N respectively (which are corresponding nearest points on the network) and travel PQ and MN distance before being collected. The nearest wire distance for all individual pixels of the image are calculated using self-written Fortran and Python codes (see Figure 2.18 for details) which is shown in Figure 2.17b. As seen, the nearest wire distance is lower for the pixels closer to wires (see blue colour near the wires) and it increases going along the centre of a polygon (see red colour in the centre of polygons). Figure 2.17d-e shows charge collection probability maps for two different materials with different diffusion lengths, ($\gamma = 10 \mu\text{m}$ and $20 \mu\text{m}$) based on Eq. (2.42) by substituting x with nearest wire distance at the pixel. Charge collection probability decreases with increase in nearest wire distance and increases with diffusion length. In other words, charge carriers

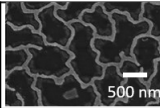
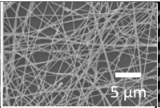
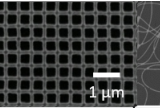
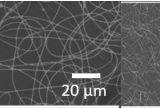
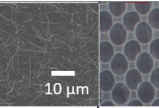
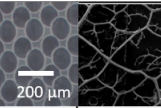
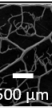
Literature images							
Method	(a) Grain Boundary lithography	(b) Spider web (4 layers)	(c) Electron beam Lithography	(d) Electrospinning	(e) Ag NW by dip coating	(f) Coffee ring effect	(g) Leaf venations
Reference	Nat. Commun. 5, 3121 (2014)	Nat. Commun. 5, 5674 (2014)	Opt. Express 23, A62–A70 (2015)	Mater. Lett. 115, 187–189 (2014)	Sol. Energy Mater. Sol. Cells 125, 318 (2014)	ACS Appl.Mater. Interfaces 6, 18668 (2014)	Nat. Commun. 5, 5674 (2014)
R (in μm)	0.25	0.6	0.22	3.5	2.4	50	150
V	77%	54%	46%	80%	77%	70%	80%

Fig. 2.19 Comparison of different transparent electrodes in terms of calculated equivalent ring radius (R), void fraction (V) and efficiency (η) at $1\mu\text{m}$. The calculation procedure is based on Figure 2.17. (a) Reproduced with permission from Ref. [46] Copyright 2014 Nature Publishing Group. (b and g) Reproduced with permission from Ref. [54]. Copyright 2014 Nature Publishing Group. (c) Reproduced with permission from Ref. [181]. Copyright 2015 OSA Publishing. (d) Reproduced with permission from Ref. [6] Copyright 2014 Elsevier.(f) Reproduced with permission from Ref. [100] Copyright 2014 Royal Society of Chemistry.

generated near the conducting wires have a higher probability of being collected while charge carriers generated in the centre of polygons (especially for bigger polygons) have a lower collection probability due to enhanced charge recombination. Furthermore, since light is not absorbed by the metal network, the collection probability in metal region is taken as zero. Let us consider F to area fraction of metal and V to area fraction of voids we have $V + F = 1$; in this particular image V is 80%. The overall efficiency is computed by taking the mean of collection probability of all pixels (mean value of charge collection probability map). The collection probability map for different diffusion lengths are obtained similarly and corresponding efficiencies are shown in Figure 2.17f by solid squares. As seen, the efficiency increases with diffusion length and saturates to void fraction of 80%, limited by shadowing losses of F . As the random network possess variable polygon sizes and shapes thus it is interesting to know what is its effective mean polygon size. To obtain it, the collection efficiency of the network is compared with a circular ring of different radii. In Figure 2.17f, solid lines represent collection efficiency w.r.t diffusion length for rings of radii 10–40 μm based on Eq. (2.45). The curve ($R = 30\ \mu\text{m}$) best fits with the solid square network points representing that the network behaves effectively equivalent to a charge collecting ring with inner

radius (R) (to be called as equivalent radius henceforth) $30 \mu\text{m}$. In other words, the random network of variable polygon size behaves as if it has only equal-sized circular voids of radius $30 \mu\text{m}$ throughout the film with the void fraction of 80%.

Comparison of various networks

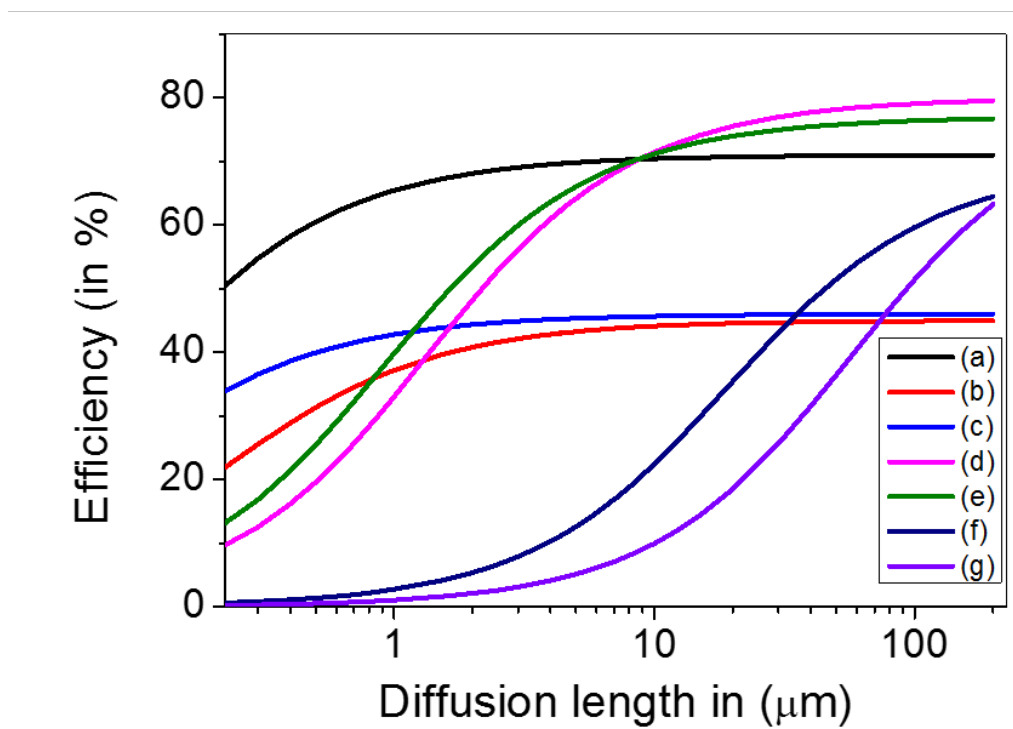


Fig. 2.20 Comparison of efficiencies of solar cells for different network structures with respect to diffusion length. The rate of increase depends on the equivalent radius (R) and the void fraction (V). Labels (a-g) represent various networks mentioned in Figure 2.19. (a) Grain boundary lithography, (b) spider web layers, (c) electron beam lithography, (d) electrospinning (e) Ag NW by dip coating (f) coffee ring effect (g) leaf ventilations.

The proposed approach can be utilised in a similar way for comparison of different network structures obtained by using other techniques. Figure 2.19 shows selected networks having varying geometrical features (wire width, wire spacing, polygonal geometry). To compare these complex structures, the proposed approach is applied to these cases. The equivalent ring radius (R), void fraction (V) and efficiency (η)

is calculated by doing best fitting using the steps, explained in Figure 2.17. These networks show R ranging from $0.25 \mu\text{m}$ to $150 \mu\text{m}$ and V varying from 46% to 80%. Note: to acquire high-efficiency solar cells, the network should possess low equivalent radius and a high void fraction. As an example, network of leaf ventilations shown in (g) despite of having high fill factor of 80% shows low efficiency of just 1% (at $\gamma = 1 \mu\text{m}$) due to high equivalent radius of $150 \mu\text{m}$ while network (c) despite of having low equivalent radius of 220 nm show efficiency of 43% (at $\gamma = 1 \mu\text{m}$) due to low void fraction of 46%. Therefore, high void fraction, as well as low equivalent radius, are necessary for high solar cell efficiency. Diffusion length of solar cells depends on quality and nature of active material having an order of 10 nm for organic, $1 \mu\text{m}$ for perovskite and $100 \mu\text{m}$ for silicon solar cells. Figure 2.20 compares the efficiency of these networks at different diffusion lengths. It is clear that efficiency increases with the diffusion length, however, the rate of increase strongly depends on R and V . To achieve high efficiency for lower diffusion lengths based solar cells, such as organic solar cells the equivalent radius should be low, such as networks (a) and (c), while for higher diffusion length based solar cells such as silicon solar cells, void fraction should be high, such as networks (d), (e) and (a). The networks having both high void fraction as well as low equivalent radius are suitable for all diffusion lengths such as (a).

This approach is not only limited to the understanding of experimental microscopic images but rather computationally drawn networks can also be studied to gain deeper insight and to obtain optimum geometry. Figure 2.21 shows modelling of AgNW and CNT-based TCE by drawing randomly conducting wire networks using pygame (Python). Figure 2.21(a) shows an example of a network with 1225 rods of aspect ratio ≈ 100 in the image of size $1200 \times 1200 \text{ pixel}^2$ (which is ≈ 1.5 times the critical density of percolation of conducting rods). Figure 2.21(b) shows corresponding nearest wire map. It is clear that non-uniformity of nanowires lead to a distribution of nearest wire distance and collection probability. Charge collection probability is evaluated for the central part of the image ($N = 850$ rods in $1000 \times 1000 \text{ pixel}^2$) to avoid error arising due to the boundary of the image. Figure 2.21(c-d) shows charge collection

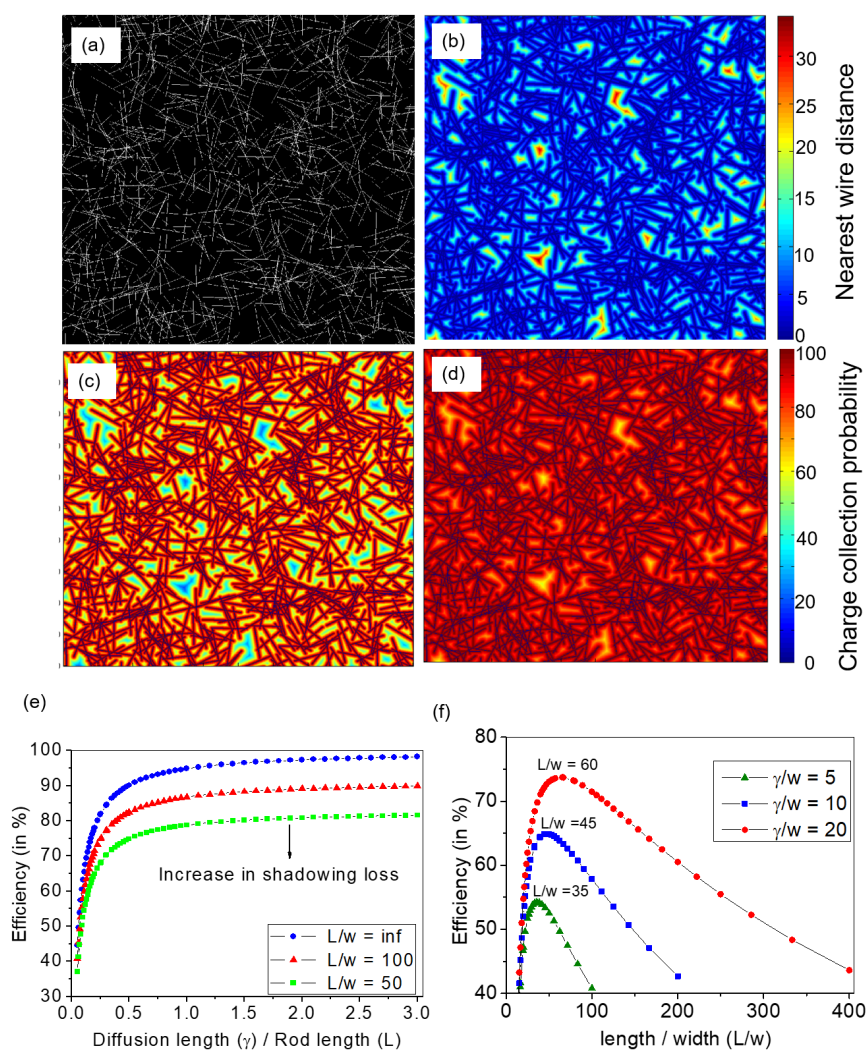


Fig. 2.21 (a) A randomly conducting wire network with density = 1.5 times critical percolation density (b) nearest wire distance map (c) charge carriers collection map for $\gamma = 0.1L$ and (d) $0.2L$ (e) Efficiency variation with ratio of diffusion length and rod length for rods of different aspect ratio (f) efficiency variation with aspect ratio of rods for different ratio of diffusion length and wire width.

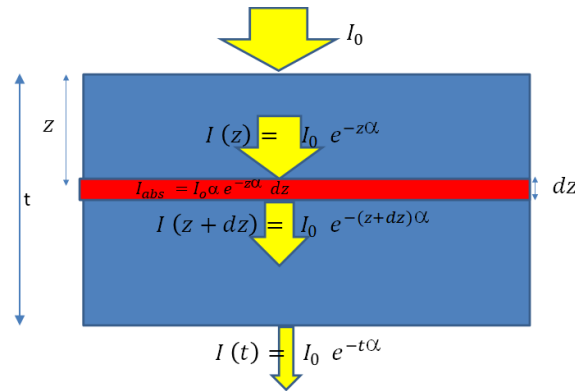


Fig. 2.22 Schematic showing light absorption by thickness dz .

map for diffusion length of $0.1L$ and $0.2L$, where L is the rod length illustrating charge collection probability increases with diffusion length. Figure 2.21(e) shows the effect of width on overall efficiency using $V = 1 - n\frac{w}{L}$, where n is density of rods in an area of L^2 . Figure 2.21(f) shows the effect of aspect ratio on the charge collection efficiency at a given ratio of diffusion length and wire width. Increase in the aspect ratio increases the absorption efficiency while decreases the collection efficiency (due to increase in the nearest wire distance). Thus, for maximum collection efficiency, an optimum value of aspect ratio ($\frac{L}{w}$) should be used. As an example, for $\frac{\gamma}{w} = 10$ the maximum efficiency is possible with an aspect ratio of 45. Thus, the approach can be used to obtain the density and dimensions of nanowires for maximum efficiency.

3-dimensional case

Consider a solar cell with active layer thickness, t having uniform dissociation efficiency n_d with transparent conducting network as an illuminating top electrode and continuous film (like Al film) as a bottom electrode. Say, uniform intensity of light from top is I_0 and optical length of active material is μ (reciprocal of absorption coefficient, α i.e. $\mu = 1/\alpha$). As explained in Figure 2.22 the intensity of light absorbed, $I_{abs}(z)$ at a distance z , from the top surface can be written as:

$$I_{abs}(z) = \frac{1}{\mu} I_0 e^{-\frac{z}{\mu}} dz \quad (2.46)$$

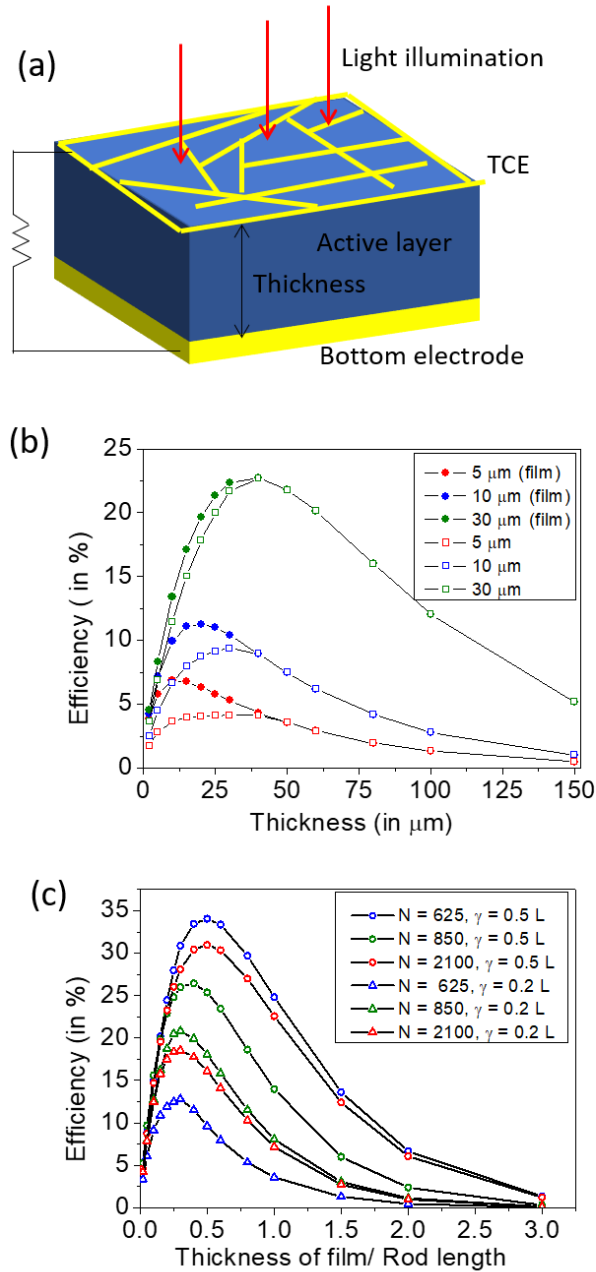


Fig. 2.23 Schematic showing the solar cell with TCE as top electrode and continuous film as bottom electrode. (b) Efficiency comparison for the random network and complete film (like ITO) based TCE at $\mu = 50 \mu\text{m}$ (c) Efficiency comparison for different rod density and diffusion length (γ) at given optical length (μ) = 0.5L for $\nu_a = \nu_b$.

Here, it is assumed that light is equally absorbed in all points of the same z plane based on Beer–Lambert law and reflected intensity from the bottom electrode is negligible. Assuming shadowing loss proportional to F with β being a proportionality of constant (which depends on the wavelength of light and thickness of network film), the transmittance, T can be written as $T = 1 - \beta F$. The number of charge carriers generated at z can be obtained as

$$N(z) = I_{abs}(z)\eta_d T = \frac{1}{\mu} I_o e^{-\frac{z}{\mu}} \eta_d (1 - \beta F) dz \quad (2.47)$$

Consider a point $P(x, y, z)$ in the active material having $s(x, y, z)$ to be the 3D nearest wire distance (distance between P and nearest point on wire). Say, $r(x, y)$ be the projected 2D nearest wire distance at P ($x, y, z = 0$) as computed in Figure 2.17a. Thus, the 3D nearest wire distance is $\sqrt{r^2(x, y) + z^2}$. Consider, γ_A to be the diffusion length of charge carrier reaching top electrode with ν_A to be mobility. Hence charge carriers collected by top surface in unit time from point $P(x, y, z)$ can be written as:

$$N_A(x, y, z) = \frac{1}{\mu} I_o e^{-\frac{z}{\mu}} (1 - \beta F) e^{-\frac{\sqrt{r^2(x, y) + z^2}}{\gamma_A}} \eta_d \nu_A \quad (2.48)$$

The distance travelled by charge carriers generated at P (x, y, z) need to travel a distance of $(t - z)$ to reach bottom electrode (which is continuous film). Hence, the number of charge carriers collected by bottom electrode from point P (x, y, z) is independent of x and y and can be written in terms of diffusion length, γ_B and mobility, ν_B as:

$$N_B(x, y, z) = \frac{1}{\mu} I_o e^{-\frac{z}{\mu}} (1 - \beta F) e^{-\frac{t-z}{\gamma_B}} \eta_d \nu_B \quad (2.49)$$

Total charge carriers collected by both electrodes from complete active material of thickness t and size $a \times b$ can be written as :

$$N_A^{total} = \frac{1}{\mu} I_o (1 - \beta F) \int_{z=0}^{z=t} \int_{y=0}^{y=b} \int_{x=0}^{x=a} e^{-\frac{z}{\mu}} e^{-\frac{\sqrt{r^2(x, y) + z^2}}{\gamma_A}} \eta_d \nu_A dx dy dz \quad (2.50)$$

$$N_B^{total} = \frac{1}{\mu} I_o (1 - \beta F) \int_{z=0}^{z=t} \int_{y=0}^{y=b} \int_{x=0}^{x=a} e^{-\frac{z}{\mu}} e^{-\frac{t-z}{\gamma_B}} \eta_d \nu_B dx dy dz \quad (2.51)$$

The total current flowing in the circuit is based on the minimum of charge carriers collected by either electrode, represented as a *Min* function. Efficiency can be written in terms of the ratio of total charge carriers generated and total incident photons (assuming no other losses).

$$\eta = \frac{1}{I_0 a b} \text{Min}[N_A^{total}, N_B^{total}] \quad (2.52)$$

Based on Eq. (2.52), Figure 2.23b shows efficiency of the network shown in Figure 2.17b as a function of active layer thickness for different diffusion lengths, γ ($\gamma_a = \gamma_b$) and $\mu = 50\mu\text{m}$. It indicates that with an increase in the film thickness the efficiency increases in beginning and then decreases for higher values of thickness which is due to competition between the increase in absorption efficiency and the decrease in collection efficiency. Thus, for a maximum efficiency, a thickness of active material, t should be chosen such that function is given in Eq. (2.52) is maximised. If both the layers are made of continuous film based TCEs such as one side ITO and another side Al film, in Eq. (2.50) $e^{-\frac{\sqrt{r^2(x,y)+z^2}}{\gamma_a}}$ can be replaced by $e^{-\frac{z}{\gamma_a}}$. If both the electrodes are made of networks as in the case of semitransparent solar cells [65], the term $e^{-\frac{(t-z)}{\gamma_b}}$ in Eq. (2.51) is replaced by $e^{-\frac{(t-\sqrt{r^2(x,y)+z^2})}{\gamma_b}}$ reducing the efficiency further. On comparing the performance of network-based TCE with continuous film of same transmittance (like ITO), the efficiency of network-based TCE is considerably lower for lower diffusion length based solar cells (see red and blue curves) while for higher diffusion length based solar cells the efficiency of continuous and network-based TCE is almost same (see green plot). Thus, network-based TCE can replace continuous film based TCE for solar cells having higher diffusion length compared to the equivalent radius. Figure 2.23c shows solar efficiency with TCE obtained from conducting rods of different densities. The nearest wire distance is evaluated by removing isolated rods from the image as they block the light while it does not participate in electrical

transport [92]. Increase in rod density reduces recombination losses (due to decrease in nearest wire distance); however, it increases the shadowing loss (due to more metal fill factor). In particular, in the case of lower diffusion lengths, the effect of recombination losses is more dominating hence, rod density should be higher while in the case of higher diffusion lengths, the influence of shadowing loss is more dominating hence rod density should be lower. Consequently, the value of optimum rod density for best efficiency reduces with increase in diffusion length. As an example, out of rod densities 625, 850 and 2100 for $\gamma = 0.2 L$, the maximum efficiency is observed for 850 rods while for $\gamma = 0.5 L$, the maximum efficiency is observed for 625 rods i.e. optimised rod density reduces with diffusion length.

The present generic technique is an important tool to predict the efficiency of a solar cell based on its TCE structure and active layer properties of various kinds of solar cells. It has direct implications in obtaining optimum thickness and network geometry for best solar cell performance. For more deeper insights based on the context one must also increase modelling precision by adding back reflection, resultant interference effects [156], calculation of resistive losses, dissociation efficiency dependence with electric field [110] and effect of additional layers, such as electron/hole transmitting layer and conducting layer etc.. The scattering effect plays an important role in light absorption distribution. Recently, Marus et al. have studied the haze and transparency for different nanowire diameters using the finite element method. [120] This data can be used instead of Beer's lambert's law for the advanced solar cell simulation. Although there are various other influencing parameters, such as sheet resistance, series resistance, contact resistance and surface recombination etc. also governing the energy losses in the solar cells. In this work, however, only attention to the role of TCE is paid in the solar cell performance. A separate study addressing the above parameters is worthy. It is one of the first attempts in understanding the role of TCE and formulation to tackle the recombination losses; hence, can be an important step for further advanced modelling.

2.3.5 Conclusion

In conclusion, a generalised theoretical approach is shown for obtaining the maximum efficiency of solar cells based on network analysis of TCEs considering shadowing and recombination losses. Wire networks obtained using different techniques are compared in terms of equivalent radius, void fraction, and derived efficiency. This study shows that sparse wire density leads to more recombination losses, while higher wire density leads to more shadowing losses. The recombination losses arising from sparse wire density (when wire network-based electrode is used) is applicable to all solar cells. However, the length and time scales of charge carriers decide the extent of recombination losses, which is more dominant if mean free path is less. Thus, an optimum density of metal fraction and the corresponding active layer thickness are desired for a better cell performance which is quantified in this article. Interestingly, a TCE well suited for a given type of solar cell may not be suitable for another kind. For high diffusion length active layers such as silicon solar cells, the network should have a high void fraction and thus networks obtained using crack pattern, leaf ventilations, etc., are more suitable. On the contrary, for low diffusion length, active materials such as organic solar cells, TCE networks with a lower equivalent radius such as networks obtained using grain boundary and electron beam lithography methods are more superior. In such cases, where the diffusion length is higher compared to the wire spacing such as silicon solar cells, the network-based TCEs show equivalent performance as compared to ITO films. Thus, the present work can be an important guide for the practical recommendation for enhancing solar cell performance.

2.4 Embedded metal mesh as a strain sensor

2.4.1 Summary

Strain sensors find diverse applications in robotics and healthcare. Recently, transparent strain sensors have been realized with metal network structure embedded on a flexible transparent substrate. The strain value calculation is based on resistance measurement, which has the particular value at given strain. The resistance increases gradually for lower strains, while the rate of increase is higher for high strains. Here, a detailed theoretical model is developed to understand the increase in resistance with the strain. The model shows that when a given strain is applied, wires below a critical angle w.r.t. the applied strain direction end up breaking, leading to increased resistance of the network. With increasing strain, the critical angle increases: in other words, wire segments extending higher angles also tend to break. The rate at which resistance increases, gradual in the beginning and faster for higher strains, going well with experimental findings. Further, the model is extended to the scenarios, where the strain is applied in the direction perpendicular to the measurement. In this way, model brings insight into the electrical transport of networks.

2.4.2 Introduction

Strain sensors find an important and necessary place in present-day technology especially in the area of robotics and health monitoring systems. [182, 179] Strain sensors are typically obtained using a material, which has different resistance values at different strain values. However, the conventional strain sensors have limitations in terms of their low sensitivity, high response time and low gauge factor. Further, the conventional semiconductor based strain sensors are optically opaque, which becomes a problem when one is looking for the applications, where their high transmittance is desired. To circumvent it, modern strain sensors are obtained by embedding nanowires networks on a transparent flexible substrate. [177, 4] On applying strain to such systems, the resistance increases in a particular fashion. Thus, knowing the resistance, one can

know the value of applied strain. However, high junction resistance, unconnected wires increases their resistance and in turn restrict their performance. Recently, our lab showed a flexible strain sensor obtained using metal mesh embedded in PDMS substrate. [141] The strain sensor outcores existing sensors in terms of cost, cyclability, extraordinary high gauge factor, and high transmittance. There are interesting features in its characteristics. The sensor showed a linear increase in resistance with applied strain at lower strain regime, while the resistance rises at a high rate at high strains. Being half embodied in the PDMS substrate, the broken wire segments reconnect at the same places leading to a recovery of conductance for several such cycles. It is interesting to know the detailed mechanism of such sensors, however, the understanding in the direction is very limited. In the theoretical model used, we have considered the breakdown of wire segments only under strain which goes well with the experimental observations. The wire junctions break less frequently. [141]

2.4.3 Scope of the present investigations

Here, a systematic study of theoretical modelling of network-based strain sensors is performed. The approach is based on consideration of breakdown of wires based on the projection w.r.t. strain direction. The study quantitatively calculates resistance and gauge factor variation with the strain. The analysis is applicable to any similar network-based strain sensor.

2.4.4 Results and discussion

To explain the mechanism of such sensors, we consider a random conducting network as discussed in section 2.1 and understand the role of application of strain on it. Consider a network shown in Figure 2.24a. Let λ is the elongated length of strain sensor along the X-axis as shown in Figure 2.24b. Since all the wires have the different angles w.r.t direction of strain. Hence, the wires experience unequal strains based on

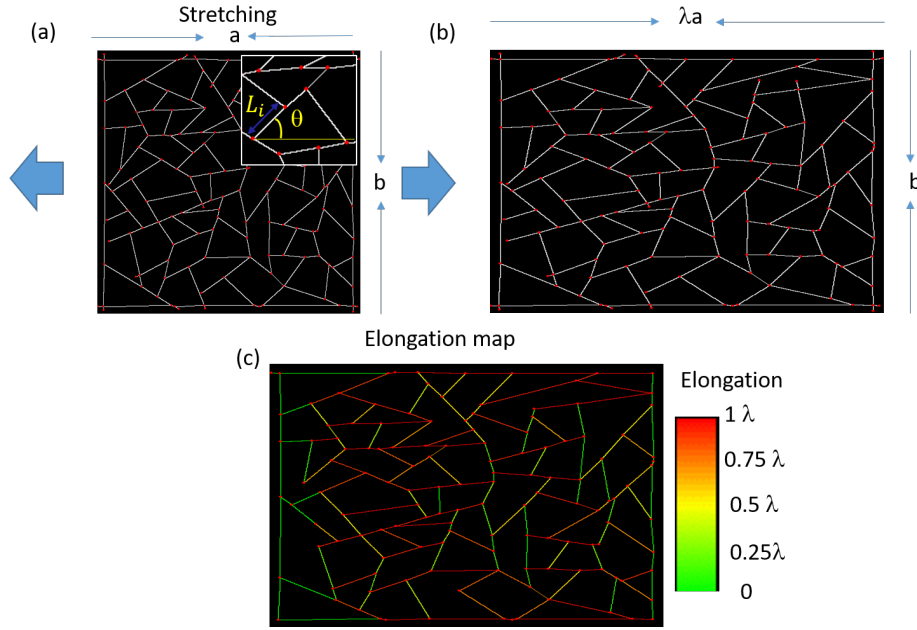


Fig. 2.24 (a) Schematic of a metal network. Inset showing the zoom in the image. θ is the angle of a wire and strain direction. (b) the metal network is elongated to $\lambda \times a$ and based on the angle, different wires are elongated. (c) elongation map of network.

the angle. The strain experienced (λ_E) by a wire having angle θ w.r.t direction of strain can be written as

$$\lambda_E = \lambda \cos \theta \quad (2.53)$$

A wire in a network breaks if the experienced strain exceeds the critical strength or strain for breakdown ($\lambda_E > \lambda_c$), here, critical strain, λ_c depends on the strength of the wire. In other words, the wires with angle lesser than critical angle breaks ($\theta < \theta_C$) which can be defined as

$$\theta_C = \cos^{-1} \frac{\lambda_c}{\lambda} \quad (2.54)$$

Consider an edge of length L_i placed in electric field E at an angle θ_i (see Figure 2.25a). The potential difference across the edge, V_i , therefore depends on the orientation of edge-maximum if placed in the direction of electric field, and zero, if placed on an equipotential line

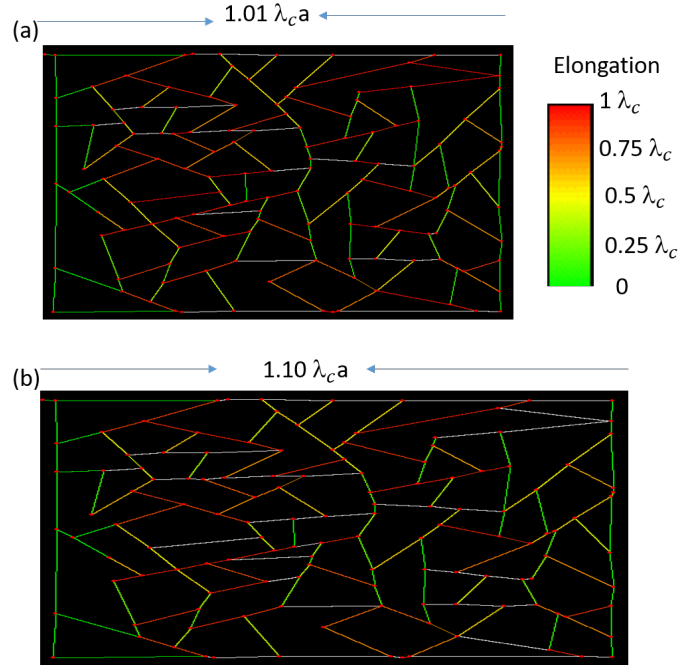


Fig. 2.25 (a-b) Elongation profile for $\lambda = 1.01\lambda_c$ and $1.10\lambda_c$. On stretching the network to $\lambda = \lambda_c$, the wires which experience this elongation breaks down (shown in white).

$$V_i = EL_i \cos\theta_i \quad (2.55)$$

If θ_C is critical angle such that wire segments below critical angle breaks down. Thus, average potential of all unbroken wires can be calculated as

$$V_{am} = \frac{\int_{\theta_C}^{\frac{\pi}{2}} EL_i \cos\theta_i d\theta_i}{\int_{\theta_C}^{\frac{\pi}{2}} d\theta_i} \quad (2.56)$$

$$V_{am} = EL \frac{\sin\theta_C}{\frac{\pi}{2} - \theta_C} \quad (2.57)$$

The mean current, I_{am} passing through an individual edge of conductivity σ , can be written as $\frac{\sigma A_{cs} V_{am}}{L_{am}}$, Here, A_{cs} is the cross-sectional area of an individual wire which equals wt in case of rectangular wires obtained from a template with rectangular grooves.

Using the value of V_{am} from Eq. (2.57), one can write as

$$I_{am} = \frac{Ewt}{\rho} \frac{1 - \sin\theta_C}{\pi/2 - \theta_C} \quad (2.58)$$

Consider N is the edge density and N_b is the density of broken wires and N_{ub} is the density of unbroken wires. The current passing across an equipotential line, I_{eq} , depends on the current carried by a single edge and a total number of edges on the equipotential line which equals $\sqrt{N_{ub}}b$ by symmetry arguments.

$$I_{eq} = \frac{Ewt}{\rho} \frac{1 - \sin\theta_C}{\pi/2 - \theta_C} \sqrt{N_{ub}}b \quad (2.59)$$

Using $E = \frac{V}{a}$ and applying Ohm's law, resistance, R can be written as

$$R = \frac{\rho}{wt\sqrt{N_s}} \frac{\frac{\pi}{2} - \theta_C}{1 - \sin\theta_C} \frac{a}{b} \quad (2.60)$$

Sheet resistance can be calculated as

$$R^{\parallel} = \frac{\rho}{wt\sqrt{N_{ub}}} \frac{\frac{\pi}{2} - \theta_C}{1 - \sin\theta_C} \quad (2.61)$$

As the wires with regions up-to angle θ_C are broken

$$\sqrt{N_{ub}} = \frac{\frac{\pi}{2} - \theta_C}{\pi/2} \sqrt{N} \quad (2.62)$$

Using it,

$$R^{\parallel} = \frac{\pi}{2} \frac{\rho}{wt\sqrt{N}} \frac{1}{1 - \sin\theta_C} \quad (2.63)$$

If R_{sn}^0 is the resistance in unstreched state.

$$R^{\parallel} = \frac{R_{sn}^0}{1 - \sin\theta_C} \quad (2.64)$$

Substituting $\theta_C = \cos^{-1} \frac{\lambda_c}{\lambda}$ from Eq. 2.54, the resistance parallel to direction of strain can be written as

$$R^{\parallel} = \frac{R_{sn}^0}{1 - \sin(\cos^{-1} \frac{\lambda_c}{\lambda})} \quad (2.65)$$

While if one is measuring resistance perpendicular to direction of strain, the average potential difference V_{am}^{\perp} across unbroken wires can be written as

$$V_{am}^{\perp} = \frac{\int_0^{\frac{\pi}{2}-\theta_C} EL_i \cos\theta_i d\theta_i}{\int_0^{\frac{\pi}{2}-\theta_C} d\theta_i} \quad (2.66)$$

It becomes

$$V_{am}^{\perp} = EL \frac{\cos\theta_B}{\frac{\pi}{2} - \theta_C} \quad (2.67)$$

$$R^{\perp} = \frac{R_{sn}^0}{\cos\theta_C} \quad (2.68)$$

On substituting $\theta_C = \cos^{-1} \frac{\lambda_c}{\lambda}$ from Eq. 2.54

$$R^{\perp} = R_{sn}^0 \frac{\lambda}{\lambda_c} \quad (2.69)$$

The ratio of strain along parallel and perpendicular direction from Eq. 2.65 and Eq. 2.69 can be written as

$$\frac{R^{\parallel}}{R^{\perp}} = \frac{\lambda}{\lambda_c} \frac{1}{1 - \sin(\cos^{-1} \frac{\lambda_c}{\lambda})} \quad (2.70)$$

If the network has strain along both the direction with λ being applied strain in each direction. For measurement carried out in any direction

$$V_{am}^{both} = \frac{\int_{\theta_C}^{\frac{\pi}{2}-\theta_C} EL_i \cos\theta_i d\theta_i}{\int_{\theta_B}^{\frac{\pi}{2}-\theta_C} d\theta_i} \quad (2.71)$$

$$R^{both} = \frac{R_{sn}^0}{\cos\theta_C - \sin\theta_C} \quad (2.72)$$

$$R^{both} = \frac{R_{sn}^0}{\frac{\lambda_c}{\lambda} - \sin(\cos^{-1} \frac{\lambda_c}{\lambda})} \quad (2.73)$$

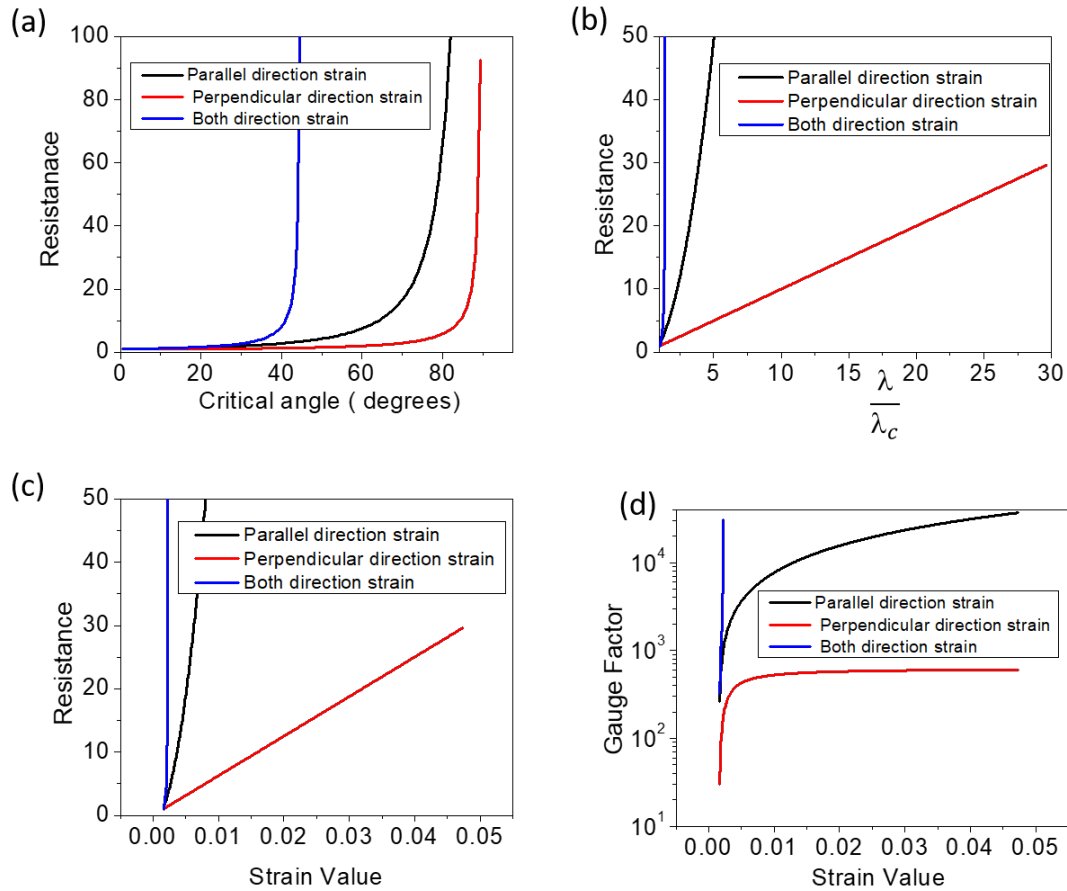


Fig. 2.26 (a) Resistance variation when wires having angle less than critical angle breaks during elongation, (b) variation of resistance with elongation, (c-d) theoretical resistance and gauge factor variation with strain for Au network.

Starting with the unstretched state having resistance unity, three cases are studied in (Figure 2.26a-b); (a) resistance is measured along the direction of strain, (b) resistance is measured perpendicular to the direction of strain and (c) strain is applied in both directions and resistance is measured along one of the direction. In all the cases, resistance increases with strain, however, the trends are significantly different. The increase in resistance to strain is fastest in case (c) and slowest in case (b). It can be explained by considering the importance of current carried by the broken wires. In case (b), for lower strains, only wires which are nearly perpendicular to the direction of measurement are broken. As these wires were nearly on equipotential lines and carrying negligible current, there is very less effect on resistance after their breakdown. On the other hand in case (a) wires in the direction of the electric field are broken,

which were carrying maximum current, thus their breakdown leads to more increase in overall resistance. In case (c) both kinds of wires are broken, leading to their maximum increase in resistance.

The critical strain before breakdown is a mechanical property of a material. To convert into a material property, example of Au network is considered by substituting mechanical parameters for gold. The critical strain depends on Yield strength (G) and Young Modulus (Y) as $S = \frac{G}{Y}$. For Au, $G = 50$ to 200 MPa depending on preparation condition of Au and $Y = 78$ GPa, [171] thus $S = 0.64 \times 10^{-3}$ to 2.56×10^{-3} . Taking mean value of 1.6×10^{-3} for critical strain, the resistance-strain relation is derived and shown in Figure 2.26c. Gauge factor defined as $\frac{\Delta R}{R}$ is also calculated for the system in Figure 2.26d. It is seen clearly, for resistance measurement along the direction of strain, the resistance increases slowly for lower strain, while it increases drastically for higher strain values. Further, the working range of strain sensor in all cases is different. As for parallel direction (case(a)), resistance shoots up at relatively lower strains as compared to the perpendicular direction (case (b)), thus, for higher strain measurement case (b) may be more appropriate. While the increase in resistance is maximum if one is having a strain in both the directions and gauge factor takes huge values even for very low strains, thus, the working range for the strain sensor is minimum in case (c). In this way, one can choose the direction of measurement based on sensitivity and working strain range.

The generic treatment of breakdown of wires of network based on strain can also be used on specific metal network images. Figure 2.27a shows an optical microscope image of metal network obtained from a crack template. For a given strain, wires with projection angle lower than critical angle break down. Figure 2.27b-c show current carrying backbone of the networks at given strain value. The backbone is further used for calculating resistance using the approach developed in section 2.2. It is clearly seen that on applying strain in the network, the current carrying backbone decreases, which in turn increases the corresponding resistance (figure 2.27d-e). The resistance increases gradually for lower strain values while the increases in resistance are very

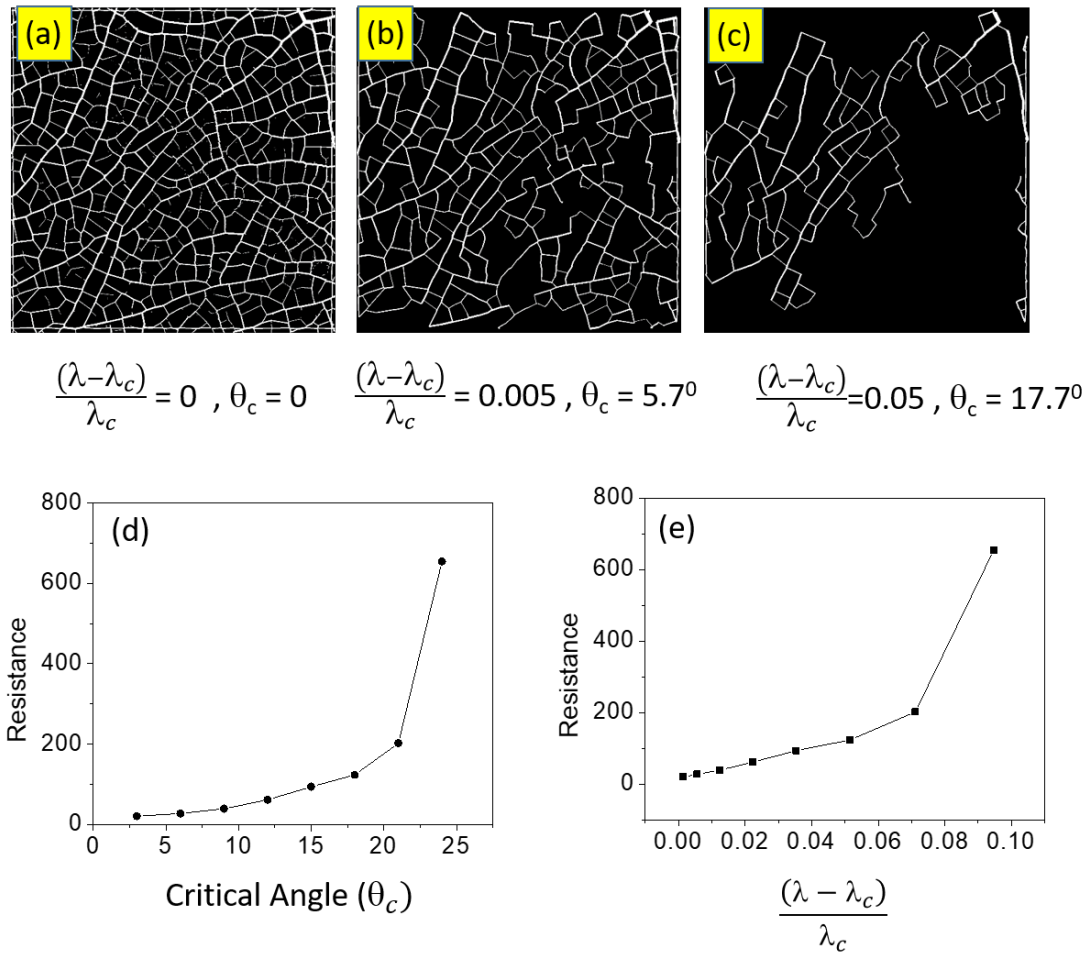


Fig. 2.27 (a) An optical microscope image of metal wire network obtained from crack template and (b-c) are numerically calculated backbone of networks after breakdown of wires at different strain values. (d-e) Resistance of network varying with critical angle and strain.

sharp for high strain values. Further, analysis of gauge factor can also be performed for these numerical images by plugging material properties as discussed in figure 2.26.

Thus, the abstract treatment, as well as the numerical treatment, is successful to model the nature of network-based strain sensor on applying strain. However, the limitation of the analytical model is that it considers all non-broken wires to be effective for current transport, however, there is a significant fraction of a dangling region as well. On the other side, the image analysis based calculation identifies current carrying region correctly, however it suffers from limited ensemble size of the

wires and image artefacts. Thus, there is a scope to improve and modify this model further. Nevertheless, both the models can provide a qualitative understanding of the process and successfully explain the resistance characteristics of the network-based strain sensor.

2.4.5 Conclusion

A geometrical model is presented to understand the increase in resistance of a network structure with strain. It is found that increase in resistance of such networks can be explained based on the preferential breakdown of wires as a function of strain. Further, it is observed the resistance increases slowly for lower strains while it increases with high rate at higher strain values. The study also showed the rate of increase in resistance, if the measurement is carried in the perpendicular direction.

Chapter 3

Modulating crack network patterns for efficient transparent electrodes

3.1 Designing optimum crack pattern template for fabricating transparent conducting electrodes: A spring network simulation in 3 dimensions

3.1.1 Introduction

Crack formation in various materials is a familiar phenomenon and finds an important place in physics and engineering research. In recent times study of desiccation cracks[43] has become especially important as technical applications of intentionally designed cracks are coming up. For example, transparent conducting electrodes (TCE) [87] are being fabricated using crack templates and lithographical techniques. Crack networks with specific geometry are required for such applications [92, 91]. The challenge is to identify appropriate materials and conditions to create the required network.

What would be the most satisfactory approach towards choosing the right materials and conditions for the perfect crack template, suited for a specific application? Ideally, a theoretical model incorporating the relevant material properties and ambient conditions which could predict the final crack pattern should give the answer to this problem. However, a full theoretical analysis of such a complex system is too involved to be practicable. In this work, a more feasible route and simulate the sample through a simple model consisting of a lattice of nodes connected by springs. Such models have been used by many groups to create realistic crack patterns generated under different conditions [60, 150, 77]. By establishing a correspondence between parameters used in the theoretical model and physical properties of the cracking system, we expect to identify the system and conditions which will produce the ideal crack pattern.

There are some efforts in the literature to model the crack physics using spring fusion model addressing cracking of composite materials [126], an effect of adhesion, and competition between cracking and peeling have been done in 2-dimensional models [148, 31]. Vogel et al. [164] and Khatun et al [77] introduced topological concepts to analyse crack patterns. Recently some authors have tried to relate material

properties of the medium with crack formation [3]. However, accurate prediction of crack morphology on the basis of physical and ambient conditions is yet to be achieved. In this work, using codes developed by Sadhukhan et al. [147, 148, 150, 149], the parameters affecting crack patterns are studied for efficient TCE.

3.1.2 Scope of the present investigations

Herein, patterns formed by desiccation are studied by using 3-dimensional spring network model. The objective is to study crack network morphology with special relevance to optimizing electrical conductivity and transparency on a transparent substrate. A pattern with wider and denser cracks gives higher conductivity to the surface but compromises on the transparency. Thus, there is a trade-off between conductance and transmittance, so identifying materials and techniques to optimize high conductivity and good transparency is essential.

3.1.3 Experiment

TiO₂ nanoparticles mixed with appropriate proportions of methanol/ethanol form a suspension through rigorous ultrasonication. This suspension is then drop coated on various substrates. The suspension when allowed to desiccate in air, form cracks. Metal Au is then vapour deposited at this stage. The metal can deposit on the substrate only if it finds a straight vertical channel. The TiO₂ is washed in water with mild sonication leaving behind the metallic mesh on the substrate. This mesh serves as the template for transparent conducting electrode [87]. In Figure 3.5 (a), the TiO₂ used is P25 Degusa and in Figure 3.5 (b) TiO₂ is prepared using sol gel method with the mean diameter of 25 nm and 16 nm respectively. Studies for Figure 3.7 are carried out by TiO₂ obtained from Sigma Aldrich with mean nanoparticle size of 21 nm. TiO₂ used in Figure 3.11 is obtained from P25 Degussa. The SEM images for the measurement of cluster size are provided in the inset of Figure 3.5.

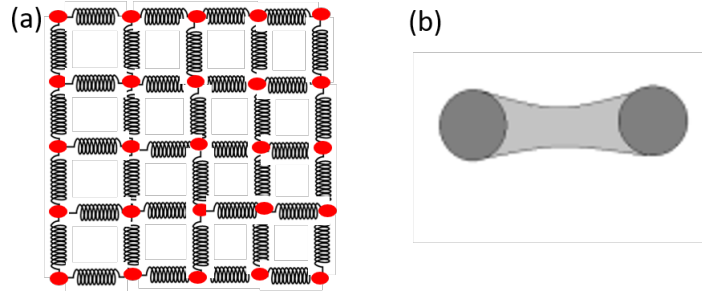


Fig. 3.1 (a) Schematic of spring fusion model. It is the 2D view of 3D geometry. (b) Dark grey denote particles and light grey denote the liquid bridging the two.

3.1.4 The Simulation Procedure

Basic algorithm

The system consists of a regular arrangement of nodes on a cuboidal lattice $L \times L \times H$, of side length L and height H . Here $L=200$ units while H ranges from 1 to 14 units. Here, $L \gg H$ to replicate the experimental set up where the corresponding dimensions are $5 \times 5 \text{ cm}^2$ in size and $20 \mu\text{m}$ in height. The edge boundaries of the system are free to move under the action of forces (Figure 3.1a). The nearest neighbour nodes are connected by Hookean springs vertically and horizontally except for the lowest layer which has only the vertical spring attachment. The lowest layer of nodes is distinct from all the other nodes as they represent the topmost layer of the substrate on which the film is deposited. The vertical springs attached to the lowest layer of nodes represent adhesion of the material to the substrate. Other nodes are connected to their nearest neighbours by vertical and horizontal springs which represent cohesion among particles of the desiccating material. Each spring has a natural length which is the length of the force-free condition. The desiccation of the material is realized through a reduction of the natural length of the springs. Reduced natural length implies that the springs are no longer in force-free condition but are strained. Each spring is attributed with a stiffness Y and a breaking threshold S . Both these parameters characterize the substance undergoing desiccation. Y is related to elastic properties of the substance. The breaking threshold (S) signifies the maximum permissible

accumulated strain beyond which a stretched spring breaks. Initially, the springs have unit natural length. In this model, we only allow breaking of the springs representing cohesion in the material. The lowest layer of nodes may be permitted to slip until a less strained configuration is reached [149]. For the present study, the slip is not allowed. Dessiccation is implemented by reduction of the natural length of the springs with time according to the rule

$$d_{n+1} = d_n(1 - b/r^n) \quad (3.1)$$

Here d_n and d_{n+1} are the natural lengths of a springs at timesteps n and $n + 1$ respectively, while b and r are constants. The form in equation (3.1) is integrated to the final form given in equation (3.2), which is used in the present work.

$$d_n = exp(br^{-n}/ln(r)) \quad (3.2)$$

We have normalised d_n by d_0 , the natural length at at $n=0$. With increasing n , d_n decreases. At a high n , the difference in natural lengths for two consecutive timesteps, viz d_n and d_{n+1} become negligible and the system is said to have saturated to d_{min} . We have chosen b and r such that d_{min} is 70% of the initial d_0 .

Each time the desiccation rule is employed, stress builds up in the system. It is assumed that a node experiences force only due to its nearest neighbours. Each strained node is allowed to move under the action of the force. The displacement between the n^{th} timestep to $(n+1)^{th}$ is implemented using a simple form of the Verlet's algorithm according to the relation $r_{n+1} = r_n + f\delta t^2$. Here f is the force acting on the concerned node and δt is the time during which the node moves. δt is judiciously assigned a value of 0.005 units. A very small δt increases cumulative error for a finite time-step, while a large value is in conflict with the assumption that force acting in the system remains constant for the time span. After the system relaxes, the strains in all the springs except the layer attached to the substrate are determined. The spring with the largest strain is broken if it exceeds the breaking threshold. The processes

of (a) desiccation, (b) displacement of the nodes under the resultant force, followed by (c) breaking of the springs on satisfying the requisite condition is iterated until the system saturates as mentioned above [148, 31]. The system is then checked for straight vertical crack connectivity spanning from the topmost layer to the lowest layer. This is done to mimic the experimental procedure in which metal is vapour deposited vertically downward on the film system. Metal can only deposit on the substrate if a vertical straight crack spanning from top to bottom layer is present.

If one or more such vertical cracks are obtained then the simulated sample film is checked for horizontal crack connectivity spanning across the substrate plane. This is done to simulate the experimental situation after the material is washed away, leaving behind a metallic crack network on the substrate. The properties of the metallic crack network are studied in order to optimise conductivity and transparency.

3.1.5 Conductivity calculation

The conductivity is determined using the Laplace's equation. In order to solve for conductivity, the crack network on the substrate is discretized by spreading on it a virtual mesh of square cells. The portion of the mesh covered by the cracks corresponds to the vacant cells while the rest correspond to solid cells. We consider that each pair of adjacent vacant cells is connected by a unit resistor and unit potential the difference is applied to the sample under study. The potential distribution in the vacant cells is determined by solving the Laplace's equation as shown below [147].

$$\nabla^2 V(x, y, z) = 0 \quad (3.3)$$

$$\frac{V_{i-1,j} - 2V_{i,j} + V_{i+1,j}}{(\Delta x)^2} + \frac{V_{i,j-1} - 2V_{i,j} + V_{i,j+1}}{(\Delta y)^2} = 0 \quad (3.4)$$

Δx is the spatial discretization unit. This unit is equal to the side length of a grid cell. In our case $\Delta x = \Delta y$. Rewriting the above equation

$$V_{i,j}^{n+1} = \frac{1}{p}[V_{i-1,j}^n + V_{i+1,j}^n + V_{i,j-1}^n + V_{i,j+1}^n] \quad (3.5)$$

Here p is the sum of the nearest neighbouring vacant cells. The Gauss-Seidel iterative method is employed to solve equation (3.5). At $n = 0$, $V^n = 0$ in all the cells. A steady state is attained when the potential distribution does not vary with time. The tolerance limit for achieving steady state is set to 10^{-7} . At steady state the sum of the potential differences of the vacant cells at the inlet or the outlet is numerically equal to the conductance as the potential difference across the sample is unity. Since the size of the sample along the horizontal directions is fixed ($L \times L$), the conductance and conductivity scales linearly by a fixed factor. Typically 3 configurations are taken for each measurement.

Estimation of transparency

The solid peds, i.e. the regions of the colloidal layer which are intact after crack formation, will be transparent after vapour deposition and wash removing away the colloid layer. So, the greater the area fraction of these regions, higher is the transparency of the TCE. In the figures of crack patterns, these regions are shown as black. The goal, therefore, is to maximise the transparent region, while simultaneously maximising the conductivity.

Correspondence between model parameters and physical properties

The parameters used in the model can be listed as -(i) spring network parameters - spring constant Y , spring breaking threshold S (ii) desiccation parameters - b and r (iii) system size parameters L and H . The real system being extremely complex, it is not possible to give a one to one correspondence between the parameters of sets (i) and (ii) with physically measurable properties of the materials and ambient conditions in the experiment. Let us review the situation in some detail.

The desiccating material is a visco-elastic colloidal suspension or gel. We cannot define Young's modulus for it, which can be directly linked to the parameter Y . In the colloidal suspension, one may think of an attractive interaction between two particles (say spherical) through a liquid bridge (Figure 3.1b), formed by the solvent [43]. According to Goehring et al.[43] the colloidal particles are bound by van der Waals interaction, whose strength depends on the dielectric properties of both particle and solvent. In this case, the Hamaker constant of the fluid-solid combination would be the measurable physical property associated with the spring parameter. The attraction or adhesion between the colloid and the substrate can be similarly represented, using van der Waals interaction between the substrate and the colloid. The breaking threshold of the springs in the model depends on the breaking stress of the material. For example, in polymers, this stress is extremely high, whereas in a brittle clay suspension it is low. The effect of adding increasing fractions of polymer to a Laponite water gel was clearly demonstrated in experiments and simulation [126]. Cracks reduced drastically as a polymer with high breaking stress was added and for a 50-50 clay-polymer composite, no sample spanning crack formed.

During desiccation, when a little solvent evaporates, the particles are drawn closer together, as we envisage in our model by shrinking of the spring. The parameters b and r control this process. The empirical law is framed such that desiccation reduces with time and finally, the spring natural length saturates to d_{min} on complete drying. Experimentally the rate of drying is therefore related to b and r . To make matters more complicated, drying rate depends on temperature and relative humidity as well as properties of the solvent and its interaction with the suspended solid particle. So at best, we can make qualitative comments, such as increasing b and decreasing r produce more rapid shrinking, which may correspond to low humidity, high temperature and/or high vapor pressure of the solvent.

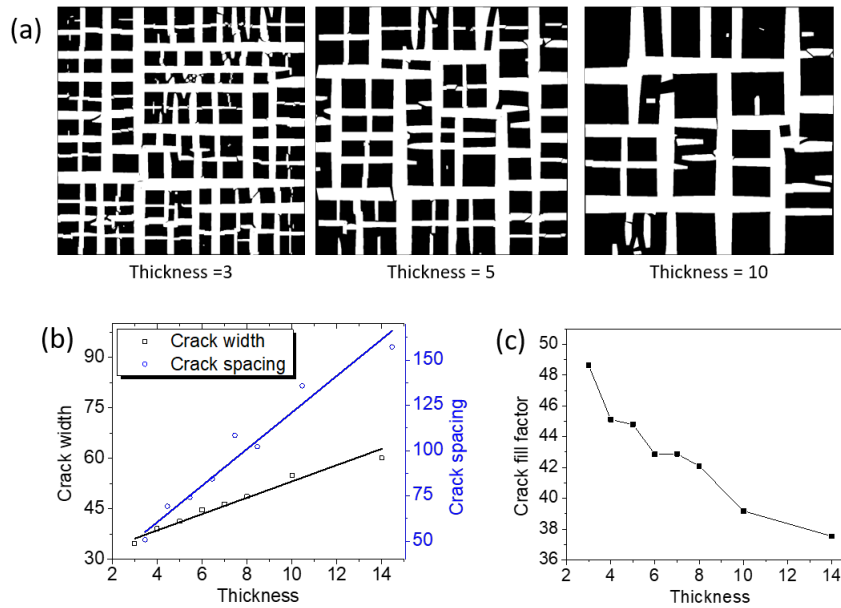


Fig. 3.2 Simulated crack patterns of different film thicknesses

3.1.6 Simulation Results

In this section, we study the role of the different input parameters and simulation model parameters controlling crack geometry, varying each individually. The effect of variation of real input parameters, such as film thickness can be compared directly with experiments, but other model parameters may be correlated with each other and the comparison between simulation and experiment is not so transparent.

Effect of Film Thickness

Figures 3.2a show the top view of a typical simulated sample of various heights after complete drying, i.e. saturation of the spring natural length. The increase in crack spacing and crack width with height is clearly discernible [150], and closely follows the experimental works. Figure 3.2b shows that both crack spacing and crack width scales linearly with thickness. The 'crack fill factor' representing the fraction of the area under observation covered by cracks, by and large decreases in sample height (Figure

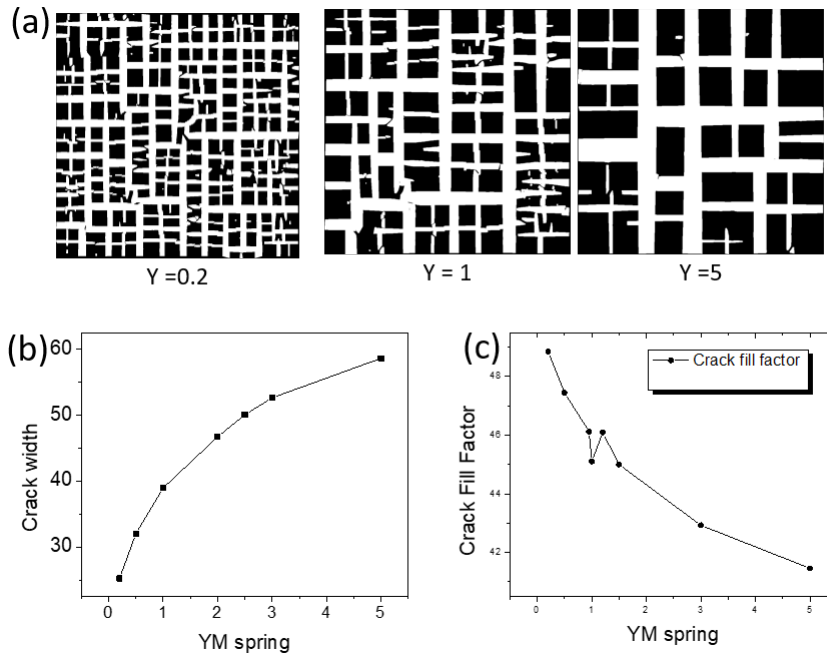


Fig. 3.3 Simulated images at different Y

3.2c). It agrees with experimental findings (see Figure 1.4) which also show crack spacing and width increases with the film thickness. [142]

Effect of varying spring stiffness Y

Figure 3.3 shows the top view of a sample in which Y has been varied. These images clearly show that the crack spacings and width increase with Y (Figure 3.3b), while the fill factor decreases with Y (Figure 3.3c).

Effect of distribution in Y on conductivity

In the simulation model the stiffness of the Hookean springs, Y , characterizes the sample under study. A single value for Y for all springs implies that the sample is made up of an ideally pure constituent. The pure constituent has particles of identical composition and size and a perfectly uniform solvent. Addition of particles of the same size but different composition, or vice-versa, induces an inhomogeneity in the

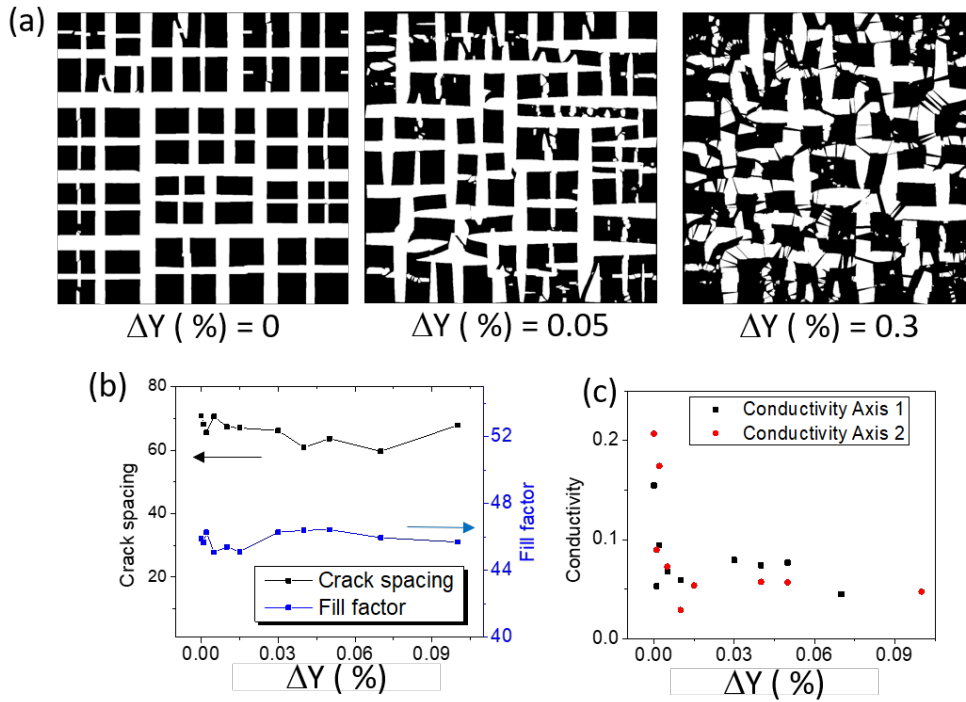


Fig. 3.4 Crack patterns with distribution in constant Y value.

form of a range of Y . We have introduced a deviation δY and studied the effect on the conductivity of the cracked and dried sample after saturation.

Figure 3.4a shows that with deviation δY , randomness in crack formation increases, which in turn decreases connectivity and conductivity as shown in Figure 3.4c. It is observed that there is an initial sharp fall in the conductivity even with the slightest deviation from Y but subsequently the conductivity remains more or less constant for larger deviations. The fractal dimension of the sample with $\delta Y=0$ is 1.66 while that for $\delta Y=0.3$ is 1.71 indicating that the fractal nature increases with the deviation, implying a rougher crack path. It also goes with experimental findings showing that cracks on nanofilms made of uniform size particles were observed to be straight and connected while that of non-uniform size showed randomness [87] with lower connectivity and increased fractal nature (Figure 3.5). A similar trend is observed by adding Al_2O_3 in TiO_2 (Figure 3.7) and was also previously observed on adding clay in laponite. [126] Despite the drastic change in conductivity, neither the crack spacing nor the

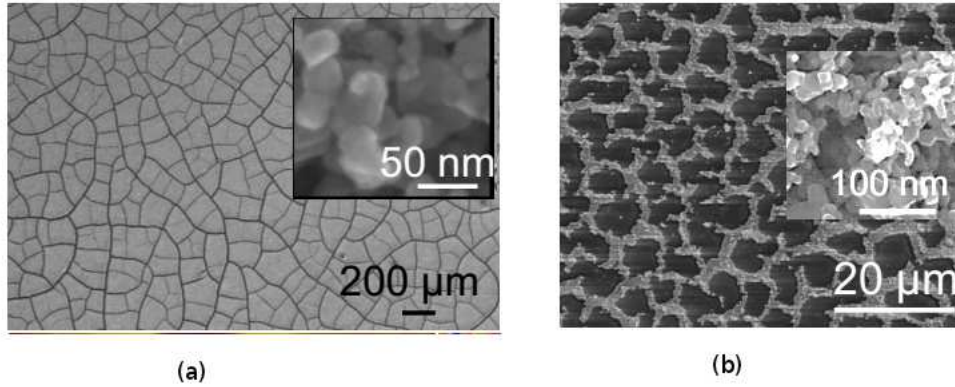


Fig. 3.5 Crack geometry on the film obtained from TiO_2 nano-particles of (a) uniform size of 25 nm diameter and (b) non uniform size with mean diameter of 16nm.

fill factor exhibit any remarkable change with δY (Figure 3.4b). Thus, deviation in Young modulus has a huge impact on connectivity and conductivity of network.

Variation of breaking threshold

Figure (3.8) shows no marked differences for simulation experiments done for $S = 0.025$ and $S = 1.0$, here crack spacing is measured from boundary to boundary (internal distance). The crack width is almost unaltered while the change in crack fill factor is only by 10% within this range (Figure 3.9).

Variation of drying rule through b and r

As discussed in Eq. 3.1, parameters b and r jointly control the drying rate with higher b and lower r lead to more rapid drying. Figure 3.10 shows that on increasing b , cracks become more well connected, which is good for high conductivity, but at the same time cracks become very wide, i.e. fill factor increases, this improves conductivity but

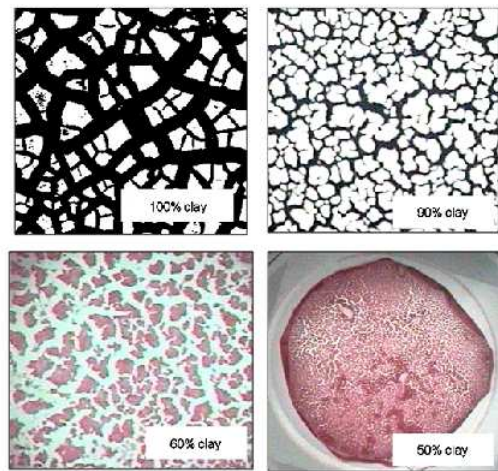


Fig. 3.6 Change in crack geometry of clay on addition of polymer. Reproduced with permission from ref [126]. Copyright 2010 IOP Publications.

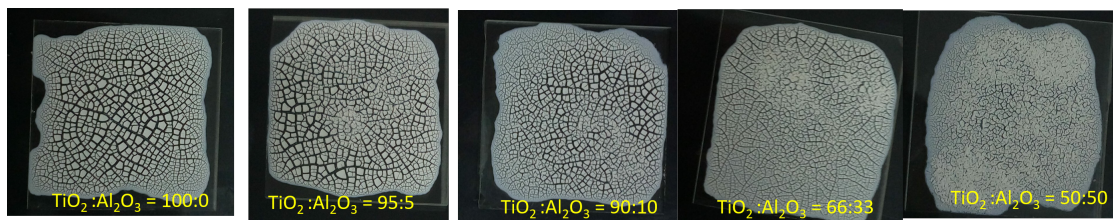


Fig. 3.7 Deviation in crack geometry of TiO₂ colloidal film on addition of Al₂O₃

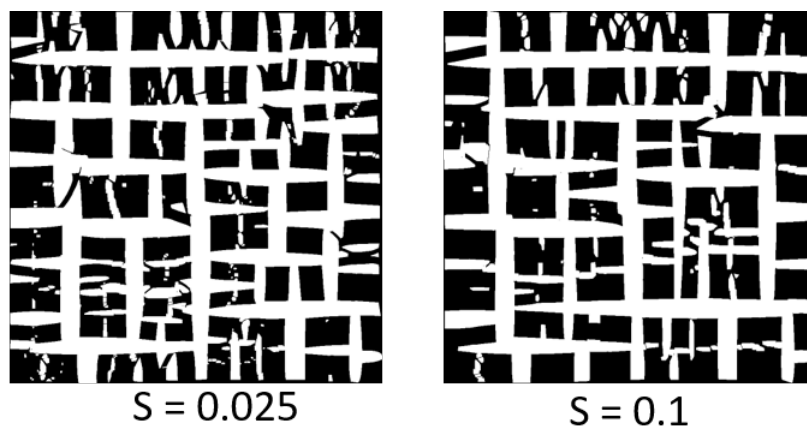


Fig. 3.8 Variation in breaking threshold S of the springs.

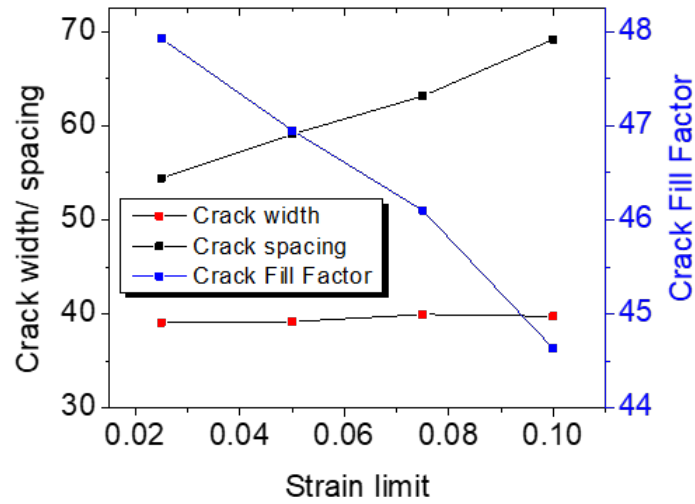


Fig. 3.9 Crack properties versus breaking threshold S

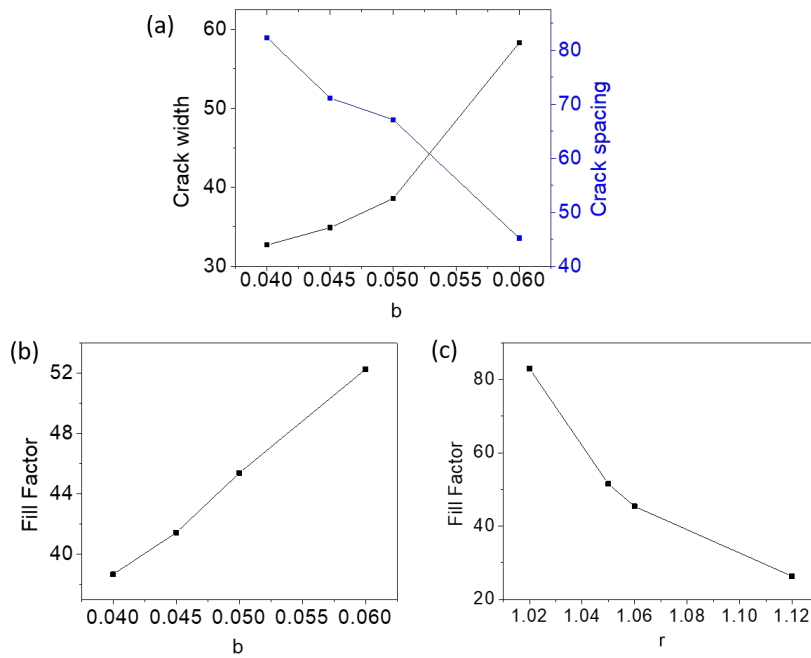


Fig. 3.10 Variation of crack parameters with variable b and r used in the drying rule.

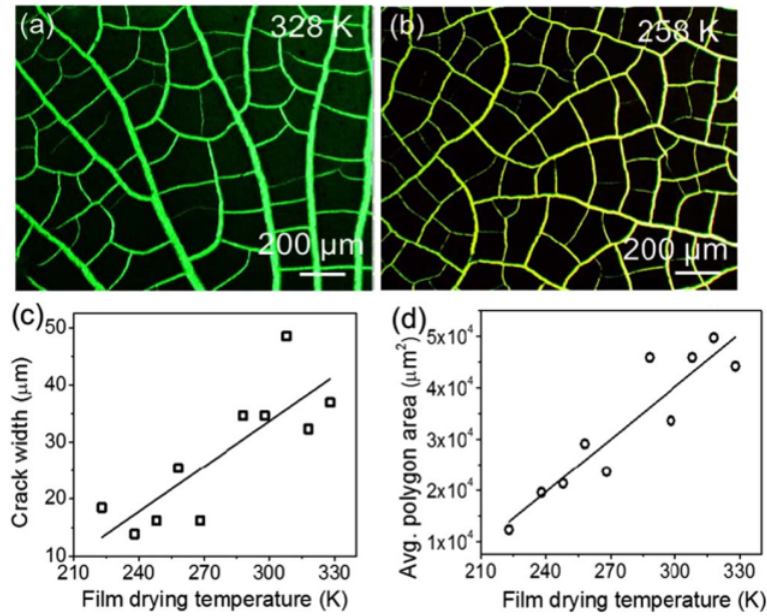


Fig. 3.11 Effect of drying temperature on crack patterns of TiO_2 film.

reduces transparency. The decrease of r has a similar effect. Clearly, the influence of drying rate is very strong on the crack pattern, so it has to be tuned judiciously during applications to optimise conductivity and transparency. Figure 3.11 shows experimental observation of the increase in crack width with the drying temperature (drying rate).

3.1.7 Discussion

Thus using the spring fusion model, the effect of various parameters that control crack geometry is investigated. When used as a template for fabricating TCE, the parameters should be such that good conductivity, as well as high transparency, is obtained. Since the model parameters can be related to physical properties of the materials and ambient conditions during drying, the simulation gives us an idea of the type of materials and the conditions to implement for best results. The most striking result is the necessity for homogeneity in the material. Addition of even a small amount of impurity to the uniform composition of a desiccating material causes a marked change in crack

geometry. Hence for any non zero δY deviation, the randomness in crack pattern comes into play and conductivity falls drastically. Figure 3.4 shows a very sharp fall in conductivity, on introducing slightest polydispersity.

It is shown crack width and spacing increase with the thickness of a film agreeing with experiments. [142]

Variation in strain limit S does not show any marked differences (Figures 3.8 and 3.9). Crack width and fill factor change only by a negligible amount. One may infer if the limit is not infinitely large, as, in the case of polymers, which are very difficult to break, there will be no significant change in crack morphology with S .

Besides materials, the drying conditions are to be chosen carefully as well. It is observed that higher the drying rate (controlled by b and r) wider are the cracks formed from the suspension (Figure 3.10). Two materials having approximately the same Y can behave very differently if one desiccates faster than the other. In the same time interval, a faster desiccation rate leads to a greater stress built up within the system. As a result, a spring is stretched more before it reaches its yielding point. hence, faster desiccation leads to broader cracks.

3.1.8 Conclusion

In conclusion, spring fusion model is able to understand the variation in TCE performance on crack template formation conditions. For any optimum TCE, the film thickness should be low to have high edge density required for efficient TCE performance. Young modulus should have minimum distribution and drying rate should be lower.

3.2 Modulation via wet-drying cycles of crack template

3.2.1 Introduction

Crack formation is a ubiquitous phenomenon manifested in different scales in drying mud, paint, soil, rocks and various other materials. [43] Cracks are generated due to desiccation stress; in this process, evaporation of solvent leads to capillary force driven rearrangement of particles, [160] while the film-substrate friction (adhesion) resists this movement. This generates stress in the film, which is released in the form of cracks. [157, 108] The normalized effect of friction reduces with film thickness, thus the crack spacing increases linearly with the film thickness. [157, 101] However, for a very thin film having a thickness below critical film thickness (CFT), the film does not crack at all or just forms a few nucleating cracks due to inadequate stress as compared to defects in the film. [101] In most of the cases, these cracks are unwelcome, as they degrade material performance; hence, stress modulation techniques such as using binders, depositing films step by step below CFT, [138] gelation driven film formation [72] etc. are used for preventing films from cracking. Cracks form very interesting hierarchical structures [15] based on their stress field and there has been considerable interest in the research community to modulate these crack patterns by playing with the stress field. The stress field for cracks have been modulated using the electric field for radial cracks, [76] vibrational memory or directional drying for parallel cracks, [89] substrate texturing for wavy cracks, [128] polymer addition for hexagonal cracks [73] etc. The stress field of the film is also controlled by wettability, [40] drying temperature, [87, 73] light induced solvent gradient, [161] solvent, [131] interaction between colloids [117] and nature of substrate etc. [157] leading to different geometrical features in different conditions. Goehring et al. have studied the reorganization of already formed cracks pattern by repeated wetting and drying of the film. They observed the interesting conversion of crack intersection angles from 90° to 120° and

transition of the crack network from a rectangular brick-layer pattern towards a hexagonal network [42] by this treatment. However, despite the conversion of angles, we find that some new cracks are also formed in the film, which was not given attention. Inspired by this observation, we study here, micro-nano crack patterns formed under repeated drying cycles with the specific purpose of producing improved transparent conducting electrode (TCE) templates.

Recently random crack patterns have been utilized as a template for obtaining metal network based transparent conducting electrodes. [81, 90, 22] Here, the metallic network is electrically conducting, while voids between the wires are electrically insulating and transmit light. These metallic networks find diverse applications as an essential component of solar cells, [91] touchscreens, [56] transparent heaters, [87, 142] electro-magnetic shielding [58] etc. as a convenient substitute for the commonly used TCE, indium tin oxide, which has various limitations, being brittle, costly and unstable at higher temperature. [90] However, the challenge remains in these networks to reduce the size of insulating voids, which is important for better charge collection and uniform performance of the device. [92, 91] To achieve it, the crack spacing in the crack template should be lower; however critical film thickness restricts minimum possible crack spacing as discussed earlier. Thus, it is necessary to reduce crack spacing and crack width by modulating the stress field by other means. The techniques for reducing drying temperature have been attempted to obtain high crack density; however, it increases drying time from seconds to several hours making it impractical. [87]

3.2.2 Scope of the present investigations

In this work, the stress field of the cracks, using repeated drying cycles is modulated, leading to higher crack density and more hierarchical pattern. The study shows that networks obtained from repeated drying cycle have lower insulated void size, an order of magnitude lower sheet resistance, higher interconnectivity of wires and better charge collection efficiency.

3.2.3 Results and Discussion

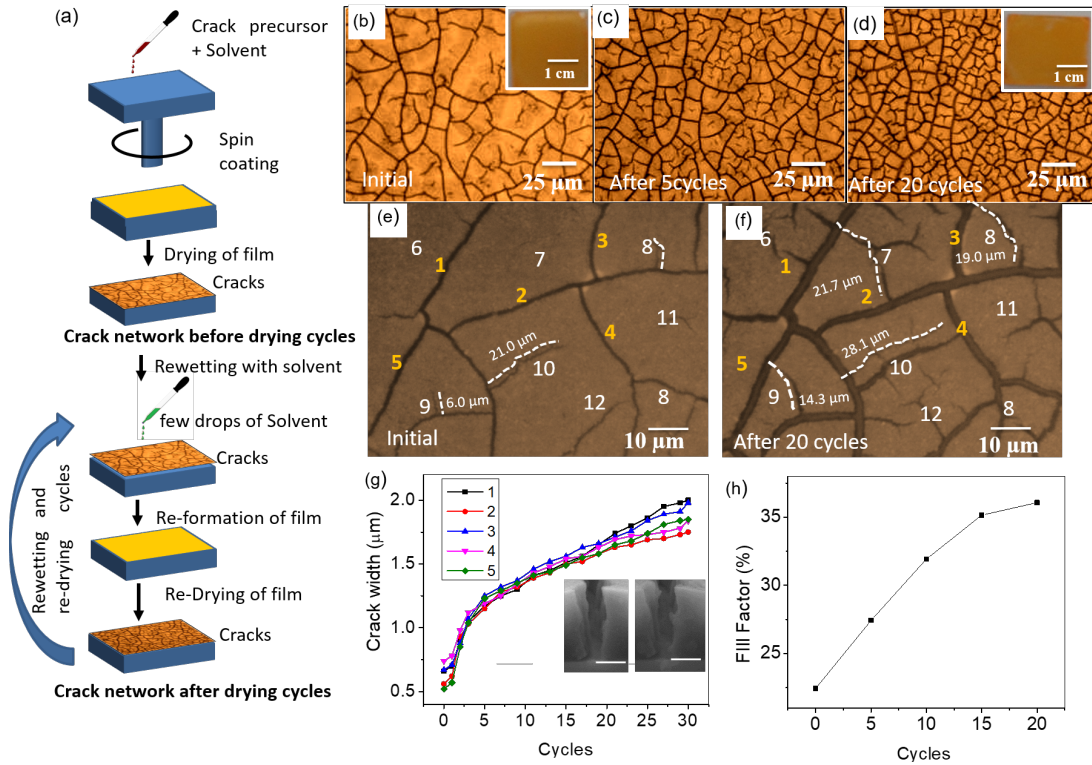


Fig. 3.12 (a) Schematic showing the steps to obtain crack network with repeated wet-drying cycles. Crack network obtained after (b) first desiccation and (c-d) 5 and 20 repeated wet-drying cycles. The insets show the complete film of size $2.5 \times 2.5 \text{ cm}^2$ showing there is not a much visual difference in the film (e-f) Comparison of features before drying cycles and after 20 drying cycles. (g-h) variation of crack width and crack fill factor with wet-drying cycles. Inset of (g) shows cracks are U-shaped before drying cycles and are more V-shaped after drying cycles. Scale bar = $2 \mu\text{m}$.

Crack templates are formed using an acrylic resin based colloidal dispersion on a transparent substrate (glass in this case) by spin coating drops of the dispersion for 60 s as shown in Figure 3.12a; the optimisation details may be found in earlier publications. [142] Here, the film thickness can be controlled using angular speed (rpm) and concentration of crackle precursor (CP). Figure 3.12b shows one such crack network of film of size $2.5 \text{ cm} \times 2.5 \text{ cm}$ of film thickness $1.7 \mu\text{m}$ having a crack width $\approx 700 \text{ nm}$ obtained by coating $60 \mu\text{l}$ solution of 0.4 g/mL concentration at 1000 rpm. It may be noted that the cracks are not entirely connected with each other in the network.

The obtained crack template was rewetted with 20 μl of isopropyl alcohol solution and re-dried in ambient condition for 60 s. The process of wet-drying cycles was repeated 20 times. Figures 3.12c-d show the crack network after 5 and 20 cycles, respectively. As shown, the drying cycles lead to increase in length and width of existing cracks and formation of new cracks. To gain a deeper insight, crack patterns before and after drying cycles are compared at different locations. Interestingly, there is an enormous variation in the connectivity of the pattern. In Figure 3.12e-f, isolated nucleating points of cracks (see label 11) propagate enough to become part of the main backbone and most of the dangling cracks propagate further to form connected closed networks (8-10). Furthermore, the process also creates new nucleating (see label 6 and 12) and propagating cracks (11) during the process. The process creates an even higher order of hierarchical cracks (Figure 3.13). The process is found to increase the crack width by a factor of 3, while the increase in crack length is observed (Figure 3.12f) to be up to $\approx 150\%$. The phenomena may be due to excess stress formation due to wetting of the film; the wetting leads to rearrangement of particles of the top, while substrate friction prevents the movement of lower-most particles leading to stress and further cracking of the film. [157] More the wet-drying cycles, more is the rearrangement of colloidal particles, which in turn leads to more stress, and cracking of the film. The method is quite stable, we made more than 10 samples of different film thicknesses and found every time the crack density and connectivity was rising significantly with drying cycles.

The enormous increase in crack density can be utilized for improvement of derived TCE. To compare the TCE performance, metal (Cu) was deposited by physical vapour deposition on an as-prepared template and that obtained after 20 drying cycles (detailed steps are explained in Figure 3.16) and the sheet resistance and transmittance were measured. Three such examples are illustrated in Figure 3.14.

Table 3.1 shows the comparison of TCE obtained from crack templates before and after drying cycles. It is clear that the mean sheet resistance decreases from 410 Ω/sq to 29 Ω/sq with a little compromise in transmittance, from 91.5% to 85.7%. FoM

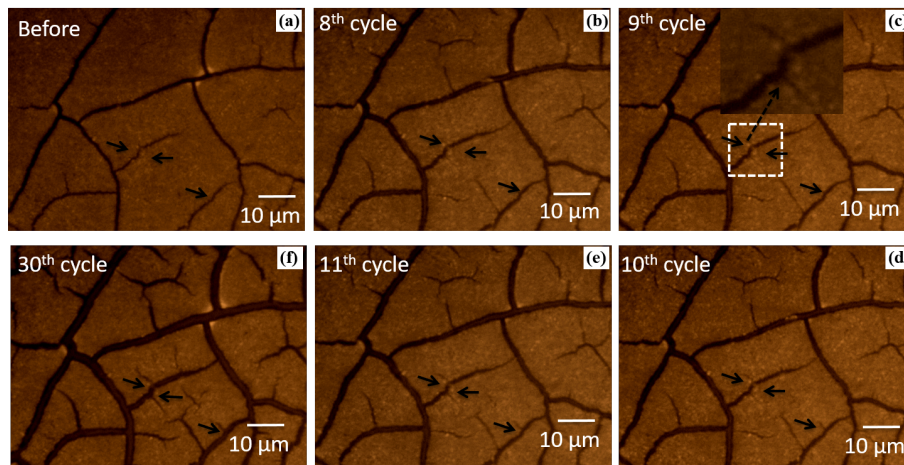


Fig. 3.13 Newly formed cracks are acting as a backbone and initiated new cracks formation as indicated by arrows inside (a-f) to show the progress in crack formation.

Table 3.1 Sheet Resistance (R_s), Transmittance (T) and Figure of merits of TCE defined by Coleman et al. (F_C) and Haacke (F_H).

	Sample 1		Sample2		Sample3		Mean	
	Before	After	Before	After	Before	After	Before	After
R_s	523	31	485	32	223	23	410	29
$T(\%)$	91.6	88.3	92.2	85.3	90.8	83.5	91.5	85.7
F_c	8.0	94.7	9.4	71.2	17.1	86.9	11.5	84.2
F_H	8.0×10^{-4}	9.2×10^{-3}	9.1×10^{-4}	6.3×10^{-3}	1.7×10^{-3}	7.1×10^{-4}	1.1×10^{-3}	7.5×10^{-3}

F_C increases from 11.5 to 84.2 and F_H increases from 1.1×10^{-3} to 7.5×10^{-3} . Thus, the study shows that the modified geometry by drying cycles can increase the TCE performance by an order. Note that as discussed in section 2.1 the resistance and FoM depend on the geometry of the pattern as well as thickness and resistivity of metal. Since a typical crack template itself can provide $F_c \approx 1350$ on increasing metal film thickness to $\approx 300\text{nm}$. Thus, with this modified geometry of crack pattern, FoMs can increase drastically.

The process of crack pattern modification into a good template with re-wetting drying is also observed on a flexible plastic substrate such as polyethylene terephthalate (PET) (see Figure 3.15), which can be utilized to make flexible devices. The drying-wetting cycles discussed in this work can be utilized to obtain more efficient flexible devices such as transparent flexible heaters, transparent capacitors, and solar cells etc.

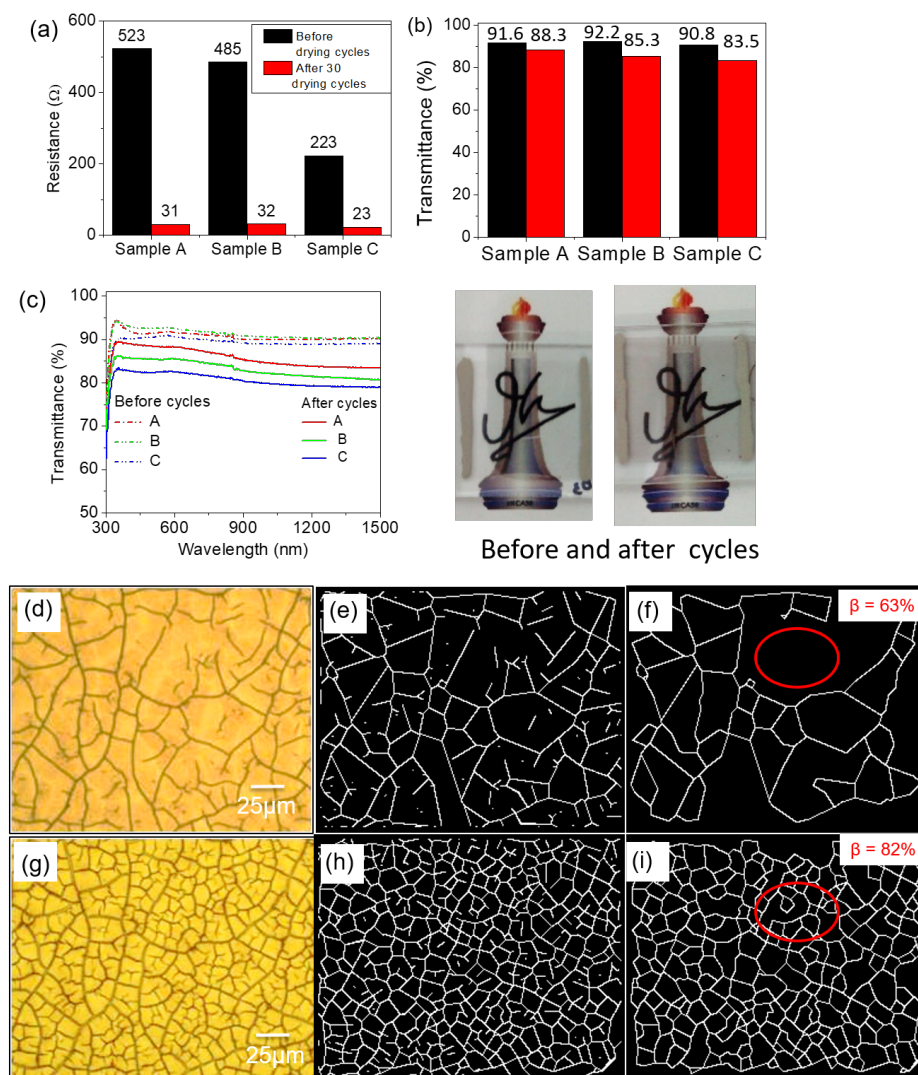


Fig. 3.14 (a-c) Comparison of sheet resistance and transmittance of the metal network obtained from the templates before and after drying cycles and shows real images of derived TCE on institution logo showing high transmittance in both the cases. Microscopic images of a crack network (d) before and (g) after 20 drying cycles, (e and h) represents corresponding binary skeletonized images and (f and i) are corresponding current carrying backbone wires. Note that dangling and isolated wires are ineffective for current transport. The circle represents an area, which is not having any backbone wire initially (f) has considerable backbone wires after drying cycles (i).

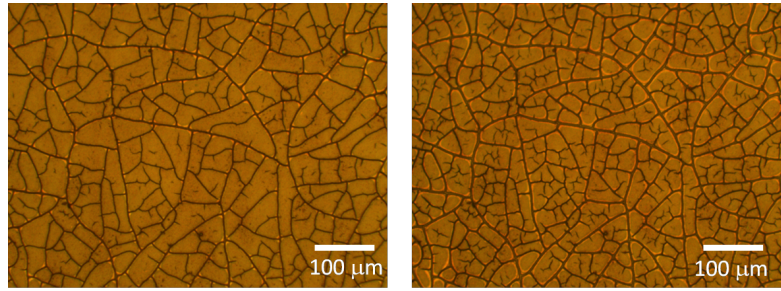


Fig. 3.15 Crack patterns on PET substrate before and after 10 drying cycles.

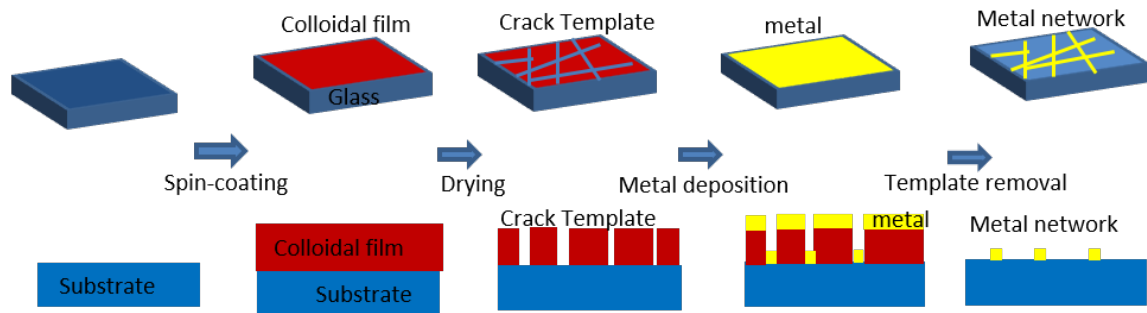


Fig. 3.16 Steps for transparent electrode fabrication for top and cross-section view. Briefly, a crackle precursor is spin-coated resulting in the crack template formation. Metal is evaporated on the crack template using physical vapor deposition technique and the template was then removed by dissolving in the solvent (chloroform).

To gain deeper insight into the electrical transport of these networks, the current effective backbone (β) of these wires are quantified using our algorithm discussed in Figure 2.4. [92] Here, the microscopic images of metal network as shown in Figure 3.14(d) and 3.14(g), before and after drying cycles are converted to skeletonized images Figures 3.14 (e) and (h) and the corresponding effective region for current transport (backbone) is classified. It is clearly seen, the backbone before drying cycles is 63% while after 20 drying cycles, it increases to 82% with 150% increase in total backbone length. Importantly, before imposing repeated drying cycles on the template, the backbone is highly non-uniform with a high density of the wires present in very few regions. As an example, there is no backbone wire within the red circle before repeated wetting-drying cycles (Figure 3.14e), the wire density increases and becomes even after 20 drying cycles as shown in Figure 3.14f. Thus, the current distribution is hugely improved with drying cycles. The increase in wire density is very important

for a TCE network as it leads to a reduction in sheet resistance and uniformity in performance, which can be helpful in obtaining high-resolution touch screens, highly efficient solar cells, the low response time of transparent heaters etc.

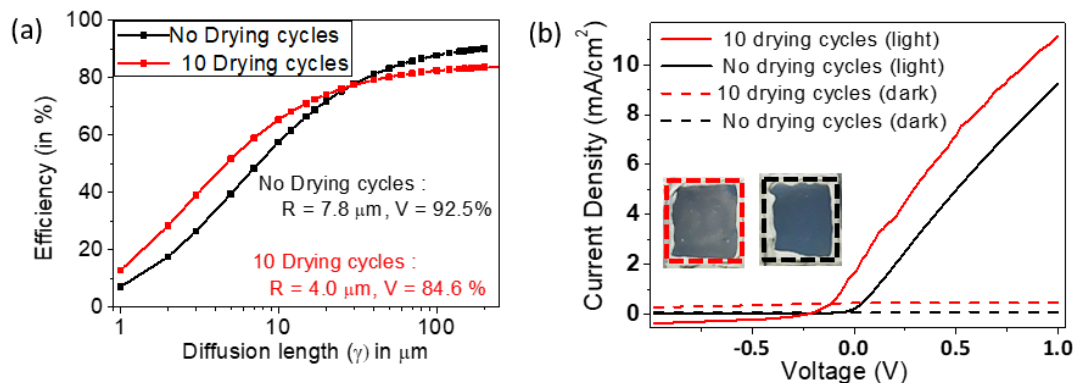


Fig. 3.17 Comparison of theoretical solar cell efficiency of TCE obtained from the crack template (a) before drying cycles (b) after 10 drying cycles showing the equivalent radius is reduced to half. Here, R is the equivalent radius and V is area fraction occupied by voids. (c) Comparison of current collection for n-doped Si for networks using networks without and with drying cycles. The inset shows photographs of n-Si coated with Au network before (black) and after (red) drying cycles. The increase in wire density in Si sample with wetting drying cycles is apparent from the golden tinge on the substrate.

The increase in wire density is important for efficient solar cell current extraction. When a solar cell is illuminated, charge carriers are generated within the active material and based on polarity, one type of charge is collected by the metal mesh. Higher wire spacing in the TCE leads to more recombinations thereby lowering the efficiency. Figure 3.17a shows the theoretical solar cell efficiency (2 D case) of TCE obtained for these networks using approach developed in section 2.3 . [91] From the analysis, it is obtained that the equivalent radius of network before drying cycle is $\approx 8 \mu\text{m}$ while after drying cycles it is $\approx 4 \mu\text{m}$ resulting in increase in efficiency from 7.1% to 12.8% for diffusion length of $1 \mu\text{m}$. As is previously studied, Au wire network grown on Si by electroless process shows very high photocurrent compared to bare Si. [49] To study the influence of increasing the wire density by repeated wetting-drying cycles, Au wire network was grown for Si samples (see Figure 3.18) with and without

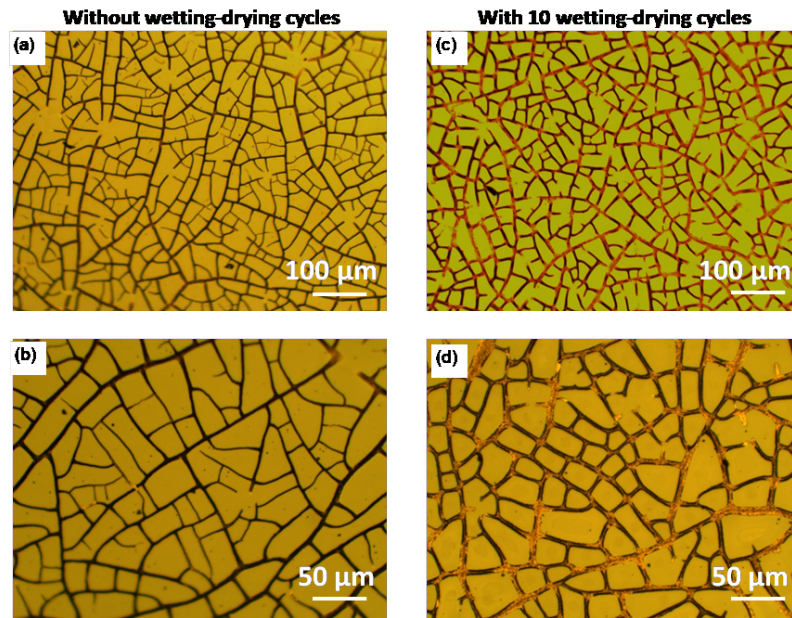


Fig. 3.18 (a-b) Au network on Si before drying cycles and (c-d) after drying cycles.

Table 3.2 Comparison of the crack spacing of different networks from the literature of similar transmittance. The resistance values are not mentioned as it depends on film thickness, which is different in different studies

S.No.	Material	Average crack spacing (μm)	Remarks
1	Crackle paint template [86]	400	T = 77%
2	TiO ₂ NPs 318K [87]	165	...
3	TiO ₂ gel [56]	100	T = 86%
4	TiO ₂ NPs 238K [87]	125	...
5	TiO ₂ NPs 238K [87]	125	...
6	Acrylic resin [142]	85	T = 87%
7	Egg template [134]	50	T = 88%
8	Before cycles (this work)	30	T = 92% , $R_s = 523\Omega/sq$
9	After cycles (this work)	15	T = 88% , $R_s = 21\Omega/sq$

wetting-drying cycles on crackle template. Owing to the considerable reduction in recombination losses of photogenerated charge carriers due to increasing wire density, $\approx 2 \text{ mA/cm}^2$ enhancement in photocurrent density was observed for the voltage range 0 – 1V compared to the sample without wetting-drying cycles (see Figure 3.17b). To check the reproducibility, we have measured the photoconductivity measurement of two more samples. All three samples showed significant enhancement in photoconductivity. Thus, wetting-drying cycles when applied for wire network used as an electrode can efficiently increase the performance of charge collection in a device. The study shows that crack patterns manifested during multiple drying cycles can be significantly different from what results from a single drying cycle, an insight which should be an important addition to the known crack physics. Thus, if one is looking for minimum cracks in a film such as a wall paint then repeated wetting and drying should be avoided as far as possible. The study may also be useful to infer the number of times a system such as soil has undergone drying cycles. The technique has a special significance in the area of crack lithography for applications like transparent conducting electrodes where a high density of cracks is desirable. The above technique can prepare templates of uniform, dense and highly connected cracks which are found to be exceptional in the literature (see Table 3.2 for comparison).

3.2.4 Conclusion

In conclusion, the work discusses the modulation of stress in crack networks following repeated drying cycles and found that crack density, connectivity, and their uniformity increase exceptionally well; when used as templates, TCEs with enhanced performance arising from the low sheet resistance and efficient charge collection resulted.

3.3 Modulation by using mixture of solvents

3.3.1 Introduction

Crack template based metal networks are promising candidates for transparent conducting electrodes. Here, the voids between wires are transparent for light while the metallic mesh is conducting. However, high crack spacing, broad crack width, and limited connectivity limit the performance of derived TCE. For an ideal transparent conducting electrode, it is desirable to use a mesh with narrow wire spacing, low wire width, and high interconnectivity, which offers high transmittance, low sheet resistance, and efficient charge collection. However, obtaining narrow, dense and highly connected large-scale crack patterns for the purpose is always a challenge. The colloidal film thickness is reduced generally for achieving low crack width and spacing, however, below a certain film thickness, known as the critical film thickness of cracking, a drying film does not crack at all. [142] The drying temperature is another important parameter to decrease crack scaling, however, it increases the drying time from seconds to several hours, making the process impractical. [87] As discussed in section 3.2 stress modulating techniques such as re-wetting and drying of colloidal films have also been investigated for the purpose, however, that brings additional steps and increases the crack width up to four times, reducing the transmittance further. [93] Thus, an alternative simple process is desirable to reduce the crack width, reduce crack spacing and increase connectivity. The simple process can involve changing crack precursor, crack substrate or solvent. However, there is a very little control on a substrate as it has to be flexible and transparent, thus PET is a natural choice. The solvent variation could be the simplest way to reduce crack width further as solvent properties determine the evaporation properties, which influences the cracking. Theoretical studies have shown a strong influence of solvent effect on crack scales which is experimentally confirmed as well. As an example, Ogale group found that mud cracks are formed finer with methanol solvent as compared to water solvent and in benzene, the crack does not form at all. [131] However, the studies were limited in considering only the

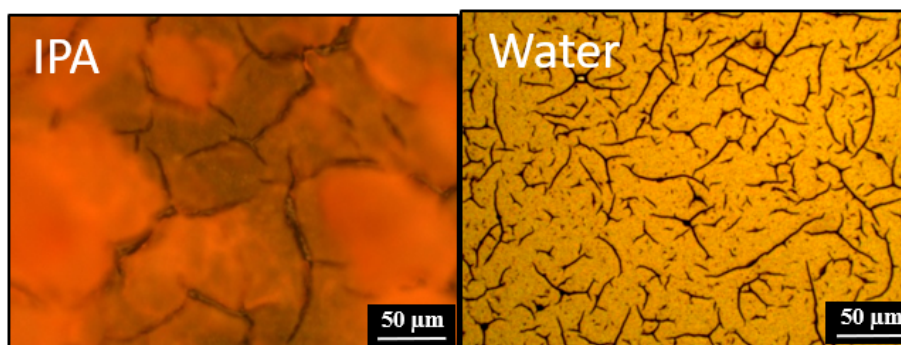


Fig. 3.19 Crack patterns formed with pure IPA and water.

effect of surface tension in the solvent studies and were applied to systems like mud which gives cracks of centimetres scale, not useful for lithography purpose.

3.3.2 Scope of the present investigations

Here, instead of using a single solvent mixture of solvents are used for the colloidal dispersion. The cracks by using IPA: water with $\approx 85:15$ showed well connected and narrow cracks. The reason for this unusual nature is explored.

3.3.3 Results and Discussions

To choose a suitable solvent for achieving minimum crack spacing and crack width, the crack precursor was made from the equal amount of acrylic resin nanoparticle with various solvents such as chloroform, petrol, dimethylformamide, isopropyl alcohol (IPA), ethyl acetate, acetone etc. Thus obtained crack precursors were spin coated on a glass substrate, leading to the formation of different kind of crack patterns. It is found that out of them, isopropyl alcohol and water formed a good dispersion and better tendency to form cracks (Figure 3.19). However, the cracks formed by these solvents are unconnected and have high width and spacing. As the mixture of solvents can have different properties, here properties of a mixture of solvents is studied for the crack behaviour.

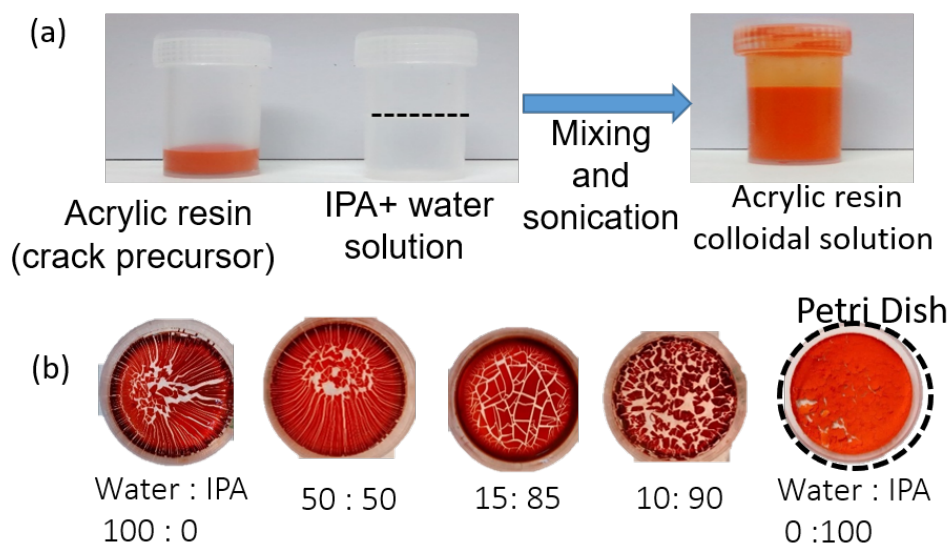


Fig. 3.20 (a) Preparation of colloidal solution of acrylic resin with solvents consisting of water and IPA of variable compositions. (b) Crack networks formed after ambient drying of 5 ml colloidal solutions in the petri dish.

Figure 3.20a shows the process of preparation of a colloidal solution of acrylic resin in a solution consisting of water and IPA of variable composition. Firstly, a solution of water and IPA of the variable composition is made by mixing water and IPA of desired ratios which is mixed with a given mass (in this case 3.5 gm) of acrylic resin and sonicated well to form well dispersed acrylic resin colloidal solution of variable IPA composition. Next, we compare the cracks patterns formed on dried colloidal films in a petri dish after complete drying of solvents typically taking 3-10 hours based on the solution. Interestingly, the crack patterns were found to be entirely different for different solvents (Figure 3.20b). With pure water, the cracks are found to be radial from the boundary of petri dish towards the center and appear to be parallel locally, the pattern was observed similarly for 50% IPA. However, most interestingly, increasing IPA concentration to 85%, the cracks become random, hierarchical and uniform and film showed good adhesion. While, films with even higher IPA composition show lower hierarchical nature of cracks, non-uniformity and very low adhesion of film with the substrate. Nature was seen to be reproducible. Thus, the colloidal films with 85% IPA composition show exceptional cracking behaviour.

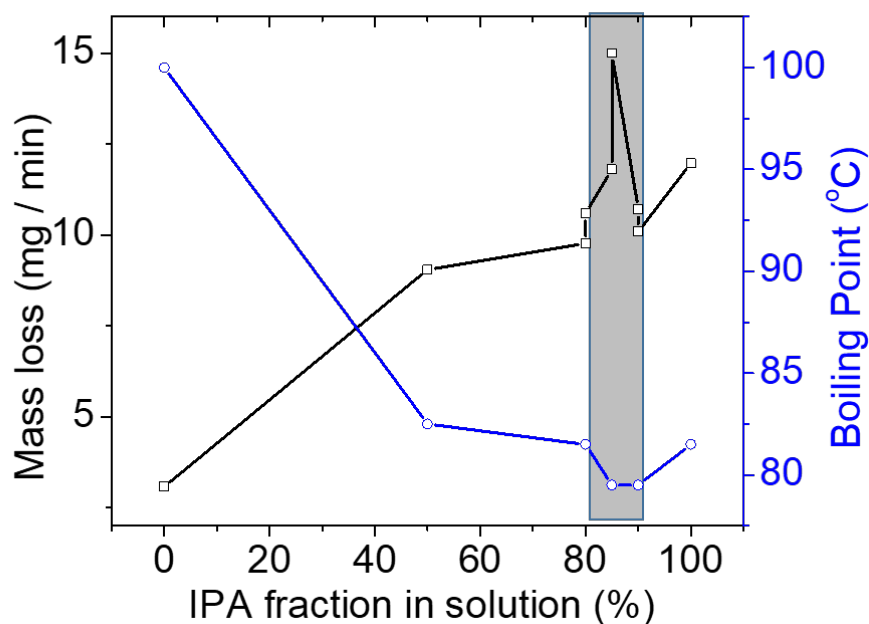


Fig. 3.21 Comparison of evaporation rate and boiling points of different compositions.

To gain a deep insight, the evaporation rate of these colloidal solutions is studied by allowing it to dry in a petri dish and weighing it during the drying process. Although the complete drying takes 3-10 hrs, the mass loss per minute is calculated from initial 20 minutes measurements to assume non-variation of concentration during the process. As shown in Figure 3.21, as expected, the evaporation rate of the colloidal solution increases with increase in IPA composition due to the higher vapor pressure of IPA as compared to water. However, strikingly, for 85% IPA composition, the mass loss was exceptionally higher, suggesting the unusual behaviour of this particular composition. To confirm its unusual evaporation behaviour, the boiling point of a solution is also determined for various compositions (Figure 3.21 blue curve), which reflects that 85% IPA has a minimum boiling point. We are not the first one to observe this unusual property of 85% IPA composition, it was observed way back in 1921 by Lebo, [102] and is closer to its azeotropic mixture value. The unusual higher evaporation rate and lower boiling point suggest that 85% IPA has unusual evaporation and interaction property.

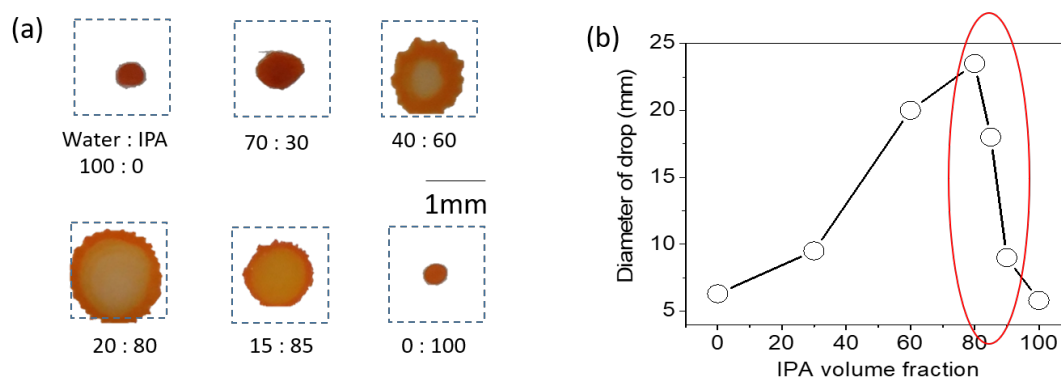


Fig. 3.22 (a) Optical images of films formed by drop coating 20 μ l solutions of different compositions. The box size is 2 cm x 2 cm. (b) Variation of size of drop for different compositions

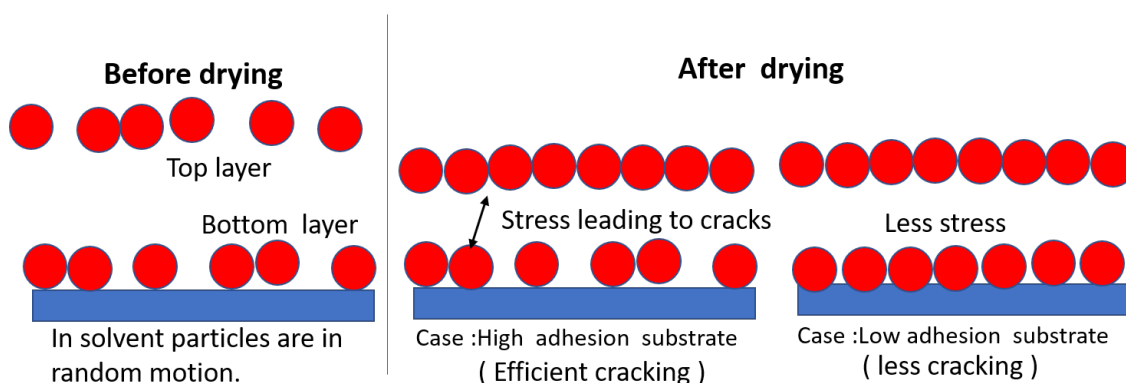


Fig. 3.23 Effect of substrate adhesion on cracking.

As the cracking nature strongly depends on the wettability of film, the wetting nature of these colloidal solutions is studied by drop coating 20 μ l of the solution on a glass substrate. Figure 3.22a shows the images of dried drops formed from different colloidal solutions. As seen, different solutions give different drop sizes and height profiles. Colloidal drops formed from pure water and IPA did not show any spreading after drop-coating and eventually formed small drop size of less than 5mm. While, interestingly, the colloidal drop made from mixtures of these solvents showed significant spreading in bigger drop size and low height and for 80% - 85% IPA the drop size $>$ 20mm of uniform thickness. Thus the particular composition \approx 85% IPA has the highest wettability.

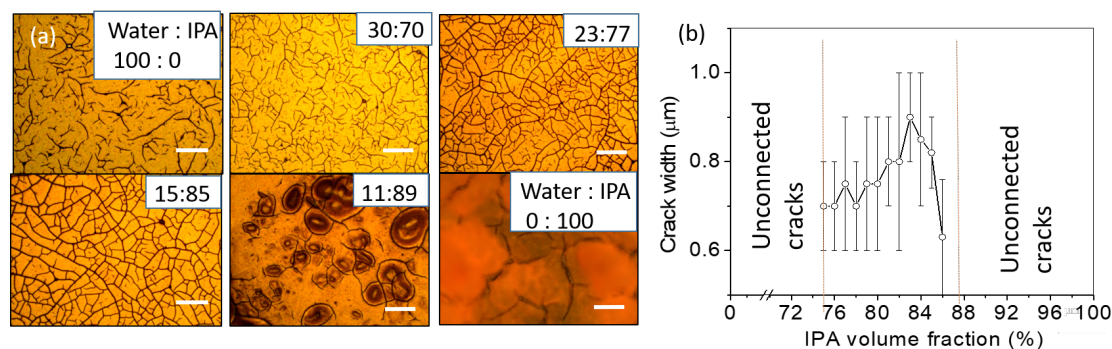


Fig. 3.24 Crack patterns obtained by spin coating for different compositions.

The entirely different wetting and cracking nature of 85% IPA could be due to its inherent cohesion property. Note that, the wetting property is related to the adhesion of the colloidal solution with the substrate and cohesion of the solution with itself. If cohesion of solution with itself is less as compared to adhesion of solution with the substrate, the solution wets better. As 85% IPA has lower cohesion based on our evaporation experiments, thus it may lead to its better wetting. Further, for efficient cracking adhesion should be more as cracks are formed due to the adhesion with the substrate as explained in Figure 3.23. In detail, the cracks are formed due to desiccation stress, which arises because the particles present on the top surface of the film rearrange to form close-packed arrangement due to capillary force, while particles near the substrate can not rearrange themselves due to adhesion, leading to stress in the film, which is released in form of cracking. Thus, higher the adhesion, higher the stress and more the crack density. As 85% IPA composition has high adhesion to substrate due to its low cohesion forces, it leads to more crack density. Figure 3.24 shows the crack pattern obtained with spin coating technique to obtain low film thickness. Interestingly, the cracks formed with composition window around 85% IPA has high connectivity, while a colloidal film with pure water or IPA solvent gives unconnected and less dense cracks. Thus, adhesion can be tuned to the mixture of solvents to obtain well-connected cracks.

Further, low adhesion also leads to slipping of the film and in turn broadening of the cracks during the drying process (Figure 3.25). Higher the adhesion, lower is

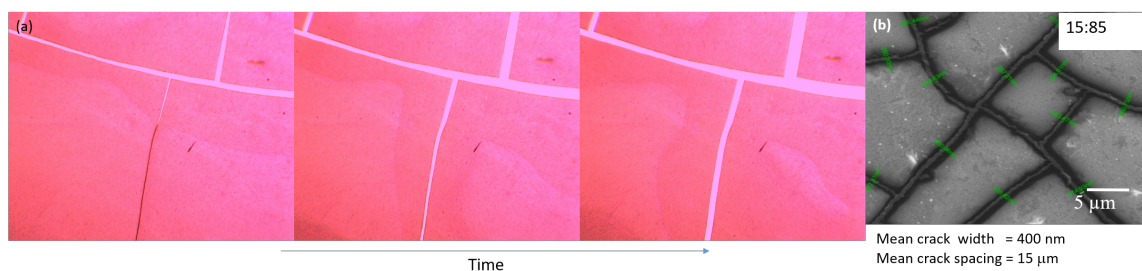


Fig. 3.25 Effect of substrate adhesion on cracking.

the slipping and in turn cracks formed are narrower. As the 85% IPA composition has better adhesion, thus it can lead to narrow crack formation. It is also observed experimentally and one can obtain mean crack of just 400 nm. Interestingly, it is minimum crack width reported for desiccating cracks. Previously, optimised crack patterns on the similar substrate and acrylic resin offered crack width of 2-6 μm [142] as compared to 400 nm in the present case. Thus, 85% IPA has least cohesion, which leads to high adhesion with the substrate important for high crack density and low crack width.

In this way, a particular mixture of solvents can be employed to increase the adhesion of the film with the substrate required for the better crack pattern. Note that cracks with low crack width and high density can provide wire network of high edge density and wire width required for efficient TCE.

3.3.4 Conclusion

Desiccation cracks are studied with the mixture of solvents. It was found that mixture of IPA: Water (85:15) solvent offers exceptionally narrow cracks of width 400 nm with high density and interconnectivity. The reason for the unusual behaviour of the composition is understood in terms of high evaporation rate and wetting behaviour.

3.4 Designing of parallel cracks using a simple gravity flow method

3.4.1 Introduction

Desiccating crack patterns are seen in various natural and artificial materials such as mud, rock, soil, paint etc. due to shrinkage of material during the drying process. [43] Cracks generally considered to be undesirable and detrimental to material performance have recently gained enormous attention as a form of lithography templates, [127] especially in the area of transparent conducting electrodes. [142, 55] For this purpose, micro-nano cracks are formed by drying a thin film of colloidal suspension on a transparent substrate, which is used as a sacrificial template to deposit metal for obtaining conducting metal mesh mimicking the random crack pattern. These metal meshes are used as a transparent conducting electrodes (TCEs) for the applications of transparent heaters, [51] solar cells, [91], EMI shielding, [58] touch screens [55] etc. However, the random network structure of these networks has many shortcomings in the performance of an electrode due to unequal wire width, wire spacing, and limited connectivity. The random wire width and network structure lead to non-uniform current flow, nonuniform charge collection and importantly, limits the smallest possible pixel size of a network. [92, 91] To obtain uniform and predictable electrical performance for reducing pixel size, a random structure should be replaced with a well periodic structure. The present lithography techniques (e.g., electron beam lithography, photolithography etc.) to fabricate a periodic structure are expensive, instrument intensive and in many cases, non-scalable. [71] The Inkjet printing resolution is typically above 100 μm and preparation of the ink involves multi-steps and therefore, not cost effective. Using a simple technique such as crack template method to fabricate periodic structures, can be a versatile solution for fabricating periodic patterns over large areas. There have been several attempts to fabricate such periodic patterns by controlling the evaporation process or the drying direction of a colloidal suspension. In one instance,

a colloidal suspension held between a set of parallel plates is exposed by computer-controlled movement of the top plate thereby causing directional drying. [57, 111] In few studies, colloidal suspension is dried in capillary confinement in which parallel cracks move from open to the closed end. [67, 30, 2, 178, 38, 29] Several other techniques for parallel crack formation have been applied such as confining colloidal suspension between curved and flat surfaces or between crossed cylinders, [114] else drop coating and dragging colloidal suspension, [157] substrate texturing, [41] and substrate shaking at controlled frequency based on Nakahara effect. [88] While these studies have been successful in giving theoretical insights into crack formation mechanisms, the methods suffer from sophisticated requirements of precise control of forces, although natural desiccation induced cracking is in itself spontaneous. In other words, the advantages associated with such a spontaneous process are lost while bringing in a mechanical control. What is desirable is to develop a method which jells well with the natural process of crack formation yet produces parallel cracks with fine control.

3.4.2 Scope of the present investigations

Here a simple gravity flow based method is reported, wherein, the colloidal dispersion dropped over an inclined substrate is made to develop thickness gradient required for parallel crack formation. By varying the inclination angle, the crack width and spacing could be well controlled in the range, 1-6 μm and 10-40 μm , respectively. The influence of the drying temperature on the lateral interconnects forming ladder-shaped cracks has also been investigated.

3.4.3 Results and Discussions

Herein, parallel cracks by gravity flow are achieved by induced thickness gradient in the film. Figure 3.26a shows the experimental design of the process in which a glass substrate ($7.5 \times 2.5\text{cm}^2$) is kept on an inclined plane at an angle 30° at an elevated temperature. The crack precursor (CP), modified from a commercially

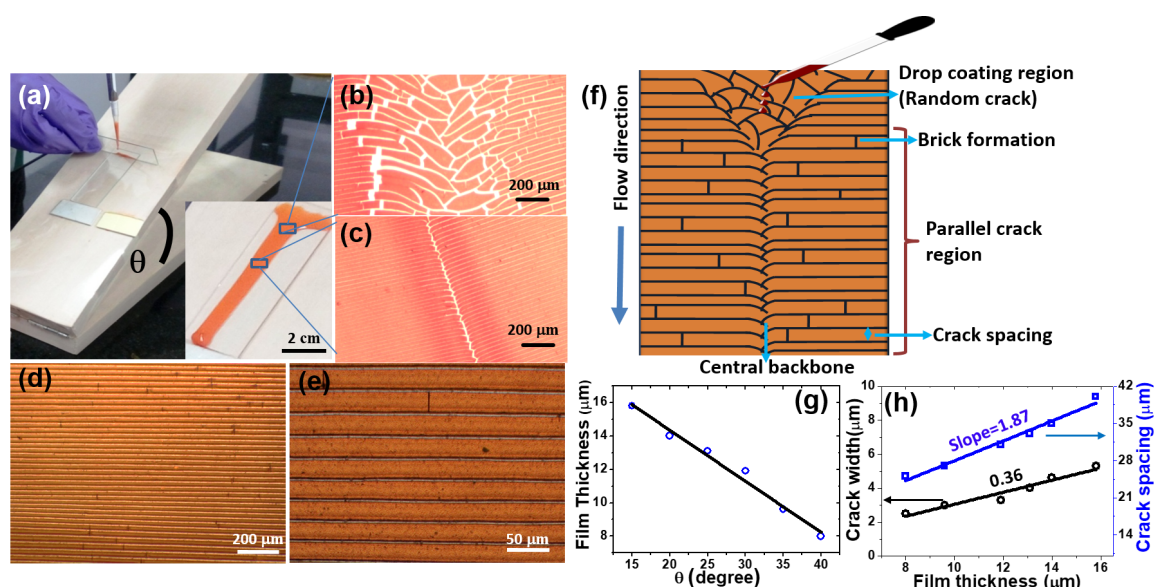


Fig. 3.26 (a) Photograph demonstrating film formation process using gravity flow. Here, θ represents the inclination angle. The inset shows a typical film formed on a glass substrate by the process. Optical microscopy images of the film showing cracks at (b) the drop coating region and (c) central region. (d) and (e) are images of parallel crack covering most of the area of the film at low and high magnification respectively (f) Schematic illustrating crack formation at different regions of the substrate. (g) Variation of film thickness with respect to θ (h) Variation of crack width and periodicity with the film thickness.

available product (Ming Ni Cosmetics Co., Guangzhou, China) as described in previous work, [142] consists of acrylic resin nanoparticles of size 40-80 nm of concentration 1g/ml in water. Approximately, $100 \mu\text{l}$ of crackle precursor (CP) was poured at the top end of the substrate which under gravity spread to form a thin film strip as shown in the inset of Figure 3.26a.

The drying process started from the edges inwards towards the center and as drying progressed beyond 15-20 seconds parallel cracks began to emerge perpendicular to the drying front (long edge of the substrate). On the basis of crack geometry, three distinct regions may be identified: (1) drop coating region with random cracks (Figure 3.26b), (2) central region with broad backbone with scattered cracks (Figure 3.26c), and (3) the remaining region with parallel cracks of equal periodicity (Figure 3.26d and e). All these regions are schematically shown in Figure 3.26f with $> 90\%$ region of the

whole film occupied by the parallel cracks. As pointed in the schematic, some short vertical interconnects are also formed in the film, giving the appearance of brick-like structures, which is temperature dependent as explained later. It may be observed from the Figure 3.26e that the cracks are nearly parallel to each other and highly periodic with periodicity $30 \mu\text{m}$ and crack width $4 \mu\text{m}$ for the obtained film thickness of $12 \mu\text{m}$. The film thickness is found to decrease with increasing inclination (Figure 3.26g) as the dragging force due to gravity increases with increasing θ . The crack width and periodicity are observed to increase linearly with the film thickness (Figure 3.26h), a behaviour which is well generalized for desiccating cracks as due to decreasing stress with film thickness. [157] In the present case, the inclination angle controls the film thickness which can be used to obtain desired crack periodicity and width.

To understand the dynamics of the process, the video of the film during drying process was captured under the optical microscope. The gravity-induced spreading of the CP solution leads to uniform film thickness from top to bottom; however, there is increasing thickness gradient from the edge to the center as shown in Figure 3.27a and b. As the lower thickness region starts drying earlier, the dried region first gets formed at the boundary and propagates towards the center with velocity \vec{P} . Since the film formation and its evaporation start from the top, there is another drying front in top-to-bottom direction moving with velocity \vec{Q} . The contributions of these two vectors lead to a resultant drying front with velocity \vec{R} , hence the drying front is not completely perpendicular to the flow direction but exhibits a slight downward inclination (see Figure 3.27d).

The direction of the drying front dictates the direction of parallel cracks, which should be in the same direction for maximum stress release. [132, 2] The time progress of parallel crack formation is illustrated in schematic Figure 3.27c. By visual inspection, three regions can be identified: (1) cracked region (CR), (2) drying front (DF) and (3) wet region (WR); with the progress of time, the wet region dries up and its drying front followed by parallel cracks moves toward the center. Two similar drying fronts start moving from the opposite edges towards the center and meet approximately

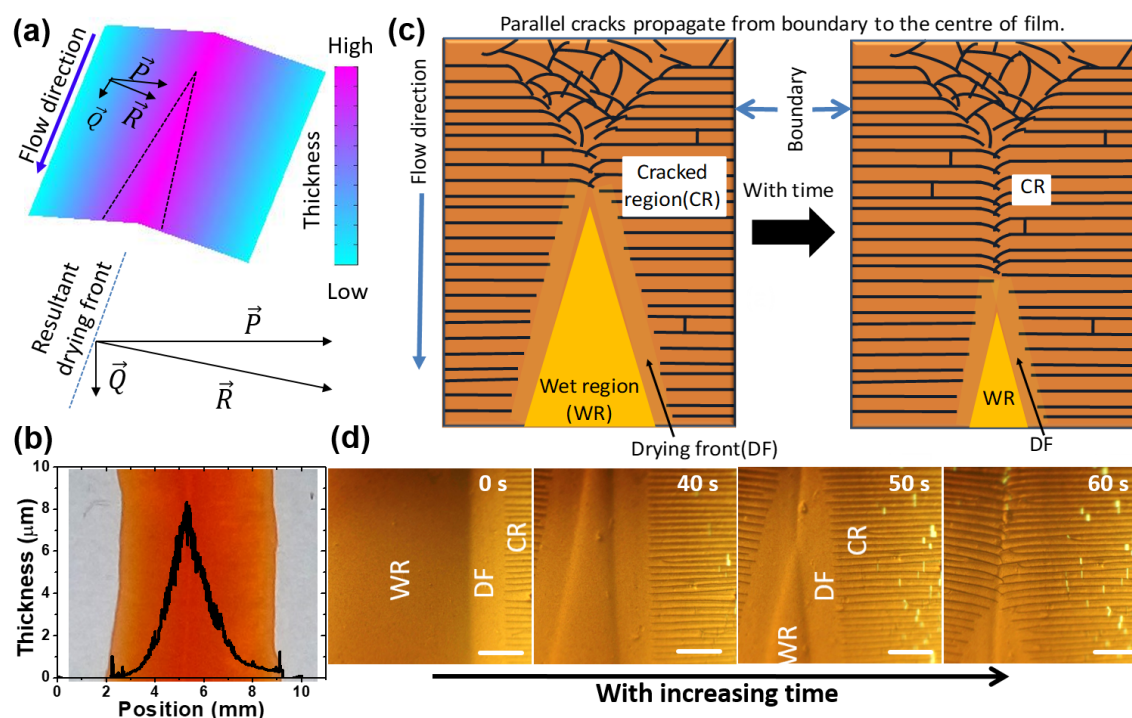


Fig. 3.27 (a) Schematic showing the thickness gradient of the film and vectors of drying front velocities which control the resultant crack direction. Here \vec{P} and \vec{Q} are the velocities of the drying front, from boundary to the center and from top to bottom, respectively and \vec{R} , the resultant velocity = $\vec{P} + \vec{Q}$. (b) Stylus thickness measurements of the film shown in the background depict that there is a thickness gradient from the edge to the center. (c) Schematic representing the time progress of parallel crack formation. Cracks move parallelly while being perpendicular to the drying front to converge at the center. (d) Optical microscopy images of the crack formation process recorded since the drying process began. (Scale bar $200 \mu\text{m}$)

at the center of the film leading to the formation of cracks intersection named as backbone formed by scattered cracks as shown in Figure 3.27d. Crack patterns showed self-improvement to become more periodic with propagation by rearrangement of cracks path. As shown in Figure 3.28, the periodicity of the crack pattern is not much affected by the defects in the film, as cracks slow down on the defects and move with faster speed after it to match the speed of neighbouring cracks. The parallel crack formation is sensitive to the drying temperature as one may expect (see Figure 3.29). To achieve the desired temperature, the glass substrate was kept at the required temperature on a hot plate. The hot plate was further inclined to achieve desired

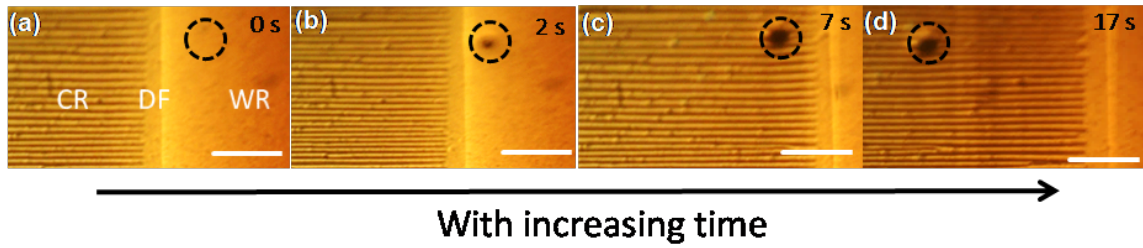


Fig. 3.28 (a)-(d) Optical images showing the effect of defects on crack propagation. The black circle represents a defect. The periodicity of the crack pattern is not much affected by the defects in the film, as cracks slow down on the defects and move with faster speed after it to match the speed of neighbouring cracks. Note: a shift in the microscope field of view in (d). (Scale bar $200 \mu\text{m}$)

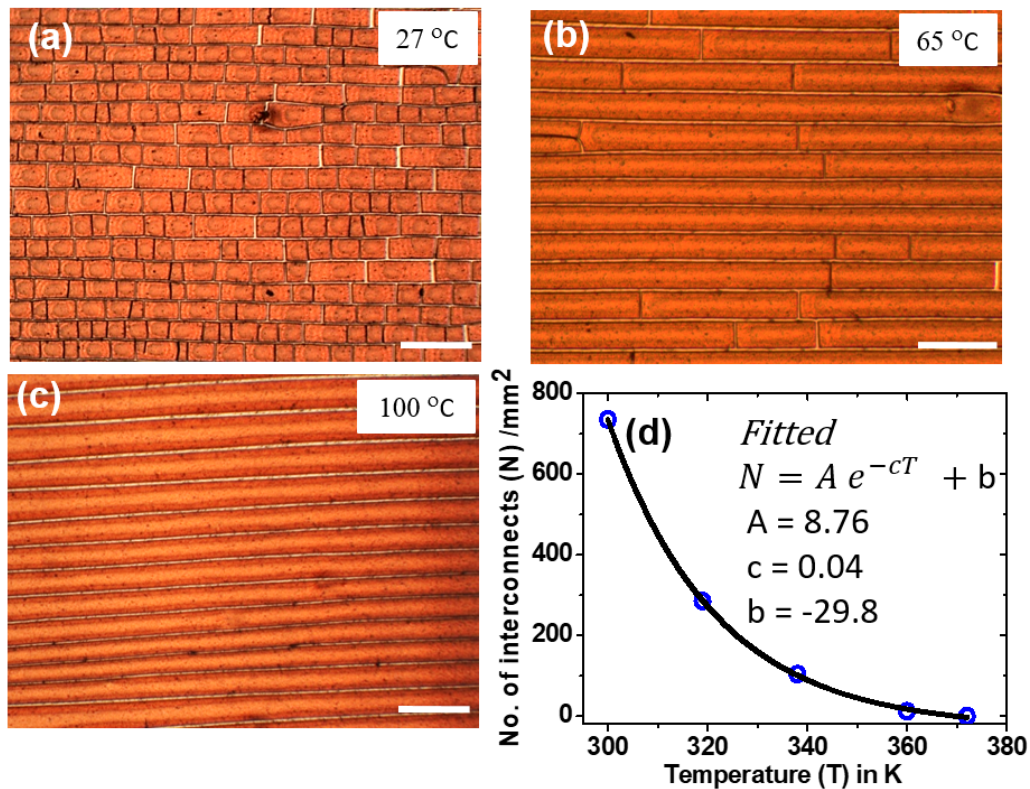


Fig. 3.29 Optical images of parallel cracks at different drying temperatures. (a) Drying at room temperature. The short perpendicular interconnects lead to brick-wall like appearance. Drying at (b) $65 \text{ }^\circ\text{C}$ and (c) $100 \text{ }^\circ\text{C}$. (d) Variation of the number of perpendicular interconnects with respect to drying temperature. (Scale bar $100 \mu\text{m}$)

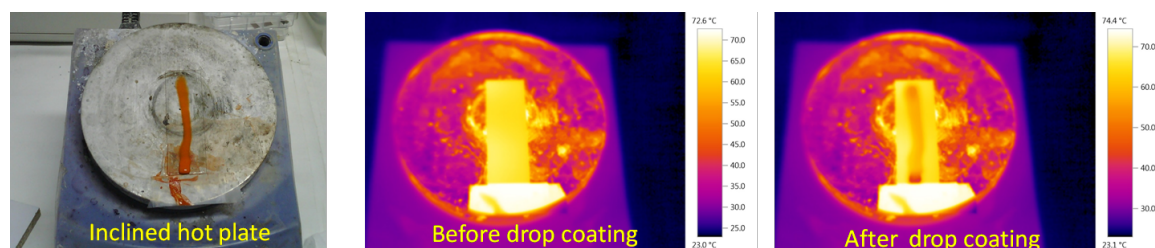


Fig. 3.30 Experimental setup of preparing cracks at higher temperatures. The hot plate was inclined at certain angle and temperature of hot plate was maintained at desired temperature.

gravity flow required for the experiment. The temperature was confirmed to be uniform and constant during the experiment by IR camera imaging shown in Figure 3.30. It is found that after drying the film at room temperature, many short perpendicular interconnects get formed giving the appearance of a brick wall for the dried film. As drying progresses, the parallel crack formation is seen much ahead of the perpendicular interconnect formation as though the latter appears to release the residual stress left behind the primary crack formation. At room temperature, this is quite possible as drying is rather slow (see Figure 3.29a). With the solvent evaporation being faster at higher drying temperatures, the perpendicular interconnects are seen less and less as expected, to an extent that at 80 °C, we hardly came across any perpendicular interconnect throughout the film (see Figure 3.29b and c). Accordingly, the number of perpendicular interconnects vary exponentially with the temperature as shown in Figure 3.29d, which has much to do with the release of residual stress following the parallel crack formation. The perpendicular interconnect formation may be due to the release of stress created from the residual water evaporation after the primary crack formation. [57] Thus, the number of perpendicular interconnects may be directly proportional to the residual water concentration in the film. As the residual water concentration exponentially decreases with the increasing temperature, the number of perpendicular interconnects also decreases exponentially with the temperature. Thus, the study reflects that the drying temperature can be utilized as a mean to

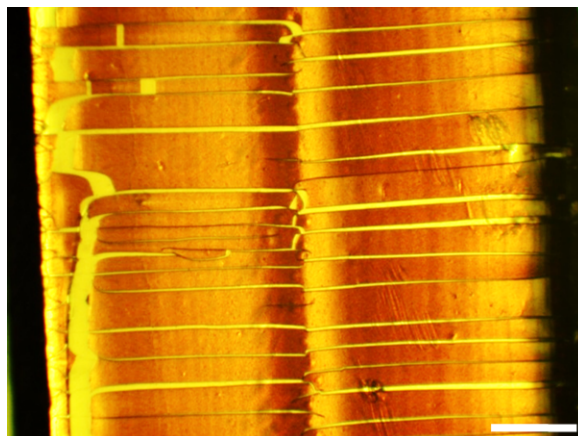


Fig. 3.31 Optical image of cracks with no downward inclination at the center (backbone) as CP flow was confined on a narrow strip of PET (scale bar 200 μm).

obtain cracks with perpendicular interconnects or completely parallel, based on the application.

One may consider many special cases for the better understating of the parallel crack formation. As the parallel crack formation requires finite separation between the drying fronts, a substrate with narrow width would impose confinement on the drying fronts thereby influencing the crack trajectory. This aspect was experimentally examined by the confined CP flow to form a narrow film on a PET substrate of width 0.1 cm and length 6 cm. In a film with negligible width, the contribution of \vec{Q} (Figure 3.27a) is negligible as compared to \vec{P} which leads to cracks with no downward inclination as shown in Figure 3.31. To validate the influence of thickness gradient in the formation of parallel cracks, we deliberately inhibited the outward spreading of CP solution by sticking scotch tape to define the boundary as shown in Figure 3.32. This leads to the absence of film thickness gradient at the scotch tape side resulting in the formation of random cracks rather than parallel cracks, implying that the thickness gradient due to natural spreading is important for parallel crack formation.

A suitable CP solvent is also essential in deciding the film thickness gradient. To verify it, we tried water-IPA mixtures as a solvent instead of only water. Since such mixtures tend to have higher evaporation rates and good wettability, a thickness gradient was not observed in the obtained film. As expected, random cracks rather

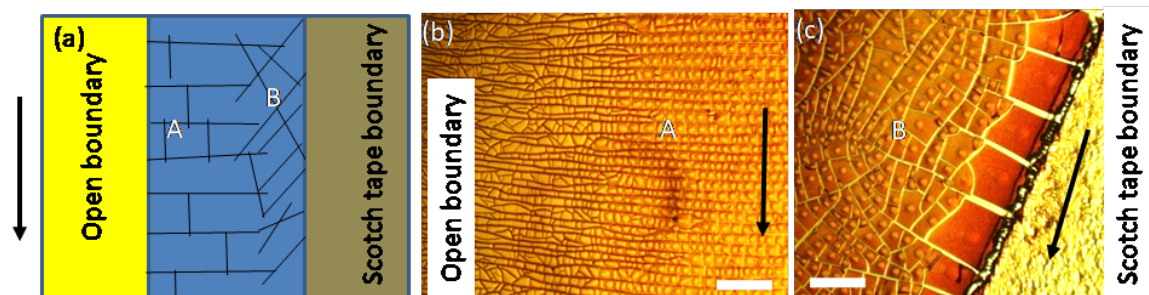


Fig. 3.32 (a) Schematic showing the film with a random crack at the scotch tape boundary side and parallel cracks at the open boundary side. (b) and (c) is the optical images of crack at the open boundary and scotch tape boundary side respectively. The absence of film thickness gradient at the scotch tape side results in the formation of random cracks rather than parallel cracks. (scale bar $200\ \mu\text{m}$). Arrow represents the direction of gravity flow.



Fig. 3.33 Optical image of cracks formed by using water-IPA mixtures as a solvent instead of only water. Since such mixtures tend to have higher evaporation rates and good wettability, a thickness gradient was not observed in the obtained film. As expected, random cracks rather than parallel cracks were observed to be formed (scale bar $100\ \mu\text{m}$)

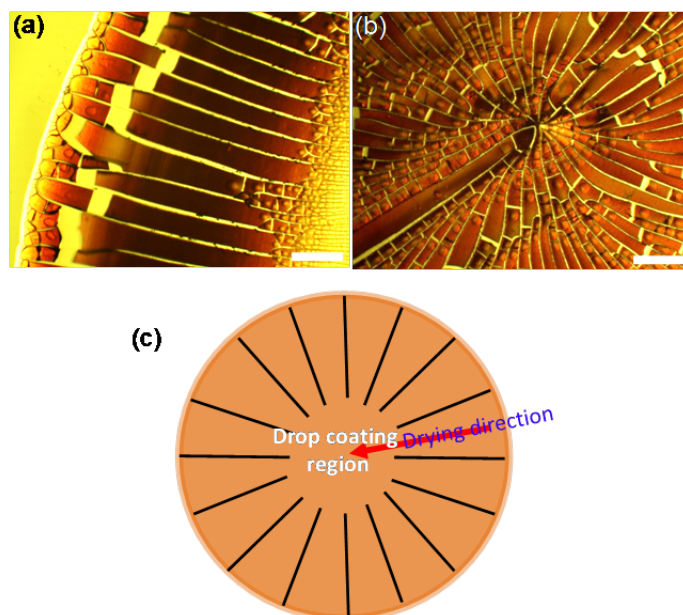


Fig. 3.34 Optical images of radial cracks at the (a) edge and (b) center respectively (scale bar $200\ \mu\text{m}$). (c) schematic of radial cracks propagating towards center

than parallel cracks were observed to be formed, bringing out the importance of solvent gradient (see Figure 3.33). The thickness gradient can be controlled in many other ways to obtain desired crack patterns. As an example, a drop of CP solution was coated on a glass substrate to create a circular film having thickness gradient in the radial direction. The thickness gradient leads to a drying front moving from periphery of the circle to the center resulting in radially inward cracks as shown in the Figure 3.34.

The gravity flow exploited in this work has played an important role in obtaining uniform colloidal film ($< 20\ \mu\text{m}$) with crack widths down to $\approx 4\ \mu\text{m}$ which is not easily realizable by simply drop coating as it invariably leads to non-uniform high film thicknesses ($>100\ \mu\text{m}$) producing wider cracks ($>100\ \mu\text{m}$). Any external aid such as spin coating is incapable of controlling the shape of the drying front leading to a random crack formation. The novelty of the present work is that it not only makes use of a natural resource (gravity) aiding another natural process namely drying but also brings in a fine control on the crack formation. The projected technique in this work for fabricating parallel crack pattern can be utilized in creating masks for lithography

purposes in the field of optoelectronics, photonics, microfluidics, sensors etc. as many such applications require periodic patterns. Future work should address the large-scale patterning of parallel cracks and its utilization for the applications mentioned above.

3.4.4 Conclusion

In summary, a simple, instrument-free and scalable technique has been employed to produce parallel crack pattern using film thickness gradient formed under gravity flow of a colloidal dispersion. The detailed mechanism of parallel crack formation has been explored. The experimental parameters have been optimized to control periodicity, crack width and perpendicular interconnects. Thus, obtained parallel cracks can act as a sacrificial template for obtaining a parallel metal grating structure which has potential applications in optoelectronic devices.

Chapter 4

Thermal transport properties of metal networks

4.1 Microscopic evaluation of electrical and thermal conduction in metal wire networks

4.1.1 Introduction

Transparent and flexible conducting films are essential for modern devices such as touch screens, solar cells, organic light emitting diodes, and transparent heaters. [109] In particular, transparent heaters [167, 17] play an important role in defogging and defrosting of display panels, windows of automobiles, and lenses of optical instruments. Further, the combination of optical transparency and controlled application of heat are essential for devices requiring uniform operating temperatures such as transparent heated stages, transparent sensors, and LCD displays. Transparent heaters use Joule heating to control temperature; thus, the films should have high optical transmittance and low sheet resistance simultaneously. Several types of transparent heaters have been recently developed including periodic metal meshes, [37, 95, 86, 153] CNTs, [69] graphene [7] metal nanowires, [18] transparent and hybrid networks [95, 70, 79, 80] deposited on transparent and flexible substrates. In such systems, the open space between the conductive network is transparent, while the network itself, which facilitates the Joule heating, may be opaque. For those heaters fabricated from deposited nanowires (NWs), high junction (or contact) resistances, as well as non-uniform density or distribution of the NWs, results in non-uniform temperatures (i.e., hot spots) that are detrimental to performance. Template-based metallic wire networks have been developed using techniques such as electro-spinning, leaf venation architectures, and nano-trough or crackle templates. [54, 174, 173] The excellent electrical and thermal conductivities of these continuous metal wire networks with negligible junction effects, complete connectivity, and tuneable metal thickness make them particularly suitable for transparent heater applications. Thus, it is unlike a conventional nanowire-based network, and ultimately demonstrates lower sheet resistance and high transmittance. Furthermore, the fabrication methods for these networks are highly scalable using

industrial techniques such as roll coating, [85] rod coating and spray coating and result in highly robust, flexible, transparent heaters that are stable under harsh oxidation conditions. An efficient wire network should achieve a uniform operating temperature with a fast response time, low operating voltage, and sufficiently high operating temperature for the desired application. Such networks find great to use as heaters in small-sized micro-electromechanical systems (MEMS), lab on chip (LoC), heatable textiles, [27] smart sensors, and bio-medical devices. [176] Microheaters are also utilized in microfluidic channels for chemical reactions as well as localized heating applications. [116, 25] Usually, the device size is of the order of few hundred microns for heating in multiple temperature zones. For example, DNA amplification in micro scale polymerase chain reaction (PCR) devices can be performed on a single chip with different temperatures by Joule heating of such networks. [75] The thermal response of transparent heater networks has predominantly been studied by non-contact methods such as infrared (IR) thermography. [184, 66] The spatial and temporal resolutions of such cameras limit the measurement to local average temperatures. However, many projected applications of transparent heaters such as temperature-dependent spectroscopy and studies of reactions on heater stages require knowledge of the local temperature profile with precise spatial and temporal resolution. [167] For accurate local temperatures, the wire width must be larger than the spatial resolution of the imaging system. The performance of transparent heaters is usually measured using IR camera which enables local variations of temperatures at a nominal resolution of ≈ 1 mm, much longer than the wire width. In this context, an infrared thermal microscopy is a powerful tool for studying local temperatures with high spatial resolution. Using a typical liquid nitrogen cooled Mid-Wavelength IR (MWIR) microscope, a spatial resolution of $1.6 \mu\text{m}$ is achievable at the diffraction limit. [62] Such a tool has been deployed in a variety of applications including measuring the thermal conductivity of vertically aligned CNTs, [119] Joule and heating effects on solder joints. [20].

4.1.2 Scope of the present investigations

Here, the first measurements of local, transient temperature profiles in a flexible, transparent conducting heater is demonstrated. This work focuses on the thermal response of metallic wire networks formed by a crack template method with wire widths ranging from 2 to 100 μm . First, the thermal, electrical, and optical properties are analyzed theoretically in terms of measurable and controllable geometrical and material priorities to provide insight into the design of the transparent heater network. Then, the spatially and temporally resolved temperature distributions in the metal and the substrate are measured experimentally using an infrared microscope. Finally, a theoretical model of the thermal response is developed, which agrees well with experimental results. The IR microscopy is also explored to understand breakdown of the network.

4.1.3 Results and Discussion

Characteristics of metal network heaters

The transparent heater is characterized by its maximum allowable temperature, dissipation losses, a response time for temperature saturation, and power density. The steady state temperature of a heater is achieved when its collective dissipation losses (convection and radiation to surrounding) equals its input Joule heating energy. The steady state rise in the temperature based on power balance can be written as described by Coleman et al. [158] as

$$\Delta T = \frac{V^2}{Rh_{eff}ab} = \frac{V^2}{R_{sn}h_{eff}a^2} \quad (4.1)$$

Here, V is the applied voltage, R and R_{sn} are the resistance and sheet resistance of network of size $a \times b$ (with a in the direction of the field and b along perpendicular direction of the field as shown in Figure 4.1d), and h_{eff} is the effective heat transfer coefficient considering convection and radiation losses to the surroundings that can be

written approximately for low temperature rise as[158]:

$$h_{eff} = (h_t + h_b) + 4(\epsilon_t + \epsilon_b)T_0^3 \quad (4.2)$$

Here, h_t and h_b represent the convection heat transfer coefficients and ϵ_t and ϵ_b are the emissivities of the top and bottom surfaces of substrate, respectively. Here, $h_t = (1 - f)h_{sub} + fh_{metal}$, $h_b = h_{sub}$, $\epsilon_t = (1 - f)\epsilon_{sub} + f\epsilon_{metal}$, and $\epsilon_b = \epsilon_{sub}$. Note that h_{sub} and h_{metal} are the convection heat transfer coefficients and ϵ_{sub} and ϵ_{metal} are the emissivity of the substrate and the metal, respectively. The net heat transfer coefficient can also be written in terms of a two-dimensional metal fill factor, f , as [158] :

$$h_{eff} = 2h_{sub} + 4\epsilon_{sub}T_0^3 - f(h_{sub} - h_{metal}) - 4fT_0^3(\epsilon_{sub} - \epsilon_{metal}). \quad (4.3)$$

The sheet resistance of this type of network is obtained by us using geometrical approach as shown in section 2.1 as following:

$$R_{sn} = \frac{\pi}{2} \frac{\rho}{wt\sqrt{N_E}} \quad (4.4)$$

Here ρ is the resistivity of the metal, w is the wire width, t is film thickness, and N_E is the edge density of the network (i.e., the number of wire segments per unit area). Note that sheet resistance of a continuous film is $R_s = \frac{\rho}{t}$. Thus, in other words, the effective thickness of a network (t_{eff}) is reduced from t to $t_{eff} = \frac{2}{\pi}wt\sqrt{N_E}$ for a network with $R_{sn} = \frac{\rho}{t_{eff}}$. The sheet resistance as derived by us in section 2.1 can also be evaluated as a function of metal fill factor(f) and other geometric parameters as:

$$R_{sn} = \frac{\pi}{2} \frac{\rho}{t} \frac{1}{\beta f} \sqrt{\frac{P_{cell}^2}{2A_{cell}}} \frac{1}{\sqrt{n_s}} \quad (4.5)$$

where β is the fraction of wires in the current carrying backbone (removing isolated and dangling edges), P_{cell} is the mean perimeter of the cell, A_{cell} is the mean area of each polygonal cell, and n_s is an average number of sides of the polygonal cells.

Combining Eq. (4.1) and Eq. (4.4), the estimated average temperature rise of the heater (considering both the wired network and the substrate), ΔT is

$$\Delta T = \frac{V^2}{h_{eff} a^2} \frac{2}{\pi} \frac{wt \sqrt{N_E}}{\rho} \quad (4.6)$$

It can also be written in terms of fill factor as

$$\Delta T = \frac{V^2}{h_{eff} a^2} \frac{2}{\pi} \frac{t}{\rho} \sqrt{\frac{2A_{cell}}{P_{cell}^2}} \beta \sqrt{n_s} f \quad (4.7)$$

These relationships illustrate that the maximum temperature rise is obtained at high voltages, wide wire widths, thick metal film, and for an edge density with a minimum material resistivity at the constant voltage. Importantly, these equations enable estimation of sheet resistance, temperature and thermal properties of a sample using only its template image before metallization, electrical measurement, and IR imaging assuming that the processing is performed free of defects. However, in addition to the thermal performance, a transparent heater also requires high optical transmittance, T_R , which is achieved by minimizing the fill factor, f , described by Bergin et al. [12] as

$$T_R = 1 - \eta f \quad (4.8)$$

where η is a parameter that depends mostly on metal film thickness and the wavelength of light. Thus, a trade-off exists between optical transmittance and thermal characteristics. An increase in the metal fill factor raises the maximum achievable temperature range but decreases the transmittance concomitantly. The fill factor needs to be optimized in order to achieve an ideal balance for a given application. A heater network must possess low wire widths and wire spacings, high interconnectivity, and large film thicknesses. For meeting such requirements, crack templates with small crack widths, narrow spacing, and high interconnectivity is used in this study. However, the network geometry can be tuned by optimizing conditions for crack formation.

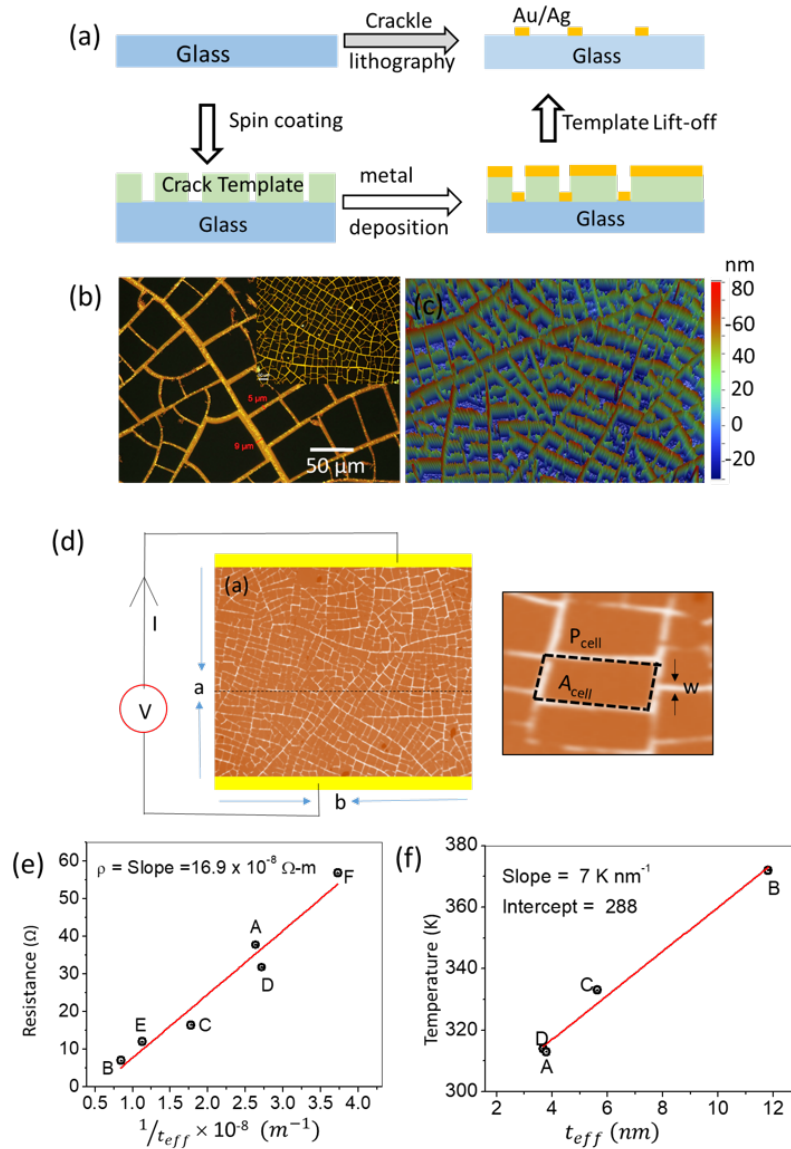


Fig. 4.1 (a) Schematic demonstrating the steps involved in the fabrication of metal networks using crack templating method. Briefly, a crackle precursor is spin-coated resulting in the crack template formation. Au metal is evaporated on the crack template and the latter is then removed by dissolving in a solvent. (b) Optical microscope image of the network at 20X (inset shows 5X image) and the corresponding (c) three-dimensional optical profilometric image of the Au network showing metal wire widths in the range of 2-10 μm and wire spacings of 50-100 μm for the film thickness of 80 nm. (d) Schematic showing the set up for Joule heating of the wire-network of dimensions $a \times b$. The inset shows a magnified image of the crack network illustrating that P_{cell} and A_{cell} are the mean cell perimeter and mean cell area, respectively. N_E is the mean wire segment density (wire segments per unit area), $\sqrt{N_E}$ is the number of wire segments intersected by equipotential line (shown as the dashed black line) and corresponding (e) Variation in the measured resistance with respect to the inverse of effective thickness ($1/t_{eff}$). Each network possesses different geometrical features and, thus, the slope of this curve is the resistivity. (f) Steady state temperature of different networks as a function t_{eff} .

Table 4.1 Approximate geometrical parameters of various Au networks prepared over an area of $2 \times 2 \text{mm}^2$. Network (A-D) are made of quartz and networks (E-F) are made on glass.

Sample No.	w	t	$\sqrt{N_E}$	$\sqrt{N_E}wt$	$R_s(Exp.)$
	μm	nm	per mm	m	Ω/sq
A	9.62	90	20.6	5.95×10^{-9}	37.8
B	8.25	90	25	18.5×10^{-9}	6.94
C	9.62	35	26.25	8.84×10^{-9}	16.4
D	11	30	17.5	5.77×10^{-9}	31.8
E	9.62	90	18.75	13.9×10^{-9}	12.01
F	8.25	20	21.8	4.2×10^{-9}	56.9

Structural and electrical characterization of the micro-heater

The Ag wire network is fabricated on various substrates with the crackle lithography technique shown in Figure 4.1(a). The crackle precursor film forms a network of well-connected channels upon drying. The process of formation can be tuned to produce a desired crack network geometry. The metal mesh based random network is prepared by crack template method. [140] Briefly, a commercially-available crack nail polish (Ming Ni Cosmetics, Co., Guangzhou, China) is mixed with diluter, sonicated for 30 minutes, and spin coated on to polyethylene terephthalate (PET) and glass substrates at 500-2000 rpm for 30-120 s. Upon drying, the coated layer forms a network of well-connected cracks. The metals (Ag and Au) are deposited by physical vapor deposition (PVD) by physical masking and the crack template is removed by dissolving in chloroform leaving behind Au and Ag network on PET/glass substrate. The patterned substrates were examined using an Optical Microscope (Laben, India) and Optical Profilometer. An optimized Ag metal network (shown in Figure 4.1(b)) with wire of widths 2-10 μm and wire spacings of 50 -100 μm on glass was chosen for characterizing the transient heating response. The wires have a metal 2D fill factor, f , of approximately 15% and nearly complete connectivity (Figure 4.1(c)). The network produces a sheet resistance $R_{sn} = 1.5\Omega/sq$, which is lower than networks obtained from CNTs (130-190 Ω/sq) [78]and Ag NWs ($\approx 33 \Omega/sq$). [98] The model discussed above is verified with experimental data collected from six different thin film

network-based heaters (labelled as A-F) of varying wire width, spacing, and thickness (see Table 4.1). The geometric parameters of the six different network heaters and their experimentally obtained sheet resistances and temperature values at an applied voltage of 1.5 V are also given in Table 4.1. The measured resistance of these samples increases approximately linearly with the inverse of the effective thickness ($1/t_{eff}$), as shown in Figure 4.1(e), with an extracted resistivity value of $17 \times 10^{-8} \Omega - m$. This estimated resistivity is close to the bulk resistivity of Au ($2.2 \times 10^{-8} \Omega - m$), [121] thus supporting equation (4.4). The higher resistivity may be due to the non-crystallinity of the physically deposited Au metal. [140] As shown in Figure 4.1(f), the corresponding temperatures of the network heaters increase approximately linearly with t_{eff} in agreement with Equation 4.6. Thus, these results illustrate that the approximate model developed above can be used to estimate sheet resistance and the temperature profile for a given network with known geometric parameters that contribute to the effective thickness, t_{eff} .

The heaters are further examined in detail using IR microscopy (Figure 4.2a,b) at different magnifications. Prior to thermal measurements, a calibration procedure accounts for the spatial variation of emissivity in the sample. Before applying the bias voltage, the radiance emitted from the heater surface at room temperature is measured and compared to that of a blackbody at the same temperature in order to obtain an emissivity map (Figure 4.2c). The metal wires have a lower infrared emissivity compared to the glass/PET substrate, as expected. With 4X magnification ($\approx 5\mu m$ resolution), the wire network is clearly distinguishable, with the substrate having a higher emissivity than the wire. The average emissivity of the Au wire observed by the microscope is 0.42, which is lower than that of the bare PET substrate (0.65). Within the Au wire network, the emissivity is observed to vary, as a secondary wire network of thinner wires seems to have a higher emissivity than the primary network of thicker wires, probably due to the resolution limits ($1.6\mu m$). Further, the measured emissivity of Au is higher than the expected value (> 0.1), likely due to contributions from the substrate or residual crackle precursor on Au during lift-off. After emissivity

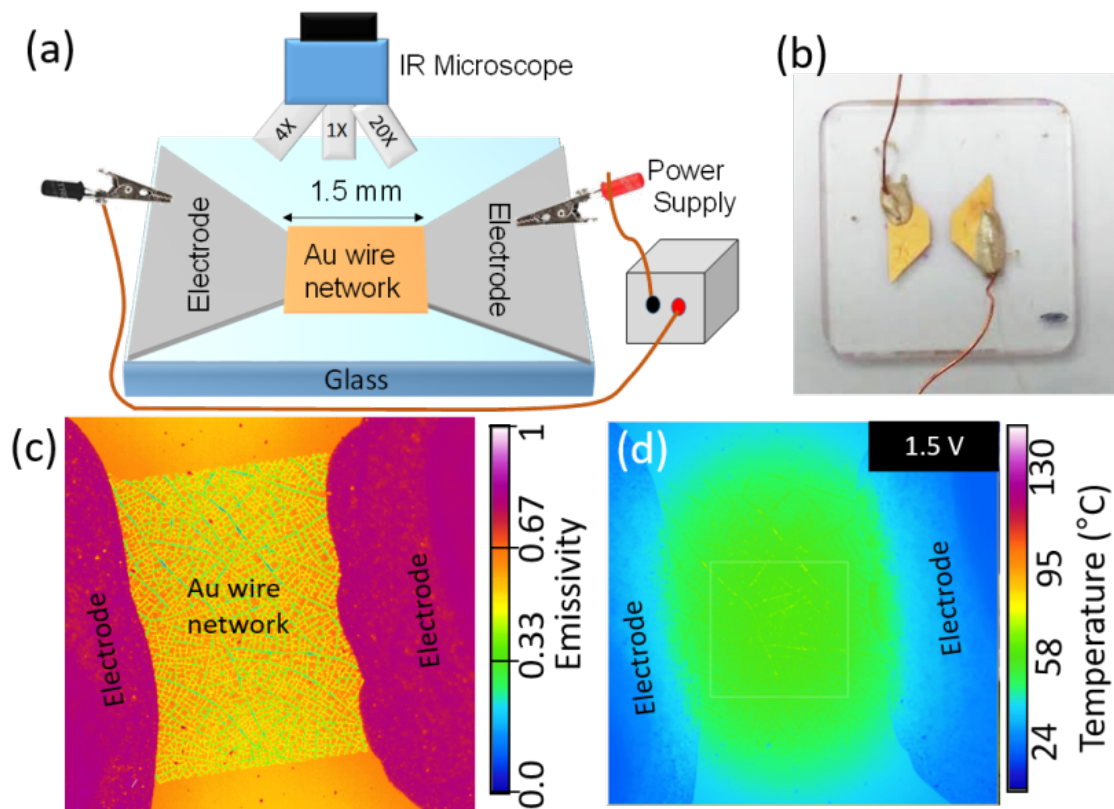


Fig. 4.2 (a) Experimental set-up for infrared thermal imaging consisting of the Au metal wire network ($1.5 \text{ mm} \times 1 \text{ mm}$ area) connected to a power supply and placed under the IR microscope for imaging. (b) Optical image of a typical Au metal wire network on glass used for thermal analysis. (c) Typical emissivity map as obtained by the calibration step. (d) Thermal map of the Au wire network at an applied voltage of 1.5 V at $1 \times$ resolution.

calibration, thermal images were obtained during Joule heating. The 4X magnification thermal image in Figure 4.2d shows the temperature distribution with a maximum temperature of $60 \pm 0.5 \text{ }^\circ\text{C}$ at the middle of the network and a minimum temperature ($25 \pm 0.5 \text{ }^\circ\text{C}$) at the contacts under an applied voltage of 1.5 V. Note that from these large-area images, the temperatures in the middle region of the heater and some thicker wires are higher than those at the periphery. Clearly, the microscopic details of heat transport can be observed by thermal imaging only at a higher resolution.

The wire-substrate thermal profile is probed by measuring the emissivity and temperature distributions via imaging at 20X magnification (Figure 4.3a). The

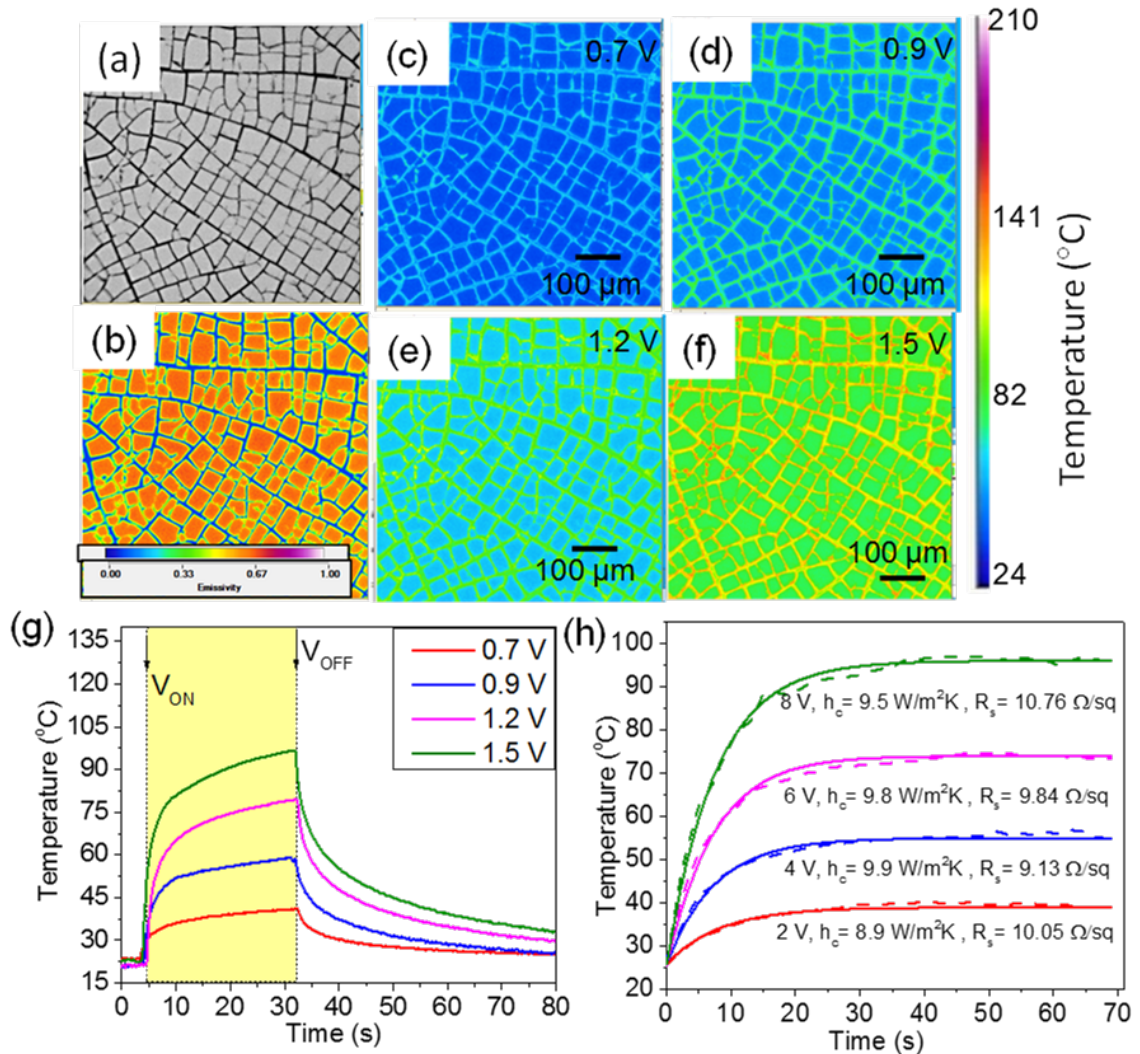


Fig. 4.3 (a) Infrared radiance image, (b) emissivity map, and the corresponding infrared thermal maps of Au/PET at (c) 0.7, (d) 0.9, (e) 1.0 and (f) 1.2 V, respectively. Note that at 20X magnification with the $1.6 \mu\text{m}$ resolution, the temperature distribution in the metal network is well resolved. (g) The average rise in the temperature of Au/PET heater with time from the data shown in c-f. The bias voltage is applied from ≈ 5 s to 33 s, after which the voltage is turned off and the films cool. A clear saturation in temperature was not seen, which means that the device did not reach steady state within the first ≈ 30 s. (h) Temperature profiles from another Au/PET sample with a resistance of 7Ω at applied voltages of 2, 4, 6 and 8 V fitted using the approximate lumped capacitance model (dashed lines) with the label indicating the fitted convection coefficient (h_c) and fitted theoretical sheet resistance values (R_s). This sample reaches steady state within ≈ 30 s of heating.

emissivity map in Figure 4.3b displays regions of high and low emissivities corresponding to PET and Ag respectively. At higher magnification of 20X, metals display lower emissivity (≈ 0.1) than that observed at 4X as evident from the blue color of the emissivity map (Figure 4.3b). The applied voltage is ramped up gradually through the Au wire network until the current increased linearly without significant change in resistance. Thermal maps are acquired at 0.5 s intervals until the steady state temperature is obtained at the final applied voltage. Figure 4.3c-f shows a steady state temperature map of the Au wire network/PET at different applied voltages. Note that the wire temperatures are slightly higher than of the substrate, even at steady state. Given that the time gap between the two frames is 0.5 s and that the temperature equilibrates at a much faster rate, the transient information related to local heat diffusion could not be obtained. Steady state is achieved at the time when conductive, convective, and radiative heat losses from the sample are balanced by the Joule heating (Figure 4.3g). The dynamics of temperature change in the heater (average of wire and substrate temperature) are studied with a lumped capacitance model [13]:

$$(m_{metal}C_{metal} + m_{sub}C_{sub})\frac{dT_h}{dt} = Q_{joule} - Ah_{conv}(T_h - T_{amb}) - \epsilon_{sub}A_{sub}(T_h^4 - T_{amb}^4) - \epsilon_{metal}A_{nw}(T_h^4 - T_{amb}^4) \quad (4.9)$$

where m_{metal} and C_{metal} are the mass and specific heat of the metal (Ag) forming the wire network, m_{sub} and C_{sub} are the mass and specific heat of the substrate (PET), T_h and T_{amb} are the heater and ambient temperatures, Q_{joule} is the Joule heating given by $\frac{V^2}{R}$, and h_{conv} the convective heat transfer coefficient. The emissivities are extracted from the infrared calibration procedure as $\epsilon_{sub} = 0.7$ and $\epsilon_{metal} = 0.07$. Thus, the radiative heat losses from the metal wires are smaller than those from the PET substrate. Note that the sensor measures the emissivity in the mid-wavelength infrared regime, and here we assume this emissivity applies across all wavelengths.

Here, Q_{joule} and h_{conv} are fitting parameters used to match the simulated temperature profiles to the experimental curve shown in Figure 4.3h. The temperature according to the lumped capacitance model depends on thermal mass and heat losses (radiation and convection losses. The substrate radiative losses dominate compared to the radiative heat losses from the Au wire network. The Joule heating rate, Q_{joule} , is extracted from fitting the experimental data resulting in an effective sheet resistance of $\approx 10 \Omega/sq$ (see Figure 4.3h). This value is slightly higher than the measured sheet resistance of $7 \Omega/sq$, but the lumped capacitance model is approximate as it neglects thermal contact resistance, considers temperature throughout the elements to be uniform, and does not consider thermal losses to the contacts.

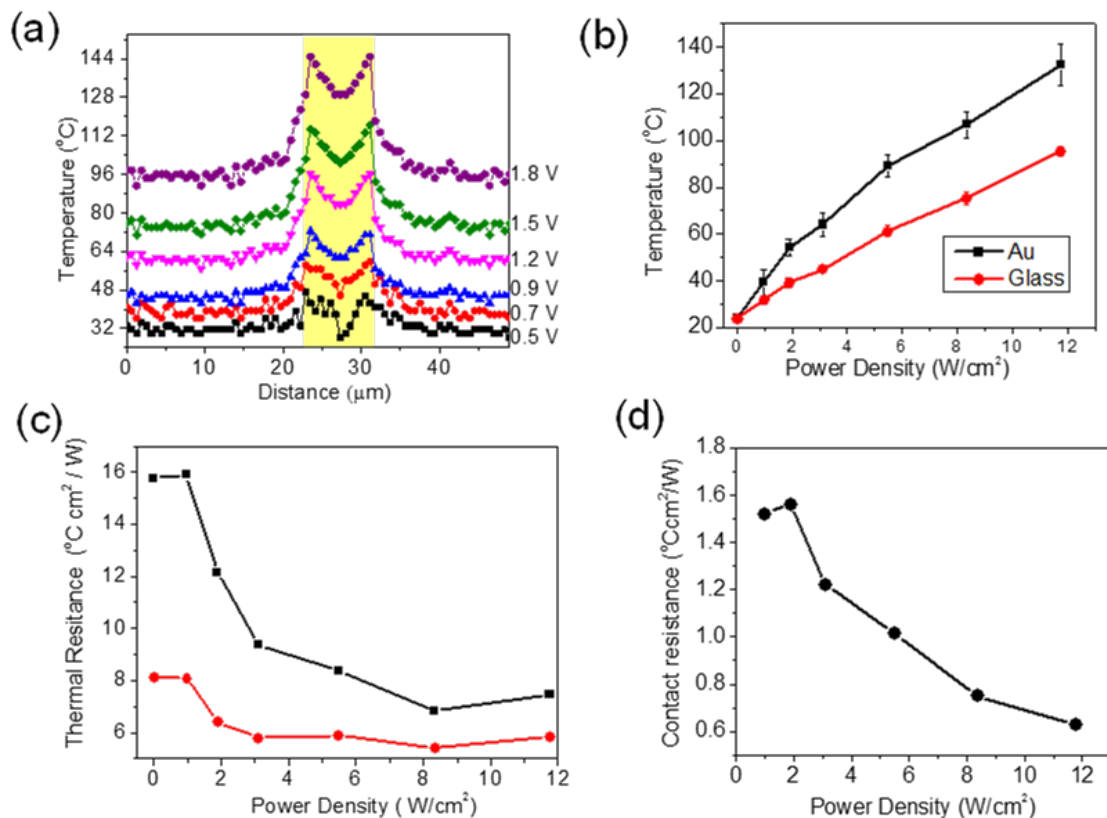


Fig. 4.4 (a) Temperature distribution across a wire on PET substrate at different power densities. Here, the yellow shaded area represents the region with the wire, while the unshaded region represents the bare PET substrate. (b) Variations of the temperature of wire and the PET substrate with power density with error bars corresponding to measurements from 10 different wires.

An example temperature profile across the metal and the substrate (in the direction perpendicular to the wire axis) from the high-resolution thermal images at different voltages is shown in Figure 4.4a. The temperature in the center region of the metal wire is relatively lower than at the edges of the substrate. Hereafter, the temperature of the wire surface, T_{metal} , is measured from the center of the wire, and the temperature of the substrate, T_{sub} , is measured 20 μm away from the wire. The temperature difference between metal and the substrate increases with applied power, P , (see Figure 4.4(b)) indicating that there is a thermal resistance between the metal network and the glass substrate. The higher temperature at the edge of wire is likely an artefact due to a pixel having combined emissivity value of Ag and PET. From the temperature difference, the effective thermal resistance for wire and the substrate to the environment are calculated separately from the derivative of the temperature difference with power dT_{metal}/dP and dT_{sub}/dP and are shown in Figure 4.4(c). These resistances represent the temperature rise per applied power for the two components in the system. The thermal resistances decrease with power density, which is a reflection of the increase in heat loss coefficient with temperature. The value of effective heat transfer coefficient, h_{eff} , is calculated using $dT/dP = 1/h_{eff} \approx 0.15W/cm^2/K$. The temperature of wire network is higher than that of the substrate, likely due to the contact resistance between the wires and the substrate, which is also illustrated by the large temperature drop across the interface of Au wire and the substrate. The thermal contact resistance, $R_{t,c}$, is calculated from $R_{t,c} = \frac{T_{Au} - T_{glass}Af}{P}$ where P is the power and A is the total 2D area of the metal network and f is the fill factor (see Figure 4.4(d)). The existence of the finite contact resistance ($0.6 - 1.8W/cm^2/K$) is principally due to surface roughness effects possibly due to surface contamination from the crackle precursor. The contact resistance can be further reduced by surface treatment of substrate and tune the metal deposition conditions.

Another important parameter for transparent electrodes is the stability against high current density. A wire network may breakdown if its current density is higher

than a particular critical value $J_c (J_{avg} < J_c)$. The average current density of a wire network [92], J_{avg} , may be expressed in terms of electric field, E as:

$$J_{avg} = I_{avg}/A = \frac{2Ewt}{\pi\rho} = \frac{2}{\pi\rho} \frac{V}{h_{eff}} \quad (4.10)$$

The maximum critical temperature, T_c of the metal wire network can be deduced in terms of a critical voltage, V_c using Eq. 4.6 for temperature rise as:

$$T_c = T_0 + \frac{V_c^2}{h_{eff}a^2} \frac{2}{\pi} \frac{wt\sqrt{N_E}}{\rho} \quad (4.11)$$

and in terms of current density as

$$T_c = T_0 + \frac{V_c^2}{h_{eff}a^2} J_c^2 \pi \rho bwt \quad (4.12)$$

Thus, the maximum obtainable temperature depends on the critical current density of wires and can be increased with increasing wire width, thickness, and edge density. For a typical sample size of $2 \times 2 \text{ mm}^2$ at a voltage bias of 1 V, the average current density according to the Eq. (4.12) is $2 \times 10^6 \text{ A/cm}^2$.

Finally, infrared microscopy is used to study breakdown of wire network at high current densities. This is useful for locating and identifying the hotspots within the network which lead to the breakdown of the network. As soon as the voltage is applied, the temperature of the wires starts rising, while the bulk of the substrate remains at room temperature (Figure 4.5a). As time progresses, the wire temperature continues to increase and heat from the wire is gradually transferred to substrate thus increasing the overall temperature of the substrate as seen in IR image in Figure 4.5b. With continued heating, hot spots appear in the middle region of the network (Figures 4.5c). Due to the localization of heat, the temperature of the wires in the middle of the network exceeds $200 \text{ }^\circ\text{C}$, while wires at the periphery remain at a temperature below 100°C .

Ultimately, this leads to a lack of current paths in those regions (upper, the central portion of the network as seen in Figure 4.5d and 4.5e) and a reduction in temperature

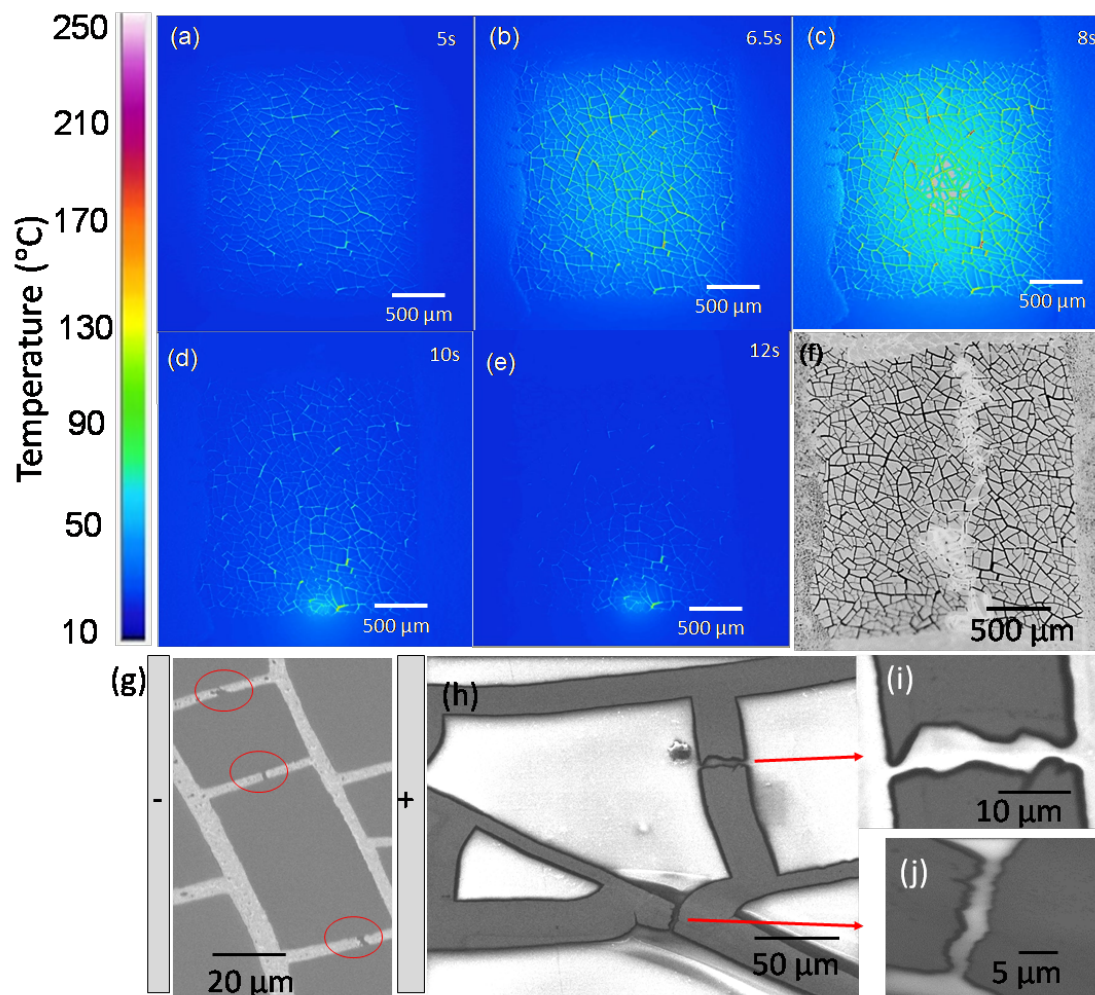


Fig. 4.5 (a-e) Sequential thermal images at different times showing the breakdown of Au wire network on PET at 1.3 V. The temperature of Au wire network increases with time, leading to hotspots, and finally to the breakage of the wire network. Note that in panel c, grey regions near the center of the heater indicate image saturation and are indicative of the hottest spots in the heater network. (f) Infrared radiance image of the unpowered network after breakdown clearly showing the broken wires in the light region near the center of the network. (g) SEM images of the network from the breakdown regions (highlighted by the red circles). (h-i) High magnification optical images showing the breakdown locations.

at these regions. The temperature in the lower region of sample continues to increase due to a higher current density in surviving current paths, but ultimately those portions fail as well. Figure 4.5f indicates the microscopic infrared image of the network after the complete breakdown. As shown, the burnt/broken wires are confined in a region approximately centered between the two electrodes. This is the hottest portion of the network as it is farthest from the heat sinks at the contacts. The current density of the network is expected to be around $2.6 \times 10^6 A/cm^2$ according to Eq. (4.12). Even as the current density redistributes after the wires are initially broken, the central portion remains the hottest. As seen from the SEM images in Figure 4.5g, burnt wire segments are not random, rather a complete strip is burnt. Interestingly, wire segments are typically broken in the center of junctions or near the junctions. The elevated temperature in the center leads to breakage of the network (potentially due to the local melting of thin metal wires or substrate as seen by the opening of gaps in Figure 4.5h and i. The breakage pattern is observed to be similar to that observed in case of CNT based network films. [11]

The study is extended to a network fabricated at larger length scale over a large area using a silica-based crackle precursor as shown in Figure 4.6. The network consists of thicker wires of width (60-80 μm) and wider spacing (300-500 μm), which is 5 times larger than the previous network studied in Figure 4.3. The Ag wire network possesses an average transmission of 78% with a sheet resistance, R_{sn} of $\approx 3.88 \Omega/sq$. Despite different polygon sizes, wire widths and network structure, the temperature of PET in the regions enclosed by the metallic network is found to be uniform, 56 $^{\circ}C$ within an error of 1 $^{\circ}C$ as seen from the statistical average over four different regions. This is because, at steady state, the temperature of the substrate at the middle region only involves convection and conduction losses since the contact pads are much away due to the large size of the film heater.

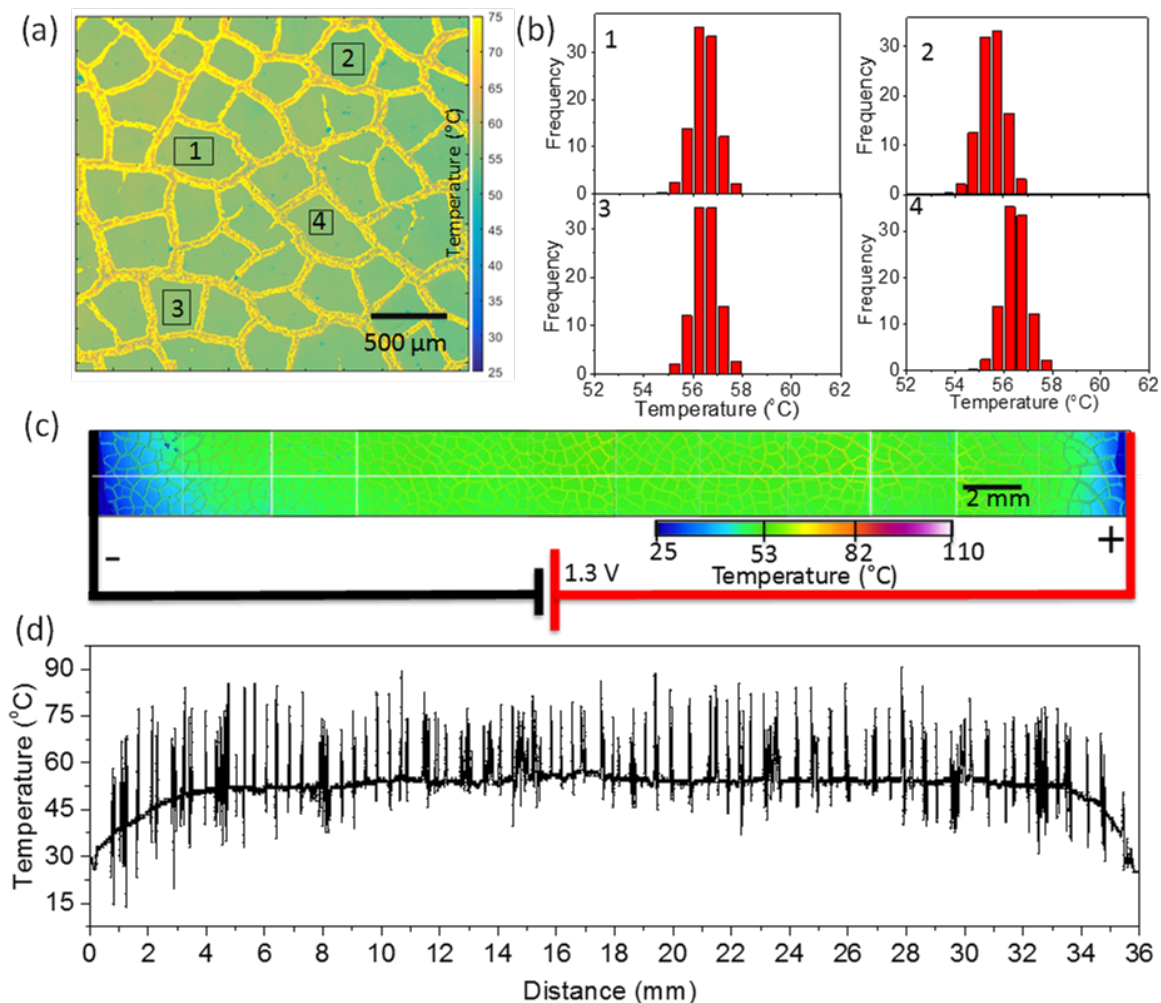


Fig. 4.6 (a) High-resolution thermal map of the wider Ag wire network on PET. (b) Bar-graph representing statistical analysis of the temperature distribution in regions 1, 2, 3, and 4 marked in a. (c) Spatial temperature distribution between the two electrodes measured from twelve consecutive thermal maps at high resolution for the network for 1.3 V applied voltage. (d) Temperature profile across the two electrodes extracted from the combined images in (c). Note that the spikes in the profile correspond to the temperature of the wires in the network while the background at ≈ 56.1 °C represents the substrate temperature.

4.1.4 Conclusion

In this study, infrared thermal microscopy technique has been employed to quantify thermal transport in transparent heaters obtained from randomly conducting wire networks with a wire width of $\approx 2 - 10\mu\text{m}$, wire spacing of 50-100 μm , and thickness of ≈ 80 nm fabricated by a crack template technique. The thermal properties of transparent heaters are predicted based on the network geometry. An important insight obtained is that the competition between geometrical and material properties that results in good thermal response and good optical transmittance in such heater systems leads to a complex optimization process. Interestingly, heaters achieve a uniform temperature throughout the substrate despite the random crack network structure (e.g. unequal sized polygons created by metal wires). The temperature of wires in the network was observed to be significantly higher than the substrate due to contact resistance at the interface between metal and substrate. The thermal resistance between the substrate and wire was observed to be $\approx 1^\circ\text{C cm}^2/\text{W}$. The thermal response was found to be in agreement with the lumped capacitance model of the composite network. Furthermore, breakdown mechanisms within the network were examined by IR microscopy illustrating that breakdown starts at hot spots of the central part and finally network breaks along the nearly central line perpendicular to the field. The outcomes of this work may be applicable to various other kinds of network-based heaters that need not be transparent. Future studies should attempt to minimize the thermal contact resistance by better adhesion or surface treatment to achieve uniform temperature on the metal network and substrate and effect of contact pads should be included in the treatment.

4.2 Transient studies of thermal transport using Green's function

4.2.1 Summary

Emerging candidates of transparent heaters include conducting wire-based networks on a transparent substrate. Here, the network is biased and Joule heated which further transfer heat to the substrate. In many applications, it's important to know the transient behaviour of heatmap of the heater. However, the infrared microscopes used for studying heat transfer have a low temporal resolution as compared to the time scale of the heat transfer process. Thus one needs to rely on theoretical treatment for the same. Here, thermal transient studies of the heater are done by an analytical approach using Green's function solution equations. For the analytical solution, the polygon voids enclosed by wires are approximated with rings, and a network is modelled as a pattern of rings. The study gives the quantitative analysis of heat transfer of this problem and evaluates the response time of heater for uniform temperature.

4.2.2 Introduction

Transparent heaters having the combination of high optical transparency and controlled application of heat are essential for modern devices requiring uniform operating temperatures such as transparent heated stages, transparent sensors, and LCD displays. Transparent heaters use Joule heating to control temperature; thus, the films should have high optical transmittance and low sheet resistance simultaneously. Transparent heaters rely on Joule heating mechanism of heat production for which material should be transparent as well as conducting, a property restricted to few materials like ITO which has various limitations. Emerging candidates of transparent heaters include periodic metal meshes, [37, 95, 86, 153] CNTs, [69] graphene [7] metal nanowires, [18] transparent and hybrid networks [95, 70, 79, 80] deposited on transparent and flexible substrates. In such systems, the void between the conductive network is transparent, while the

network itself is transparent and joule heats. It finds applications in small-sized micro-electromechanical systems (MEMS), lab on chip (LoC), heatable textiles, [27] smart sensors, and bio-medical devices. [176] In many of the cases its important to study the temperature profile with time

Although, most of the industrial heat transfer problems are solved numerically, however, an analytical approach can be much more insightful in explaining physical phenomena. The Green's function solution equation techniques have been widely used in modelling transient heat transfer problems of basic geometries and classical boundary conditions [10] due to their simplicity as compared to other analytical tools such as Laplace transformation, Fourier series, and series summation etc. There have been various efforts in obtaining a solution by Green's function solution equation for various boundary conditions which are tabulated in the treatise of heat transfer books which have been successful in various practical situations. [21] However, the heat transfer problem for an important geometry, a circular ring source has not been understood. Note that the transient heat study of a ring source is an important geometry in various heat transfer scenarios such as modern flexible heaters, which have a conducting polygons acting as a heat source to heat the voids in between them. The experimental techniques can't show transient temperature profile information as the temporal resolution of these instruments is far lower than the time scale of heat transfer of the process. Thus, the only theoretical process can be insightful in this direction. Apart from network-based heaters, most of the joule based heaters have coils which are circular in nature, thus the treatment can be useful in understanding their transient heat profiles as well.

4.2.3 Scope of the present investigations

The present study models the transient temperature profile around a circular heat source. The network-based heaters having variable void sizes enclosed by wires are modelled as multiple ring sources of variable sizes. Thus, the present treatment can be

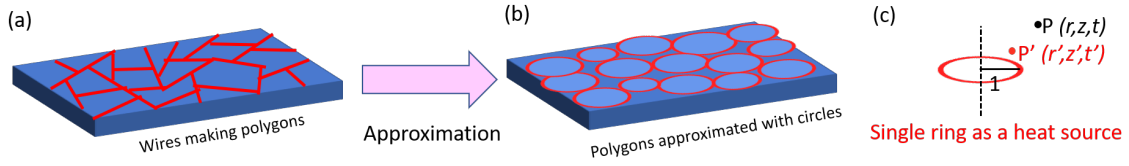


Fig. 4.7 Schematic of (a) wire network based heater on transparent substrate. (b) The polygons are approximated with circles. (c) Finding temperature at P due to heat flux at P' based on Green's function.

used to study temperature profile for the network-based heater and further provides insight into transient heat transfer process.

4.2.4 Results and Discussion

The wire network is modelled as a pattern of circular rings as sources (Figure 4.7). The reason for approximation polygon with a ring is due to the symmetrical structure required for analytical modelling.

Transient study of source of ring in infinite space

Consider a ring of radius a as a source of heat in the infinite space. Consider Initial temperature to be 0K (if initial temperature is T_0 the transient temperature can simply be written as $T_0 + T(r, z, t)$). The transient temperature $T(r, z, t)$ is given by Green's Function solution equation (GFSE). Here, there is no boundary hence the Green function Equations (4.13 -4.15) according to reference G_{R00Z00} [21] are :

$$T(r, z, t) = \frac{\alpha}{k} \int_{\tau=0}^t \int_{r'}^{\infty} \int_{z'}^{\infty} G_{R00Z00} g(r, z, t) 2\pi r' dz' dr' d\tau' \quad (4.13)$$

Here, k is the thermal conductivity, α is thermal diffusivity, $g(r, z, t)$ is the energy generation.

The GF is given by the product of two one dimensional functions, $G_{R00Z00} = (G_{R00})(G_{Z00})$ Here, G_{R00} can be written as

$$G_{R00}(r, t | r', \tau) = \frac{1}{4\pi\alpha(t-\tau)} \exp\left(-\frac{r^2 + r'^2}{4\alpha(t-\tau)}\right) I_0\left[\frac{rr'}{2\alpha(t-\tau)}\right] \quad (4.14)$$

Here, I_0 is modified bessel function of first kind of order zero. and

$$G_{Z00}(z, t | z', \tau) = \frac{1}{\sqrt{4\pi\alpha(t-\tau)}} \exp\left[-\frac{(z-z')^2}{4\alpha(t-\tau)}\right] \quad (4.15)$$

By converting in the Non-Dimension form with new dimensions $t = \alpha t/a^2$, $r = r/a$, $z = z/a$ it can be written as:

Here, G_{R00} can be written as

$$G_{R00}\left(ar, \frac{a^2t}{\alpha} | ar', \frac{a^2\tau}{\alpha}\right) = \frac{1}{4\pi a^2(t-\tau)} \exp\left(-\frac{r^2+r'^2}{4(t-\tau)}\right) I_0\left[\frac{rr'}{2(t-\tau)}\right] \quad (4.16)$$

and

$$G_{Z00}\left(az, \frac{a^2t}{\alpha} | az', \frac{a^2\tau}{\alpha}\right) = \frac{1}{a\sqrt{4\pi(t-\tau)}} \exp\left(-\frac{(z-z')^2}{4(t-\tau)}\right) \quad (4.17)$$

Now, in the present case, ring is a heat source which means

$$g(r, z, t) = q_0 \delta(1-r') \delta(0-z') H(t') \quad (4.18)$$

Here $H(t')$ is the Heaviside Step Function. Substituting value of $g(r, z, t)$ in Eq. 4.13 we obtain :

$$T(r, z, t) = \frac{\alpha}{k} \int_{\tau=0}^t \int_{r'}^{\infty} \int_{z'}^{\infty} G_{R00} G_{Z00} q_0 \delta(1-r') \delta(0-z') H(t') 2\pi a r' a dz' a dr' \frac{a^2}{\alpha} d\tau' \quad (4.19)$$

The transient temperature can be written using shifting property of dirac delta function as:

$$T(r, z, t) = \frac{q_0}{k} \int_{\tau=0}^t \frac{2\pi a^2}{[4\pi(t-\tau)]^{3/2}} \exp\left(-\frac{r^2+z^2+1}{4(t-\tau)}\right) I_0\left[\frac{r}{2(t-\tau)}\right] d\tau \quad (4.20)$$

Modified Bessel Function can be written as series sum as $I_0(x) = \sum_{k=0}^{\infty} \frac{(\frac{1}{4}x^2)^k}{(K!)^2}$. Substituting it we obtain

$$T(r, z, t) = \frac{q_0}{k} \int_{\tau=0}^t \frac{2\pi a^2}{[4\pi(t-\tau)]^{3/2}} \exp\left(-\frac{r^2+z^2+1}{4(t-\tau)}\right) \sum_{k=0}^{\infty} \frac{1}{(k!)^2} \left(\frac{r}{4(t-\tau)}\right)^{2k} d\tau \quad (4.21)$$

$$\frac{T(r, z, t)}{q_0 a^2/k} = \frac{1}{4\sqrt{\pi}} \int_{\tau=0}^t \exp\left(-\frac{r^2+z^2+1}{4(t-\tau)}\right) \sum_{k=0}^{\infty} \frac{r^{2k}}{(k!)^2 4^{2k}} \left(\frac{1}{t-\tau}\right)^{2k+\frac{3}{2}} d\tau \quad (4.22)$$

Using integration result $\int \frac{\exp(-b/x)}{x^n} dx = b^{1-n} \Gamma\left(n-1, \frac{b}{x}\right)$ and using $\Gamma(n, \infty) = 0$. Here, Γ is upper incomplete gamma function defines as $\Gamma(s, x) = \int_x^{\infty} t^{s-1} e^{-t} dt$.

$$\frac{T(r, z, t)}{q_0 a^2/k} = \frac{1}{4\sqrt{\pi}} \sum_{k=0}^{\infty} \frac{r^{2k}}{(k!)^2 4^{2k}} \left(\frac{4}{r^2+z^2+1}\right)^{2k+\frac{1}{2}} \Gamma\left(2k+\frac{1}{2}, \frac{r^2+z^2+1}{4t}\right) \quad (4.23)$$

$$\frac{T(r, z, t)}{q_0 a^2/k} = \frac{1}{2\sqrt{\pi}} \left(\frac{1}{r^2+z^2+1}\right)^{\frac{1}{2}} \sum_{k=0}^{\infty} \frac{1}{(k!)^2} \left(\frac{r}{r^2+z^2+1}\right)^{2k} \Gamma\left(2k+\frac{1}{2}, \frac{r^2+z^2+1}{4t}\right) \quad (4.24)$$

Converting into Regularized Gamma Function defined as $Q(a, z) = \frac{\Gamma(a, z)}{\Gamma(a)}$ [169]

$$\frac{T(r, z, t)}{q_0 a^2/k} = \frac{1}{2\sqrt{\pi}} \sum_{k=0}^{\infty} \frac{r^{2k}}{(k!)^2} \left(\frac{1}{r^2+z^2+1}\right)^{2k+\frac{1}{2}} \Gamma\left(2k+\frac{1}{2}\right) Q\left(2k+\frac{1}{2}, \frac{r^2+z^2+1}{4t}\right) \quad (4.25)$$

Using $\Gamma\left(n+\frac{1}{2}\right) = \frac{(2n)!}{4^n n!} \sqrt{\pi}$.

$$\frac{T(r, z, t)}{q_0 a^2/k} = \frac{1}{2} \left(\frac{1}{r^2+z^2+1}\right)^{\frac{1}{2}} \sum_{k=0}^{\infty} \frac{1}{(k!)^2} \left(\frac{r}{r^2+z^2+1}\right)^{2k} \frac{(4k)!}{4^{2k} (2k)!} Q\left(2k+\frac{1}{2}, \frac{r^2+z^2+1}{4t}\right) \quad (4.26)$$

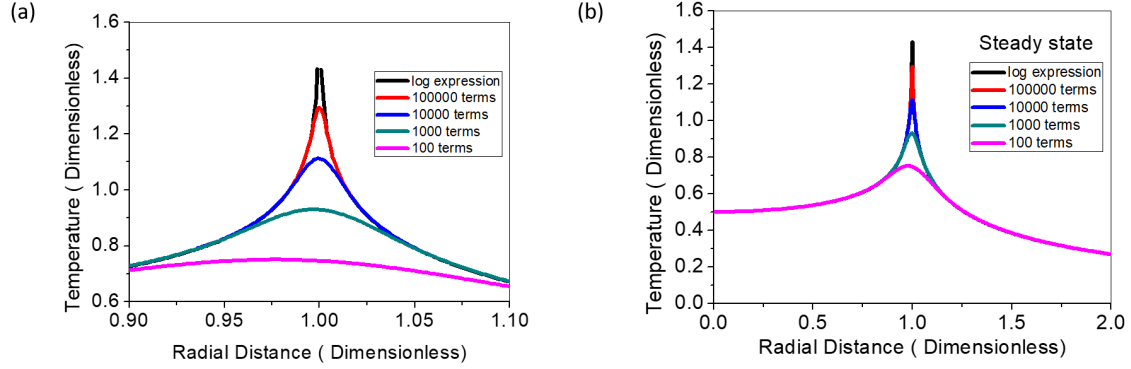


Fig. 4.8 Steady state temperature as a function of radial distance. The calculations are performed based on series summation (Eq. (4.27)) and log expression (Eq. (4.30)). (a) in range 0.9 - 1.1 and (b) 0 - 2. It shows the series summation is slow converging and thus > 100 terms are required to model it accurately near the ring.

Using Stirling's approximation at higher values of k given by $n! \approx \sqrt{2\pi n} \left(\frac{n}{e}\right)^n$

$$\frac{T(r, z, t = \infty)}{q_0 a^2 / k} = \frac{1}{2\sqrt{\pi}} \sum_{k=p}^{\infty} \frac{r^{2k}}{2\pi k \left(\frac{k}{e}\right)^{2k}} \left(\frac{1}{r^2 + z^2 + 1}\right)^{2k + \frac{1}{2}} \frac{\sqrt{8\pi k} \left(\frac{4k}{e}\right)^{4k}}{4^{2k} \sqrt{4\pi k} \left(\frac{2k}{e}\right)^{2k}} \sqrt{\pi} Q\left(2k + \frac{1}{2}, \frac{r^2 + z^2 + 1}{4t}\right) \quad (4.27)$$

$$\frac{T(r, z, t = \infty)}{q_0 a^2 / k} = \frac{1}{2} \left(\frac{1}{r^2 + z^2 + 1}\right)^{\frac{1}{2}} \left[1 + \sum_{k=1}^{\infty} \left(\frac{1}{\sqrt{2\pi k}} \left(\frac{2r}{r^2 + z^2 + 1}\right)^{2k}\right) + E\right] Q\left(2k + \frac{1}{2}, \frac{r^2 + z^2 + 1}{4t}\right) \quad (4.28)$$

Here E is the term due to error in approximation of Stirling's approximation at lower value of k (lesser than p)

$$E = \sum_{k=1}^p \left(\frac{r}{r^2 + z^2 + 1}\right)^{2k} \left(\frac{1}{(k!)^2} \frac{(4k)!}{4^{2k} (2k)!} - \frac{2^{2k}}{\sqrt{2\pi k}}\right) \quad (4.29)$$

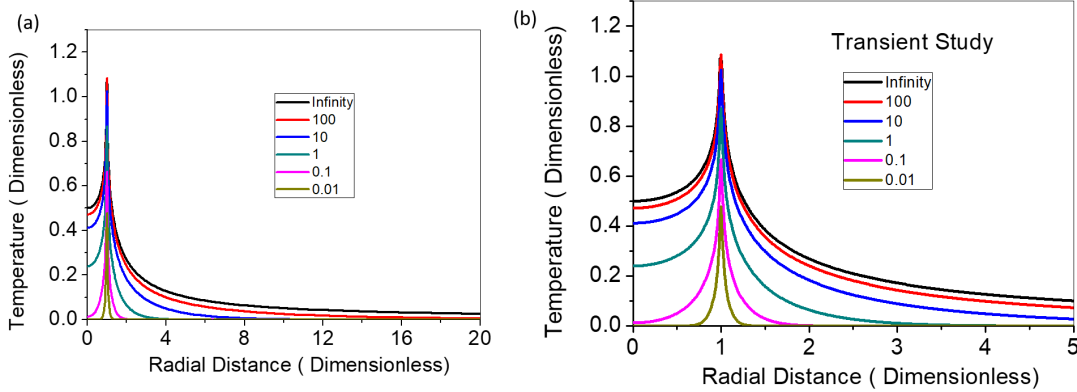


Fig. 4.9 Temperature as a function of radial distance at different time. In beginning, only the ring is at higher temperature. With increase in time, the temperature increases and heat distributes within and outside the ring.

Special cases: At $t = \infty$.

$$\frac{T(r, z, t = \infty)}{q_0 a^2 / k} = \frac{1}{2} \left(\frac{1}{r^2 + z^2 + 1} \right)^{\frac{1}{2}} \left[1 - \frac{1}{\sqrt{2\pi}} \log \left(1 - \left(\frac{2r}{r^2 + z^2 + 1} \right)^2 \right) + E \right] \quad (4.30)$$

The temperature calculation based on Eq. (4.27) and approximation expression Eq. (4.30) is shown in Figure (4.8). It reflects that the approximation is justifiable and if one is using the series summation one needs to take > 100 terms to understand temperature near the ring as the summation converges slowly. Thus 1000 terms are used to compute the temperature in the further study. As shown in Figure (4.27) (b) the temperature is not uniform, it is higher inside the ring than outside due to contribution from other ring points.

The temperature profile based on Eq. (4.27) is calculated at different time as shown in Figure 4.9. It shows in beginning ($t = 0.001$), the temperature shows only a single peak at $R = 1$ i.e. on the ring, suggesting the only ring attains higher temperature, while inside and outside ring temperature is not increased. With the increase in time, the temperature increases and distributes within and outside the ring.

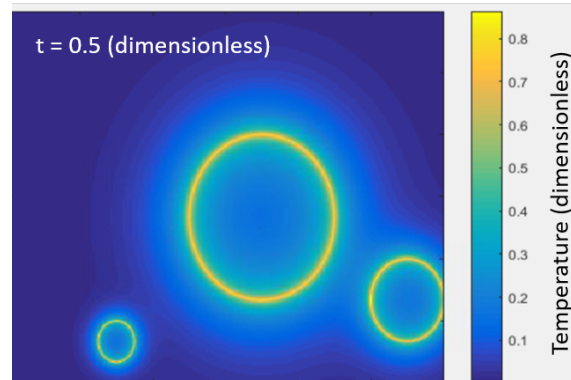


Fig. 4.10 Temperature profile by using 3 rings at different time

Superposition of multiple rings

For a single heat ring source kept in space with (x_0, y_0) being the centre of ring, the temperature at any point (x, y) can be written as $T_1(r, t)$ with $r = \sqrt{(x - x_0)^2 + (y - y_0)^2}$. As the temperatures are scalar and additive, thus the principle of superposition can be applied to obtain the resultant temperature for multiple rings sources. Figure 4.10 shows the resultant temperature profile for 3 rings as heat sources of different sizes based on superposition principle as

$$T(x, y, t) = T_1(x, y, t) + T_2(x, y, t) + T_3(x, y, t) \quad (4.31)$$

To approximately model that scenario we use the strategy of superposition of temperatures of variable ring sizes as shown in Figure (4.11). On starting the heater, in the beginning, only the region near rings are heated up, while as the time progresses heat is distributed throughout.

In a practical situation like transparent network based heaters. the void sizes are non-uniform and few wires are non-effective. To approximately model such scenario, we design 10,000 rings pattern in nearly closed pack arrangement with some intentional defects representing regions with no wires as shown in Figure 4.12. It is found that rise in temperature, in the beginning, is only restricted to the rings, while the regions without rings don't achieve high temperature. However, as the time progresses, even the

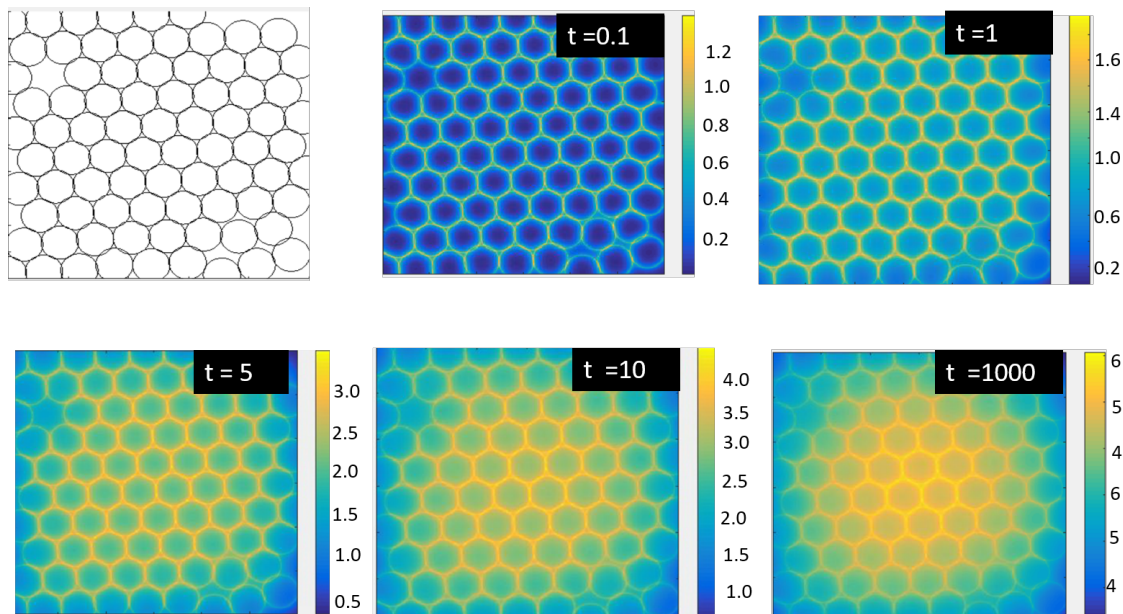


Fig. 4.11 Temperature profile of multiple ring with time.

regions having no rings, achieves the higher temperature. It is found that temperature near the corner of the sample is lower than central region, implying heat transfer is a long-range effect. In the corner since from one direction, there is no heat flow, the temperature in corner up to ≈ 5 rings are significantly lower than the central regions. Similarly, there is a slightly higher temperature in space around the heater, which is also due to a long range of heat transfer. Thus, if void size is $100 \mu\text{m}$ the corner most $\approx 500 \mu\text{m}$ regions can be at slightly lower temperature. The study can be useful in knowing the minimum possible heater size for uniform temperature profile.

To introduce the variation in void size, different size of ring pattern can be used. To consider wire width variation, the heat flux of a ring may have distribution. The study is preliminary and should consider these aspects in future to have its one to one correspondence with experiments. Another, limitation of the present work is neglecting of convection and radiation losses, which could complicate the analytical equations even further.

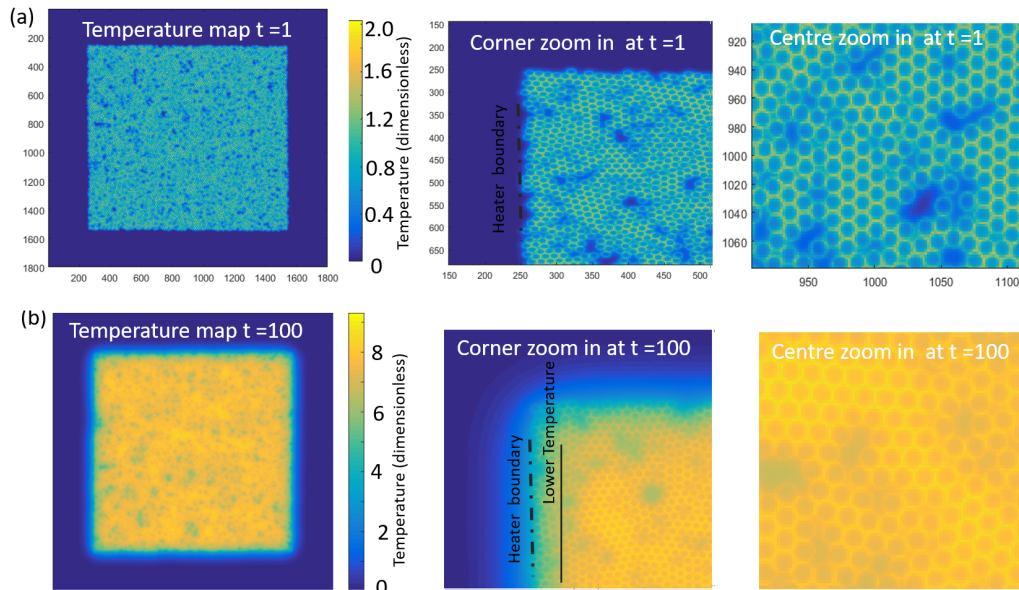


Fig. 4.12 Temperature profile in different regions for large number of rings at two different times.

4.2.5 Conclusion

In this work, we propose an analytical approach to obtain transient temperature profiles of circular rings based heaters. Thus, the technique can be used to understand temperature profile of network-based heater. The study shows, in the beginning only the ring heats up which gradually transfers heat inside and outside the ring to attain uniform temperature. It also reflects that temperature is considerably lower in the boundary of a heater than the center. The study can be useful in knowing the response time of heater to achieve uniform temperature profile.

Chapter 5

Attempts to explore Hierarchical networks

5.1 Prediction of time evolution and hierarchy of cracks

5.1.1 Introduction

The beauty of cracks from drying layers is ubiquitous; painted walls cemented floor, soil or mud fields, river beds and even giant rocks exhibit wide range of length and crack patterns. [43] These also occur over varying time scales, from seconds to decades. The network of cracks, formed from stress formation during desiccation drying, although superficially appears to be random, unpredictable and disordered, on close inspection, various subtle but systematic features can be observed. Crack width, crack spacing, intersecting angles and fractal dimension etc. depend on the stress profile of the drying film which in turn is governed by film thickness, drying temperature and mechanical properties of the film. [108, 160] As the understanding of cracks is important in respective domains from geological studies [63] to lithography methods [142] and therefore a deep insight into the crack formation may assist one to either completely avoids in layers or to obtain a desired crack pattern. Crack formation is an interesting dynamical phenomenon in which new crack forms, old cracks grow further and new cracks intersect the older ones. A crack once formed, grows to reach out to other neighbouring cracks, increases its width all the while. Importantly, cracks are born at different times and grow to different extents., leading to hierarchical nature of these patterns. [15] However, there are only limited reports focusing on the dynamic aspect of cracks and generally, only static parameters like crack width, spacing, angles are calculated from the final image of the completely dried film. For understanding the sequence of steps Bohn et al. [15] studied sound recording of cracks in which each crack segment formation gives a click from which temporal order was predicted, and classified cracks into different generations, however, it is cumbersome to perform. Vogel et al. [166] attempted to study few of these crack parameters with time and calculated variation of Minkowski numbers with time; however, it was not interpreted

in terms of hierarchy. On the basis of intersecting angles of cracks Perna et al. [135] labelled crack segments with generation number (primary, secondary etc.) by the knowledge that new crack hits already existing crack perpendicularly. These studies are focused on intersecting angles and not much attention has been paid to cracks widths influencing hierarchical structure.

5.1.2 Scope of present investigations

The present work addresses the time evolution aspect of cracks using TiO_2 colloidal film as a model system by studying continuous variation in crack area fraction, crack width and crack length with time to examine any possible transitions. This understanding has been applied to predict time evolution of crack patterns by using only the end crack pattern. The study is also successful in classifying primary, secondary and tertiary cracks from dynamic and final crack pattern. We have also developed an algorithm to classify cracks based on hierarchical nature on the basis of intersecting angles and edge width.

5.1.3 Experimental

The present study takes network cracks formed on drying film prepared from TiO_2 nanoparticles (NPs) of size 20 nm (from Sigma Aldrich) as our model crack system. 60 mg TiO_2 NPs were dispersed in 1ml methanol solution, 425 μl of the above solution was drop coated on a glass substrate of size 2.5 cm \times 2.5 cm. Dynamic images were captured during crack formation in the film by the optical microscope (Laben TPS 1000RT). Image analyses and calculations were performed by Image J and self-written Fortran codes and batch processing of 800 images was done by shell script programming. Film thickness was varied by drop coating different volume of TiO_2 solution and was measured by the optical profiler.

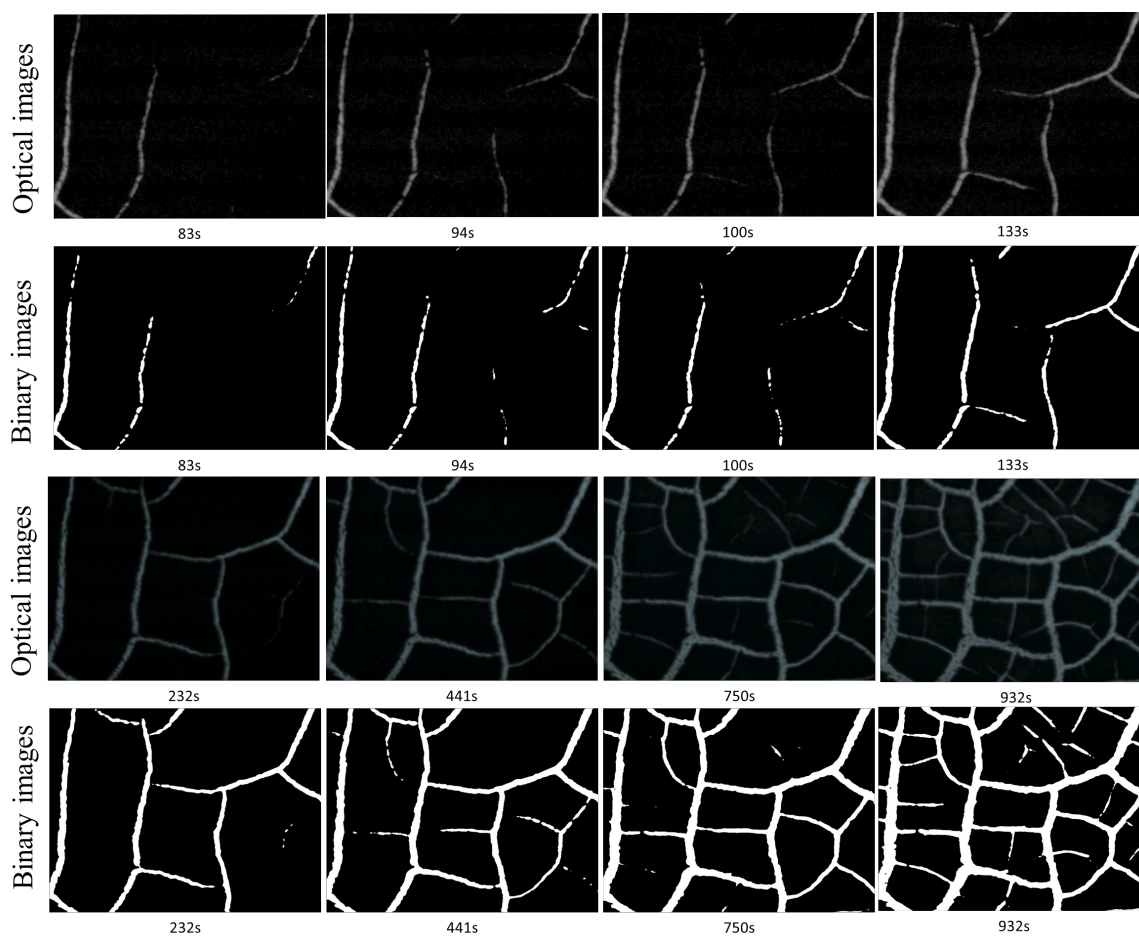


Fig. 5.1 Optical microscope images and corresponding binary images of the film undergoing crack formation with time ($t=0$ represents initiation of cracks)

5.1.4 Results and Discussion

Drying of the film and formation of cracks was monitored under an optical microscope and images were captured with the interval of 3 s for 2500 s. Cracks begin to form after 15 min of film deposition. Figure 5.1 shows snapshots of film undergoing drying induced stress leading to the formation of interconnecting networked cracks and corresponding binary images calculated by image J with auto binary function, here threshold is calculated as, $\text{threshold} = (\text{average background} + \text{average object}) / 2$ by the isodata algorithm. As shown in Figure 5.2, the chosen threshold is optimum to obtain binary images. The broken lines in the cracks are the artefact arising from the image analysis in judging cracked and non-cracked are based on light contrast.

Figure 5.3 shows the various stages of crack formation. As shown, in the beginning only a few cracks develop in the film which increases in length by propagation (green circles). With the passage of time, new cracks nucleate (red circles) usually at places far removed from the previous locations. Once these primary cracks grow, secondary cracks begin to form interconnecting the primary cracks and this process continues following the formation of tertiary cracks (shown in pink circles) which bring in next level of interconnectivity.

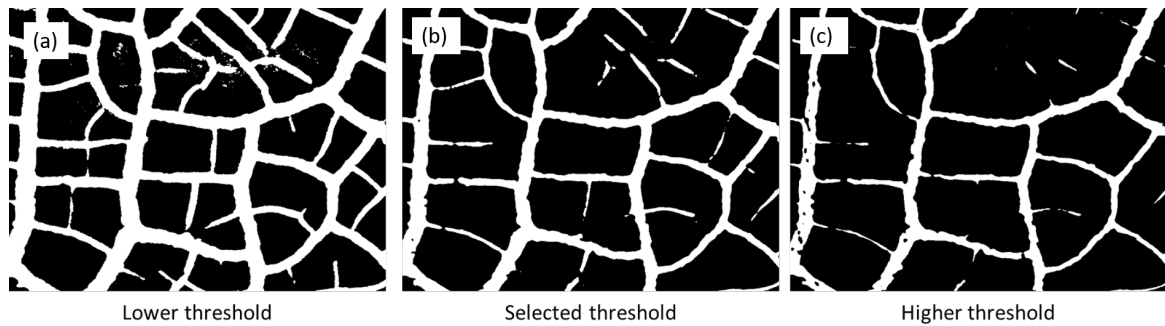


Fig. 5.2 Binary images at different threshold

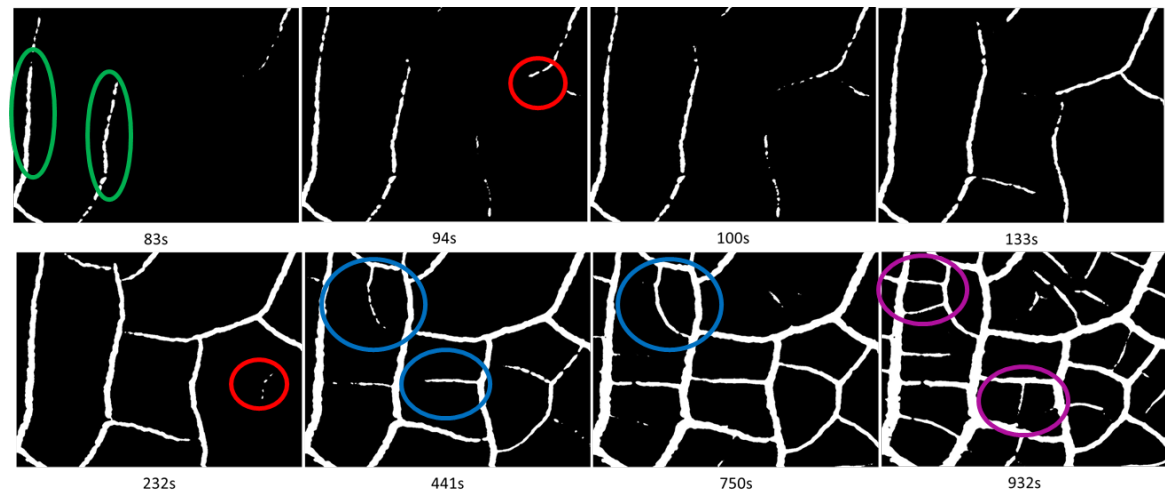


Fig. 5.3 Dynamic images of crack formation after image processing ($t=0$ represents initiation of cracks). With passage of time new cracks nucleates with crack propagation and broadening of existing cracks. It shows nucleation (Red) propagation of primary (green), secondary (blue) and tertiary (pink) cracks.

To study it quantitatively, the area fraction of all dynamic crack images is calculated and is plotted with time (Figure 5.4a). From the plot, it can be observed that area

fraction increases non-linearly with time and shows distinct regions which are marked as AB, BC, CD, and DE. Assuming the function to follow the power law

$$a = kt^p \quad (5.1)$$

Where a is area fraction of cracks, k is arbitrary constant and t is time taken from crack initiation), the corresponding values of p were derived from ln-ln scale plots as shown in Fig 5.4b. The different values of p indicate different rates of the crack formation with time. The images at transition points are shown in Fig 5.4d. From images, these transitions can be identified as a formation of the new generation of cracks. The region AB, BC, CD may be the propagation of primary, secondary and tertiary cracks while there is no further progress after it and DE represents saturation with corresponding p values as 2.15, 0.57 and 1.29 respectively. The crack formation in the first regime (primary cracks) is observed to be most rapid ($p = 2.15$), possibly because of very fast evaporation in the initial phase leading to the higher increase in the rate of stress. In case of second and third regime (secondary and tertiary crack formation), the rate of formation of tertiary cracks ($p = 1.29$) is observed to be quite higher than the secondary ones ($p = 0.57$), the reason may be due to more availability of surface area formed from former cracks for the solvent evaporation. We currently do not understand quantitative nature of slopes; a separate study is worthy to gain deeper insight.

Since stress can be released in propagation as well as broadening of already existing cracks. To study the effect of stress on the crack width, crack width is studied with time measured at four different locations (Figure 5.4c). The crack width is found to increase with time and interestingly here also similar transitions are observed in crack width increase rate shown in the linear and ln-ln plot. The transition points observed for crack width variation completely matches with the transitions observed for area fraction variation. Since, cracks formation depends on the stress profile of the drying film, therefore, the area fraction of cracks as well as the rate of broadening of the crack width both are governed by the rate of increase of stress of the film which

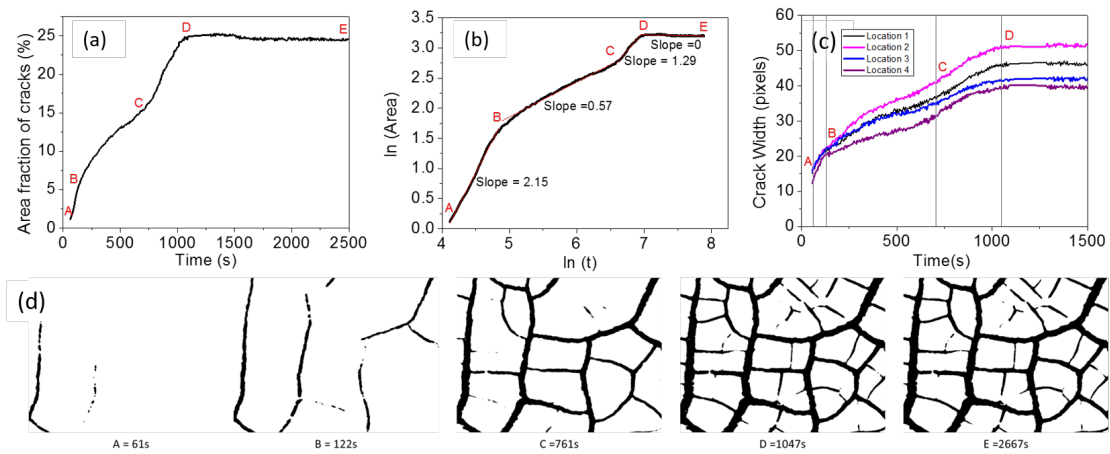


Fig. 5.4 Variation of area fraction of cracks in (a) linear and (b) log-log scale. (c) Broadening of crack at four locations with time (d) Images of the film at transition points.

changes abruptly on the formation of higher generation interconnecting cracks. The crack length which excludes the effect of broadening is plotted w.r.t. time in Figure 5.5a-b. The transitions observed in area fraction and crack width is also observed in this case though transitions are not observed to be very sharp may be because of mixed dynamics of formation of new cracks and the simultaneous increase in the length of already formed cracks. Fig 5.5c shows the dynamic formation of cracks in a single image for different time regimes A to B (green), B to C (blue), C to D (pink) which shows broadening, formation and propagation of cracks with time.

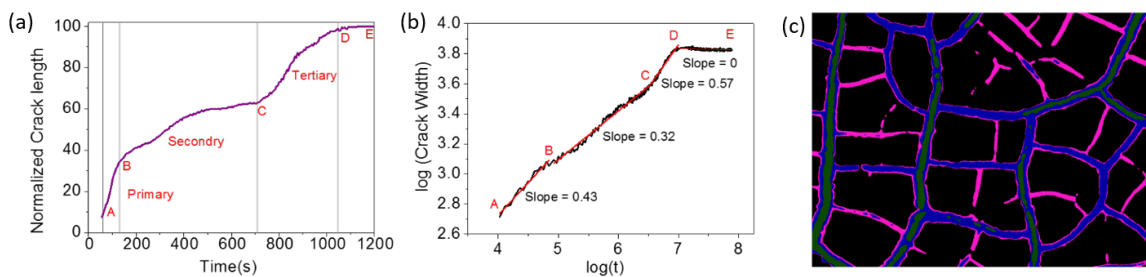


Fig. 5.5 Variation of crack length in (a) linear and (b) log scale (c) Cracks formation shown in different time regimes, A to B (green) , B to C (blue) , C to D (pink) .

Thus, we find that crack broadens with time which goes well with intuition, thus one can expect that older cracks should be wider than the new cracks, which is in

agreement with Lecocq. [103] To check the hypothesis, crack width of all cracks were measured and crack network has been filtered according to crack width as shown in Figure 5.6. Here each image consists of only those cracks segments which are broader than the threshold mentioned below as an example the first image has only that region of the network which has a crack width more than 45 pixels. As older cracks are broad and newer cracks are thinner, thus, the sequence of images show expected time evolution of cracks. Interestingly, the predicted sequence of steps by this approach excellently matches with the actual dynamic images (compare Figures (5.3 and 5.6). The crack feature observed in actual dynamic images can also be seen in these theoretical images. One can observe in Figure 5.6, direction of propagation of cracks (see green circles representing propagation of primary cracks), formation of Y junction (angle of 120°) during nucleation of new cracks (see red circles), propagation and T junction formation (perpendicular intersection) of secondary cracks (see blue circles) and tertiary cracks (see pink circles) which matches very well with the actual dynamic images (Figure 5.3). Thus, the complete time evolution of the cracks with steps like nucleation, propagation, intersections, and termination etc. which can give information related to stress in the film can be observed from the final image itself without the need of dynamic images.

Since crack dynamics shows a nice correlation between passage of time and broadening of crack, thus, the information which one extract from dynamics may emerge from crack width knowledge itself. To check this hypothesis crack length with particular crack width was measured. In Fig 5.7(a) crack length of cracks above a threshold value is calculated (integrated crack length of cracks). The plot shows certain transitions at B (32 pixels) and C (14pixels) with respective images shown in Fig. 5.8. The transitions observed in integrated crack width plot matches well with the actual crack dynamics transitions (Fig 5.5). The predicted and actual images of transitions also go in hand to hand (compare Figure 5.8 and Figure 5.4d) with each other confirming our postulate once more. Based on the transition points, cracks with width $> 32p$ are labeled as primary cracks, cracks with width $< 32p$ and $> 14p$ are labelled as

secondary cracks while cracks having width $< 14p$ are considered tertiary cracks (Figure 5.7b). It is found that most of the crack area is occupied by primary (46%) followed by secondary (43%) and tertiary (13%) cracks shown in Fig 5.7c.

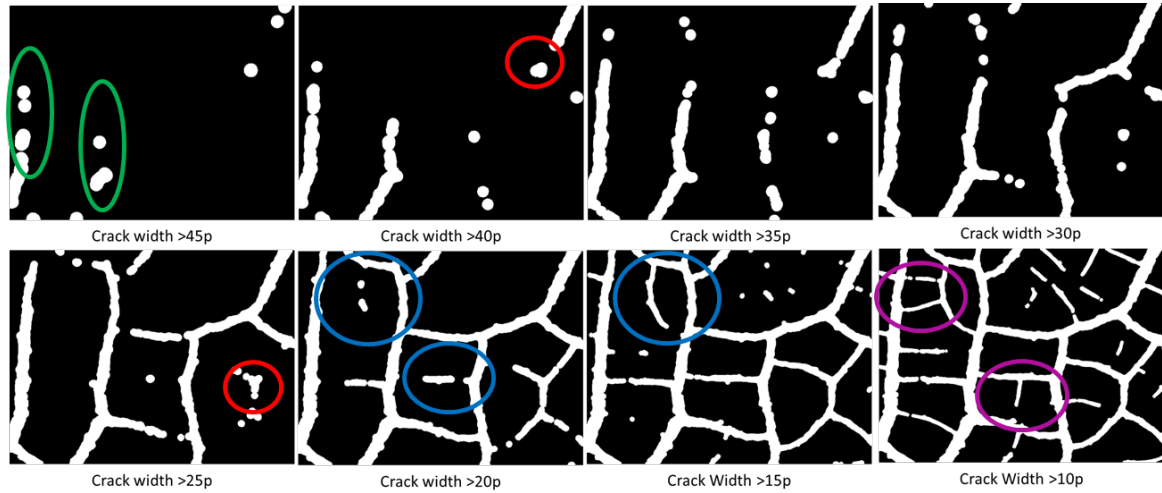


Fig. 5.6 Theoretically predicted time evolution on the basis of crack width filters. The filtered image shows cracks regions only above certain crack width mentioned below here 1 pixel represent $0.64 \mu\text{m}$.

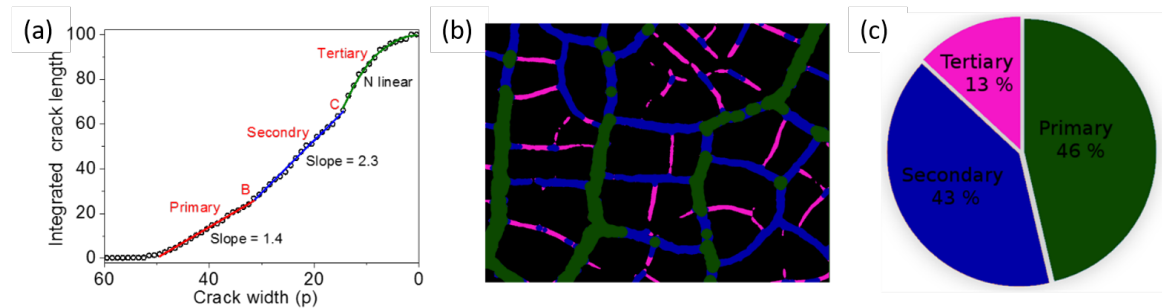


Fig. 5.7 (a) Commutative distribution of Crack length w.r.t crack width of final image (b) Labeling of Primary (green), secondary (blue) and tertiary cracks (pink) based on crack width filters (c) Pie chart showing area fraction of different generation cracks.

The theoretical idea of predicting time evolution of cracks from crack width filtration is applied to literature images as shown below. Here the top images are experimentally obtained images of Vogel et al. [166] and bottom images are predicted images based on crack width filtration. It is found that the experimentally obtained crack pattern

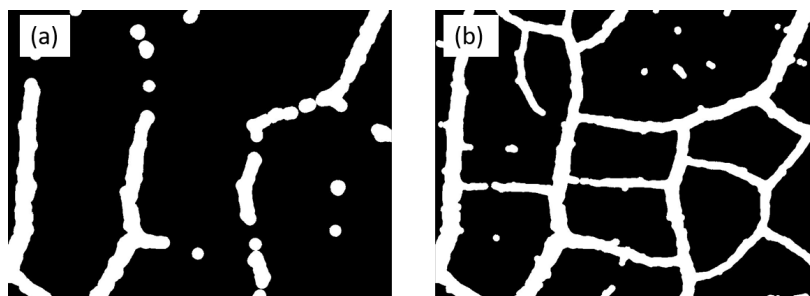


Fig. 5.8 Predicted images of transition points B and C based on crack width filters.

evolution goes well with the predicted evolution as shown in Figure 5.9. However, there are certain errors possibly due to image artefacts.

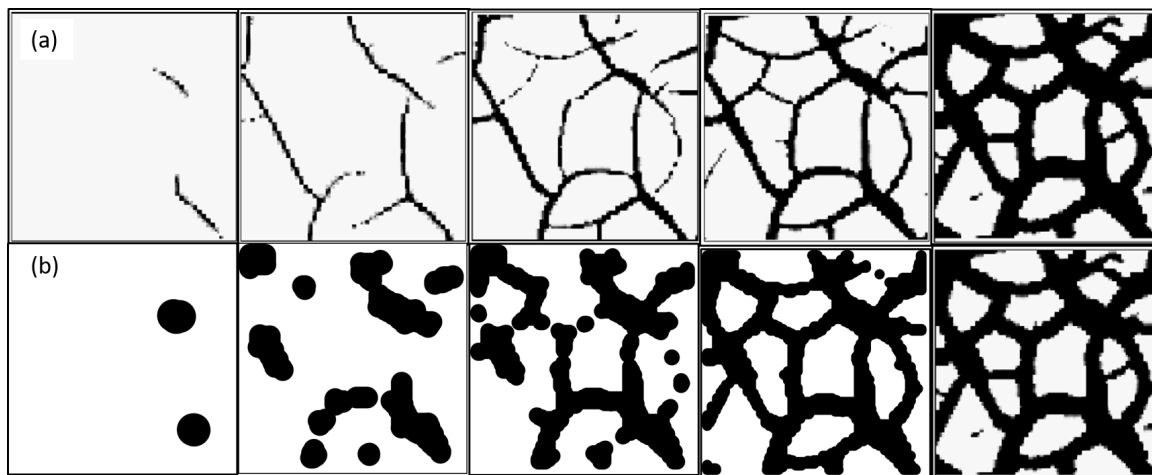
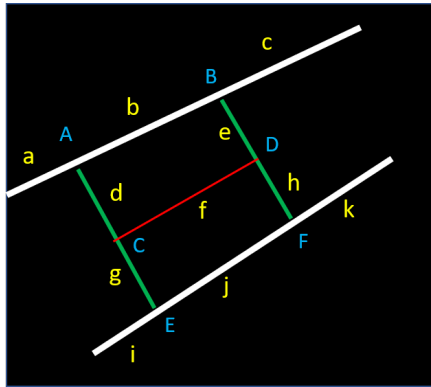


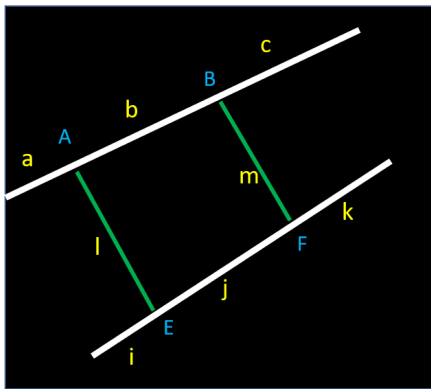
Fig. 5.9 The experimental time evolution reported by Vogel et al. and below corresponding theoretically predicted time evolution based on crack width filters on final pattern. Slight deviation may be due to low resolution of images. Reproduced with permission from ref [165]. Copyright 2005 Elsevier.

Cracks generate a hierarchical structure based on their timing of formation with new crack segments having a lesser crack width and intersect older cracks perpendicularly. An algorithm is developed to classify the crack segments based on their generation(see Figure 5.10). For the simplicity, we consider only three generations, primary (oldest), secondary (intermediate) and tertiary (newest). Firstly, the hierarchical nature of a network is determined considering the intersection angles of crack segments. Crack network consists of junctions with three crack segments, two being part of old crack



Junction	Crack segment	Old crack segments	New Crack segment
A	a, b, d	a, b	d
B	b, c, e	b, c	e
C	d, f, g	d, g	f
D	e, f, h	e, h	f
E	g, i, j	i, j	g
F	j, h, k	j, k	h

f is tertiary as it is new according to all junctions.



Junction	Crack segment	Old crack segments	New Crack segment
A	a, b, l	a, b	l
B	b, c, m	b, c	m
E	l, i, j	i, j	l
F	m, j, k	j, k	m

l,m are secondary as they are new according to all junctions.

Fig. 5.10 Algorithm for identifying generation of crack segments. The algorithm can be used for N generations, here only 3 generations are classified for clarity.

while one being new. As new crack intersects the older crack perpendicularly to relieve maximum stress, the new crack segment can be identified as a crack segment having intersection angle of around 90° with other two crack segments, while old crack segments form angle around 90° and 180° with other two crack segments. The process is repeated at all junctions. The crack segments which are identified as new according to all junctions are labelled as cracks of highest generation (tertiary) shown in red while the crack segments which are old according to any junction are left unlabeled. The tertiary crack segments (red colour) are removed from the image and the same procedure is applied to the remaining image. The crack segments found to be new in this step are labelled as secondary (shown in green). The remaining image after

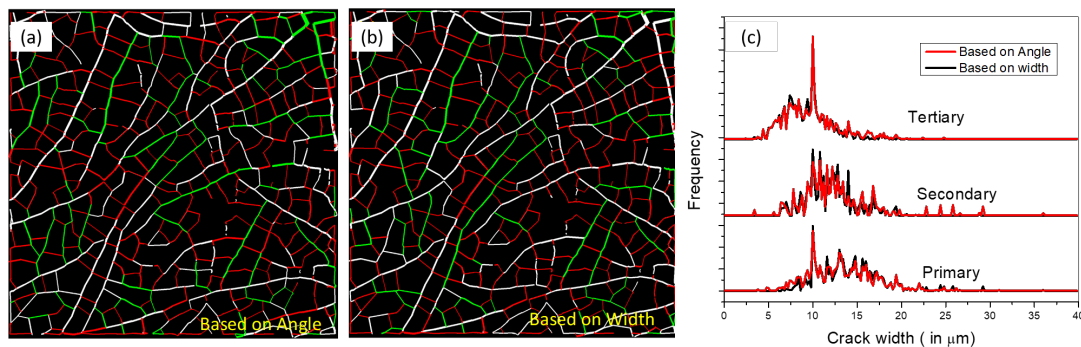


Fig. 5.11 The hierarchical nature of cracks is obtained from width or angle. Classified cracks segment based on (a) angle and (b) width. (c) Frequency distribution of primary secondary and tertiary cracks. Please note that the distribution obtained by angle analysis matches well with the distribution obtained using width analysis.

removing secondary crack segments as well are labelled as primary (white colour). Thus, the algorithm can classify the crack segments into different hierarchical order.

Next, the hierarchy is evaluated based on crack segment widths. As new crack segments are thinner than old crack segments, thus width information of the cracks can also be used to predict their temporal order. As a junction consists of three crack segments, two being old of higher width and one being new of lower width. Thus crack width of all three crack segments are compared in all junctions to identify the new crack segment. The crack segment which is found to be new based on all junctions is labelled as tertiary (red). The tertiary cracks are removed from the image and again widths of crack segments are compared at all junctions. The crack segments which are found to be new in this step are labelled as secondary. The remaining pattern is labelled as primary. Figure 5.11b shows the hierarchical pattern obtained from width information. On comparing Figure 5.11a and b, one can see that hierarchy pattern by both approaches are closely matching. Figure 5.11c shows the frequency distribution of widths of the different generation of cracks. It is clear, each generation consists of cracks of broad width distribution, thus one needs to perform this iterative algorithm for the identification. The width distribution obtained from angles and widths analysis match with each other. Thus, hierarchical nature of network can be understood from

the angle as well as width information. The discrepancy can be due to artefacts of the image analysis.

Thus, In this work, an attempt is made to understand hierarchical nature of desiccating cracks. The iterative algorithm is applicable even for understanding more generation of patterns. However, due to image artefacts arising from low resolution and contrast of images, only primary, secondary and tertiary are presently classified. The algorithm can be very useful to understand how experimental conditions influence the hierarchy. The approach is generic in nature and can easily be applied to other hierarchical networks such as leaf veins, road networks etc.

5.1.5 Conclusion

The present study gives insight into the dynamic aspect of cracks and shows the correlation between temporal information and spatial crack width. The predicted time evolution based on crack filtering shows remarkable matching with the actual dynamic images. Thus, the final image of a crack is not just a static image but whole movie consisting of a sequence of steps of crack formation can be extracted out of it. The study is also successful to distinguish and classify primary, secondary and tertiary cracks from the final crack pattern. The study can be useful in better understanding of stress dynamics of drying film, hierarchical structures exhibited by cracks and locating defects from nucleation center. Future work can be done in the direction of analyzing, how experimental conditions influence the crack hierarchy.

5.2 Optimum hierarchical network for efficient transport

5.2.1 Summary

Hierarchical networks are widely seen in road networks, leaf vein networks, solar cell electrodes etc. In general, the transport channel has a decreasing width with generations, such as road network consist of national highways, state highways, district roads and local roads such that the width and the speed limit decreases in each hierarchical step. It is not well understood which kind of geometry of the hierarchical pattern to be used for dividing the space for efficient transport. In other words, what design of network pattern and width to be assigned to different roads for efficient transport at minimum road size. A detailed study on transport system can be useful to control traffic jam and reduce effective distance between two points. Here, a generic approach is developed to calculate transport properties of a hierarchical network. The various parameters of a hierarchical structure are considered for their influence on the weighted path length (travel time). Under the condition of width reduction rate and space reduction rate to be equal, conditions for minimum path length for given fill factor is obtained, which corresponds to 4.92 (≈ 5) divisions per generation step. Any other structure is compared with it, for the relative comparison. Thus, the present work can be an important step for the better understanding of hierarchical networks.

5.2.2 Introduction

Network models play an important role in describing and predicting various natural and artificial systems such as social interaction, disease spreading, communication, biochemical reactions, wealth distribution etc. Watts and Strogatz model [168] of the small-world network is a good example, which gave a simple idea that just a few random connections in a periodic lattice can make the network more effective. Similarly, the scale-free model of Barabasi [8] describes that preferential attachment

in an evolving network creates a power law distribution, which is widely seen in economics, collaboration etc. One more important feature of most of the natural and artificial networks is the property of hierarchical aspect, which is especially seen in transport-related networks. In this case, space divides recursively into smaller and smaller cells by transport channels whose width (weight) reduces in each step. As an example, a nation is divided into various cells by road network recursively by national highways, state highways and local roads with the speed limit and width of roads decreasing in each step. [96] Similarly, biological transportation system such as vascular systems in leaves, [170] circularity systems in blood vessels, respiratory systems in lungs has also evolved themselves in a hierarchical fashion for transporting metabolic chemicals effectively. For an efficient network, the time taken to reach two points be least with minimum road size as roads production or veins formation are energy expensive process. The hierarchical patterns are also utilized in artificial networks such as power grid, and in a form of charge collector metal grid of solar cells to minimize the resistive losses. In a metal grid of a solar cell, the network should be designed to have minimum resistance, better collection and less shadowing losses. [91] The hierarchical aspect is also utilized in efficient information transfer and search algorithms. Challenge in all these cases is to choose an optimum hierarchical network for reducing travel time between points at minimum transport channel size.

Despite its omnipresent nature, the hierarchical prospective of above networks have not been paid enough attention and not detailed analysis is done before their design. As an example in India, National highways constitute 1.7% of the road network but carries 40% of the vehicles creating the problem of a traffic jam. Although, there are significant works proving small-world nature of roads and other transport systems, hierarchical weights are neglected in them. [96] The generations of cities have been calculated based on image analysis. [135] However, it is not well understood which geometry of hierarchical network is more suitable for effective transportation in the above scenarios. Interestingly, the scale invariance property has been studied using concepts of fractals starting from the problem calculation of coastline by Mandelbrot, [118]

however fractal dimensions provide information of only complexity in the structure and not on transportation.

5.2.3 Scope of the present investigations

Herein, a hierarchical network is characterized and its transport properties are studied in detail. Path length, which corresponds to travel time between two points is calculated for different hierarchical networks. Various symmetrical systems are compared to know which kind of network parameters are optimum for efficient transportation.

5.2.4 Results and Discussion

In general, a hierarchical structure divides the space channel and reduces transport channel width (weight) recursively. Consider, N to be total generations, d_i to be space division rate per step and r_i to width division rate per step such that spacing between i generation channel is $S_i = \frac{S}{\prod_1^i d_i}$ and width of channel is $w_i = \frac{W_o}{\prod_1^i r_i}$. Higher the generation (i), lower the width (w_i) and inter-channel distance (S_i). Figure 5.12(a) shows a typical hierarchical structure of size $S \times S$ which is recursively divided by green, blue and red lines into 3×3 , 4×4 , 2×2 cells and weight of channel reduces in each step which is 1 unit for green is, $\frac{1}{2}$ for blue and $\frac{1}{6}$ units for red. Here, $d_1 = 3$, $d_2 = 4$ and $d_3 = 2$ and $r_1 = 1$, $r_2 = 2$ and $r_3 = 3$. Figure 5.12b shows corresponding uniform width network. Note that fill factor, mean width and geometry are same in 5.12(a) and (b), only the former is having hierarchical decreasing widths with the generations while the latter is having uniform width given by

$$w_{mean} = \frac{\sum_{i=1}^N w_i \left((d_i - 1) \prod_{k=1}^{i-1} d_k \right)}{\sum_{i=1}^N (d_i - 1) \prod_{k=1}^{i-1} d_k} = \frac{[6(2)] + [3(3)] + [1(3 \times 4)]}{2 + (3) + (3)} = 2.21 \text{ units} \quad (5.2)$$

Before comparing the transport properties of both, let us see the basic principle of transportation occurring in a hierarchical network. In general, in a hierarchical structure, an object at source is typically at high generation and starts moving to lower

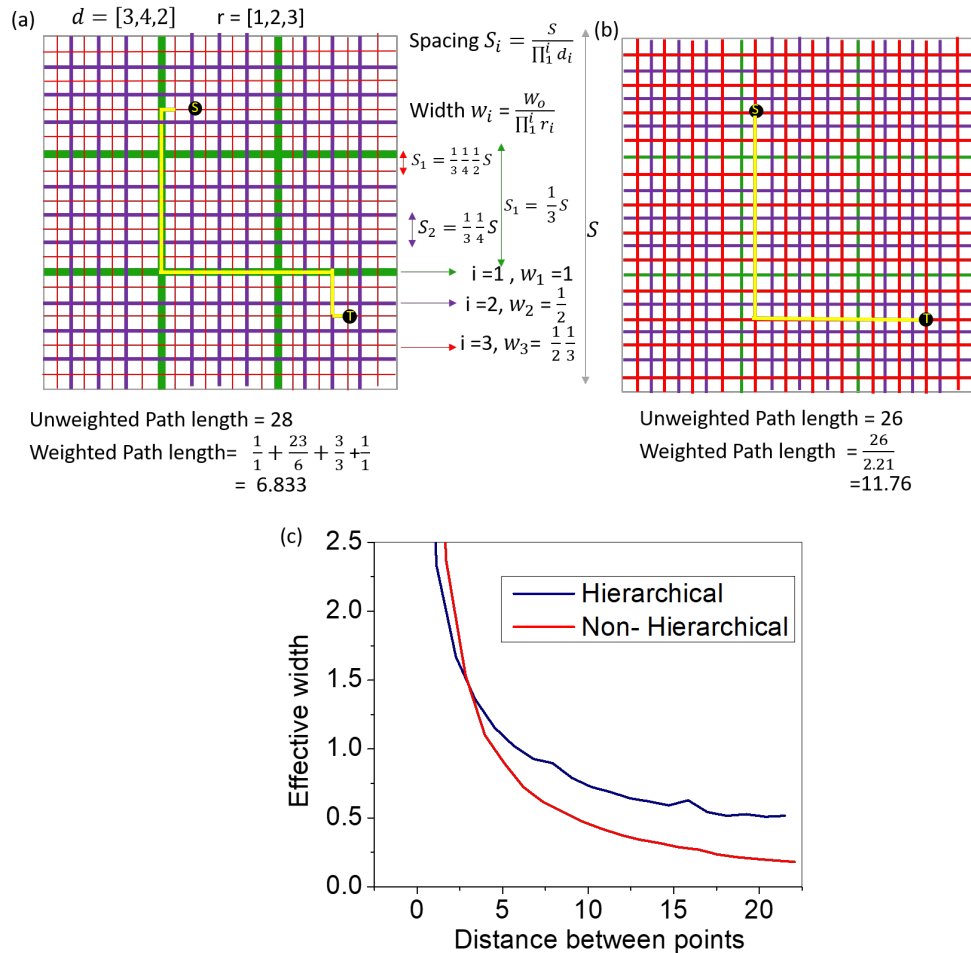


Fig. 5.12 (a) A typical example of a hierarchical network with division matrix [3,4,2] bisecting spacing into 3,4,2 divisions respectively and (b) Network of equal width but having same fill factor as shown by (a). For very small distances, the path length is lower for the non-hierarchical network, while for rest of the region path length is lower for the hierarchical network. S and T show an example of a source and a target having the path length of 6.833 and 11.76 in the hierarchical and non-hierarchical network. (c) Comparison of Variation of effective width with distance between points.

generation and then again returns back to the target point of typically high generation. As an example, in case of the road network for a long journey, firstly, a vehicle begins the journey at highest hierarchy such as rural/urban road then moves step by step to the lower order of hierarchy i.e. district roads, state roads and finally national highways where he spends the maximum time. Further, the vehicle moves upward in hierarchical order, to reach the target by choosing state and rural road of target place respectively. In leaf ventilation case, nutrients are transferred from trunk to the individual cells using lower to higher hierarchy pathway and food from photosynthesis is transferred from higher to lower hierarchical order. In the case of solar cells, the charge carriers are collected from fine wires, at the high hierarchy and move to broad main collectors at the low hierarchy. Thus, in general, a transportation process involves moving from highest to lowest hierarchical step progressively or the vice versa. Now, consider a vehicle at S moving towards T on a hierarchical network (Figure 5.12a), the vehicle will try to minimize its weighted path length (time), thus typically object moves down the hierarchical pattern and then travel maximum distance there and then move upward in the hierarchy. Here path length is equivalent of total time spent on a road and can be evaluated as $\sum \frac{l_j}{w_j}$, where summation involves path from S to T. In this case path length becomes $= \frac{1}{1} + \frac{23}{6} + \frac{3}{3} + \frac{1}{1} = 6.83$. On the other hand, for the same points S and T, if a vehicle moves on uniform width network with the width being an average of the former pattern (Figure 5.12b), the path length increases to 11.76, almost double than the former hierarchical case. Similarly, the path length between all the pair of junctions was calculated and is plotted w.r.t their actual distance as shown in Figure 5.12c. Thus, a hierarchical pattern can be much more effective for information transfer.

In the above example, the network has particular space division rate and width division rate. However, a hierarchical network can be made in various ways, with different sets of space division matrix and width division. It is important to know, which hierarchical structure is more suitable for better transport. However, the numerical ways discussed in Figure 5.12 may be computationally expensive especially

for a deep hierarchical network. To make it more insightful and simple, here, we also show the analytical ways to know path length. Consider a hierarchical structure shown in Figure 5.13a and object has to move one step down in the hierarchical pattern. As an example, an object at P moves to Q , similarly, object at R moves to S . For any arbitrary point X moving towards the road of one step lower, it is important to choose a way to take nearest possible distance $(\frac{D}{2} - x)$. Thus, average distance (s) covered by a point can be obtained by integrating over all points as

$$s = \frac{1}{D^2} \int_0^{D/2} \left(\frac{D}{2} - x \right) 8x dx = \frac{D}{6} \tag{5.3}$$

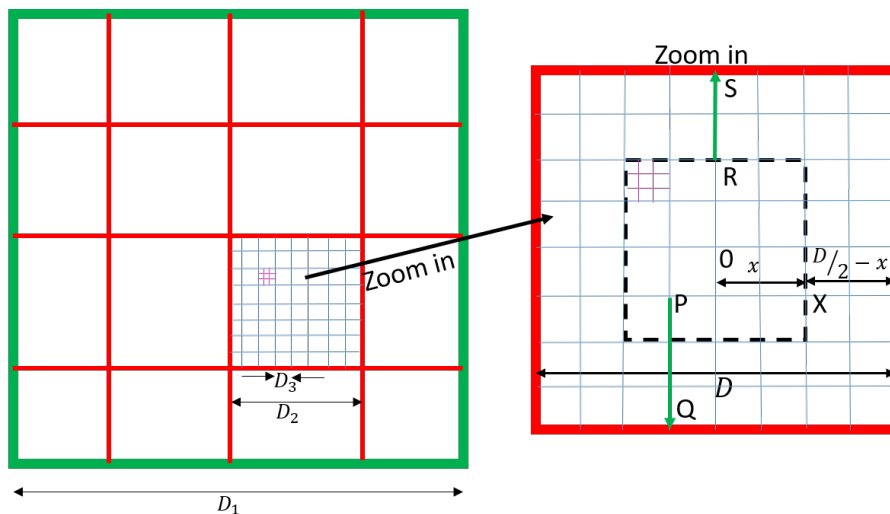


Fig. 5.13 A network with 3 generations and zoom in of 2nd generation. For transportation an object from lower to higher hierarchical order with the shortest path. An object at P takes PQ way to reach red line, while an object at R takes RS way to reach red line. Consider an object is at position x from the center of the red circle, it needs to travel $\frac{D}{2} - x$ distance to reach the red line.

Thus, averagely distance travelled by an object to go from higher hierarchical to one step lower upper hierarchical is $\frac{D}{6}$ and weighted path length becomes $\frac{D}{6} \frac{1}{w}$. In a generalised hierarchical transportation, there may be multiple levels, the above expression can be used to add up path lengths in individual steps. The path distance L travelled by an object at i generation to move to $i - 1$ generation need to travel

$\frac{D_i}{6w_i}$ distance with $D_i = \frac{S}{d_{i-1}}$ here, $d_0 = 1$. Path length for 1 to N generations can be written as

$$L = \frac{1}{6} \sum_i^N \frac{D_i}{w_i} = \frac{1}{6} \frac{S}{W_o} \sum_i^N \prod_{k=1}^i \frac{r_k}{d_{k-1}} \quad (5.4)$$

The mean width can be written as

$$w_{mean} = W_o \frac{\sum_{i=1}^N w_i (d_i - 1) \prod_{k=1}^{i-1} d_k}{\sum_{i=1}^N (d_i - 1) \prod_{k=1}^{i-1} d_k} \quad (5.5)$$

It is important to study the properties of some symmetrical hierarchical structures.

Case : ($r_k = r$, $d_{k-1} = d$) , In other words, If reduction in space and reduction in width remains same with generations.

Substituting $r_k = r$ and $d_{k-1} = d$ with $d_0 = 1$ and $r_1 = 1$

$$L = \frac{1}{6} \frac{S}{W_o} \left(1 + \sum_i^{N-1} \left(\frac{r}{d} \right)^i \right) \quad (5.6)$$

On series expansion, it can be written as

$$L = \frac{1}{6} \frac{S}{W_o} \frac{d}{d-r} \left(1 - \left(\frac{r}{d} \right)^N \right) \quad (5.7)$$

The mean width in this case can be written as

$$w_{mean} = W_o \frac{\sum_{i=1}^N (d-1) \frac{d^{i-1}}{r^{i-1}}}{\sum_{i=1}^N (d-1) d^{i-1}} \quad (5.8)$$

It can be expressed as

$$w_{mean} = W_o \frac{(d-1) (d^N - r^N)}{r^{N-1} (d^N - 1) (d-r)} \quad (5.9)$$

From Eq. (5.6) and Eq. (5.9), it can be written as

$$L = \frac{1}{6} \frac{S}{W_{mean}} \frac{(d^N - r^N)^2}{(d-r)^2} \frac{d(d-1)}{d^N r^{N-1}} \quad (5.10)$$

Case : $r_k = d_{k-1}$ From Eq. (5.4) the path length can be written as:

$$L = \frac{1}{6} \frac{N}{W_o} \quad (5.11)$$

From Eq. (5.5)

$$w_{mean} = W_o \frac{\sum_{i=1}^N (d_i - 1)}{\sum_{i=1}^N (d_i - 1) \prod_{k=1}^{i-1} d_k} \quad (5.12)$$

Which can be simplified as:

$$w_{mean} = W_o \frac{\sum_{i=1}^N d_i - N}{\prod_{i=1}^N d_i - 1} \quad (5.13)$$

Path length can be written as

$$L = \frac{1}{6} \frac{SN}{W_{mean}} \frac{\sum_{i=1}^N d_i - N}{\prod_{i=1}^N d_i - 1} \quad (5.14)$$

Note that it shows that the path length depends on product of d_i and not on order of d_i . Thus $d = [4,5,6,7]$ are equivalent to $d = [6,5,4,7]$ or $[5,4,7,6]$ etc. Substituting total number of cells C as $C = \prod_{i=1}^N d_i$.

$$L = \frac{1}{6} \frac{SN}{W_{mean}} \frac{\sum_{i=1}^N d_i - N}{C - 1} \quad (5.15)$$

For given cells, its better to have $\sum_{i=1}^N d_i$ to be minimum. As an example, to have 100 divisions, division rate of $[10,10]$ is best and based on less path length, $[10,10] > [5,20] > [4, 25] > [2, 50]$.

Case : $r = d$

$$w_{mean} = \frac{N (d - 1) W_o}{(d^N - 1)} \quad (5.16)$$

Path length can be written as

$$L = \frac{SN^2 (d - 1)}{6} \frac{1}{d^N - 1} \frac{1}{w_{mean}} \quad (5.17)$$

$$L = \frac{S}{6} \left(\frac{\ln C}{\ln d} \right)^2 \frac{d-1}{d^N - 1} \frac{1}{w_{mean}} \quad (5.18)$$

The minimum value of L based on Eq. 5.18 is obtained as $d^* = e^{W(-\frac{2}{e^2})+2}$, here W is product log function and d^* comes out as 4.92.

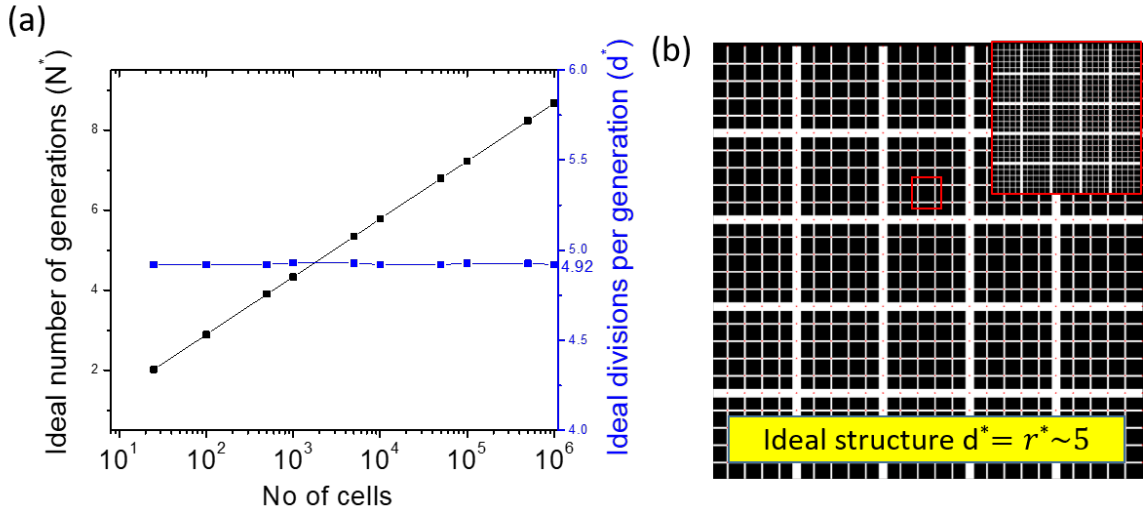


Fig. 5.14 (a) Parameters of ideal network with least Path length (b) A schematic of ideal network. For least path length, the divisions per generation should be ≈ 5 .

Thus, importantly, the optimum no of generations for minimum path length is 4.92 (≈ 5) and optimum generations number is given by $N = \frac{\ln C}{d^*}$ (Figure 5.14a). Figure 5.14 b shows an ideal hierarchical structure with division per generation and width reduction per generation ≈ 5 .

The transport properties of a hierarchical network may be quantified in terms of its path length compared to the ideal structure. A term ideality factor is defined to check how much close a network with path length L^{real} is as compare to the best performing network with same no of total cells and mean wire width (which means same fill factor).

$$\eta = \frac{L^{real}}{L^*} \quad (5.19)$$

As an example for hierarchical network with $d = (5, 7, 4)$ and $w = (1, 2, 5)$, $L^{real} = 1.68$, $w_{mean} = 0.21w_0$, $C = 140$, $N^* = 3.10$, $L^* = 1.29$ and $\eta = 0.76$. In this way, if there are more than one network with same fill factor and a total number of cells, one can compare their ideality factor to know which one is better.

The present analytical treatment assumes there are no hubs and there is an equal probability of moving between all distant points. However, an actual road network involves non-symmetrical roads and non-uniform distribution of travelling between the points, thus, the additional modification is desired for bringing those aspects. The numerical approaches may be combined with it to consider more realistic scenarios. The approach is also useful to modify metal grids of solar cells, where minimum resistance and minimum grid area is desired. The study may also be applied to biological hierarchical networks such as leaf veins for their better understanding. The model is one of the first attempts to have insight in transport property of hierarchical networks which may be useful for advanced modelling.

5.2.5 Conclusion

In conclusion, an attempt is made to model the transport in the hierarchical network to obtain optimum network. Some interesting optimization properties are observed such as under special conditions, space division rate should be equal to width reduction rate, the order of space division does not affect overall path length. The ideal hierarchical structure is attained with space division and width division ≈ 5 per generation. Different hierarchical patterns may be compared with each other in terms of the path length.

Chapter 6

Summary and Outlook

ॐ पूर्णमदः पूर्णमिदं पूर्णात्पूर्णमुदच्यते
पूर्णस्य पूर्णमादाय पूर्णमेवावशिष्यते ॥

Om, that is infinity, this is infinity, From the infinity comes the infinity. If infinity is taken away from infinity, infinity still remains.

6.1 Summary

The thesis essentially discusses the approaches to compare conducting wire based transparent electrodes and proposes the strategies for the improvement. Further, the study is explored in studying the transport of generic networks. Chapter 1 discusses the diversity of patterns in nature and utilization of the naturally occurring crack network pattern as a template for lithography in fabricating metal networks for the application of transparent conducting electrodes. An optimum structure is required for such networks. Chapter 2 discusses the new models for comparison of such networks. An analytical model to evaluate sheet resistance and an effective current carrying region is developed. The modelling of network-based strain sensor is also explored, Chapter 3 discusses the strategies for modulating crack templates. Chapter 4 discusses the thermal transport of such networks. Chapter 5 focusses on an understanding

hierarchy of crack patterns and evaluates the optimum hierarchical structure for efficient transportation.

6.2 Outlook

The sheet resistance and current map evaluated in this study (section 2.1 and 2.2) can be compared with experimental measurements. Further, the proposed models can be very useful in choosing an optimum network structure and nanowire density for a TCE application.

In the present solar cell modelling (section 2.3), a simple geometry of solar cell consisting of transparent electrodes, active material, and a bottom continuous electrode is considered. However, many solar cells have additional layers such as electron and hole transporting layers, conducting polymers etc. These layers should be added in the future advanced models. The model can also be extended for other optoelectronic devices such as light emitting diodes and liquid crystal device screens, where TCE is a performance deciding parameter.

The breakdown of a network at high voltage is studied using Infrared microscopy (section 4.1). The current map studies (section 2.2) can be utilized to understand this behaviour. One may see the cascade effect during the numerical breakdown as well. The numerical study may be useful to design more robust networks.

Currently, spring fusion model (section 3.1) is applied on a square lattice which limits crack patterns to be nearly linear. However, if one works on a hexagonal lattice, the simulated crack patterns are expected to be closer to experimental images. The theoretical model should also incorporate additional parameters such as viscoelastic properties of the material which may influence crack patterns significantly.

Azeotropic mixtures showed interestingly high wetting property, which was used to obtain narrow and well-connected cracks (section 3.3). The high wetting property may be explored for printing purpose, where high wetting avoids the problem of dewetting.

The analytical model derived for heat transfer (section 4.2) may be explored to match experimental results. The losses may also be incorporated into the Green's function solution equation treatment.

The algorithm discussed to classify crack segments of different generations (section 5.1) can be useful to study how experimental conditions change the hierarchy. The study will be important to achieve crack patterns of optimum hierarchical nature.

The hierarchical transport model (section 5.2) is currently applied on only symmetrical patterns, assuming uniform transport between distant points. Additional parameters such as travel distance distribution and hubs in the city may be added to advanced city planning model. The models can be used to compare road networks of different cities. The work may also be utilized for improving the design of solar cell's grid which is hierarchical in the structure for maximum charge collection at minimum resistive losses. Further, the study may also be applied to understand transport in leaves and answering why nature would have chosen a variety of hierarchical structure in leaves.

Thus, the thesis attempts to bring new interesting insights in transport properties of networks which can be extended to understand many fascinating problems.

References

- [1] AGO, H., PETRITSCH, K., SHAFFER, M. S., WINDLE, A. H. & FRIEND, R. H. 1999 Composites of carbon nanotubes and conjugated polymers for photovoltaic devices. *Advanced Materials* **11** (15), 1281–1285.
- [2] ALLAIN, C. & LIMAT, L. 1995 Regular patterns of cracks formed by directional drying of a colloidal suspension. *Physical Review Letters* **74** (15), 2981.
- [3] AMARASIRI, A. L., KODIKARA, J. K. & COSTA, S. 2011 Numerical modelling of desiccation cracking. *International Journal for Numerical and Analytical Methods in Geomechanics* **35** (1), 82–96.
- [4] AMJADI, M., PICHITPAJONGKIT, A., LEE, S., RYU, S. & PARK, I. 2014 Highly stretchable and sensitive strain sensor based on silver nanowire–elastomer nanocomposite. *ACS nano* **8** (5), 5154–5163.
- [5] ANGMO, D., HÖSEL, M. & KREBS, F. C. 2012 All solution processing of ito-free organic solar cell modules directly on barrier foil. *Solar Energy Materials and Solar Cells* **107**, 329–336.
- [6] AZUMA, K., SAKAJIRI, K., MATSUMOTO, H., KANG, S., WATANABE, J. & TOKITA, M. 2014 Facile fabrication of transparent and conductive nanowire networks by wet chemical etching with an electrospun nanofiber mask template. *Materials Letters* **115**, 187–189.
- [7] BAE, J. J., LIM, S. C., HAN, G. H., JO, Y. W., DOUNG, D. L., KIM, E. S., CHAE, S. J., HUY, T. Q., VAN LUAN, N. & LEE, Y. H. 2012 Heat dissipation of transparent graphene defoggers. *Advanced Functional Materials* **22** (22), 4819–4826.
- [8] BARABÁSI, A.-L. & ALBERT, R. 1999 Emergence of scaling in random networks. *Science* **286** (5439), 509–512.

- [9] BAUHOFFER, W. & KOVACS, J. Z. 2009 A review and analysis of electrical percolation in carbon nanotube polymer composites. *Composites Science and Technology* **69** (10), 1486–1498.
- [10] BECK, J., BLACKWELL, B. & HAJI-SHEIKH, A. 1996 Comparison of some inverse heat conduction methods using experimental data. *International Journal of Heat and Mass Transfer* **39** (17), 3649–3657.
- [11] BEHNAM, A., SANGWAN, V. K., ZHONG, X., LIAN, F., ESTRADA, D., JARIWALA, D., HOAG, A. J., LAUHON, L. J., MARKS, T. J., HERSAM, M. C. *et al.* 2012 High-field transport and thermal reliability of sorted carbon nanotube network devices. *ACS Nano* **7** (1), 482–490.
- [12] BERGIN, S. M., CHEN, Y.-H., RATHMELL, A. R., CHARBONNEAU, P., LI, Z.-Y. & WILEY, B. J. 2012 The effect of nanowire length and diameter on the properties of transparent, conducting nanowire films. *Nanoscale* **4** (6), 1996–2004.
- [13] BERGMAN, T. L., INCROPERA, F. P., DEWITT, D. P. & LAVINE, A. S. 2011 *Fundamentals of heat and mass transfer*. John Wiley & Sons.
- [14] BID, A., BORA, A. & RAYCHAUDHURI, A. 2006 Temperature dependence of the resistance of metallic nanowires of diameter $\geq 15\text{nm}$: applicability of bloch-grüneisen theorem. *Physical Review B* **74** (3), 035426_1–035426_8.
- [15] BOHN, S., PAUCHARD, L. & COUDER, Y. 2005 Hierarchical crack pattern as formed by successive domain divisions. *Physical Review E* **71** (4), 046214.
- [16] BONDY, J. A., MURTY, U. S. R. *et al.* 1976 *Graph theory with applications*, , vol. 290. Citeseer.
- [17] CELLE, C., MAYOUSSE, C., MOREAU, E., BASTI, H., CARELLA, A. & SIMONATO, J.-P. 2012 Highly flexible transparent film heaters based on random networks of silver nanowires. *Nano Research* **5** (6), 427–433.
- [18] CHEONG, H.-G., SONG, D.-W. & PARK, J.-W. 2015 Transparent film heaters with highly enhanced thermal efficiency using silver nanowires and metal/metal-oxide blankets. *Microelectronic Engineering* **146**, 11–18.
- [19] CHEUK, K. W., PEI, K. & CHAN, P. K. 2016 Degradation mechanism of a junction-free transparent silver network electrode. *RSC Advances* **6** (77), 73769–73775.

- [20] CHIU, S., SHAO, T., CHEN, C., YAO, D. & HSU, C. 2006 Infrared microscopy of hot spots induced by joule heating in flip-chip snag solder joints under accelerated electromigration. *Applied Physics Letters* **88** (2), 022110.
- [21] COLE, K. D., BECK, J. V., HAJI-SHEIKH, A. & LITKOUHI, B. 2010 *Heat conduction using Green's functions*. Taylor & Francis.
- [22] DAS, S. R., SADEQUE, S., JEONG, C., CHEN, R., ALAM, M. A. & JANES, D. B. 2016 Coperculating networks: An approach for realizing high-performance transparent conductors using multicomponent nanostructured networks. *Nanophotonics* **5** (1), 180–195.
- [23] DE, S., HIGGINS, T. M., LYONS, P. E., DOHERTY, E. M., NIRMALRAJ, P. N., BLAU, W. J., BOLAND, J. J. & COLEMAN, J. N. 2009 Silver nanowire networks as flexible, transparent, conducting films: extremely high dc to optical conductivity ratios. *ACS Nano* **3** (7), 1767–1774.
- [24] DE, S., KING, P. J., LYONS, P. E., KHAN, U. & COLEMAN, J. N. 2010 Size effects and the problem with percolation in nanostructured transparent conductors. *ACS Nano* **4** (12), 7064–7072.
- [25] DEMELLO, A. J. 2006 Control and detection of chemical reactions in microfluidic systems. *Nature* **442** (7101), 394–402.
- [26] DEO, N. 2017 *Graph theory with applications to engineering and computer science*. Courier Dover Publications.
- [27] DOGANAY, D., COSKUN, S., GENLIK, S. P. & UNALAN, H. E. 2016 Silver nanowire decorated heatable textiles. *Nanotechnology* **27** (43), 435201.
- [28] DU, F., FISCHER, J. E. & WINEY, K. I. 2005 Effect of nanotube alignment on percolation conductivity in carbon nanotube/polymer composites. *Physical Review B* **72** (12), 121404.
- [29] DUFRESNE, E., CORWIN, E., GREENBLATT, N., ASHMORE, J., WANG, D., DINSMORE, A., CHENG, J., XIE, X., HUTCHINSON, J. & WEITZ, D. 2003 Flow and fracture in drying nanoparticle suspensions. *Physical Review Letters* **91** (22), 224501.

- [30] DUFRESNE, E., STARK, D., GREENBLATT, N., CHENG, J., HUTCHINSON, J., MAHADEVAN, L. & WEITZ, D. 2006 Dynamics of fracture in drying suspensions. *Langmuir* **22** (17), 7144–7147.
- [31] DUTTA, T. & TARAFDAR, S. 2014 Competition between cracking and peeling in composites: a simulation in 2-d. *Journal of Materials Science* **49** (21), 7507–7512.
- [32] ELLMER, K. 2012 Past achievements and future challenges in the development of optically transparent electrodes. *Nature Photonics* **6** (12), 809–817.
- [33] FAIRFIELD, J. A., RITTER, C., BELLEW, A. T., MCCARTHY, E. K., FERREIRA, M. S. & BOLAND, J. J. 2014 Effective electrode length enhances electrical activation of nanowire networks: experiment and simulation. *ACS Nano* **8** (9), 9542–9549.
- [34] FENG, L., XIE, N. & ZHONG, J. 2014 Carbon nanofibers and their composites: A review of synthesizing, properties and applications. *Materials* **7** (5), 3919–3945.
- [35] FORREST, S. R. 2005 The limits to organic photovoltaic cell efficiency. *MRS bulletin* **30** (01), 28–32.
- [36] FRANK, S. A. 2009 The common patterns of nature. *Journal of Evolutionary Biology* **22** (8), 1563–1585.
- [37] GAO, T., WANG, B., DING, B., LEE, J.-K. & LEU, P. W. 2014 Uniform and ordered copper nanomeshes by microsphere lithography for transparent electrodes. *Nano Letters* **14** (4), 2105–2110.
- [38] GAUTHIER, G., LAZARUS, V. & PAUCHARD, L. 2007 Alternating crack propagation during directional drying. *Langmuir* **23** (9), 4715–4718.
- [39] GHOSH, D., CHEN, T. & PRUNERI, V. 2010 High figure-of-merit ultrathin metal transparent electrodes incorporating a conductive grid. *Applied Physics Letters* **96** (4), 041109.
- [40] GHOSH, U. U., CHAKRABORTY, M., BHANDARI, A. B., CHAKRABORTY, S. & DASGUPTA, S. 2015 Effect of surface wettability on crack dynamics and morphology of colloidal films. *Langmuir* **31** (22), 6001–6010.
- [41] GOEHRING, L., CLEGG, W. J. & ROUTH, A. F. 2011 Wavy cracks in drying colloidal films. *Soft Matter* **7** (18), 7984–7987.

- [42] GOEHRING, L., CONROY, R., AKHTER, A., CLEGG, W. J. & ROUTH, A. F. 2010 Evolution of mud-crack patterns during repeated drying cycles. *Soft Matter* **6** (15), 3562–3567.
- [43] GOEHRING, L., NAKAHARA, A., DUTTA, T., TARAFDAR, S. & KITSUNEZAKI, S. 2015 *Desiccation cracks and their patterns: formation and modelling in science and nature*. John Wiley & Sons.
- [44] GROISMAN, A. & KAPLAN, E. 1994 An experimental study of cracking induced by desiccation. *Europhysics Letters* **25** (6), 415.
- [45] GUO, C. F. & REN, Z. 2015 Flexible transparent conductors based on metal nanowire networks. *Materials Today* **18** (3), 143–154.
- [46] GUO, C. F., SUN, T., LIU, Q., SUO, Z. & REN, Z. 2014 Highly stretchable and transparent nanomesh electrodes made by grain boundary lithography. *Nature Communications* **5**, 3121.
- [47] GUO, H., LIN, N., CHEN, Y., WANG, Z., XIE, Q., ZHENG, T., GAO, N., LI, S., KANG, J., CAI, D. *et al.* 2013 Copper nanowires as fully transparent conductive electrodes. *Scientific reports* **3**, 2323.
- [48] GUO, X., LIU, X., LUO, J., GAN, Z., MENG, Z. & ZHANG, N. 2015 Silver nanowire/polyimide composite transparent electrodes for reliable flexible polymer solar cells operating at high and ultra-low temperature. *RSC Advances* **5** (32), 24953–24959.
- [49] GUPTA, N., RAO, K. M., GUPTA, R., KREBS, F. C. & KULKARNI, G. U. 2017 Highly conformal ni micromesh as a current collecting front electrode for reduced cost si solar cell. *ACS Applied Materials & Interfaces* **9** (10), 8634–8640.
- [50] GUPTA, R. & KULKARNI, G. U. 2013 Holistic method for evaluating large area transparent conducting electrodes. *ACS Applied Materials & Interfaces* **5** (3), 730–736.
- [51] GUPTA, R., KUMAR, A., SADASIVAM, S., WALIA, S., KULKARNI, G. U., FISHER, T. S. & MARCONNET, A. 2017 Microscopic evaluation of electrical and thermal conduction in random metal wire networks. *ACS Applied Materials & Interfaces* **9** (15), 13703–13712.

- [52] GUPTA, R., RAO, K., SRIVASTAVA, K., KUMAR, A., KIRUTHIKA, S. & KULKARNI, G. U. 2014 Spray coating of crack templates for the fabrication of transparent conductors and heaters on flat and curved surfaces. *ACS applied materials & interfaces* **6** (16), 13688–13696.
- [53] HAACKE, G. 1976 New figure of merit for transparent conductors. *Journal of Applied Physics* **47** (9), 4086–4089.
- [54] HAN, B., HUANG, Y., LI, R., PENG, Q., LUO, J., PEI, K., HERCZYNSKI, A., KEMPA, K., REN, Z. & GAO, J. 2014 Bio-inspired networks for optoelectronic applications. *Nature Communications* **5**, 5674.
- [55] HAN, B., PEI, K., HUANG, Y., ZHANG, X., RONG, Q., LIN, Q., GUO, Y., SUN, T., GUO, C., CARNAHAN, D., GIERSIG, M., WANG, Y., GAO, J., REN, Z. & KEMPA, K. 2014 Uniform self-forming metallic network as a high-performance transparent conductive electrode. *Advanced Materials* **26** (6), 873–877.
- [56] HAN, B., PEI, K., HUANG, Y., ZHANG, X., RONG, Q., LIN, Q., GUO, Y., SUN, T., GUO, C., CARNAHAN, D. *et al.* 2014 Uniform self-forming metallic network as a high-performance transparent conductive electrode. *Advanced Materials* **26** (6), 873–877.
- [57] HAN, W., LI, B. & LIN, Z. 2013 Drying-mediated assembly of colloidal nanoparticles into large-scale microchannels. *ACS Nano* **7** (7), 6079–6085.
- [58] HAN, Y., LIN, J., LIU, Y., FU, H., MA, Y., JIN, P. & TAN, J. 2016 Crackle template based metallic mesh with highly homogeneous light transmission for high-performance transparent emi shielding. *Scientific reports* **6**, 25601.
- [59] HAUGER, T. C., AL-RAFIA, S. I. & BURIK, J. M. 2013 Rolling silver nanowire electrodes: simultaneously addressing adhesion, roughness, and conductivity. *ACS Applied Materials & Interfaces* **5** (23), 12663–12671.
- [60] HAZRA, S., SIRCAR, S., KHATUN, T., CHOUDHURY, M. D., GIRI, A., KARMAKAR, S., DUTTA, T., DAS, S. & TARAFDAR, S. 2016 Unstable crack propagation in laponite® gels: selection of a sinusoidal mode in an electric field. *RSC Advances* **6** (69), 64297–64305.

- [61] HEITZ, J., LEROY, Y., HÉBRARD, L. & LALLEMENT, C. 2011 Theoretical characterization of the topology of connected carbon nanotubes in random networks. *Nanotechnology* **22** (34), 345703.
- [62] HIERL, T., SCHREER, O., ZETTNER, J., GROSS, W. & SCHULZ, M. J. 1999 Thermal infrared microscopy (tim) with sub-10- μm spatial resolution. In *AeroSense'99*, pp. 446–452. International Society for Optics and Photonics.
- [63] HIESINGER, H. & HEAD, J. W. 2000 Characteristics and origin of polygonal terrain in southern utopia planitia, mars: results from mars orbiter laser altimeter and mars orbiter camera data. *Journal of Geophysical Research: Planets* **105** (E5), 11999–12022.
- [64] HU, L., HECHT, D. & GRÜNER, G. 2004 Percolation in transparent and conducting carbon nanotube networks. *Nano Letters* **4** (12), 2513–2517.
- [65] HUNGER, C., RAO, K. D. M., GUPTA, R., SINGH, C. R., KULKARNI, G. U. & THELAKKAT, M. 2015 Transparent metal network with low haze and high figure of merit applied to front and back electrodes in semitransparent ito-free polymer solar cells. *Energy Technology* **3** (6), 638–645.
- [66] IM, K., CHO, K., KWAK, K., KIM, J. & KIM, S. 2013 Flexible transparent heaters with heating films made of indium tin oxide nanoparticles. *Journal of Nanoscience and Nanotechnology* **13** (5), 3519–3521.
- [67] INASAWA, S. & YAMAGUCHI, Y. 2012 Self-organized pattern formation of cracks perpendicular to the drying direction of a colloidal suspension. *Soft Matter* **8** (8), 2416–2422.
- [68] JOHNSON, R. C. 2014 (accessed February 11, 2015) *Conductive Polymer Beats Indium Tin Oxide by 10x*. http://www.eetimes.com/document.asp?doc_id=1322697.
- [69] JUNG, D., KIM, D., LEE, K. H., OVERZET, L. J. & LEE, G. S. 2013 Transparent film heaters using multi-walled carbon nanotube sheets. *Sensors and Actuators A: Physical* **199**, 176–180.
- [70] KANG, J., JANG, Y., KIM, Y., CHO, S.-H., SUHR, J., HONG, B. H., CHOI, J.-B. & BYUN, D. 2015 An ag-grid/graphene hybrid structure for large-scale, transparent, flexible heaters. *Nanoscale* **7** (15), 6567–6573.

- [71] KANG, M.-G. & GUO, L. J. 2007 Nanoimprinted semitransparent metal electrodes and their application in organic light-emitting diodes. *Advanced Materials* **19** (10), 1391–1396.
- [72] KAPPERT, E. J., PAVLENKO, D., MALZBENDER, J., NIJMEIJER, A., BENES, N. E. & TSAI, P. A. 2015 Formation and prevention of fractures in sol-gel-derived thin films. *Soft Matter* **11** (5), 882–888.
- [73] KATTOUF, B., WARWAR, C., BALLA, I., SHASHA, H., SHERMAN, D. & FREY, G. L. 2015 Hexagonal patterns in thin films: experiments and modeling. *Extreme Mechanics Letters* **2**, 65–71.
- [74] KAYES, B. M., ATWATER, H. A. & LEWIS, N. S. 2005 Comparison of the device physics principles of planar and radial pn junction nanorod solar cells. *Journal of Applied Physics* **97** (11), 114302.
- [75] KHANDURINA, J., MCKNIGHT, T. E., JACOBSON, S. C., WATERS, L. C., FOOTE, R. S. & RAMSEY, J. M. 2000 Integrated system for rapid pcr-based dna analysis in microfluidic devices. *Analytical Chemistry* **72** (13), 2995–3000.
- [76] KHATUN, T., CHOUDHURY, M. D., DUTTA, T. & TARAFDAR, S. 2012 Electric-field-induced crack patterns: experiments and simulation. *Physical Review E* **86** (1), 016114.
- [77] KHATUN, T., DUTTA, T. & TARAFDAR, S. 2015 Topology of desiccation crack patterns in clay and invariance of crack interface area with thickness. *The European Physical Journal E* **38** (8), 83.
- [78] KIM, D., LEE, H.-C., WOO, J. Y. & HAN, C.-S. 2010 Thermal behavior of transparent film heaters made of single-walled carbon nanotubes. *The Journal of Physical Chemistry C* **114** (13), 5817–5821.
- [79] KIM, D., ZHU, L., JEONG, D.-J., CHUN, K., BANG, Y.-Y., KIM, S.-R., KIM, J.-H. & OH, S.-K. 2013 Transparent flexible heater based on hybrid of carbon nanotubes and silver nanowires. *Carbon* **63**, 530–536.
- [80] KIM, H., KIM, Y., KIM, K. S., JEONG, H. Y., JANG, A.-R., HAN, S. H., YOON, D. H., SUH, K. S., SHIN, H. S., KIM, T. *et al.* 2013 Flexible thermochromic window based on hybridized vo₂/graphene. *ACS Nano* **7** (7), 5769–5776.

- [81] KIM, M., KIM, D.-J., HA, D. & KIM, T. 2016 Cracking-assisted fabrication of nanoscale patterns for micro/nanotechnological applications. *Nanoscale* **8** (18), 9461–9479.
- [82] KIM, N., UM, H.-D., CHOI, I., KIM, K.-H. & SEO, K. 2016 18.4%-efficient heterojunction si solar cells using optimized ito/top electrode. *ACS Applied Materials & Interfaces* **8** (18), 11412–11417.
- [83] KIRKPATRICK, S. 1971 Classical transport in disordered media: scaling and effective-medium theories. *Physical Review Letters* **27** (25), 1722.
- [84] KIRKPATRICK, S. 1973 Percolation and conduction. *Reviews of modern physics* **45** (4), 574.
- [85] KIRUTHIKA, S., GUPTA, R., ANAND, A., KUMAR, A. & KULKARNI, G. 2015 Fabrication of oxidation-resistant metal wire network-based transparent electrodes by a spray-roll coating process. *ACS Applied Materials & Interfaces* **7** (49), 27215–27222.
- [86] KIRUTHIKA, S., GUPTA, R. & KULKARNI, G. U. 2014 Large area defrosting windows based on electrothermal heating of highly conducting and transmitting Ag wire mesh. *RSC Advances* **4** (91), 49745–49751.
- [87] KIRUTHIKA, S., RAO, K. D. M., KUMAR, A., GUPTA, R. & KULKARNI, G. U. 2014 Metal wire network based transparent conducting electrodes fabricated using interconnected crackled layer as template. *Materials Research Express* **1** (2), 026301.
- [88] KITSUNEZAKI, S. 2009 Crack propagation speed in the drying process of paste. *Journal of the Physical Society of Japan* **78** (6), 064801–064801.
- [89] KITSUNEZAKI, S., NAKAHARA, A. & MATSUO, Y. 2016 Shaking-induced stress anisotropy in the memory effect of paste. *Europhysics Letters* **114** (6), 64002.
- [90] KULKARNI, G. U., KIRUTHIKA, S., GUPTA, R. & RAO, K. 2015 Towards low cost materials and methods for transparent electrodes. *Current Opinion in Chemical Engineering* **8**, 60–68.
- [91] KUMAR, A. 2017 Predicting efficiency of solar cells based on transparent conducting electrodes. *Journal of Applied Physics* **121** (1), 014502.

- [92] KUMAR, A. & KULKARNI, G. 2016 Evaluating conducting network based transparent electrodes from geometrical considerations. *Journal of Applied Physics* **119** (1), 015102.
- [93] KUMAR, A., PUJAR, R., GUPTA, N., TARAFDAR, S. & KULKARNI, G. U. 2017 Stress modulation in desiccating crack networks for producing effective templates for patterning metal network based transparent conductors. *Applied Physics Letters* **111** (1), 013502.
- [94] KUMAR, A. & ZHOU, C. 2010 The race to replace tin-doped indium oxide: which material will win? *ACS Nano* **4** (1), 11–14.
- [95] KWON, N., KIM, K., HEO, J., YI, I. & CHUNG, I. 2014 Study on ag mesh/conductive oxide hybrid transparent electrode for film heaters. *Nanotechnology* **25** (26), 265702.
- [96] LÄMMER, S., GEHLSSEN, B. & HELBING, D. 2006 Scaling laws in the spatial structure of urban road networks. *Physica A: Statistical Mechanics and its Applications* **363** (1), 89–95.
- [97] LANGLEY, D., GIUSTI, G., LAGRANGE, M., COLLINS, R., JIMÉNEZ, C., BRÉCHET, Y. & BELLET, D. 2014 Silver nanowire networks: physical properties and potential integration in solar cells. *Solar Energy Materials and Solar Cells* **125**, 318–324.
- [98] LANGLEY, D., GIUSTI, G., MAYOUSSE, C., CELLE, C., BELLET, D. & SIMONATO, J.-P. 2013 Flexible transparent conductive materials based on silver nanowire networks: a review. *Nanotechnology* **24** (45), 452001.
- [99] LAST, B. & THOULESS, D. 1971 Percolation theory and electrical conductivity. *Physical review letters* **27** (25), 1719.
- [100] LAYANI, M., BERMAN, R. & MAGDASSI, S. 2014 Printing holes by a dewetting solution enables formation of a transparent conductive film. *ACS Applied Materials & Interfaces* **6** (21), 18668–18672.
- [101] LAZARUS, V. & PAUCHARD, L. 2011 From craquelures to spiral crack patterns: influence of layer thickness on the crack patterns induced by desiccation. *Soft Matter* **7** (6), 2552–2559.

- [102] LEBO, R. B. 1921 Properties of mixtures of isopropyl alcohol and water. *Journal of the American Chemical Society* **43** (5), 1005–1011.
- [103] LECOCQ, N. & VANDEWALLE, N. 2002 Experimental study of cracking induced by desiccation in 1-dimensional systems. *The European Physical Journal E: Soft Matter and Biological Physics* **8** (4), 445–452.
- [104] LEE, D.-E., GO, S., HWANG, G., CHIN, B. D. & LEE, D. H. 2013 Two-dimensional micropatterns via crystal growth of Na_2CO_3 for fabrication of transparent electrodes. *Langmuir* **29** (39), 12259–12265.
- [105] LEE, J.-Y., CONNOR, S. T., CUI, Y. & PEUMANS, P. 2008 Solution-processed metal nanowire mesh transparent electrodes. *Nano Letters* **8** (2), 689–692.
- [106] LEE, S.-M., CHAE, J.-S., KIM, D.-Y. & CHOI, K. C. 2014 Plasmonic nanomeshes as large-area, low-resistive transparent electrodes and their application to ito-free organic light-emitting diodes. *Organic Electronics* **15** (11), 3354–3361.
- [107] LEE, W., LEE, J., LEE, S., YI, W., HAN, S.-H. & CHO, B. W. 2008 Enhanced charge collection and reduced recombination of cds/ tio2 quantum-dots sensitized solar cells in the presence of single-walled carbon nanotubes. *Applied Physics Letters* **92** (15), 153510.
- [108] LEE, W. P. & ROUTH, A. F. 2004 Why do drying films crack? *Langmuir* **20** (23), 9885–9888.
- [109] LEEM, D.-S., EDWARDS, A., FAIST, M., NELSON, J., BRADLEY, D. D. & DE MELLO, J. C. 2011 Efficient organic solar cells with solution-processed silver nanowire electrodes. *Advanced Materials* **23** (38), 4371–4375.
- [110] LENES, M., KOSTER, L., MIHAILETCHI, V. & BLOM, P. 2006 Thickness dependence of the efficiency of polymer: fullerene bulk heterojunction solar cells. *Applied physics letters* **88** (24), 243502–243502.
- [111] LI, B., JIANG, B., HAN, W., HE, M., LI, X., WANG, W., HONG, S. W., BYUN, M., LIN, S. & LIN, Z. 2017 Harnessing colloidal crack formation by flow-enabled self-assembly. *Angewandte Chemie* **129** (16), 4625–4630.

- [112] LI, C., THOSTENSON, E. T. & CHOU, T.-W. 2008 Effect of nanotube waviness on the electrical conductivity of carbon nanotube-based composites. *Composites Science and Technology* **68** (6), 1445–1452.
- [113] LIM, J. W., LEE, Y. T., PANDEY, R., YOO, T.-H., SANG, B.-I., JU, B.-K., HWANG, D. K. & CHOI, W. K. 2014 Effect of geometric lattice design on optical/electrical properties of transparent silver grid for organic solar cells. *Optics Express* **22** (22), 26891–26899.
- [114] LIN, Z. & GRANICK, S. 2005 Patterns formed by droplet evaporation from a restricted geometry. *Journal of the American Chemical Society* **127** (9), 2816–2817.
- [115] LIU, C., TANG, C.-S., SHI, B. & SUO, W.-B. 2013 Automatic quantification of crack patterns by image processing. *Computers & geosciences* **57**, 77–80.
- [116] LIU, L., PENG, S., NIU, X. & WEN, W. 2006 Microheaters fabricated from a conducting composite. *Applied Physics Letters* **89** (22), 223521.
- [117] MAILER, A. G. & CLEGG, P. S. 2014 Cracking in films of titanium dioxide nanoparticles with varying interaction strength. *Journal of Colloid and Interface Science* **417**, 317–324.
- [118] MANDELBROT, B. B. & PIGNONI, R. 1983 *The fractal geometry of nature*, , vol. 173. WH freeman New York.
- [119] MARCONNET, A. M., YAMAMOTO, N., PANZER, M. A., WARDLE, B. L. & GOODSON, K. E. 2011 Thermal conduction in aligned carbon nanotube–polymer nanocomposites with high packing density. *ACS Nano* **5** (6), 4818–4825.
- [120] MARUS, M., HUBAREVICH, A., FAN, W., WANG, H., SMIRNOV, A., WANG, K., HUANG, H. & SUN, X. 2018 Optical haze of randomly arranged silver nanowire transparent conductive films with wide range of nanowire diameters. *AIP Advances* **8** (3), 035201.
- [121] MATULA, R. A. 1979 Electrical resistivity of copper, gold, palladium, and silver. *Journal of Physical and Chemical Reference Data* **8** (4), 1147–1298.
- [122] MINAMI, T. 2008 Present status of transparent conducting oxide thin-film development for indium-tin-oxide (ito) substitutes. *Thin Solid Films* **516** (17), 5822–5828.

- [123] MONTERO, R. S. & BRIBIESCA, E. 2009 State of the art of compactness and circularity measures. In *International Mathematical Forum*, , vol. 4, pp. 1305–1335.
- [124] MORAG, A., PHILOSOF-MAZOR, L., VOLINSKY, R., MENTOVICH, E., RICHTER, S. & JELINEK, R. 2011 Self-assembled transparent conductive electrodes from au nanoparticles in surfactant monolayer templates. *Advanced Materials* **23** (37), 4327–4331.
- [125] MUTISO, R. M., SHERROTT, M. C., RATHMELL, A. R., WILEY, B. J. & WINEY, K. I. 2013 Integrating simulations and experiments to predict sheet resistance and optical transmittance in nanowire films for transparent conductors. *ACS Nano* **7** (9), 7654–7663.
- [126] NAG, S., SINHA, S., SADHUKHAN, S., DUTTA, T. & TARAFDAR, S. 2009 Crack patterns in desiccating clay–polymer mixtures with varying composition. *Journal of Physics: Condensed Matter* **22** (1), 015402.
- [127] NAM, K. H., PARK, I. H. & KO, S. H. 2012 Patterning by controlled cracking. *Nature* **485** (7397), 221.
- [128] NANDAKISHORE, P. & GOEHRING, L. 2016 Crack patterns over uneven substrates. *Soft Matter* **12** (8), 2253–2263.
- [129] NIRMALRAJ, P. N., LYONS, P. E., DE, S., COLEMAN, J. N. & BOLAND, J. J. 2009 Electrical connectivity in single-walled carbon nanotube networks. *Nano Letters* **9** (11), 3890–3895.
- [130] O’CALLAGHAN, C., DA ROCHA, C. G., MANNING, H. G., BOLAND, J. J. & FERREIRA, M. S. 2016 Effective medium theory for the conductivity of disordered metallic nanowire networks. *Physical Chemistry Chemical Physics* **18** (39), 27564–27571.
- [131] PASRICHA, K., WAD, U., PASRICHA, R. & OGALE, S. 2009 Parametric dependence studies on cracking of clay. *Physica A: Statistical Mechanics and its Applications* **388** (8), 1352–1358.
- [132] PAUCHARD, L., ADDA-BEDIA, M., ALLAIN, C. & COUDER, Y. 2003 Morphologies resulting from the directional propagation of fractures. *Physical Review E* **67** (2), 027103.

- [133] PEI, K., WANG, Z., REN, X., ZHANG, Z., PENG, B. & CHAN, P. K. 2015 Fully transparent organic transistors with junction-free metallic network electrodes. *Applied Physics Letters* **107** (3), 033302.
- [134] PENG, Q., LI, S., HAN, B., RONG, Q., LU, X., WANG, Q., ZENG, M., ZHOU, G., LIU, J.-M., KEMPA, K. *et al.* 2016 Colossal figure of merit in transparent-conducting metallic ribbon networks. *Advanced Materials Technologies* **1** (6).
- [135] PERNA, A., KUNTZ, P. & DOUADY, S. 2011 Characterization of spatial networklike patterns from junction geometry. *Physical Review E* **83** (6), 066106.
- [136] PIVRIKAS, A., SARICIFTCI, N. S., JUŠKA, G. & ÖSTERBACKA, R. 2007 A review of charge transport and recombination in polymer/fullerene organic solar cells. *Progress in Photovoltaics: Research and Applications* **15** (8), 677–696.
- [137] PRESTON, C., XU, Y., HAN, X., MUNDAY, J. N. & HU, L. 2013 Optical haze of transparent and conductive silver nanowire films. *Nano Research* **6** (7), 461.
- [138] PROSSER, J. H., BRUGAROLAS, T., LEE, S., NOLTE, A. J. & LEE, D. 2012 Avoiding cracks in nanoparticle films. *Nano letters* **12** (10), 5287–5291.
- [139] RAO, K., HUNGER, C., GUPTA, R., KULKARNI, G. U. & THELAKKAT, M. 2014 A cracked polymer templated metal network as a transparent conducting electrode for ito-free organic solar cells. *Physical Chemistry Chemical Physics* **16** (29), 15107–15110.
- [140] RAO, K. & KULKARNI, G. U. 2014 A highly crystalline single au wire network as a high temperature transparent heater. *RSC Advances* **6** (11), 5645–5651.
- [141] RAO, K. D. M. 2014 Novel electrodes and active materials for optoelectronics and memory devices (phd thesis) pp. 139–150.
- [142] RAO, K. D. M., GUPTA, R. & KULKARNI, G. U. 2014 Fabrication of large area, high-performance, transparent conducting electrodes using a spontaneously formed crackle network as template. *Advanced Materials Interfaces* **1** (6), 1400090.
- [143] RAO, K. D. M., HUNGER, C., GUPTA, R., KULKARNI, G. U. & THELAKKAT, M. 2014 A cracked polymer templated metal network as a transparent conducting

- electrode for ito-free organic solar cells. *Phys. Chem. Chem. Phys.* **16**, 15107–15110.
- [144] REUTELER, J., HÜTTER, M. & GAUCKLER, L. J. 2011 Backbone of conductivity in two-dimensional metal-insulator composites. *Journal of Applied Physics* **110** (2), 024909.
- [145] DA ROCHA, C. G., MANNING, H. G., O'CALLAGHAN, C., RITTER, C., BELLEW, A. T., BOLAND, J. J. & FERREIRA, M. S. 2015 Ultimate conductivity performance in metallic nanowire networks. *Nanoscale* **7** (30), 13011–13016.
- [146] ROWELL, M. W., TOPINKA, M. A., MCGEHEE, M. D., PRALL, H.-J., DENNLER, G., SARICIFTCI, N. S., HU, L. & GRUNER, G. 2006 Organic solar cells with carbon nanotube network electrodes. *Applied Physics Letters* **88** (23), 233506.
- [147] SADHUKHAN, S., DUTTA, T. & TARAFDAR, S. 2007 A bidisperse ballistic deposition model for simulating porous media: the effect of grain size, composition and relaxation. *Journal of Statistical Mechanics: Theory and Experiment* **2007** (06), P06006.
- [148] SADHUKHAN, S., DUTTA, T. & TARAFDAR, S. 2011 Crack formation in composites through a spring model. *Physica A: Statistical Mechanics and its Applications* **390** (4), 731–740.
- [149] SADHUKHAN, S., MAJUMDER, S. R., MAL, D., DUTTA, T. & TARAFDAR, S. 2007 Desiccation cracks on different substrates: simulation by a spring network model. *Journal of Physics: Condensed Matter* **19** (35), 356206.
- [150] SADHUKHAN, S., PREHL, J., BLAUDECK, P., HOFFMANN, K., DUTTA, T. & TARAFDAR, S. 2008 Desiccation of a clay film: Cracking versus peeling. *The European Physical Journal E: Soft Matter and Biological Physics* **27** (4), 391–395.
- [151] SANNICOLO, T., LAGRANGE, M., CABOS, A., CELLE, C., SIMONATO, J.-P. & BELLET, D. 2016 Metallic nanowire-based transparent electrodes for next generation flexible devices: a review. *Small* .
- [152] SELZER, F., FLORESCA, C., KNEPPE, D., BORMANN, L., SACHSE, C., WEISS, N., EYCHMÜLLER, A., AMASSIAN, A., MÜLLER-MESKAMP, L. & LEO, K.

- 2016 Electrical limit of silver nanowire electrodes: Direct measurement of the nanowire junction resistance. *Applied Physics Letters* **108** (16), 163302.
- [153] SEONG, B., YOO, H., NGUYEN, V. D., JANG, Y., RYU, C. & BYUN, D. 2014 Metal-mesh based transparent electrode on a 3-d curved surface by electrohydrodynamic jet printing. *Journal of Micromechanics and Microengineering* **24** (9), 097002.
- [154] SEPULVEDA-MORA, S. B. & CLOUTIER, S. G. 2012 Figures of merit for high-performance transparent electrodes using dip-coated silver nanowire networks. *Journal of Nanomaterials* **2012**, 9.
- [155] SHIMONI, A., AZOUBEL, S. & MAGDASSI, S. 2014 Inkjet printing of flexible high-performance carbon nanotube transparent conductive films by “coffee ring effect”. *Nanoscale* **6** (19), 11084–11089.
- [156] SLOOFF, L., VEENSTRA, S., KROON, J., MOET, D., SWEELSEN, J. & KOETSE, M. 2007 Determining the internal quantum efficiency of highly efficient polymer solar cells through optical modeling. *Applied Physics Letters* **90** (14), 143506.
- [157] SMITH, M. & SHARP, J. 2011 Effects of substrate constraint on crack pattern formation in thin films of colloidal polystyrene particles. *Langmuir* **27** (13), 8009–8017.
- [158] SOREL, S., BELLET, D. & COLEMAN, J. N. 2014 Relationship between material properties and transparent heater performance for both bulk-like and percolative nanostructured networks. *ACS Nano* **8** (5), 4805–4814.
- [159] STEVENS, P. S. 1974 Patterns in nature .
- [160] TIRUMKUDULU, M. S. & RUSSEL, W. B. 2005 Cracking in drying latex films. *Langmuir* **21** (11), 4938–4948.
- [161] TOGA, K. & ALACA, B. E. 2006 Junction formation during desiccation cracking. *Physical Review E* **74** (2), 021405.
- [162] TOKUNO, T., NOGI, M., JIU, J., SUGAHARA, T. & SUGANUMA, K. 2012 Transparent electrodes fabricated via the self-assembly of silver nanowires using a bubble template. *Langmuir* **28** (25), 9298–9302.

- [163] VANROSSUM, G. & DRAKE, F. L. 2010 *The Python Language Reference*. Python Software Foundation.
- [164] VOGEL, H.-J., HOFFMANN, H., LEOPOLD, A. & ROTH, K. 2005 Studies of crack dynamics in clay soil: II. a physically based model for crack formation. *Geoderma* **125** (3), 213–223.
- [165] VOGEL, H.-J., HOFFMANN, H. & ROTH, K. 2005 Studies of crack dynamics in clay soil: I. experimental methods, results, and morphological quantification. *Geoderma* **125** (3), 203–211.
- [166] VOGEL, H.-J., HOFFMANN, H. & ROTH, K. 2005 Studies of crack dynamics in clay soil: I. experimental methods, results, and morphological quantification. *Geoderma* **125** (3), 203–211.
- [167] WALIA, S., GUPTA, R. & KULKARNI, G. U. 2015 Disposable heater arrays using printed silver patterns on polyethylene terephthalate for multipurpose applications. *Energy Technology* **3** (4), 359–365.
- [168] WATTS, D. J. & STROGATZ, S. H. 1998 Collective dynamics of small-world networks. *Nature* **393** (6684), 440–442.
- [169] WEISSTEIN, E. W. (accessed October 10, 2014) *Wolfram Alpha*. <http://mathworld.wolfram.com/RegularizedGammaFunction.html>.
- [170] WEST, G. B., BROWN, J. H. & ENQUIST, B. J. 1999 A general model for the structure and allometry of plant vascular systems. *Nature* **400** (6745), 664–667.
- [171] WU, B., HEIDELBERG, A. & BOLAND, J. J. 2005 Mechanical properties of ultrahigh-strength gold nanowires. *Nature materials* **4** (7), 525–529.
- [172] WU, F.-Y. 2004 Theory of resistor networks: the two-point resistance. *Journal of Physics A: Mathematical and General* **37** (26), 6653.
- [173] WU, H., HU, L., ROWELL, M. W., KONG, D., CHA, J. J., McDONOUGH, J. R., ZHU, J., YANG, Y., MCGEHEE, M. D. & CUI, Y. 2010 Electrospun metal nanofiber webs as high-performance transparent electrode. *Nano Letters* **10** (10), 4242–4248.

- [174] WU, H., KONG, D., RUAN, Z., HSU, P.-C., WANG, S., YU, Z., CARNEY, T. J., HU, L., FAN, S. & CUI, Y. 2013 A transparent electrode based on a metal nanotrough network. *Nature Nanotechnology* **8** (6), 421–425.
- [175] XIE, S., OUYANG, Z., JIA, B. & GU, M. 2013 Large-size, high-uniformity, random silver nanowire networks as transparent electrodes for crystalline silicon wafer solar cells. *Optics Express* **21** (103), A355–A362.
- [176] XU, B.-B., XIA, H., NIU, L.-G., ZHANG, Y.-L., SUN, K., CHEN, Q.-D., XU, Y., LV, Z.-Q., LI, Z.-H., MISAWA, H. *et al.* 2010 Flexible nanowiring of metal on nonplanar substrates by femtosecond-laser-induced electroless plating. *Small* **6** (16), 1762–1766.
- [177] XU, F. & ZHU, Y. 2012 Highly conductive and stretchable silver nanowire conductors. *Advanced Materials* **24** (37), 5117–5122.
- [178] XU, Y., GERMAN, G. K., MERTZ, A. F. & DUFRESNE, E. R. 2013 Imaging stress and strain in the fracture of drying colloidal films. *Soft Matter* **9** (14), 3735–3740.
- [179] YAMADA, T., HAYAMIZU, Y., YAMAMOTO, Y., YOMOGIDA, Y., IZADINAJAFABADI, A., FUTABA, D. N. & HATA, K. 2011 A stretchable carbon nanotube strain sensor for human-motion detection. *Nature Nanotechnology* **6** (5), 296–301.
- [180] YANG, G., LIU, B., CHENG, K. & DU, Z. 2015 Modulation of optical transmittance and conductivity by the period, linewidth and height of au square mesh electrodes. *Optics Express* **23** (3), A62–A70.
- [181] YANG, G., LIU, B., CHENG, K. & DU, Z. 2015 Modulation of optical transmittance and conductivity by the period, linewidth and height of au square mesh electrodes. *Opt. Express* **23** (3), A62–A70.
- [182] YAO, S. & ZHU, Y. 2014 Wearable multifunctional sensors using printed stretchable conductors made of silver nanowires. *Nanoscale* **6** (4), 2345–2352.
- [183] YE, S., RATHMELL, A. R., CHEN, Z., STEWART, I. E. & WILEY, B. J. 2014 Metal nanowire networks: The next generation of transparent conductors. *Advanced Materials* **26** (39), 6670–6687.

-
- [184] YOON, Y.-H., SONG, J.-W., KIM, D., KIM, J., PARK, J.-K., OH, S.-K. & HAN, C.-S. 2007 Transparent film heater using single-walled carbon nanotubes. *Advanced Materials* **19** (23), 4284–4287.
- [185] YU, Z., LI, L., ZHANG, Q., HU, W. & PEI, Q. 2011 Silver nanowire-polymer composite electrodes for efficient polymer solar cells. *Advanced Materials* **23** (38), 4453–4457.
- [186] ŽEŽELJ, M. & STANKOVIĆ, I. 2012 From percolating to dense random stick networks: Conductivity model investigation. *Physical Review B* **86** (13), 134202.

List of Publications

1. **Kumar, Ankush**, Vidyadhiraja, N. S. V, & Kulkarni, G. U. (2017) Current distribution in conducting nano-wire networks. *Journal of Applied Physics*, 122, 045101
2. **Kumar, Ankush**, Rajashekhar , P, Gupta, N, Tarafdar S & Kulkarni, G. U. (2017) Stress modulation in desiccating crack networks for producing ective tempaltes for patterning metal network based transparent conductors. *Applied Physics Letter*, 111, 013502.
3. Gupta, R,# **Kumar, Ankush**,# Sridhar, S., Kulkarni, G. U., Fisher T, & Marconnet, A (2017) Microscopic Evaluation of Electrical and Thermal Conduction in Random Metal Wire Networks. *ACS Applied Materials & Interfaces*, 9, 13703. #Share equal Ist authorship
4. **Kumar, Ankush** (2017) Predicting efficiency of solar cells based on transparent conducting electrodes, *Journal of Applied Physics*, 121, 014502.
5. **Kumar, Ankush** & Kulkarni, G. U. (2016) Evaluating conducting network based transparent electrodes from geometrical consideration, *Journal of Applied Physics*, 119, 015102.
6. Kiruthika, S., Rao, K. D. M., **Kumar, Ankush**, Gupta, R. & Kulkarni, G. U. (2014) Metal wire network based transparent conducting electrodes fabricated using interconnected crackled layer as template, *Materials Research Express*, 1, 026301.
7. Mondol, I.#, **Kumar, Ankush**#, Rao, K. D. M & Kulkarni, G. U. Parallel cracks from a desiccating colloidal layer under gravity flow and their use in fabricating metal micro-patterns. (Accepted, *Journal of Physics and Chemistry of Solids*), # Share Equal First authorship.
8. **Kumar, Ankush** and Kulkarni G. U Time evolution and hierarchical nature of cracks. (submitted)
9. **Kumar, Ankush**, Pujar R., Rao K. D. M, Tarafdar,S., Kulkarni G. U. Modulating crack network for efficient transparent electrodes using mixture of solvents. (submitted)
10. Sadhukhan, S., **Kumar, Ankush**, Kulkarni G . U., Tarafdar S., Dutta T. Designing optimum crack pattern template for fabricating transparent conducting electrodes: A spring network simulation in 3 dimensions (under preparation)
11. **Kumar, Ankush** and Kulkarni G. U. Hierarchical networks for efficient transport (under preparation)

12.. Rao K. D. M, Gupta N., Srivastava K., Gupta R., **Kumar, Ankush**, Marconnet A., Fisher T and Kulkarni G. U. Ultra-sensitive transparent electronic skin-like strain sensor based on single Au wire network (under preparation)

13. **Kumar, Ankush**, Srivastava, I., Kulkarni, G. U. & Fisher, T. Transient studies of thermal transport using Green's function solution equations (under preparation)

Publications not part of thesis:

14. Kiruthika, S, Mondal, I., M. Janani, **Kumar, Ankush**, Madhuri, V., Nair G., Prasad S. K & G. U. Kulkarni, Metal mesh as transparent electrodes for liquid crystal devices (under preparation)

15. Kiruthika, S., Gupta, R, Anand A., **Kumar, Ankush** & Kulkarni, G. U. (2014) Fabrication of oxidation-resistant metal wire network-based transparent electrodes by a spray-roll coating process, ACS Applied Materials & Interfaces, 49, 27215

16. Gupta, R., Rao, K. D. M., Srivastava, K., **Kumar, Ankush**, Kiruthika, S., & Kulkarni, G. U. (2014) Spray Coating of Crack Templates for the Fabrication of Transparent Conductors and Heaters on Flat and Curved Surfaces. ACS Applied Materials & Interfaces, 6, 13688.